Kai Sandvold Beckwith

# Micro- and nanostructured devices for cell studies

Avhandling for graden philosophiae doctor

Trondheim, august 2015

Norges teknisk-naturvitenskapelige universitet
Fakultet for naturvitenskap og teknologi
Institutt for fysikk

NTNU
Kunnskap for en bedre verden

**NTNU**
Norges teknisk-naturvitenskapelige universitet

Avhandling for graden philosophiae doctor

Fakultet for naturvitenskap og teknologi
Institutt for fysikk

© Kai Sandvold Beckwith

ISBN 978-82-326-1136-2 (trykt utg.)
ISBN 978-82-326-1137-9 (elektr. utg.)
ISSN 1503-8181

Doktoravhandlinger ved NTNU, 2015:240

Trykket av NTNU Grafisk senter

# *Abstract*

Cell culture is a fundamental and valuable tool for modern biomedical research. The purpose of this work has been to expand the possibilities and methods of cell culture through engineering of the cell culture substrate. A range of micro- and nanofabrication tools were used to structure new material systems and combinations that could be applied as cell interfaces.

Several different material systems and applications were explored. Soft lithography was used to produce patterns of cell-adherent polydopamine on cell-repellent poly(vinyl alcohol) hydrogels as an effective and stable cell patterning and patterned co-culture platform. Microscopic wells and a reference grid were thermomoulded into aclar polymer films and used as substrate enabling efficient correlative 3D optical and electron imaging of the same cells. Surfaces with high aspect ratio CuO nanowires were controllably produced and explored as a surface-based delivery platform for genetic material to cultured cells. Particular emphasis was put on better understanding the cell-nanowire interface, with the important result that membrane engulfment of the nanowires likely inhibits efficient gene transfer. The idea of better understanding the interface between cells and surface nanostructures was further pursued in the development of a tunable, high aspect ratio polymer nanostructure platform. This platform enabled high resolution optical imaging of cell interactions with the polymer nanostructures. Details of cell morphology, membrane conformations and cytoskeletal organization in response to nanopillars and nanolines was explored. Further, this platform was applied to study the dynamics of migrating cells on polymer nanopillar arrays, showing strong interactions that alter migration mechanisms and speed.

In summary, this work demonstrates how the bio-focused design of micro- and nanostructured platforms can pave the way to novel, functional devices and surfaces. In turn such devices contribute to furthering the use of advanced cell culture systems for modern biomedical research.

# *Acknowledgements*

During the four years I have been researching and teaching as a PhD-student at biophysics at NTNU there are many people who have played important roles in the end result contained herein. And more importantly, people who have been friends and colleagues, making my time as a PhD student a rewarding and interesting experience.

First and foremost, I would like to thank my supervisor Pawel. His attentive supervision, open-door policy and enthusiasm for science and technology has been a pleasure and inspiration for me to experience during my PhD.

The members of our group and other co-workers including Magnus, David, Sindre, Nina, Jonas, Sylvie and Armend have been important contributors to a good social and academic environment. Gjertrud, Kristin and Astrid and the NTNU NanoLab staff have patiently assisted with all the numerous practicalities encountered during research. Astrid Lægreid, Bjørn Torger Stokke and Catharina Davies at NTNU and Oddmund Bakke at UiO have provided valuable discussions, materials and laboratory facilities for this work.

It has also been a pleasure to work with all co-authors and contributors to this work, including Karen Martinez and Sara Bonde at KU, Justin Wells and Simon Cooil at physics, Trude Helen Flo and Øyvind Halaas at DMF and Gerbrand Koster, Frode Skjeldal and Cinzia Progida at UiO. In particular I have been lucky to have had the opportunity to both work with and have the support of my wife Marianne. She has been a constant presence and enthusiastic partner during my PhD. Recently, our son Edvin has also greatly contributed with his good spirits and helping me get up in the morning.

I have had the opportunity to co-supervise several talented master students including Åsmund Flobak, Jonathan Torstensen, Frederic Linboe and Rasmus Schanke. They have performed valuable research, aiding me in my work and contributing positively to our group environment.

Finally, I would like to commemorate Florian Mumm, who co-supervised me as a master student and I worked closely with during the first months of my PhD. He was a talented and dedicated researcher, and a good friend and colleague who passed much too soon.

# *List of papers*

The following publications are included in this thesis.

(I) **Patterned cell arrays and patterned co-cultures on polydopamine-modified poly (vinyl alcohol) hydrogels.**

Beckwith, K. M. and Sikorski, P.

*Biofabrication*, 2013, 5(4), 45009.

P.S. and I designed the study, I performed all experiments and wrote the paper. All authors contributed in revision and discussion of the paper.

(II) **Seeing a mycobacterium-infection in nanoscale 3D: Correlative imaging by light microscopy and FIB/SEM tomography.**

Beckwith, M.S., Beckwith, K.S., Sikorski, P., Flo, T.H. and Halaas, Ø. (2015).

*PLoS ONE, in press.*

Ø.H., T.H.F and M.S.B. designed the study. M.S.B. performed cell work, FIB/SEM tomography and optical imaging. P.S. and K.S.B. developed the fabrication methods of the correlative imaging substrate and contributed to data overlay methods. M.S.B. performed the data analysis and wrote the paper. All authors contributed in revision and discussion of the paper.

(III) **A Transparent Nanowire-Based Cell Impalement Device Suitable for Detailed Cell-Nanowire Interaction Studies.**

Mumm, F., Beckwith, K. M., Bonde, S., Martinez, K. L. and Sikorski, P.

*Small*, 2013, 9(2), 263-272.

F.M., P.S. and I designed the study. Based on previous work, F.M. and I further developed the fabrication concepts. I performed the cell experiments and imaging, with the exception of the cell membrane imaging and related analysis which was performed by S.B.. F.M. and I wrote the paper. All authors contributed in revision and discussion of the paper.

(IV) **Tunable High Aspect Ratio Polymer Nanostructures for Cell Interfaces.**

Beckwith, K. S., Cooil, S. P., Wells, J. W. and Sikorski, P.

*Nanoscale*, 2015, 7(18), 8438–8450.

P.S. and I designed the study. I developed the fabrication and surface chemistry methods and performed related experiments and cell experiments and imaging. XPS experiments and analysis was performed by S.P.C. and J.W.W.. I wrote the paper. All authors contributed in revision and discussion of the paper.

(V) **Influence of nanopillar arrays on fibroblast motility, adhesion and migration mechanisms .**

Beckwith, K. S., Schanke, R. and Sikorski, P.

*In preperation*

P.S. and I designed the study. R.S. and I performed the fabrication, cell experiments and imaging together. I wrote the paper. All authors contributed in the data analysis and revision and discussion of the paper.

### Related publications

The following publications fall outside the scope of this thesis.

1. **Dissolution of copper mineral phases in biological fluids and the controlled release of copper ions from mineralized alginate hydrogels.**

   Bassett, D. C., Madzovska, I., Beckwith, K. S., Melø, T. B., Obradovic, B. and Sikorski, P.

   *Biomedical Materials*, 2015, 10(1), 015006

# Contents

**Abstract** **i**

**Acknowledgements** **iii**

**List of papers** **v**

**Contents** **vii**

**1 Introduction** **1**
1.1 Aim of thesis . . . . . . . . . . . . . . . . . . . . . . . . . . . . . . 2

**2 Background** **5**
2.1 Relevant aspects of cell biology . . . . . . . . . . . . . . . . . . . . . 5
2.1.1 Cell membrane and cytoskeleton . . . . . . . . . . . . . . . . 5
2.1.2 Cell adhesion . . . . . . . . . . . . . . . . . . . . . . . . . . . 8
2.1.3 Cell migration . . . . . . . . . . . . . . . . . . . . . . . . . . 9
2.1.4 Passing the cell membrane . . . . . . . . . . . . . . . . . . . 12
2.2 Selected methods of studying, controlling and perturbing cells . . . 14
2.2.1 Microscopy . . . . . . . . . . . . . . . . . . . . . . . . . . . . 14
2.2.2 Transfection . . . . . . . . . . . . . . . . . . . . . . . . . . . 16
2.2.3 Controlling cell adhesion on surfaces . . . . . . . . . . . . . 19
2.3 Micro- and nanoscale fabrication of cell devices . . . . . . . . . . . 20
2.3.1 Microscale patterning . . . . . . . . . . . . . . . . . . . . . . 20
2.3.2 Fabrication of high aspect ratio nanostructures . . . . . . . . 23
2.3.3 Altering surface chemistry . . . . . . . . . . . . . . . . . . . 27
2.4 Biological applications of micro- and nanostructured devices . . . . 29
2.4.1 Cells on micro-patterned surfaces . . . . . . . . . . . . . . . 30
2.4.2 Surfaces for correlative electron and light microscopy of cells 31
2.4.3 Biological applications of high aspect ratio nanostructures . 33
2.4.4 Cell interactions with high aspect ratio nanostructures . . . 39

**3 Summary and discussion of papers** **49**
3.1 Brief summary of papers . . . . . . . . . . . . . . . . . . . . . . . . . 49

3.2 General discussion . . . . . . . . . . . . . . . . . . . . . . . . . . . . 54

**4 Conclusion and outlook 57**

**Bibliography 59**

**Papers 71**

# Chapter 1

# Introduction

Studying tissues and cells removed from the body traces its roots back more than 150 years, since Wilhelm Roux maintained parts of a chick embryo in warm saline solution for several days [1]. Cell culture, which involves the extraction, isolation and cultivation of dissociated cells, started during the 1940s and 1950s as a support for virology research and vaccine production. Since then, cell culture of both primary cells and cell lines [1] has been a fantastic research tool, especially as first line test systems to gain increased understanding of the molecular biology of life. Important research areas such as drug discovery, cancer biology, immunology, neurology and stem cells strongly benefit from cell culture methods. *In vitro* cell culture provides a platform were single cells or groups of cells can be studied using imaging methods such as light or electron microscopy and molecular biology methods such as PCR and blots, together providing both detailed structural and molecular information. Compared to animal experiments, cell cultures provide simplicity, low cost and ethical advantages. To expand the utility of cell cultures, significant efforts have been put into finding culture medium compositions that provide the numerous molecules that are necessary for successful *in vitro* propagation of a range of cell types. Today[2], the American Type Culture Collection (ATCC), the worlds largest repository of cell lines, list of 4000 available human cell lines, in addition to cell lines from over 150 species.

In 1885 Roux maintained his chick embryo on a glass plate. Glass is still the primary substrate used for culturing cells, supplemented by polystyrene dishes in the 1960s. In recent years, especially driven by developments in fields of tissue engineering and stem cell biology, the emerging knowledge of the links between surface topography, surface chemistry and cell responses have spurred advances in engineering of the cell-surface interface [2]. These developments range from the use of extra-cellular matrix components on flat surfaces, to full *in vivo* - like 3D matrices. Intermediate between the two are patterned and structured 2D surfaces. These provide the relatively controlled and accessible environment typical of 2D systems, while also allowing certain aspects of the cell-substratum interactions to be altered. In particular, modern developments within micro- and nanoscale surface engineering have enabled the construction of cell interfaces with control over both surface topography and chemistry. The size scale of the surface structuring is similar to or smaller than single cells, enabling more precise and directed cell perturbation, control and study. As a results, ever more detailed questions of cell processes such as adhesion, differentiation, biomechanics and motility may be addressed, in addition to implementing a range of functional attributes in the surfaces.

---

[1] Cell lines are cells propagated indefinitely in the laboratory, while primary cells are cells cultured after extraction from an organism

[2] May 2015, ATCC website

## 1.1 Aim of thesis

The primary aim of this thesis is the design, characterization and application of quasi-2D micro- and nanostructured cell culture substrates for *in vitro* cell studies.

From the applications perspective, more specific aims include:

- Design novel systems for manipulating cell-surface interactions on the micro- and nanoscale by spatially or temporally altering surface topography and chemistry.
- Explore nanowire-based alternatives to surface-based transfection methods for improvement of cell transfection performance.
- Perform detailed characterizations of cell-nanostructure interactions to provide better understanding of system functionality and potentially explore novel functionalities.

In addition, there are several secondary goals in relation to methodology:

- The substrates should be structured using comparatively simple methods to facilitate use by non-specialist laboratories.
- Materials commercially available at reasonable costs are preferred to increase large-scale production feasibility.
- Systems should be designed with emphasis on usability, integrating well with standard cell biology work-flows.
- System flexibility (i.e. the number of system parameters that can be varied) should be expanded where possible, so that multiple applications can be realized in the same device.

In this thesis, I will first introduce general concepts related to cells. In particular, I focus on cell interactions with the environment through the plasma membrane and associated processes such as endocytosis, substrate adhesion and cell migration. General methods used to study these processes will also be described. Then, selected micro- and nanofabrication methods important for this work will be introduced. Further, reported cell biological applications of systems similar to those produced in this work will be presented. I will then proceed to present the papers this work has resulted in. In particular, two classes of systems have been developed and studied: patterned polymer films (paper I and II) and vertically protruding high aspect ratio nanostructures (paper III, IV and V). Further, I will discuss the implications of the papers in a broader sense than the discussions in the individual papers. Finally, I will draw some general conclusions and present some perspectives on the field I have spent the last years working in.

# Chapter 2

# Background

## 2.1 Relevant aspects of cell biology

### 2.1.1 Cell membrane and cytoskeleton

#### The plasma membrane structure and mechanics

The cell plasma membrane is the principle barrier and interaction point between a cell and the surroundings, and consists of a mix of different lipids and membrane proteins in approximately equal weight proportions [3]. The dominating model of the cell membrane was first introduced by Singer and Nicolson as the fluid mosaic model [4]. This describes the cell membrane as a viscous fluid with both the lipids and proteins showing quite high diffusivity in the membrane, and presents the membrane as a highly dynamic structure. Since this model was launched, many refinements have been made, especially emphasizing the mosaic part of the model [5]. The consensus today is that the membrane is a rapidly changing, dynamic structure where most of the membrane is composed of functionally specific subdomains with certain types of membrane proteins, lipids or both [6]. A schematic overview of the cell membrane is shown in Figure 2.1.

Mechanical properties of cell membranes are highly variable depending on cell type and state. There are two important mechanical deformation modes that contribute to determining cell shape: cell membrane bending energy and cell membrane tension. The membrane bending energy of different biological membrane is roughly

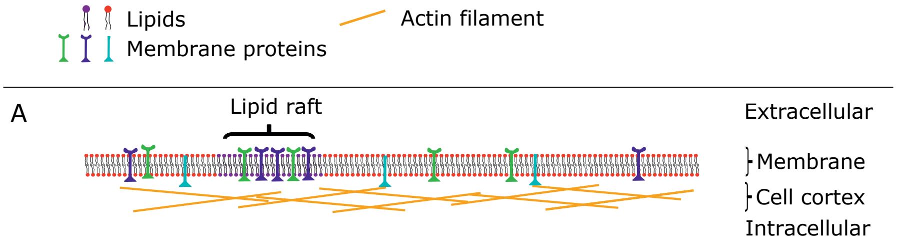

FIGURE 2.1: The cell membrane consists of a lipid bilayer with inserted membrane proteins that can have functional domains intra- or extracellularly, or both. The membrane is organized in functional sub-domains known as lipid rafts, enriched in certain membrane proteins and lipids.

constant, with typically values of $100pNnm \approx 20k_BT$ measured both in lipid vesicles and cells [7]. Estimates of membrane tension vary significantly depending on cell type and function, from about 3-250 $\mathrm{pN\,\mu m^{-1}}$[7]. This wide range reflects the fact that net membrane tension is composed of both lipid bilayer tension and cytoskeletal tension (see below). For example, resting macrophages have significantly higher membrane tension than activated macrophages, presumably related to the fact that activated macrophages are highly motile and phagocytic, processes aided by reduced membrane tension [8]. In fact, emerging evidence shows that plasma membrane tension may not only be a consequence, but also an important regulating factor in specific cell functions [9]. Another important fact to consider is that cells have quite variable requirements for cell membrane during the cell cycle (a round, mitotic cell has less surface area than a spread or migrating cell, as the cell volume stays quite constant). This is partly regulated through endo- or exocytosis to remove or add membrane respectively. In addition, cells maintain considerable membrane reserves in membrane folds and microprotrusions [10]. The sizes of these reserves vary by cell type and state. Under extreme conditions (hypotonic cell swelling) these membrane reserves were judged to be 70% more than resting cell surface area in A549 epithelial cells [11], but reserves of about 20% are more commonly reported [10]. To breach a fully stretched cell plasma membrane only 2-3% strain is required, but again due to considerable membrane reserves, significant deformation of the overall cell shape occurs before the lipid membrane itself is strained [12].

### Actin

The cytoskeleton consists of actin filaments, microtubules and intermediate filaments. Intermediate filaments are important for maintaining rigidity and integrity in certain tissue types and intracellular structures (e.g. the nucleus), while microtubules are important in cellular polarization, trafficking and during mitosis. However, it is actin that is most prominently involved in cell mechanobiology, from remodelling the plasma membrane to generating contractile forces [13]. Actin filaments are formed by the ATP-driven association of G-actin monomers, forming filamentous actin (F-actin). F-actin is polarized with a (+) end and a (-) end, indicating differential affinity for G-actin binding (see Figure 2.2A). Intracellular free G-actin concentrations are typically in the range that F-actin polymerizes at the (+) end and depolymerizes at the (-) end. The continuous polymerization and depolymerization of F-actin is known as actin treadmilling. Numerous actin binding proteins regulate polymerization or depolymerization, and link together actin filaments with each other and the cell membrane. F-actin binds to itself in different ways, allowing it to form diverse structures such as stiff, straight bundles or loosely associated meshes. The motor protein myosin binds to actin and can induce contractile motion of actin filaments, which is the mechanism of muscle contraction.

Actin is closely associated with the cell membrane via membrane protein linkages, which function both as mechanical linkages and advanced signalling networks for mechanotranduction which are further described below. An actin meshwork (sometimes called the membrane skeleton or cortical actin) supports the plasma membrane and gives it mechanical resilience, and contributes significantly to the membrane tension of cells [14]. The actin meshwork will cause a time-dependent cell elastic response to deformation, as actin remodelling causing plastic deformation can be induced rapidly [15]. The actin meshwork has a distribution of pore sizes in the mesh [16], thought to be closely related to the functional domains in the cell plasma membrane. The properties of the mesh can vary quite significantly among different cell types, with pore sizes varying broadly around 100 nm [17].

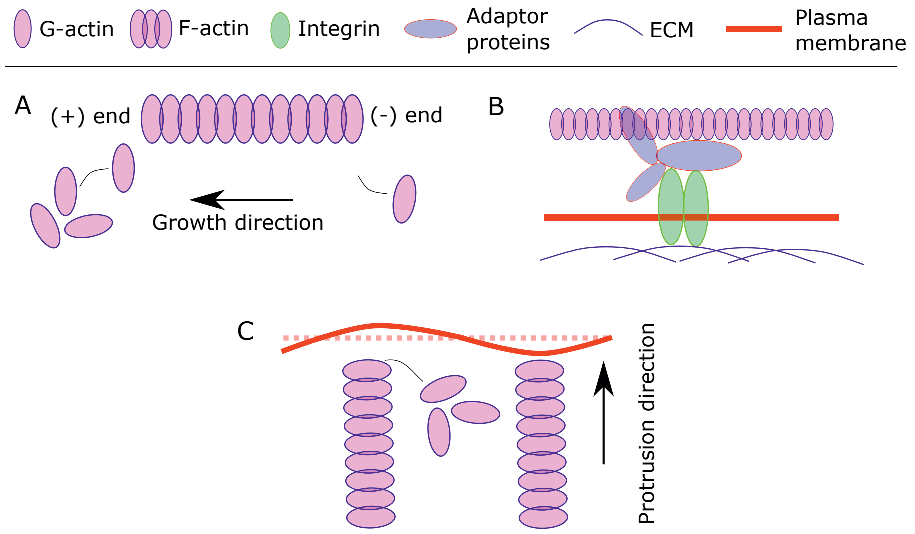

FIGURE 2.2: (A) Treadmilling model of actin, with assembly at (+) end and disassembly at (-) end, and associated adaptor proteins linking actin to the cell membrane to generate traction forces. (B) Cell adhesion protein complexes, linking the cell cytoskeleton to the extra-cellular matrix via integrin receptors and adaptor proteins. (C) Brownian ratchet model of membrane protrusion. Random membrane fluctuations allow actin assembly, inhibiting reverse fluctuations. Thousands of such occurrences cause a net protrusive force.

### 2.1.2 Cell adhesion

*In vivo*, most cells must physically interact with their surroundings, binding other cells and extracellular matrix (ECM) to form tissue, signalling other cells through cell-to-cell contacts, or migrating within the ECM. These interactions are mediated through a complex chain of events involving cell surface receptors, cell cytoskeleton and motor proteins, and initiation of downstream mechanobiological processes [18]. The most important concepts will be briefly introduced here (see also Figure 2.2B).

Although cell-to-cell contacts are of large importance for maintaining tissue integrity and function *in vivo* , *in vitro* it is the various forms of cell-ECM contacts that dominate the field, as this is what can be engineered in the materials used for cell culture. Cell-ECM contacts are mainly mediated by integrin receptors, of which 24 varieties are known (characterized by combinations of 18 $\alpha$ and 8 $\beta$ subunit domains). [19] Integrins are multimeric trans-membrane receptors that bind to a variety of ligands, but first and foremost motifs found in ECM proteins such as laminin, collagen and fibronectin. Especially the RGD (arginine-glycine-aspartate) motif is highly preserved and recognized by over half of the integrins [20]. Integrin subunits are flexible and change conformation upon binding ligands, inducing integrin clustering in the membranes, which in turn mediates signals through the cell plasma membrane to the cytoplasmic side.

In the cytosol-facing side of the cell membrane, the principle linkage occurs to actin. The linkages between actin filaments and integrins are mediated by a large number of proteins (about 150)[21] and the exact nature of these linkages are not known in detail. Adaptor proteins such as talin, vinculin and $\alpha$-actinin bind actin to integrins. In addition numerous signalling and regulating proteins such as focal adhesion kinase (FAK), zyxin and proteins of the Rho-GTPase family bind the adaptor proteins and/or actin and integrins, strengthening or weakening the linkages. The interactions occur both through chemically driven changes as well as force-sensitive proteins [18]. The resulting molecular signals and force transduction can lead to various assemblies of integrin complexes, actin bundle formation, and actin polymerization and depolymerization. The totality of surface adhesions and actin dynamics can result in cell migration.

### 2.1.3 Cell migration

Cell migration is a complex process where the functions of many of the separate contributors are known, but it is still a highly active area of research to assemble the complete picture from all the pieces. Migration of adherent cells is superficially similar to the movement of a slug. First, the front end (leading edge) is extended, forms a new attachment, then finally pulls the rear after (trailing edge).

In cells, actin polymerization drives protrusion of the cell membrane at the leading edge, forming filopodia or lamellopodia. The current model for this is a brownian-ratchet, where actin polymerization occurs when the plasma membrane fluctuates outwards due to thermal motion, hindering the reverse motion (see Figure 2.2C) [22]. Actin in lamellopodia is dendritic, forming a loosely organized mesh. However, the polymerization exerts a substantial pressure, amounting to about 1 kPa ($1\,\mathrm{nN}\,\mu\mathrm{m}^{-2}$ [23]).

After formation of a leading protrusion, cell migration requires an organized effort involving cell adhesion to generate traction and actin filaments to generate force (see Figure 2.3). Integrins in filopodia and lamellopodia bind to surface ligands, and induce signalling cascades and actin binding as described above. The integrins cluster in short-lived, small adhesive patches called nascent adhesions [21]. As the lamellopodia protrudes and the nascent adhesions reach the lamellum, they either dissolve, or are strengthened. The strengthening is force-induced, and results in the growth of focal adhesions, which present as large (several $\mu m^2$) elongated plaques with life-times of minutes to hours. Focal adhesions are associated with the distal ends of actin-myosin bundles known as stress fibers [24]. The nascent and focal adhesions also function as a molecular "clutch" [23]. This term means that focal adhesions have the ability to bind strongly (clutch enganged) or loosely (clutch disengaged) to the treadmilling actin filaments. When the clutch is disengaged, no force is transmitted to the substrate, and retrograde actin flow is high. Conversely, with the clutch engaged force is effectively transmitted to the substrate, causing further protrusion of the leading edge through actin polymerization, continuing the cycle of protrusion-adhesion. In addition to focal adhesions, other integrin-associated adhesive complexes are known, such as podosomes and invadopodia [21]. These have much shorter life-times, and are smaller than focal adhesions, but play important roles in e.g. invasive and metastatic cancer cells.

Finally, the cell body and rear of the cell must follow the leading edge. The focal adhesions in the rear of the cell loose their substratum contact, although they may persist as motile cytosolic complexes for a longer period before fully disassembling [25]. To pull the cell forward there are two proposed mechanisms for contractile forces, which have both been shown to be important [23]. The first is direct contractile forces generated by the actin myosin stress fibres attached to focal adhesions in the leading edge, which contract and pull the entire cell body forward. The second is disassembly of actin fibres towards the rear of the cell. When these fibres disassemble, their stiffness is reduced, causing more buckling and motion of the fibres. Due to entropy, this causes a net contractile force in the cell even with no active motor proteins.

External factors regulating cell migration include chemical cues (chemotaxis), substrate topography and substrate stiffness. Via integrin signalling, force transduction or other signalling processes these external cues initiate the pathways described above causing directed or random cell migration [26].

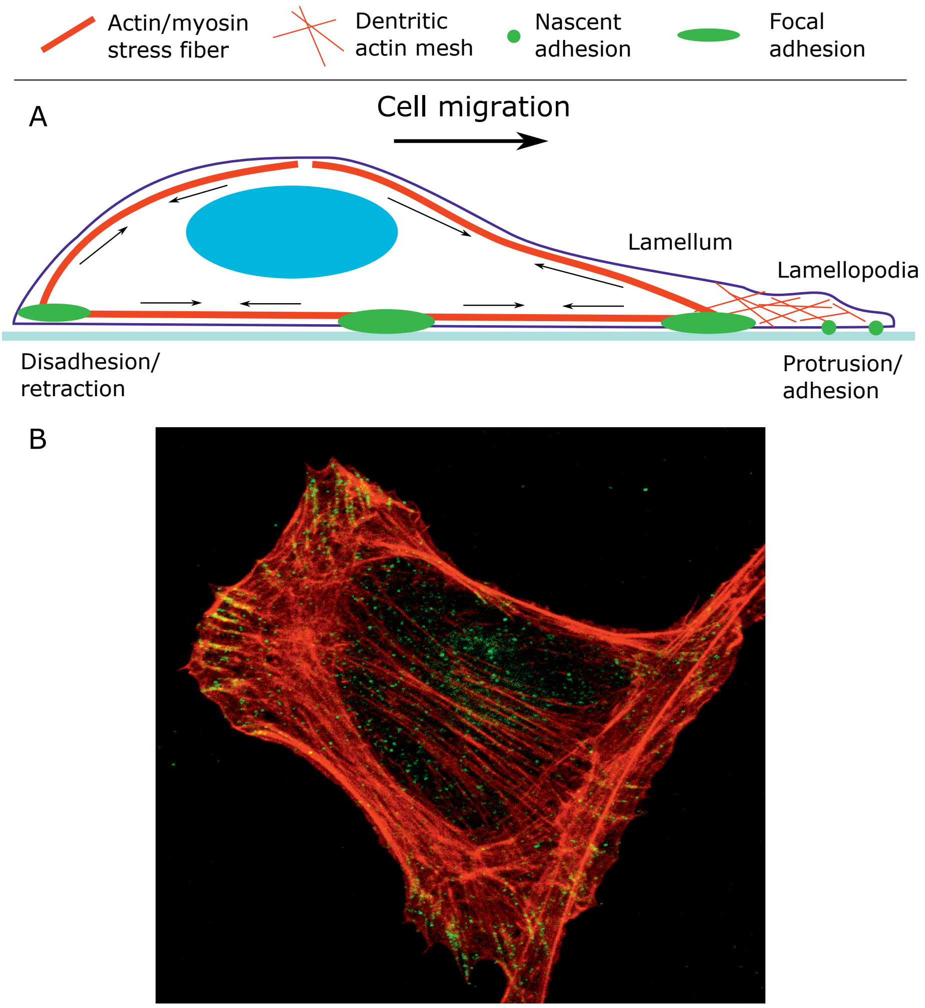
Actin/myosin stress fiber
Dentritic actin mesh
Nascent adhesion
Focal adhesion
A
Cell migration
Lamellum
Lamellopodia
Disadhesion/ retraction
Protrusion/ adhesion
B

Figure 2.3: (A) Illustration of important features of cell migration, including leading edge protrusion and attachment, maturation of nascent adhesions into focal adhesions, contraction of actin stress fibers and detachment and retraction of the trailing edge. (B) Confocal migrograph showing the distribution of actin (red) and focal-adhesion associated vinculin (green/yellow) in a NIH3T3 fibroblast. Image from our work (unpublished).

### 2.1.4 Passing the cell membrane

Cells have a large exchange of material with their environment: nutrients must enter the cell, waste and cell products must exit the cell. However, the plasma membrane and its associated structures present a barrier that is largely impenetrable for polar and ionic species due to the hydrophobic nature of the membrane. The cells have several mechanisms to transport material across the membrane [27]. These are divided into two main categories: Directly passing the membrane, or engulfment by a stretch of membrane that is budded off from the main membrane and released to the inside of the cell (or in the opposite direction going out). Directly passing the membrane by diffusion is possible for small hydrophobic molecules, and cells contain ion channels to allow the passage of vital ions, as well as pores to allow the passage of water. There are reports that some types of proteins or peptides knows as cell-penetrating peptides (CPPs) to directly pass the cell membrane, but this is still disputed as in many cases active mechanisms seem to be involved after all [28].

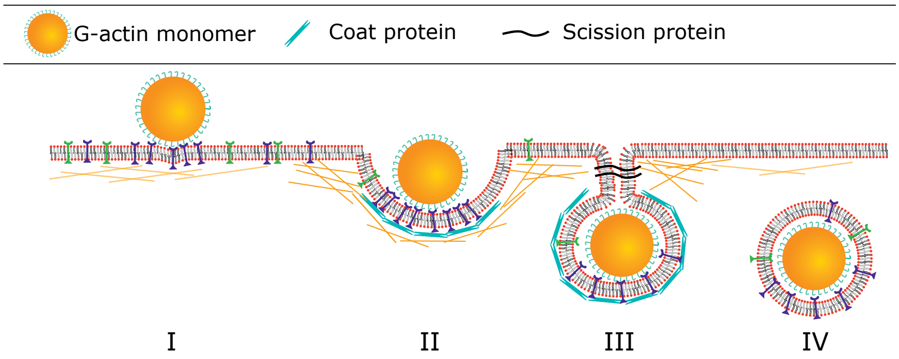

Figure 2.4: Endocytosis, here exemplified by receptor-mediated endocytosis occurs in several steps, including (I) initial membrane contact and initiation of receptor clustering, (II) actin remodeling and coat protein assembly driving membrane invagination, (III) rounded or flask-shaped unclosed vesicle formation and assembly of scission proteins and finally (IV) release of the vesicle from the membrane after action of the scission proteins, disassembly of the coat proteins, and shipping of the endocytotic vesicle for sorting and further processing.

Active mechanisms of cellular uptake are the most general method cells have of internalizing material, especially macromolecules and nanometer to micron-sized particles. The reason they are called active mechanisms is that the cell must expend energy for the uptake to occur. Active mechanisms are generally known as endocytosis, which can be constitutive in the case of pinocytosis, or activated by molecular binding in the case of receptor-mediated endocytosis and phagocytosis [29]. During endocytosis the cell membrane forms a pocket, folds inward, and finally closes off inside the cell to become a vesicle, separated from the cytoplasm by a bilayer membrane (see Figure 2.4). During receptor-mediated endocytosis, the most common form of endocytosis, there is first a clustering of membrane receptors at the site of particle interactions [30]. These clusters induce the assembly of coating proteins such as clathrin to stabilize the forming vesicle. Finally, the vesicle buds off with the help of other proteins such as the scission protein dynamin. Both coating and budding are energy intensive processes to counteract the bending rigidity of the cell membrane. Another form of endocytosis is initiated at caveola, a special type of lipid raft in the cell membrane, and associated with the protein caveolin.

The size ranges of uptake for the different forms of endocytosis are slightly different, and in the case of nanoparticles the vesicles that are formed are in the range of 120 nm and 50-60 nm for clathrin-coated and caveloa-associated vesicles respectively [31]. Actin filament involvement is seen in all forms of endocytosis and is an important driving factor in the formation of endocytotic vesicles [32]. After endocytosis the vesicle is called an endosome. Further processing includes fusion with other cellular vesicles and budding of parts of the endosome to separate cargo going to degradation in lysosomes, exocytosis out of the cell, Golgi network for sorting, or other intracellular targets [3].

For certain applications, such as cell transfection (see below) and intracellular sensing of enzymatic activity, pH or electrical activity, bypassing the plasma membrane and avoiding the endo-lysosomal degradation pathways most foreign materials are subjected to, would be advantageous. Here, high aspect ratio nanostructures are proposed as a possible route, due to their nanoscale cros-section and micron-scale length. Such structures and interfaces will be described in greater detail later.

## 2.2 Selected methods of studying, controlling and perturbing cells

### 2.2.1 Microscopy

"Seeing is believing", an old idiom states. This is increasingly true for cell biology research, where molecular biology results are often corroborated using microscopy to directly visualize structure, processes, correlations or functions. The details of microscopy instrumentation will not be presented here, but some of the main strategies and concepts of microscopy imaging will still be mentioned.

On the scale of things, a cell is quite small, a bit smaller than the smallest things we can see by the naked eye. Sub-cellular structures and features extend down to the molecular scale of nanometers. By careful control of the interactions between energetic particles (photons or electrons) with matter, these small features can be magnified until they are visible to us.

Photons have numerous interaction mechanisms with matter, specifically with electrons. Scattering, absorption, retardation and electron excitation and emission are used in microscopy methods of Raman or dark field, bright field, phase contrast or differential interference contrast and fluorescence or non-linear imaging, respectively. All these methods can introduce contrast, i.e. spatially varying signal intensity in response to variations in the sample. Introducing specifically binding probes which enhance a particular form of photon interaction to the sample allows chosen features to be visualized against the unlabelled background with increased contrast.

In general, an intuitive way to view image formation in a microscope is as follows. As light is wave-like in its propagation, diffraction will occur as light passes through the finite apertures and lenses in a microscope system. These diffraction events cause blurring of sharply defined features. In particular, if one imagines a single small point source imaged through a microscope, the resulting image will include diffractive blurring together with other possible microscope aberrations. This image is called the point spread function (PSF) of the microscope, and usually takes the shape of an Airy disk. An imaged object can be considered a series of such point sources, and thus the resulting image $I$ of an object will be the convolution between the object $O$ and point spread function $PSF$ of the microscope:

$$\begin{aligned} I(r) &= \int O(\rho)PSF(r-\rho)dr \\ &= O * PSF \end{aligned} \tag{2.1}$$

Only points separated by a certain distance $d$ can be separated in the image, known as the diffraction limit, typically described by the Rayleigh criterion:

$$d \approx \frac{\lambda}{2NA} \tag{2.2}$$

There are several practical implications from the briefly presented introduction to optics above. The first is the notion that when considering any image, one must consider both the shape of the PSF of the system, as well as the actual object. As an example, PSFs of confocal microscopes are elongated in the z-axis, so objects typically appear more extended axially than laterally during 3D imaging. The concept of the image being a convolution also leads to the idea of deconvolution. Here, by using theoretical or actual measurements of the microscope PSF, one can use different algorithms to reconstruct images better matching the actual imaged objects, although this approach is somewhat limited by system noise.

In recent years, several methods have emerged to allow localization of photon emitting probes with better resolution than the diffraction limit allows. The first class of such methods localizes excitation using evanescent decaying waves (total internal fluorescence microscopy, TIRF) or by depleting photon emitters in a volume outside a very small remaining emitting volume (stimulated emission-depletion, STED). The second class of methods uses statistical and deconvolution-based reconstructions of a large number of images of changing illumination patterns and therefore PSFs (structured illumination, SIM), or a small number of stochastically emitting sources (stochastic optical reconstruction microscopy, STORM or photoactivated localization microscopy, PALM). The latter methods require stringent sample preparation and suitable fluorophores, but can reach resolutions in the tens of nanometer range [33].

Electrons, with their large mass compared to photons, are not limited by their wave nature during biological imaging. However, electrons only penetrate from some nanometers up to perhaps a micrometer into biological tissue, and propagate in vacuum, so elaborate sample preparation is needed. Electrons interact with other electrons and nuclei, and similar to photons they can be scattered, absorbed or excite other electrons. The first two events are used in transmission microscopy (TEM), which however is limited to thin samples. Electron excitation is used in secondary electron microscopy (SEM), where sample geometry is not critical, but the emission depth of the emitted electrons is only a few nanometers. To increase contrast of biological samples, heavy atoms such as metals, uranium or osmium are introduced and bind to specific parts components of cells.

### 2.2.2 Transfection

Among the numerous approaches available for altering cells, transfection, the process of introducing foreign genetic material into cells, is one of the most widely used. There are two main efforts driving the development of transfection methods. Firstly, even after complete sequencing of the human genome [34], the function of most of our genes remains unknown. *In vitro* transfection provides a convenient tool to selectively express or disable specific genes to untangle functional relationships. Transfecting cells with functional proteins coupled to fluorescent proteins further allows live visualization of dynamics and localization of these proteins. Secondly, the promise of gene therapy to treat numerous genetically-linked diseases leads to continued efforts to improve *in vivo* transfection methods. Here, only *in vitro* transfection will be considered, as *in vivo* transfection has several additional challenges to overcome.

The goal of transfection is to deliver functionally intact plasmid DNA to the nucleus for expression, or siRNA to the cell cytoplasm to silence expression. Briefly, plasmid DNA is bacterial DNA that contains a promoter sequence for transcription factor binding, and sequences for the protein(s) one wishes to express, while siRNA are short strands of RNA that bind to and target specific mRNA for degradation [35]. To successfully reach these targets, numerous barriers must be overcome. The nucleic acids must first reach the cell plasma membrane, pass the membrane and be taken up into the cell, escape degradation in the endolysosomal pathway, navigate and avoid degradation in the cell cytoplasm, and for plasmid DNA, reach the nucleus, pass the nuclear membrane and reach active transcription sites.

The most widely used transfection techniques can be divided into viral, chemical and physical methods (see Figure 2.5). Viruses are Nature's own transfection (usually termed *transduction* when viruses are used) experts, and can be hijacked with exogeneous DNA and modified to not reproduce in their target. Viruses can be highly efficient in transduction, due to their optimized design for uptake, intracellular trafficking and targeting. However, viruses have inherent limitations on plasmid size, and although certain standardized systems are in place, there are always safety concerns with viral methods. In practice, viruses are not much used except for very routine investigations due to the efforts involved in packaging new plasmids.

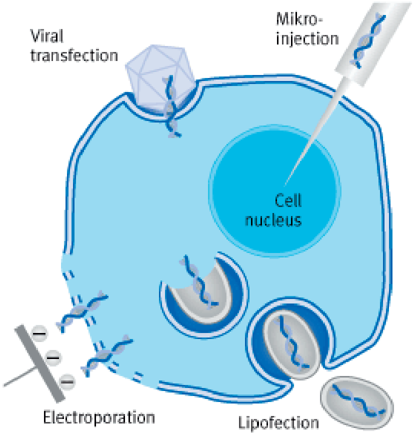

Figure 2.5: Illustration of several different common transfection methods, including viral transduction, chemical (lipid-based) transfection, and the physical transfection methods electroporation and microinjection. Image courtesy of Biontex Laboratories GmbH.

Chemical methods attempt to mimic certain aspects of the functionality of viruses, and typically employ packaging molecules, such as cationic lipids or cationic polymers, that protect the nucleic acids from degradation, and aid in escape from the endolysosomal pathways [36]. Many commercial alternatives exist, and are widely used for cell and molecular biology investigations. However, nuclear trafficking is still an issue for plasmid DNA, and together with the other barriers this causes lower transfection efficiency than for viruses, and high variability among cells in a population and among different cell types. Chemical transfection methods often rely on dividing cells, as the nuclear envelope opens up during cell divisions, allowing entry of plasmids. Thus, especially for primary, non-dividing cells, transfection using chemical methods is very inefficient. Another issue is that the chemical reagents often induce a dose-dependent cytotoxicity due to the interactions between the cell and transfection reagent.

Physical methods rely on physical forces to penetrate, such as electric fields (electroporation), ultrasound (sonoporation), mechanical perturbation (cell scraping or squeezing) or direct injection (microinjection). The processes that lead to (reversible) pore generation in the cell membrane via electroporation are quite complex, but the end result is that molecules in solution enter the cell through diffusion or possibly electrophoresis [37]. Sonoporation and cell scraping both involve mechanical stresses on the cell membrane, inducing reversible pore formation and allowing molecule entry through diffusion. Cell scraping is a quite old method [38], while an interesting modern realization is mechanical constriction of cells in microchannels for a more controlled mechanical delivery to cells [39]. As for chemical transfection, there is always a trade-off between cell viability and transfection efficiency, and careful optimization of protocols and reagents must be done for each cell type. However, especially electroporation has become quite widely used in laboratories to transfect large numbers of cells or cells that are not amiable to chemical transfection.

Microinjection relies on using a glass microcapillary to directly inject plasmid DNA into cells, preferably the nucleus. This is naturally a low throughput method, and cell viability after injection is always an issue, although the method is widely used to ensure positive transfection results, such as for *in vitro* alteration or cloning of oocytes. Lessons learned from microinjection are also important for other transfection methods. A few interesting studies have shown that injected plasmid DNA of typically used sizes (several thousand base pairs) essentially are immobile in the cell cytoplasm, and are quite quickly degraded [40, 41] unless recognized and actively transported to the nucleus via microtubules [42]. DNA injected directly into or in close proximity of the nucleus has higher transfection efficiency and is significantly less degraded [40]. Thus, if the packaging material does not aid in transporting the DNA to the nucleus (which is the case for viruses), the plasmid itself needs to have elements that are recognized and actively transported if direct nuclear delivery is not possible.

In addition to significant work in optimizing protocols and materials in physical and chemical methods, other aspects of the system design have been shown to alter transfection outcomes. One example is reverse transfection, where DNA and other materials are deposited on the surface prior to cell adhesion. It was shown that up-concentration of plasmid DNA complexed with lipid vectors on a surface onto which cells grew, enhanced transfection efficiency several fold [43]. Further developments of this concept patterned plasmids containing different genes using robotic spotters, allowing the generation of transfected cell microarrays expressing the genes of interest in distinct spots [44]. Thus, miniaturized arrays of cells expressing different genes could be studied over time, increasing throughput of gene function discovery, and is now especially used together with siRNA silencing in arrays [45].

Although few have reached routine use, nanomaterials have shown many interesting proof-of-concept applications within cell transfection, which was also an aim of this work (Paper III). Certain nanomaterial systems for transfection are reviewed later.

### 2.2.3 Controlling cell adhesion on surfaces

Substrate control over cell adhesion, spreading and migration is primarily controlled by which proteins the integrins and other cell receptors interact with. When culturing cells protein-containing medium is generally used, and cells also can produce ECM proteins on their own. Proteins tend to absorb to the culture surface, driven by electrostatics, hydrogen bonding and hydrophobic interactions [46]. However, surface protein adsorption is not a one-step process. Initially, binding will be dominated by statistics; the most abundant proteins will adsorb in the highest concentrations. When using serum, the highest abundance proteins are albumin and IgGs [47]. Over time, proteins with lower abundances but higher binding affinities will replace the initial proteins, known as the *Vroman effect* [48]. These effects have been greatly studied for nanomaterials meant for *in vivo* use, where the concepts of protein coronas and biological identity have been introduced as characteristics of which proteins adsorb in what way to a given material. A more recent concept is that of ”hard” and ”soft” protein coronas. High affinity proteins binding directly to the material surface form the hard corona, but additional proteins can bind to the hard corona by weaker, protein-protein interactions, giving the material a soft corona as well [49].

By altering the surface chemistry of the substrate, the type, abundance and conformation of absorbed proteins is altered, in turn altering integrin binding. In extreme cases, very hydrophobic surfaces (which denature proteins) or anti-fouling surfaces (which resist protein absorption) can inhibit cell attachment completely.

Otherwise, surface charge and functional groups have more subtle effects, depending greatly on cell type. Different cell types express different integrins to a varying degree, meaning some cell types grow fine on glass or plastic, while other require specific proteins or molecules deposited on the surface to adhere and proliferate.

Especially combinations of anti-fouling and cell adhesive materials have been explored in this work. Only a few, quite hydrophilic polymers such as poly(ethylene glycol) (PEG), poly(vinyl alcohol) (PVA), acrylic acid and combinations and variations of these display different degrees of anti-fouling [50]. The molecular mechanisms of resisting protein adsorption are not well established, but are generally attributed to a combination of steric hinderance and structured water binding [51]. The brush-like polymer chains extending from the surface hinder proteins from reaching the surface for absorption. In addition, adsorption to the polymer itself is hindered by tight, structure binding of water. Adsorbing proteins would involve conformation changes and water unbinding, both giving an enthalpic cost to protein binding.

Surface topography plays a less obvious role in cell adhesion. However, in the recent years it has been shown that alteration in surface topography can both influence protein adsorption [52] as well as altering the mechanical environment encountered by cells, in both cases leading to changes in cell adhesion and response [2].

## 2.3 Micro- and nanoscale fabrication of cell devices

### 2.3.1 Microscale patterning

Due to advances in the electronic industries in the 1970s and 1980s, micro-scale surface patterning and modification techniques are readily available in most fabrication facilities. Processes typically start with photolithography, where a predefined pattern is realized from a CAD drawing into a mask. By exposing a thin layer of a photosensitive polymer blend to UV light through such a mask, selective areas of the polymer are rendered soluble or insoluble in a specific solution. After development, a pattern of polymer is thus present on the substrate. This pattern can be transferred directly into the substrate by selective wet or dry etching, or indirectly by first depositing a metal layer, removing the polymer and the metal covering the polymer (lift-off), and then either using the metal patterns in the device or using them as a new etch mask (a hard mask, as opposed to the polymeric soft mask).

Although these methods are quite useful in structuring hard materials, for biological devices "soft" materials such as polymers are often preferred, due to their low cost and potential for large scale manufacturing. Naturally, the photosensitive polymer may be used themselves, but often other materials are favoured, so pattern transfer is more desirable. A typical strategy is to first produce the desired structures in a hard material, then transfer them from hard to soft materials. This process is quite routine in industry, such as by injection moulding. On the lab scale, where rapid prototyping of different designs is often desired, other methods have been developed.

Thermal embossing is one of the most straight-forward methods of transferring a pattern from hard to soft materials. Here, the hard mould and/or the polymer to be patterned is heated above the glass transition temperature or melting temperature, and the mould and polymer is pressed together, cooled and separated [53]. A variety of embossing is using UV-curable polymers instead of thermosetting polymers, avoiding issues of thermal expansion. Thermo-moulding was employed by us to pattern thermoplastic aclar films in Paper II.

Soft lithography developed,by Whitesides and collegues [54], is another widely used "soft" micropatterning method (see Figure 2.6A and B). Here, the initial process starts as above, resulting in either polymer structures on a hard substrate or a structured hard substrate. This structure is then transferred into an elastomer (elastic polymer), typically poly(dimethyl siloxane) (PDMS), which can be further used as e.g. a microchannel, or as a stamp. Immediately, the process is simplified, as the hard master can be reused multiple times to make new elastomer devices. Using PDMS as a stamp is called microcontact printing, and is a micro-scale version of the potato stamp made by most Norwegian children. Many materials, such as proteins, polymers, small molecules or even whole cells can be deposited on the PDMS stamp, which is then held in contact with a substrate and the material is transferred, resulting in corresponding patterns of the material on the surface.

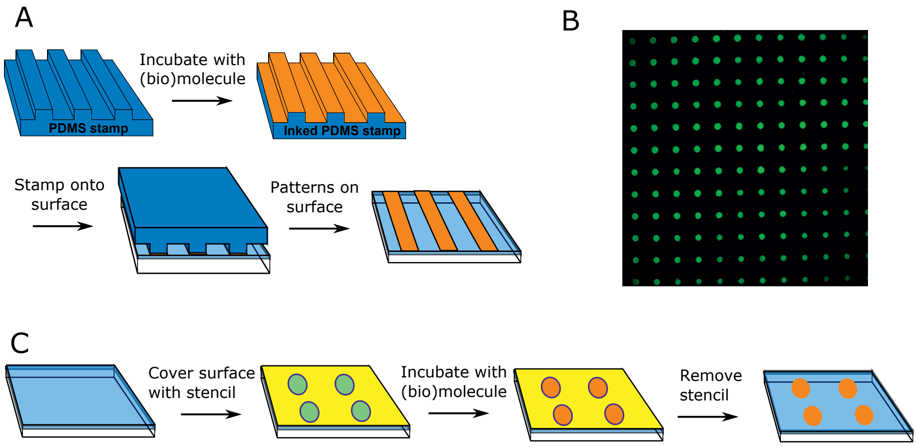
A
Incubate with (bio)molecule
PDMS stamp
Inked PDMS stamp
Stamp onto surface
Patterns on surface
B
C
Cover surface with stencil
Incubate with (bio)molecule
Remove stencil

FIGURE 2.6: (A) Microcontact printing uses an elastomeric polymer, typically PDMS, as a stamp to transfer and pattern molecules on a surface. (B) Fluorescent PEI/polydopamine patterned in 30 µm circles by microcontact printing. Our work, unpublished. (C) Stencil lithography uses a stencil mask in intimate contact with an underlying surface to pattern molecules.

A different fabrication variety that is quite widely used for generating micropatterns of molecules or even cells on a surface is stencil lithography [55–57] (Figure 2.6C). Here, a stencil mask (i.e. a continuous film with defined holes), typically made from a polymer, is placed onto a substrate. The desired materials are then deposited through the holes, before the stencil is removed, leaving a patterned surface. Although stencil masks are typically slightly more challenging to produce than e.g. PDMS stamps, the process of molecule deposition is extremely simple and highly reproducible. One limitation is the size of the patterns, as the stencil mask must remain mechanically stable enough to apply and remove. Thus small features require high aspect ratio holes in the mask, which are difficult to realize in polymers.

With the advent of high throughput automatic printing systems, or even just modified inkjet printers, direct patterning of molecules and cells has become feasible [44, 58]. Here, shapes are mainly limited to circular droplets on the surface, and resolution is also limited, but these methods still can provide quite precise patterning. A significant advantage, especially for molecule printing, is that whole libraries of molecules can be patterned densely on the surface, in contrast to one or a few in the above methods. Thus, screening different molecules or combinations thereof with very high throughput is possible.

### 2.3.2 Fabrication of high aspect ratio nanostructures

Micro-scale structuring is a matter of developing smart, efficient and simple means of transferring patterns. This is also true for nanoscale fabrication, but the small scale calls for a different toolset. Within nanofabrication, two main paradigms are usually considered: top-down and bottom-up fabrication. Top-down fabrication involves the precise definition of structures, typically by nanolithography approaches such as electron beam lithography (EBL), deep-UV lithography or nanoimprinting, and realization of these structures by etching or other forms of material removal. On the other hand, bottom-up approaches uses self-assembly of molecules or materials which, under the correct circumstances, will form nanoscale structures and materials. Examples include (self-)catalyzed growth processes, block copolymer micelles and DNA origami.

The nanostructures developed and used in this work are "high aspect ratio nanostructures" (HARNs), and the following section will therefore focus on synthesis of these types of nanostructures in general and the types of nanostructures used in this work (CuO nanowires and SU-8 nanopillars) in particular. The methods available to produce HARNs amount to numerous variations on a few main categories. These categories are illustrated schematically in Figure 2.7, and include template-directed methods, anisotropic crystallization, top-down definition and etching methods, droplet-catalysed vapour deposition, self-catalysed anisotropic growth and self-assembly of smaller nanoparticles. All of these methods have been used to fabricate HARNs for biomedical purposes, and in this work two methods have been used: self-catalysed growth of CuO nanowires (paper III) and top-down definition of SU-8 nanopillars (paper IV and V).

The production of CuO nanowires by thermal oxidation is a bottom-up template free self-catalyzed process. This process has been realized for several metals such as iron [59], zinc [60], gallium [61] and tin [62], but the most common is perhaps the growth of CuO nanowires from metallic copper [63]. The nanowire growth occurs after the formation of a thin $Cu_2O$ film on top of the copper substrate, via $Cu_2O$ grain-boundary diffusion of copper ions that combine with air oxygen atoms (see Figure 2.8) [64]. There is a large interfacial stress at these grain boundaries (copper oxide is less dense than copper), and some of this stress is relieved by vertical growth of copper oxide nanowires. Critical factors for the successful growth of CuO nanowires include temperature in the range of $400\,^{\circ}\mathrm{C}$ to $500\,^{\circ}\mathrm{C}$,

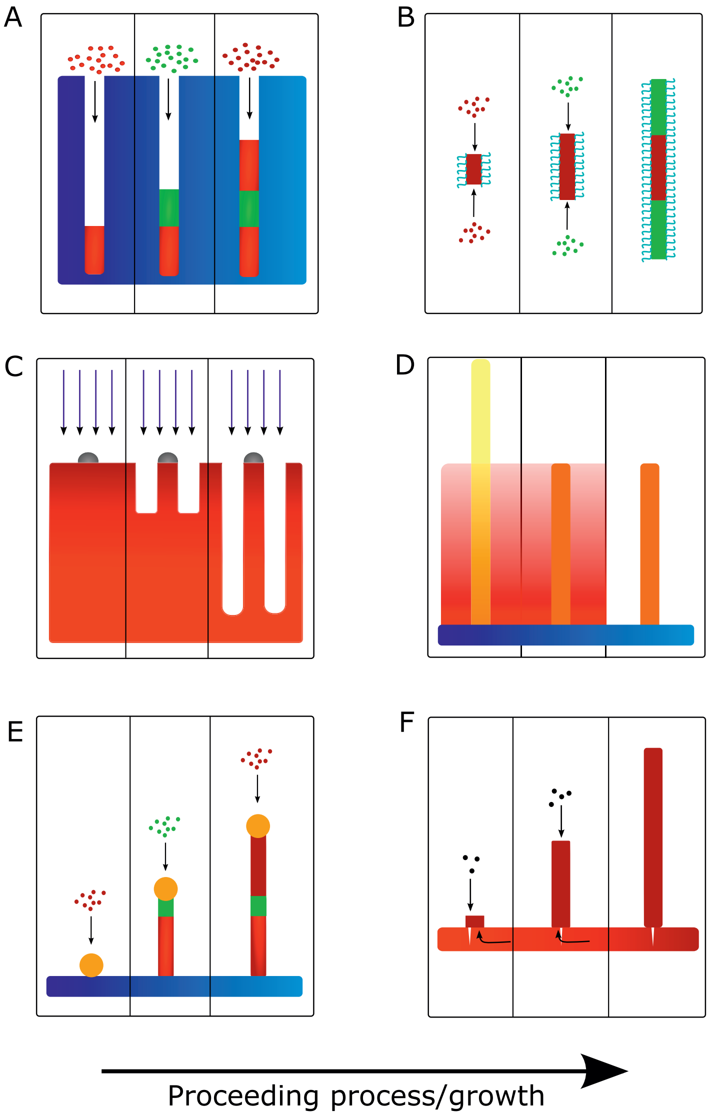

FIGURE 2.7: Illustration of selected methods produce HARNs. (A) Template assisted growth occurs by deposition from a gas or solution phase into a template, after which the template is dissolved, releasing the HARNs. (B) Anisotropic crystal growth in solution can produce HARNs. (C) Top-down etching methods use predefined masks, self-masking or direct writing to define areas to preserve, then the rest is removed by etching or sputtering. (D) Top-down definition of HARNs by direct writing using light or more commonly electrons in sensitized polymer films, followed by removal of unexposed (or exposed) material. (E) Vapor-liquid-solid (VLS) or vapor-solid (VS) techniques use liquid droplets, usually pre-deposited, as catalysts out of which a HARN precipitates and grows. Also here combinations of reagents can be introduced to produce heterostructures. (F) HARN synthesis can also occur at other catalyst sites than liquid droplets, such as at grain boundaries or steps in the underlying substrate, where anisotropic crystal growth can occur using material from the substrate or surroundings.

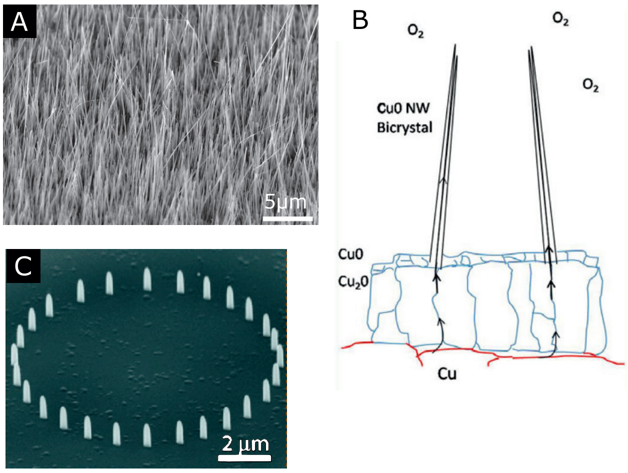

FIGURE 2.8: (A) High-throughput production is achieved by thermal oxidation of CuO nanowires as in Paper III. From our work (unpublished) (B) The generally accepted mechanism of CuO nanowire growth is by diffusion of copper ions along grain boundaries in the $Cu_2O$ layer above, assembling nanowires at the top surface upon reaction with oxygen. From [64], with permission. (C) Low throughput production but greater control over geometry and position can be achieved e.g. by ion beam deposition, as in this example of platina nanopillars. From [66], with permission.

film cleanliness and tensile stress, a sufficiently high relative humidity, oxygen content and type of copper used as a starting point. A common issue is "flaking", or delamination of the copper oxide layers from the copper substrate due to the high interfacial stress. By using quite thin copper foils (25 µm), our group was able to reliably produce large areas (several $cm^2$ per sample) of vertically aligned CuO nanowires [65], which were further developed for biological applications in Paper III. Compared to alternative processes, such as top-down etching methods or VLS-growth of nanowires, the CuO nanowire production method is low-cost and rapid, and requires very little instrumentation, but there is a significantly wider deviation in nanowire lengths, surface density and diameter. Also, there is no positional control over single nanowires. These factors can to a certain extent be controlled by the above mentioned parameters, such as temperature, process time and humidity, but there will always be a trade-off between process simplicity and control.

When more precise definition and positioning of nanostructures is needed, among the several methods available, EBL is most used at the laboratory scale. EBL uses a Gaussian shaped electron beam (typically a few nanometers probe size) to precisely define features in electron sensitive polymers. The beam is scanned at high speeds across the substrate (typically several mm per second), and switched on and off at rates of 5-20 MHz. As in photolithography, polymer resists can be positive or negative, depending on if the electron beam induces polymer chain scission or cross-linking. The limitations of the EBL lie in that it is a serial process, where process speed scales primarily with the writing area. In addition, the polymer films will induce forward scattering of the electrons. For typically acceleration voltages (30-100 kV) and 100 nm features, these issues become severe at one or several micron thickness, limiting the obtainable aspect ratios in the polymer films. Smaller features require thinner films. Finally, back-scattered electrons from the substrate will expose features nearby the ones being written (the proximity effect), limiting resolution and particularly minimum feature pitch. Despite these limitations, the advantages of being able to proceed from a CAD design to finished, nanoscale patterns in just a few hours makes this a staple method of nanofabrication. The patterned polymer resist films are typically used as mask materials for lift-off or etching processes, e.g. for defining material patches for VLS growth. However, as described below and developed in Paper IV, features defined in the polymer resists can also be used directly.

For the same reasons that polymers are attractive for micro-scale cell devices, polymers are interesting as high aspect ratio nanostructures. However, there are some natural material limitations. Most polymers have Young's moduli on the order of 1-4 GPa, while e.g. silicon and CuO nanowires have Young's moduli of 170 GPa and about 200 GPa, respectively [67]. These differences naturally limit the obtainable aspect ratios of polymer nanostructures, in practice standing polymer nanostructures might reach 1:10 to 1:20 in aspect ratios, while silicon or CuO can reach 1:100 to 1:1000. Still, the achievable aspect ratios can enable many interesting applications, if the production methods are scaled to nanosize. Recent results using injection-moulding [68] or replica moulding [69, 70] are promising for high throughput production of high aspect ratio polymer nanostructures in this regard. In Paper IV, we chose an EBL-based approach in SU-8 that has slightly lower throughput, but is significantly more flexible and allows rapid prototyping. SU-8 photoresist, a photo-curable epoxy, is quite stiff (Young's modulus of 4 GPa) and is also highly electron sensitive [71], so direct writing of high aspect ratio nanostructures was achieved.

### 2.3.3 Altering surface chemistry

As described above, surface chemistry is of critical importance for material interactions with biological systems [72]. Many factors can be affected by surface chemistry, such as the pH-dependent surface charge, hydrophilicity and hydrophobicity, protein adsorption and specific binding or reaction to certain molecules. One can employ either non-covalent or covalent molecular interactions to alter surface chemistry of the micro- or nanostructured materials, and a few selected methods relevant to this work will be introduced.

As an initial modification step of devices used for cell culture oxygen plasma cleaning is often used. Reactive oxygen species generated in the plasma react with essentially any oxidizable molecules, removing organic contaminants from surfaces and forming oxygen-rich surface groups on polymers. This renders most polymers and metals hydrophilic and negatively charged in solution, which is often enough to avoid protein denaturation and thus support adhesion of many common cell types. This is e.g. the treatment used in making "tissue culture polystyrene" (TCPS), the most commonly used cell culturing material.

By introducing other gaseous precursor molecules into a plasma, other surface functional groups can be produced in a process known as plasma polymerization [73]. The advantages of plasma polymerization is that a wide variety of surface functionalities can be obtained by e.g. mixing different precursors. A further advantage is that one can produce quite controllable gradients of surface chemistries by controlling reactor design [74].

For the most part, molecules used for cell interfaces are water soluble, and are therefore most easily deposited from solution. E.g. for cell attachment purposes, a solution (typically 0.001-0.1%) of polymers such as poly(L-lysine) or proteins such as fibronectin is applied to the surface for a time and then rinsed off. Adsorption of PLL, a cationic polymer, works best on negatively charged surfaces, such as oxygen plasma cleaned polymers or glass. Fibronectin, like all zwitterionic proteins, adsorbs readily to most surfaces regardless of chemistry, and usually no specific treatment is necessary [75]. A further variety of the simple polymer or protein adsorption from solution comes in the form of the mussel-inspired self-assembled dopamine films [76]. In slightly alkaline solutions, the catechol dopamine oxidizes to a quinone, and the interaction between the quinone and catechol groups self-assembles into highly adhesive, controllable thin films on essentially any surface, regardless of surface chemistry. The precise structure of the ”polymer” is not known, [77] but it is assembled and binds to surfaces through a rich variety of interactions, including electrostatics, covalent bonds, hydrogen bonds, hydrophobic interactions, $\pi - \pi$ stacking and chelation. Polydopamine is amenable to subsequent modification by binding nucleophilic groups, and also generally supports cell adhesion.

Self-assembled monolayers is a widely used method for introducing a particular chemical functionality on the surface of a variety of materials. The most common bi-functional molecules that are used for surface modification are silanes, which bind to multiple surfaces, including silicon, glass, metal oxides and some polymers, and thiols, which bind to noble metallic surfaces such as gold and copper.

Silanes are reactive compounds which have the general formula $X{-}Si{-}Y_3$, where X is a functional group and Y is a good leaving group, such as ethoxy or methoxy ethers or chloride (in order of increasing reactivity) [78]. These molecules react with surface silanol ($Si{-}OH$) groups, forming strong -Si-O-Si- bonds to the surface of e.g. glass or plasma oxidized PDMS [79, 80]. It has also been shown that they react well with other -OH groups, such as -C-OH groups present on many oxidized polymeric surfaces [81]. The assembly of high quality monolayers can be challenging, since the reaction is very sensitive to the amount of water present in the solution, and the silane molecules easily inter-polymerize [82]. Three main approaches to silanization exist: aqueous solvent, anhydrous solvent and vapor phase. In general vapor phase is considered the most reliable, but is also more time-consuming and requires clean vacuum equipment. Deposition from aqueous solutions (either pure water or alcoholic solutions with water added) can be quite efficient, but due to hydrolysis and inter- and intra-molecular bonding, the results depend on which silane is used. Anhydrous deposition in dry solvents (i.e. toluene) often leads to a more controlled process due to less hydrolysis, and is the most widely used method. Although they form covalent bonds and are widely used in biointerfaces, not all silanes form stable monolayers. Especially amino-silanes are prone to hydrolysis, resulting in detachment of the monolayer within hours of exposure to cell culture medium [83, 84].

Silanes can generally not be used on noble metals, whereas molecules with sulfide functionalities (typically -SH, S-S or similar) have been shown to have a high affinity to many noble metals, including Au, Ag, Pt and Cu [85]. The most common are thiols (R-SH), which form well-ordered monolayers on the metal surface, and are simpler and more reliable than silanes as they hardly inter-react. Several other functional groups can bind to surfaces and induce functionalities, including phosphides, phosphates and phosphites, which bind to many oxides and semiconductors, carboxyl groups which bind to certain oxides and metals, and amines, which bind to some metals and oxides [85].

The other end of the self-assembled monolayer molecules typically consist of standard organic groups such as alkyl (-CH3), hydroxyl (-OH), carboxyl (-COOH) and amine (-NH2). These cover the standard surface states of hydrophobic, uncharged but hydrophilic, negatively charged and positively charged (in solution), respectively. In addition, these groups allow many coupling reactions, such as the very common EDC and NHS coupling reaction that allows the covalent binding of amine groups to carboxyl groups, often used for immobilizing proteins to surfaces. Other common functional groups include fluorosubstituted alkanes, which are more hydrophobic than regular alkanes, and PEG, which is highly resistant to protein adsorption and cell adhesion. Other groups enabling more specific chemical reactions are also used, but will not be presented here.

In addition to the methods already described, other approaches from organic and inorganic chemistry might be used for modification. As en example, we further developed thiol-epoxide "click" chemistry [1] for use on SU-8 in Paper IV. There, un-reacted surface epoxide groups on the surface of the structured SU-8 were reacted with thiol-containing bifunctional molecules to form covalently tethered (via thioether linkages) functional groups.

## 2.4 Biological applications of micro- and nanostructured devices

In this work, both micro- and nanoscale surfaces have been engineered and implemented in devices used for cell biology studies. To set this work in perspective, a presentation of the literature on comparable systems follows.

---

[1] Click chemistry is not a specific reaction, but rather a class of reactions that are supposed to be simple, give high yields, and have large thermodynamic driving forces for completion.

### 2.4.1 Cells on micro-patterned surfaces

Micro-patterning of cells emerged with the simple control over patterned surface chemistries, developed especially by Whitesides and colleagues in the 1990s [86, 87]. The general idea has remained quite similar since then, although with numerous variations in methods and applications (reviewed in e.g. [88]). Typically, a cell adhesive molecule (such as fibronectin) is patterned using e.g. stencil lithography, soft lithography or UV-lithography, and the surrounding area is filled with a cell-repellent molecule such as PEG. The cells bind only to the cell adhesive areas, which allows control over both cell spreading, shape and migration possibilities.

Here follows some applications of flat (2D) micropatterned susbtrates. One quite common example initially shown by Wang et.al. is to use differently shaped micropatterns to study cell adhesive forces as a function of cell shape [89]. By utilizing the array format of micropatterns, Thery et.al. statistically investigated cell polarity and organization in response to assymetric adhesive areas (see Figure 2.9)[90]. McBeath et.al. showed that by regulating the available spreading area of human mesenchymal stem cells, commitment to different lineages could be controlled [91]. Tang et.al. studied the effect of cell-cell contact in differentiation of mesenchymal stem cells, by letting the cell adhere to micropatterns of increasing size [92]. Subtle effects of cell shape on cell migration were studied by Kumar et.al. [93], while Tchir et.al. studied the effects of cell-cell contact on membrane damage during cell cryopreservation by micropatterning [94]. Such systems have seen several developments in recent years, especially with a focus on increasing the lifetime of the devices as in many systems the cell repellent areas lose their function after a few days [95]. Further developments include means of patterning not only one cell type, but two or more cell types in patterned co-cultures. Early work on patterned co-coltures used a thermally sensitive polymer to control cell adhesion [96]. Later, patterned co-cultures have been pioneered especially by Khademhosseini and colleagues, using several methods [97]. Examples include stencil patterning of one cell type then allowing the other fill the gaps [56], or sequential deposition of adhesive and non-adhesive molecules and cells to generate patterns [98, 99]. Finally, one might simply exploit the differential adhesion of certain cell types [100]. There are certain limitations of each technique however. Stencil patterning has limited resolution as discussed above, and requires mechanical handling, while the other methods often only work with specific combinations of cell types that show

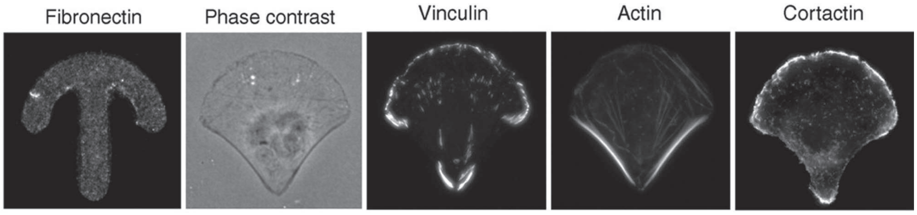

Figure 2.9: Example of an application of micropatterns for cell biology research. Here, fibronectin patterns are used to study cell polarity and distribution of cellular proteins such as actin, vinculin and cortactin as a function of cell shape. From [90], with permission ©National Academy of Sciences.

adherence to different types of surface chemistry. 2D systems in general also have some natural limitations. If one wishes to keep the areas of cells or single cells completely separate, a well geometry might be better suited. Also, in recent years greater efforts have been put into producing 3D environments for cells, as these potentially better resemble *in vivo* conditions. 3D patterning of cells is also part of this development, but will not be elaborated on further here. In a general sense, it can be argued that 2D systems have most potential when precise manipulation, control and detailed imaging are of import, while 3D systems better represent realistic systems for applications such as tissue engineering.

### 2.4.2 Surfaces for correlative electron and light microscopy of cells

Imaging the same cell or structure using both light (typically fluorescence) microscopy and electron microscopy can combine advantages from both methods. Light microscopy can be performed on live cells, molecules of interest are routinely labelled with high specificity, and e.g. confocal methods allow 3D information to be readily obtained. On the other hand, light microscopy is more or less limited to the diffraction barrier for visible photons of several hundred nanometers, while in practice electron microscopy provides as high resolution as the sample allows. The highest resolution is available by using thin sections for TEM, but modern developments in methods such as FIB/SEM dual beam tomography [101] or serial block face SEM [102] allow significantly simpler 3D volumetric imaging of cells or tissues without much loss of resolution.

Although details of different methods and sample preparations are highly interesting, for this work it is rather the methods of locating the same cell using both light and electrons that is relevant. The most straight forward method is by imaging the exact same sample using a fluorescence microscope integrated in a TEM [103], but this entails significant sacrifices of optical quality. Light and electron imaging on the same thin sections is more common, especially with the advent of superresolution methods, but loss of 3D capabilities, issues in retaining sample fluorescence and challenging preparation methods still are limitations [104]. Performing regular fluorescence imaging, followed by typical methods for electron microscopy sample preparation, provide the greatest benefits from both methods.

Then, the challenge lies in locating the same regions of the same cells using both electron and light microscopy. Although low resolution methods have been available since the 1980s [105], modern developments allowing the correlation and precise overlay of e.g. cellular features from a cell monolayers typically employ micro-patterned substrates. The substrate material can be glass, but the difficulties involved in cleanly separating glass from cells embedded in resin means that e.g. aclar, a cell-compatible, transparent and non-sticky polymer film, is often used instead. Examples of marked substrates for correlative imaging include commercial gridded glass cover slips [106], laser-etched aclar disks [107], or even just needle-scratched aclar disks [108]. A skilled microtome operator is then needed to section the embedded cell at precisely the correct location, and finally cell features or fiducial beads can be used to correlate and overlay the data. The use of FIB/SEM tomography simplifies this procedure, as the location and subsequent milling exposing the cell of interest can be done directly in the microscope, enabling quite facile full 3D correlative imaging (see Figure 2.10) [109]. We have further developed this method in Paper II by micropatterning an aclar substrate especially suitable for correlative light and FIB/SEM microscopy. This substrate enables facile location and correlation of light and FIB/SEM tomography datasets using an integrated reference grid, while the sample geometry was optimized for SEM imaging and to minimize FIB milling issues.

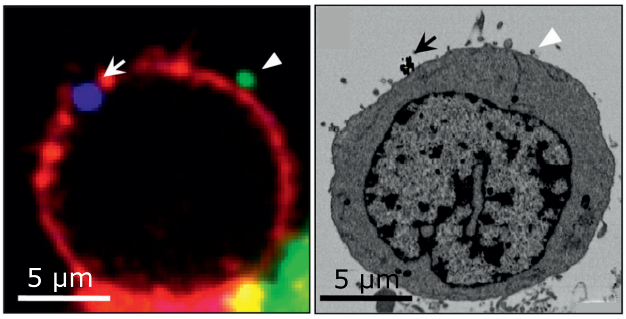

Figure 2.10: Full whole-cell 3D correlative imaging can be achieved by correlation of confocal stacks with FIB/SEM tomography stacks if the same cell can be relocated and registered. Here equivalent slices from the confocal and FIB/SEM stacks are shown, pointing out labelled features such as fluorescent gold particles (blue) and HIV viruses (green). From [109], with permission.

### 2.4.3 Biological applications of high aspect ratio nanostructures

Biomedical devices based on high aspect ratio nanostructures (HARNs) have gained increased interest in recent years due to the unconventional, highly synthetic but quite fascinating interfaces they potentially could form with cells (reviewed in [110] and [111]). The small (typically around 100 nm) cross section together with a significantly longer length (0.5 - 10 µm or more) allows them to function as nanoscale needles or probes, tightly interfacing with the cells and potentially penetrating in a minimally invasive way into the cell interior. However, high aspect ratio nanostructures also have been demonstrated in several other applications not specifically relying on this penetrating interface.

#### Surface based delivery

The general idea of using vertically aligned HARN arrays for delivery is to combine the efficient, controllable delivery of microinjection with the high throughput and multiplexing capabilities of reverse transfection cell microarrays. McKnight et.al. were the first to report successful gene delivery using aligned carbon nanofibers of about 200 nm in diameter onto which cells were impaled, and coined the term *impalefection* for transfection via cell impalement (Figure 2.11A) [112]. The nanofibers were pre-treated with DNA plasmid coding for GFP, which was either electrostatically adsorbed or covalently tethered onto the nanofibers. They

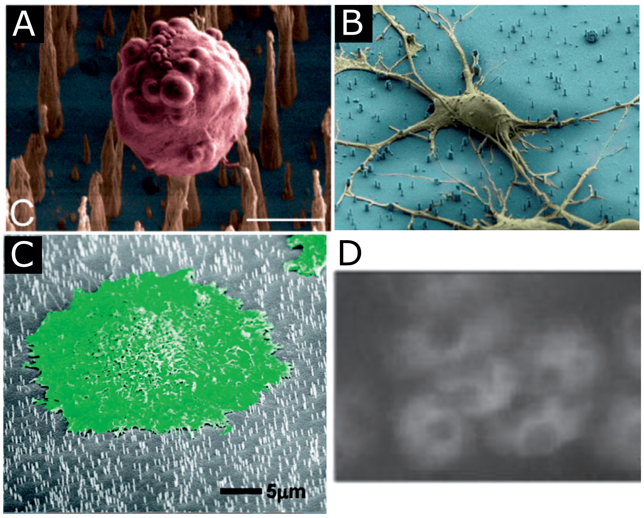

Figure 2.11: Different realizations of cell "impalefection" systems, including (A) cells on vertically aligned carbon nanofibers from [112], with permission. (B) Cells on silicon nanowires from [114], with permission ©National Academy of Science, and (C) cells on hollow alumina nanotubes from [115], with permission. (D) Micrograph of cobalt-GFP quenching assay (dark areas in bright cells) used to quantify intracellular access of nanotubes. From [116], with permission.

interfaced the cells by centrifugation and pressing the device against an elastic polymer, and achieved transfection efficiencies of around 5%. The same system was later used to deliver plasmids coding for shRNA that induce gene silencing, with an efficiency of about 50% [113].

Alternative impalement systems have been presented by several research groups since then, especially using protruding nanowires or nanopillars instead of carbon nanofibers [114, 117–123] (Figure 2.11B). In general the literature shows high cell compatibility and that the cells interface tightly with the standing high aspect ratio nanostructures. However, similar to the initial observations by McKnight, initial transfection efficiencies were low, assumed to be related to if and how the nanowires penetrate through the membrane. Kim et.al. reported plasmid delivery efficiencies of below 1% using silicon nanowires of 90 nm in diameter [117]. Shalek et.al. showed that many types of biomolecules, including fluorescently labelled DNA plasmids, RNA molecules, peptides, proteins and small molecules could be delivered into cultured cells [114]. The cells were cultured on amino-silane modified silicon nanowire arrays on which the fluorescently modified molecules had been pre-adsorbed. The nanowires varied in dimension, but were around 100 nm in diameter. Delivery of biomolecules achieved very high efficiency (close to 100%), although transfection efficiency was not stated, and it is unclear if this delivery is due to nanowire penetration or an endocytotic mechanism. A certain extent of mRNA knockdown was observed when siRNA was delivered, indicating that at least some of the delivered molecules end up in the cell cytoplasm. In addition, they showed siRNA delivery to cell lines that are typically considered difficult to transfect without perturbing cellular responses, such as neurons and primary immune cells in later work [124, 125]. This was attributed to the physical nature of nanowire impalification, in contrast to the more indirect routes of chemical transfection.

Further device developments have shown higher DNA transfection efficiencies. Peng et.al. showed greatly increased transfection efficiency of $\beta$-cyclodextrin-modified DNA/PEI/PEG nanoparticles binding to adamantane-modified silicon nanowires both *in vitro* and *in vivo* compared to flat silicon controls [121]. Wang et.al. centrifuged a substrate with diamond nanoneedles onto cells to deliver molecules in solution by a diffusion-mediated process, but needed to additionally use lipofectamine to get successful transfection [122], while Chiappini et.al. used biodegradable porous silicon nanopillars to efficiently transfect a variety of cell lines using naked DNA attached to the nanopillars [126]. Here, both centrifugation of the nanopillars onto the cells and growing cells on nanopillars was performed. Comparing the two methods by delivering both bio-active and fluorescently labelled siRNA, it was shown that centrifugation of the nanopillars onto the cells led to quick delivery, presumably through diffusion through the mechanically permeabilized membrane. On the other hand, growing cells on top of siRNA-loaded nanopillars led to no immediate delivery, but rather delivery over a 24 hour period, presumably involving a more active cellular mechanism coupled with material release from the biodegradable nanopillars.

In a slightly different type of system, Melosh and coworkers used nanostraws connected to an underlying fluidic channel to deliver molecules into cells [115] (Figure 2.11C). The nanotubes were fabricated at 100 and 750 nm in diameter, but only the 100 nm nanotubes showed successful delivery. They were able to deliver both fluorescent dyes and ions, and to some extent GFP plasmids, although transfection efficiencies were still quite low, about 5-10 %. By observing the amount of delivered fluorescent dye per cell they make a rough estimate that about 1-10% of the 100 nm nanotubes actually contribute to delivery, later refined by a cobalt quenching assay to about 7% [127] (Figure 2.11D). By including an integrated electroporation system the transfection efficiency was greatly improved (up to 80% transfected cells). In a similar set-up with nanotubes, Peer et.al. also successfully delivered dyes and nucleic acids, but only after applying a solution with saponin (a membrane permeabilizing detergent) in the nanotubes prior to delivery [128].

In conclusion, it seems that high aspect ratio nanostructures indeed can contribute to improving the delivery efficiency of molecules, but at the same time the precise role of the nanostructures in the delivery process remains unclear. In some cases it appears they destabilize or induce pores in the cell membrane, such as when applying a force by centrifugation or pressing, allowing delivery of molecules. For settling cells this mechanism is unlikely, as the gravitational forces on a settling cell is extremely low (see more about HARNs and cell membranes below). At the same time, simple upconcentration at the surface due to increased surface area does not readily explain the observed results. Chemical reactions occurring at the tight nanostructure-cell membrane interface could help explain some discrepancies, as mentioned above the widely used amino-silane hydrolyses over time, which would cause release of the surface bound molecules and make them available for uptake (but likely packaged with the aminosilane). Similarly, degradable porous silicon releases silicic acid which is known to damage cell membranes, and silica causes cell permeability to increase [129, 130]. However, in the case of nanostraws direct injection in fact does seem to occur in some cases, with temporary penetration associated with cell adhesions events [127]. In addition, membrane curvature is an important event in endocytosis [131], which thus might be influenced by the protruding nanostructures.

### Electrical, optical and sensing applications

Sensitive electrical recordings of electrically active cells is one interesting application of high aspect ratio nanostructures (recently reviewed in [132]). This idea was realized using vertical arrays of carbon nanofibers on hippocampal tissue sections by McKnight and collegues [133], and by using vertical nanowire arrays in single neurons by Robinson et.al. and in cardiomyocytes by Xie et.al. (Figure 2.12A and B) [134, 135]. In both papers, intracellular access was ensured by application of a short voltage pulse that temporarily permeabilized the cell membrane. Over time (10-30 minutes) the membrane could heal itself, and a new voltage pulse was needed to again achieve intracellular recording. Interestingly, Xie et.al. confirm the existence of pores by showing that a previously cell-impermeant dye can diffuse into the cells after the nanowire electroporation. In an alternative set-up, Duan et.al. achieved intracellular recording by using a phospholipid-modified portruding silica nanotube functioning as a channel down to a nanowire field effect transistor. The cell penetration occurred spontaneously over the course of about a minute after bringing the cells (which were grown on a PDMS sheet) gently into contact with the recording surface. Presumably the penetration mechanism was bilayer fusion. However, although the forces due to the interfacing were stated to be low, it is uncertain if they can be neglected.

Various other cellular sensing applications have also been realized using high aspect ratio nanostructures. Xie et.al. used arrays of silica nanopillars for localized imaging within cultured cells (Figure 2.12C) [136]. A specialized imaging set-up localized fluorescent excitation light to the nanopillars, allowing selective excitation of fluorophores in the immediate vicinity of the nanopillars, giving high signal and very little background noise. Na et.al. sandwiched cells between two silicon nanowire substrates to measure intracellular enzymatic activity, where the enzyme substrate was immobilized on one side of the sandwich and the cells were grown on the other [137]. Chiappini et.al. used biodegradable silicon nanopillars labelled with two fluorescent dyes to measure intracellular pH in a similar assay, except the nanopillar substrate was additionally centrifuged onto the cells [123] (Figure 2.12D). Hanson et.al. investigated the deformation of cell nuclei in response to nanopillars, and showed how the nanopillars could be used to probe nuclei mechanical properties [138]. A final form of sensing on nanowire arrays was realized by using the nanowires as sensitive force probes [139, 140]. Using well-defined nanowire arrays, deflection of the nanowires was optically measured and used to determine cell traction forces when adhering to the nanowire arrays.

### Manipulating cell adhesion, migration and differentiation

Due to the rather extreme surface topography presented by high aspect ratio nanostructures on surfaces, one might expect certain influences on substrate-mediated cell interactions. Indeed, Xie et.al. showed that neuronal migration was inhibited by the presence of nanopillars [66]. Persson et.al. showed that on GaP nanowires, fibroblast motility was severely limited, with longer nanowires

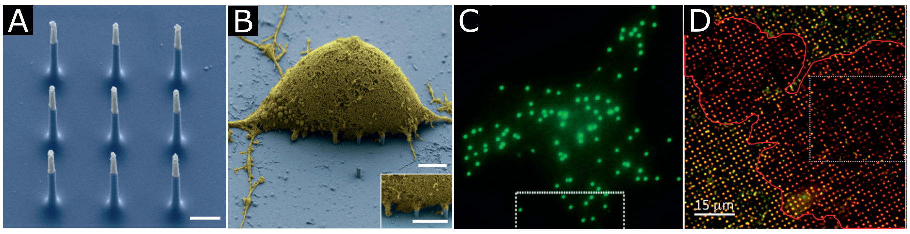

Figure 2.12: (A) Silicon nanopillars with platinum tips used for (B) intracellular recording in neurons. From [134], with permission. (C) Nanopillars were used for localized fluorescent imaging of GFP in cells using a specialized optical set-up. From [136], with permission ©National Academy of Sciences. (D) Changes in the ratio of the fluorescence of two dyes was used as an indicator of pH in cells growing on nanopillars. From [123], with permission.

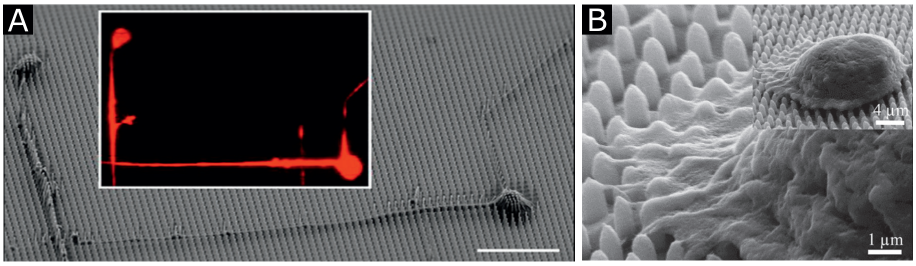

Figure 2.13: (A) Embryonic stem cells adopt highly elongated shapes in response to certain pitches in silicon nanowire arrays, which could be used to induce specific stem cell phenotypes. From [142], with permission. (B) A circulating tumour cell "captured" by adhesion onto a regular array of antibody-functionalized silicon nanopillars. From [147], with permission.

showing a stronger effect [141]. Bucaro et.al. systemetically investigated the effect of regular arrays of silicon nanowires on the spreading and polarization of embryonic stems cells [142]. They found that at short pitches the cells were suspended on top of the nanowire in a "bed of nails" fashion, and formed spindle-shaped and flatted morphologies (Figure 2.13A). On intermediate pitches (2 µm) the cells rounded and became highly polarized, with a long extension protruding from the cells. At larger pitches, the cells made contact with the substrate and formed more stellated morphologies. Cell adhesive force to HARN arrays has been reported to increase [143, 144], an effect that has been used to make circulating tumour cell capture devices out of nanostructured surfaces [145–147] both by geometry alone or in combination with capture antibodies (Figure 2.13B).

### 2.4.4 Cell interactions with high aspect ratio nanostructures

In light of the various interesting applications of high aspect ratio nanostructures presented above, the question of what the details of this interface might look like comes to mind. Especially HARN-based delivery mostly remains a "black box", where mechanisms are unclear, but also other applications would benefit from a better understanding of the cell-nanostructure interface. An alternative system that lends itself readily to investigating different aspects of this interaction is that of HARNs on probes, typically attached to an AFM tip to enable precise force monitoring.

#### Lessons learned from HARNs on probes

Pioneering this work is the group of Jun Miyake who have made silicon HARNs at the end of AFM-tips by focused ion beam etching (Figure 2.14A) [148, 149]. The HARNs were about 200 nm and 800 nm in diameter with cylindrical and cone-shaped tips. The AFM could be operated in liquid and in this way cells cultured on a glass surface could be pierced by the HARNs. By monitoring the forces acting on the nanoneedle from the cell membrane it was possible to elucidate several interesting features about the interaction. Sharp dips in the force were assumed to correspond to breaches of the cell membrane. It was shown that the nanoneedles with cylindrical tips required less force to breach the cell membrane than the corresponding cone-shaped tips, perhaps somewhat counter-intuitive compared to conventional macro-sized needles. They hypothesize that this is due to a higher shear force present on the membrane when interacting with a cylindrical tip, leading to penetration at a lower force. The depth of penetration into the cell (1.2 µm) and the required force (0.65 nN) before breaching the membrane were both lower for the 200 nm cylindrical HARN compared to the other HARNs, while the insertion probability was higher (92%).

In a comprehensive follow-up study a variety of cell types were investigated using a similar nanoneedle [150]. It was shown that the actin meshwork of the cell plays a very important role in the possibility of penetrating the membrane with a nanoneedle (Figure 2.14B and C). In model vesicles without any actin meshwork, and in cells treated so actin was depolymerized, the nanoneedles could

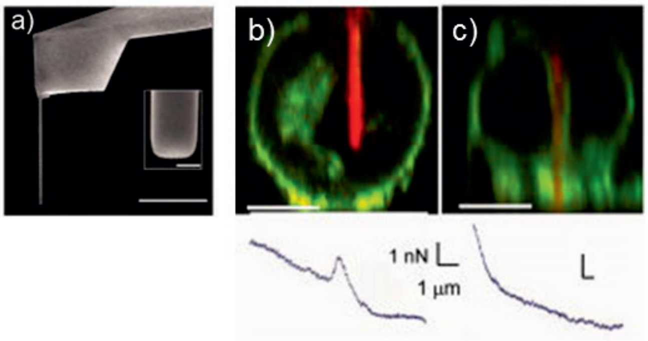

Figure 2.14: (A) Silicon nanoneedle produced by FIB milling on an AFM tip. Scale bar 10 µm, inset 100 nm. This nanoneedle was used to (B) successfully or (C) unsuccessfully penetrate into living cells, depending on the structure of the actin filament in the cell cortex. The cell membrane is labelled green, the nanoneedle is labelled red. Underneath are the force curves measured by the AFM, with a sudden drop of about 1 nN during penetration indicating membrane penetration, while a smooth force increase indicates no penetration. Scale bars 3 µm. From [150], with permission.

not penetrate the membrane. Insertion efficiencies of the nanoneedle probes were correlated both with the mesh size and the presence of actin stress fibers [150]. Following up on this work it was shown that by forming nanofilms on cells surfaces using a layer-by-layer technique the insertion efficiency of a nanoneedle could be increased, presumably due to increased stability of the cell membrane [151]. The forces involved are not discussed in detail, but are likely in the same range as above ($\sim 1$ nN). This coincides with theoretical work by the group of Nicholas Melosh, who showed via calculations using a continuum membrane elasticity model that nanoprobes interfacing with cells initially produce global deformation with large area stresses, but after a certain critical indentation depth the membrane tightly conforms to the probe (Figure 2.15) [31]. For small probes they show that cell lysis will not occur due to overall membrane strain as the global cell deformation is too small. However, in follow-work they show that sharp nanoneedles (under 100 nm diameter) might cause penetration by strain due to the large tensions generated by the strong membrane curvature at the tips [152]. Although casting an interesting light on how such interactions may occur, a limitation of the reported model and other theoretical models [153] is that they do not take into account the substantial membrane reserves and tension adjustments available to most cells, as described earlier. These factors likely alter interactions in most real-world scenarios, as we describe more carefully in Paper V.

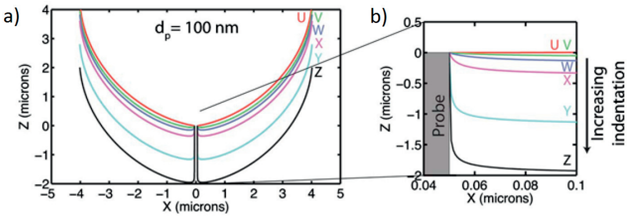

FIGURE 2.15: (A) By modelling the cell membrane as an elastic sheet surrounding an incompressible cells, membrane bending was visualized as a function of probe penetration, in this case a 100 nm probe. In this regime, at small indentations the membrane deforms globally, but then makes conformal contact with the probe as indentation is increased. (B) Higher magnification of the area near the probe. From [31], with permission.

There is some experimental evidence that indicates membrane penetration is facilitated by small probes. Vakarelski et.al. used multi-walled carbon nanotubes fortified with carbon and gold (final diameter 30-40 nm) attached to an AFM tip to penetrate living cells and deliver a quantum dot cargo [154]. At 100 pN to 200 pN the force required was several times lower than for the 200 nm silicon nanoneedles described above, and the indentation depth was only 100 nm to 200 nm compared to several microns for the larger needles.

A quite comprehensive study on the ability of HARN probes to penetrate membranes was performed recently by Angle et.al. [155]. Using three different tip geometries and 18 different surface functionalities, ranging from charged and uncharged hydrophilic coatings to hydrophobic coatings and various putative cell penetrating peptides. In this study, several of the assumptions in the studies cited above are brought into question, especially that the low reported forces in some cases might actually be cytoskeletal rearrangement events and not lipid membrane rupture. Angle et.al. clearly demonstrated that the forces required for penetrating cell membranes are independent of molecular coating, and for HEK293 cells the penetration forces are surprisingly high, around 10-30 nN depending on probe geometry. In addition, penetration in these cells only occurred after most of the cell material had been expelled from the probe area so the membranes were pressed against the substrate. However, one issue mentioned is that the relatively high loading rates used in the experiments does not allow for significant membrane or cytoskeletal rearrangements, and in some cases (e.g. for certain surface chemistries), this might hide potential longer-term effects, such as might be present when cells are allowed to settle on vertical nanostructures. In addition, as shown above cell elasticity and membrane tension are important factors in determining penetration efficiency, and these were not investigated in that report.

### Cells on vertical arrays of high aspect ratio nanostructures: Plasma membrane interactions

If applied with sufficient force on a short time-scale (high loading regime), it is quite clear that high aspect ratio nanostructures indeed are able to penetrate into the cell cytoplasm and nucleus without permanently harming the cells. For vertical arrays of high aspect ratio nanostructures, force-driven mechanisms, which could either be direct penetration, or perhaps, sufficient mechanical stress to induce temporary pore formation [152], explain e.g. intracellular delivery by centrifugation [122, 126] or tapping [112]. Indeed, in our (unpublished) experiments a certain degree of successful transfection was achieved even without nanowires present at all. Simply tapping a flat glass plate onto a monolayer of cells could induce delivery, similar to cell scraping delivery described earlier. The local electrical fields present by HARN electroporation seem to initiate similar effects [156].

What occurs in the more common low force loading regime, where the cells settle onto the HARNs without additional external forces applied, is much less clear. Here, cells will first encounter the HARNs with a very low force due to gravitational settling (piconewton scale per cell, orders of magnitude lower than the observed forces required for penetration) [152]. Cell adhesion to surfaces will then occur for most cells, but how this force will manifest on HARNs depends on the details of how the cell organizes its membrane and cytoskeleton and integrins during adhesion. A theoretical model investigating these features was developed by Xie et.al. [152], and concludes that if adhesion occurs sequentially inwards around nanostructures, pulling the membrane into substrate contact, and the cell does not contribute more membrane area to the site, then local penetration at the HARN tip may occur due to concentration of membrane tension, if HARNs are sufficiently far apart, long and thin.

Reports of spontaneous penetration are mainly based on indirect evidence of e.g. delivery or sensing. The most functional studies on penetration comes from the groups of Charles Lieber and Nicholas Melosh, in both cases using hollow vertical nanotubes for sensing or delivery, respectively [116, 127, 157]. By looking at intracellular GFP quenching by delivered cobalt ions, Xu et.al. estimate that about

7% of nanotubes penetrate cells spontaneously and have continued intracellular access. Osmotic and non-specific effects were ruled out, and penetration efficiency was related to the cell adhesion to the surface coating (no coating, polyornithine or fibronectin), and required a certain adhesion time before occurring. As mentioned above, electroporation [156] or detergents [128] can aid in causing permeabilization with nanotubes. In a study on the combined effects of membrane permeabilization (with DMSO) and actin depolymerization (with lantruncilin), it was shown that in fact DMSO only barely increased the number of penetrating nanotubes (judged by the cobalt quenching assay as above), which is quite surprising considering its membrane permeabilizing properties [116]. However, together DMSO and lantrunculin increased the number of penetrating straws from 7% to 15% , indicating that both cortical actin and the membrane are barriers to penetration. In addition, the effects were transient, after 10 minutes with PBS treatment, the 7% penetrating baseline was restored.

Direct imaging of the cell membrane-nanostructure interface has not clearly demonstrated penetration, rather the opposite is generally concluded. By developing a reliable membrane labelling method using a SNAP-tagged membrane receptors, Berthing et.al. imaged cells on InAs nanowires of various heights, spacings and surface chemistries, and in all cases could observe a cell membrane signal (both bottom and top membrane for long nanowires) following all investigated nanowires, indicating that no direct penetration occurred (Figure 2.16). The same technique together with TEM was used in our work on CuO nanowires, and showed the same situation of membrane wrapping (Paper III). By TEM observations of the interface between cells and nanopillars, Hanson et.al. also observed membrane wrapping and no evidence of membrane penetration [158] (Figure 2.16), which matches our results from fluorescent imaging of membranes using lipophilic dyes on SU-8 nanopillars (Paper IV and V). One exception is Shalek et.al., who report silicon nanowires directly penetrating various immune cells using lipophilic dye staining [124]. It is unclear why this report differs from the others, as similar protocols, nanowire dimensions and surface chemistry is used there as elsewhere. Several groups have used FIB-SEM microscopy to investigate the interface between cells and HARNs [66, 123, 126, 141], but unfortunately insufficient plasma membrane contrast is usually obtained to conclusively state if penetration occurs or not [2]. As the nuclear membrane is more clearly resolved due to its double nature (two lipid

---

[2] In my opinion, even if the authors are often more generous in their interpretations of penetration events.

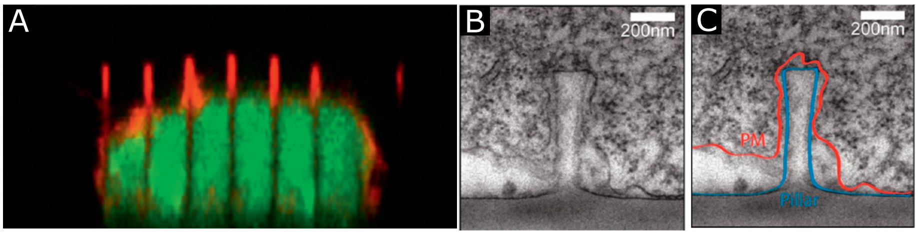

Figure 2.16: (A) By labelling a SNAP-tagged membrane protein (red), membrane wrapping of long InAs nanowires could be observed, despite them protruding nearly entirely through the cell body (green). From [159], with permission. (B) TEM imaging of cells on shorter quartz nanopillars also indicated wrapping of the cell plasma membrane (PM), as traced in (C). From [158], with permission.

bilayers), severe bending of this membrane is frequently observed [119, 138, 141], but this does not preclude additional wrapping by plasma membrane, as we have observed in our work (Paper III).

Indications of membrane penetration based on delivery by nanowires or nanopillars is also confounded by the fact that cells will endocytose materials from surfaces regardless of topography, as we show in Paper III, and as is readily observed by reverse transfection studies described above, or phagokinetic track assays [160]. This can also be observed in e.g. the work by Shalek et.al. [114, 114], where delivered material primarily locates to peri-nuclear area, indicative of active uptake rather than cytosolic delivery via nanowires. One explanation for the discrepancies between e.g. the functional nanotube studies and the imaging studies is that even the best TEM studies might not be able to reveal small, local pores or areas of increased permeability in the membrane that are not direct breaches. Especially hollow nanotube systems might be able to benefit from such features during delivery. The wide variety of HARN types used with different material properties, geometries, surface chemistries and cell types makes it hard to draw general conclusions other than that spontaneous membrane penetration might occur in a few cases, but with quite low efficiency and as an exception rather than a rule.

### Cells on vertical arrays of high aspect ratio nanostructures: Other interactions

Regardless of membrane penetration, vertical arrays of HARNs also influence cells in other ways. The conclusions from most studies is that in general cell viability remains high on substrates with protruding nanostructures, and unless cells are not able to attach due to the extreme topography, viability is quite unaffected by the presence of HARNs [110]. However, cell spreading and motility is usually affected as mentioned for certain applications above. Focal adhesions can form in cells on HARN arrays, but usually form between the HARNs and not on them [161]. Actin and possibly other proteins colocalize with nanostructure sites ([127, 138, 141, 162] and Papers III, IV and V), and in our work these puncta were revealed as ring-like or cylindrical bundles of actin around nanopillars (Paper IV). HARNs can also alter the overall organization of the cell cytoskeleton [163]. The general aspects of how cells adhere onto surfaces with vertical HARNs has been both studied and modelled in a recent paper by Buch-Månson et.al. [153] (Figure 2.17). Cells can adopt a suspended conformation by resting on top of HARNs as on a bed of nails, or the HARNs can protrude into the cell body while as the cells make surface contact. As we also have shown in Paper IV, interim states and transition between states are also possible, at least on shorter (1 µm nanopillars). Which state the cells adopt depends on a combination of HARN length, diameter, pitch and surface chemistry. Longer, thicker and denser HARN arrays with lower adhesion drive the cells towards a suspended, state, while shorter, thinner and sparser HARN arrays with higher adhesions lead to surface adhered states. The cross-over parameters vary by cell type, but for HARNs in the typical range of 100 nm diameter and 1-5µm length and standard adhesive chemistry (e.g. untreated or PLL treated), pitches of 2-3 µm mark the cross-over between suspended and adhered states [153].

As mentioned above, if the HARNs extend far enough to reach the nucleus, significant nuclear deformation is observed (Figure 2.17, Paper III, [138, 141]). Persson et.al. reported increased DNA double strand breaks in cells grown on nanowires, but this did not appear to be directly linked to the nuclear deformation and could arise from other processes. Genetic screens of cells on HARN arrays revealed upregulation of focal adhesion proteins [143, 164], but downregulation of actin cytoskeleton in one case [143]. Other genes showed small alterations, and immune regulation markers were also unaltered for several immune cells on silicon nanowire arrays [124, 125]. We have investigated endocytotic processes of cells

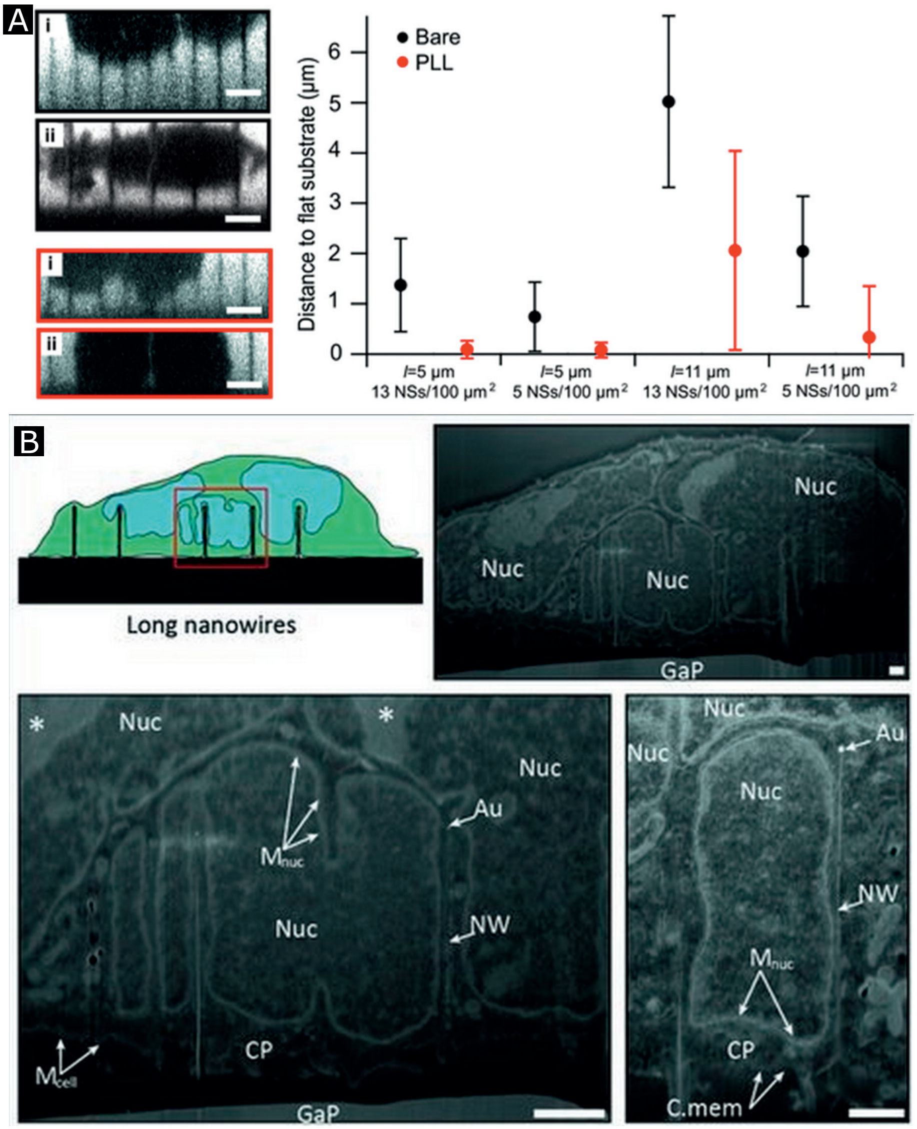

Figure 2.17: (A) By negative staining (labelling the solution instead of the cell) the distance between the surface and cells settling on nanowires of various pitch was measured. Indicating if cells were suspended as on a "bed of nails" or had the nanowires protruding into the cell body. Increased surface adhesions by PLL coating shifts the balance of suspension towards lower pitches. From [153], with permission. (B) Severe nuclear deformation is observed if protruding nanowires are long enough. From [141], with permission.

on SU-8 nanopillars (unpublished work), and no significant changes in endocytosis rates or trafficking of EGF in early and late endosomes or lysosomes was observed. However, it appeared that intracellular vesicles such as endosomes and lysosomes could get ”stuck” at nanopillar sites, presumably either due to simple geometric obstruction or due to how nanopillars interact with cell cytoskeletal components.

# Chapter 3

# Summary and discussion of papers

## 3.1 Brief summary of papers

### Paper I

2D-patterned cell cultures down to single cell resolution were realized in a novel material system consisting of a PVA hydrogel and patterned polydopamine thin films. The physically cross-linked PVA hydrogels exhibited robust cell repellency for long-term experiments (up to three weeks was investigated), while polydopamine served as a cell adhesive substrate that could be reliably patterned by microcontact printing on top of the PVA hydrogels. Patterned co-cultures were further realized by *in situ* deposition of polydopamine, allowing a second cell type to adhere in the previously cell repellent areas between the original patterned cells.

2D cell patterning systems often either lose potency after a few days of cell culture, or rely on quite complex polymer synthesis to produce more robust cell repellent materials. PVA hydrogels deposited and fixed by spin-coating and mild heating, combined with the simple and flexible patterning offered by microcontact-printed polydopamine, offers a convenient and accessible route to robust 2D cell patterning, without noticeable loss of cell repellent properties for at least 3 weeks. The hitherto unexplored aspects of *in situ* polydopamine deposition that allow, in this manifestation, realization of patterned co-cultures provides an interesting further technical development. The advantage of this form of co-cultures lies in that in principle it should work for all cell type combinations, as it does not rely on differential adhesions between cell types. In opposition to stencil methods, it also offers high resolution (single cell or less). One limitation is that only two cell types may be patterned, and the second type will adhere everywhere the first cell type did not. There was a trade-off between cell viability and deposition efficiency during *in situ* polydopamine deposition, an issue that was addressed but not fully solved, and leaves potential for further development. An interesting prospective use of the *in situ* polydopamine deposition is to tune the degree of surface adhesive sites by altering reaction time. Thus, this paper contributes to the field mainly by exploring biological applications of quite accessible, but novel material combinations.

## Paper II

Aclar films were patterned with microwells and a reference grid via a thermomoulding process, and used as a cell culture substrate for primary human macrophages infected with *M. avium* bacteria. By using the microwells and reference grid, cells could first be imaged live or fixed using confocal fluorescence microscopy, then relocated at block edges after dehydration and resin embedding for FIB/SEM 3D electron tomography. By using optimized sample preparation and imaging procedures, ultra-high resolution 3D datasets of a whole infected macrophage cell could be overlayed with specific 3D data from confocal imaging to investigate the details of the intracellular environment.

Although aclar is quite widely used as a cell culture substrate when electron microscopy is desired, it is typically used as-is or scratched by hand. In addition, as most correlative imaging systems are optimized for TEM imaging, dedicated systems for FIB/SEM imaging are lacking. Micropatterning by thermomoulding offers a reliable and convenient method to shape the substrate into a more suitable geometry and precisely define features. In this case, the well/block geometry presented a convenient substrate to perform high quality FIB/SEM tomography experiments with minimal excess milling, as the block presented a predefined flat face. The platform supported higher experimental throughput by allowing preidentification of cells of interest using light microscopy, as well as increased data specificity by correlative data overlays. Further developments lie mainly in increasing overlay precision, allowing more specific utilization of the complimentary correlative datasets. Thus, this paper contributes to the field by employing micropatterning methods to generate a useful system that simplifies and enhances important biologically relevant investigations.

## Paper III

Large, defect-free arrays of copper oxide nanowires were grown by thermal oxidation, and coated and transferred to a transparent support to increase cell compatibility and simplify cell interaction studies. The nanowires were investigated as a impalefection platform, and although delivery was observed transfection efficiency was not satisfactory. By confocal and TEM imaging of impaled cells, the cell membrane could be seen to wrap around the nanowires, excluding them from the cell cytoplasm and nucleus, potentially explaining the low transfection efficiency.

Several nanowire systems have already been explored as impalefection systems, and the main advantage of CuO nanowires lies in their extremely low-cost and high throughput production method. However, due to the difficulties inherent in imaging cells on rough, highly absorbing nanowire substrates, a nanowire transfer process that allowed retention of standing nanowires on a transparent substrate was developed. This also reduced the density of nanowires to a more suitable range. In addition, as we investigated more thoroughly in a different paper[165], copper oxide is very prone to dissolution in cell medium, leading to toxic copper ion concentrations if the CuO nanowires are not coated. Fortunately, during the developed transfer process, the nanowires were also coated with a PDMS/silica layer, isolating them from contact with the cell medium and eliminating cell toxicity. The clear indications that the cell plasma membrane excluded the nanowires, even at extreme deformations, matches other work by the co-authors on other nanowire systems [159], and explains the unsatisfactory transfection results. Thus, this paper contributed to the field both with technical innovations regarding the biological use of simply produced CuO nanowire substrates, as well as with quite detailed studies on the cell-nanowire interfaces.

## Paper IV

A system allowing definition of high aspect ratio polymer nanostructures was realized by electron beam lithography in SU-8 films on glass cover-slips. Methods to tune both size, position, shape and intrinsic fluorescence were developed. In addition, robust surface chemical modification utilizing thiol-epoxide reactions was developed and verified on micro- and nanostructured SU-8. Cell responses to and interactions with nanopillars and nanolines were characterized in significant detail, as the cover-slip substrate allowed cell imaging, including live cell imaging and super-resolution methods such as TIRF, 3D-SIM and STED, at highest possible resolution. The observations indicate that the cell membrane wraps the nanopillars as shown before for the CuO nanowires, while actin filaments can form distinct circular or cylindrical bundles around the nanopillars. Depending on nanopillar densities, cells could be suspended with a ”bed of nails” effect or adhered to the substrate fully wrapping the nanopillars. These configurations were neither absolute nor static, but could vary with time and across a single cell.

Lessons learned from developing the CuO nanowire system in Paper III indicate that to gain a good understanding of what occurs when interfacing nanostructures with a biological system, both a good control over system properties and possibilities to see what is going on are significant advantages. Both were realized in the SU-8 nanostructure system, and the results show several novel aspects of the interactivity between high aspect ratio nanostructures and cells, that are likely transferable to other systems. Especially the possibilities offered by live cell imaging and superresolution methods were valuable contributions to better understanding this interface, as these allow both dynamics of cells and greater details of specific cell interactions to be studied. The observations of actin filament co-localization with the nanopillars matches findings by others, and the details of its structure indicate that it is involved in cell membrane restructuring (i.e. wrapping or engulfing) around the nanopillars. One advantageous further development of fabrication methods would be taller nanopillars that closer resemble e.g. nanowire systems, enabling more systematic comparative studies. This paper contributes to the field by enabling high resolution optical imaging of the interface between cells and nanopillars on a surface. Further, it offers a flexible system that allows new questions regarding cell interactions with high aspect ratio nanostructures to be addressed and lays the foundation for highly controlled and biologically suitable functional nanostructured devices. In addition, the surface chemistry developments in this paper might have important applications in other SU-8 systems.

## Paper V

The nanopillar system from Paper IV was applied to study the influence of nanopillars on the adhesion, spreading and migration of NIH-3T3 fibroblasts. Dense (0.75-1 µm pitch) and sparse ((2-10 µm pitch) arrays were explored. The initial cell adhesion proceeded by engulfment of nanopillars regardless of pitch, while the later spreading and migration occurred mainly on top of the pillars (”suspended” state) on dense arrays. On sparse arrays, the cells maintained contact with the substrate, engulfing the protruding nanopillars (”adhered” state). The different states influenced cell migration rates, which were reduced compared to glass on all nanopillar arrays, but more strongly reduced on the sparse arrays. Dynamic actin puncta associated with the nanopillars, while membrane interactions were observed to be so strong that membrane tethers and residual membrane was left on nanopillars at the trailing edge of cells.

The nanopillar system developed in Paper IV provides a convenient device to study cell dynamics in response to the high aspect ratio nanostructures we are interested in. Initially, we anticipated that differences in focal adhesion formation might lead to different migration rates on nanopillar arrays of different pitches. Instead, it appears that it is the cell conformation (adhered or suspended states) that is the strongest determinant for migration rates. Theoretical models of the balance between membrane bending energy and adhesion energy in engulfment of the nanopillars appear to generally hold in our observations. However, we observed several cases where local cellular effects cause unexpected interactions, such as during initial adhesion where reduced membrane tension likely increases the amount of engulfed nanopillars on all array pitches. Large actin polymerization pressure causes engulfment at the leading edge, and dynamic actin association with nanopillars appears to be involved in cell adhesion and membrane structuring on nanopillars on all array pitches as well. This paper contributes to the field by providing more details and nuances to the interactions that might be expected when cells are interacting with surfaces with high aspect ratio nanostructures. In turn, these details can be employed to design more rational cell-interfaces, where cell responses such as pillar engulfment, migration rates and membrane states can be better predicted.

## 3.2 General discussion

The overall aim of this work was to design and characterize micro- and nanostructured surfaces for *in vitro* cell applications, a very broad goal. Narrowing the focus to more specific sub-goals led to two classes of systems: micro-patterned systems to simplify and expand cell studies by confining or patterning cells (for optical analysis in Paper I and FIB/SEM analysis in Paper II), and systems for the fundamental studies and applications of surfaces with protruding high aspect ratio nanostructures (Papers III-V).

The interest in, and resulting studies, of these classes of systems stems from several considerations. In the study of cells *in vitro* , the first goal is to recreate the *in vivo* conditions as carefully as possible, within practical limits, to ensure that the obtained results might be representative for the *in vivo* case. Secondly, one introduces a controlled perturbation to study the phenomenon of interest, such as exogenous genetic material, a drug or other cells. Finally, the effect of the perturbation should be observable, typically through direct microscopic observation or indirect methods such as molecular biology analysis, or a combination.

Micro- and nanofabrication approaches to *in vitro* cell culture platforms have mainly been focused around the application of microfluidics [166]. Microfluidics offers environmental control, reduced reagent consumption, and relevant dimensions for a range of *in vitro* cell culture applications, and is therefore especially suitable for better recreation of *in vivo*-like conditions and controlled perturbation. Ultimately, the vision of a full lab-on-a-chip system for automated analysis or even recreating whole organ-like systems on chips is a major driving force [167, 168]. Surface-based approaches have gathered somewhat less attention, perhaps as they focus less on recreating *in vivo* environments. Still, surface-based methods have great potential, as they offer the potential for highly controlled perturbations, combined with simpler instrumentation and read-out compared to most microfluidic devices. Thus, furthering surface-based methods has been the main focus of all papers in this thesis.

In particular, the different studies in this thesis have applied micro- and nanostructuring techniques to controllably introduce perturbations (such as for gene delivery with nanostructures in Paper III, cell-cell interactions in Paper I or cell-nanostructure interactions in Paper V) and also read out the effect of the perturbations through various microscopy approaches. Similar microstructured surfaces as those in Paper I and II have been described and applied in the literature in recent years [169], and nanostructured surfaces such as those in Papers III-V form a natural and useful extension for a variety of applications [2, 110]. In this context, the work in this thesis offers some novel varieties of applications, and for the later papers with SU-8 nanopillars more fundamental studies leading to interesting biophysical results stand out.

However, the main features that are specific to the papers presented here compared to other literature, lies in the approach and methodology of device design and fabrication.

From the methodology perspective, the general focus has been on using commercially available materials to avoid potential cost and availability issues. Thus, the substrates used in all systems have been standard glass cover slips or aclar films. Further, the materials used for the micro- and nanostructures were subject to the same considerations. Thus, copper oxide nanowires, patternable epoxy (SU-8), poly(vinyl alcohol) and polydopamine are all readily available and do not require highly specialized equipment to synthesise or structure, with the partial exception of electron beam lithography for SU-8 nanostructures.

A second major methodology goal was to produce systems that integrate readily into established work-flows and instrumentation. A key feature to this end was the use of transparent substrates in all systems, allowing high numerical aperture imaging in inverted microscope set-ups. This is in opposition with e.g. nearly all other high aspect ratio nanostructure systems, which are based on non-transparent materials, complicating analysis [110]. The increased possibilities offered by the choice of such substrates was especially clear in papers IV and V, where more fundamental biophysical studies could be carried out due to the imaging possibilities of the system.

Thus, although branching in slightly different directions when it comes to specific applications, this work is tied together by the common goal of producing simple, available and easy-to-use structured cell culture surfaces that expand the possibilities for perturbing and studying cells *in vitro* .

# Chapter 4

# Conclusion and outlook

The diverse range of micro- and nanostructured devices presented in this thesis demonstrates that there is significant potential for combining smart system design with facile and reproducible production methods to make devices suitable for advanced cellular perturbation or analysis. For biological applications beyond proof-of-concept experiments, simple production using low-cost materials is an advantage due to the disposable nature of most biomedical devices, although naturally this in some cases can be realized at a later point in the device development. Ease-of-use is another aspect that factors in when the device targets biologists and clinicians, and especially ready-made devices that integrate well with standard work-flows and equipment are popular.

In this work, I have observed that there are multiple trade-offs or at least considerations that must be taken in the design of devices for biomedical research applications. One example is the CuO nanowire system, which was designed from the principle of a facile and scalable production method. However, there were some practical usability disadvantages, which eventually led to the development of the less scalable, but significantly more usable system of the SU-8 nanopillars. At this stage, I think usability is more important than scalability, as demonstrated by the applicability of the SU-8 nanostructures for fundamental studies, and likely for other applications in future work. However, this is a fine balance, as the hunt for the optimal system could lead to other problems. I have encountered several very interesting nanowire systems where sample scarcity and sometimes low reproducibility were issues due to the complex fabrication methods involved. Very aware of these considerations, the methods of producing both SU-8 nanopillars and the other systems were kept as simple as possible while still aiming for high usability.

A second factor which is interesting to consider is breadth of application. Transfection is an important method, and inefficient transfection is a large problem in biomedical research. Thus, developing a system that improves or simplifies transfection would have an impact on many researchers. However, large problems are usually more difficult to solve, and not all systems will reach the bar, as was the case for our implementation of the CuO nanowires for transfection. On the other hand, 3D correlative imaging with light microscopy and FIB/SEM tomography is so far a quite limited field of research (although I anticipate it or similar systems gaining popularity quickly). Here, our developed correlative imaging platform solves a smaller problem, but is highly useful for the affected users and more easily implemented. The SU-8 nanostructure system and cell patterning system falls somewhere in between. They successfully address certain, more limited issues such as being able to easily observe the cell nanostructure interface and pattern cells for a long time, respectively. However, the general platforms and ideas have a utility beyond what was directly presented in this work, both from a materials development and applications perspective. What kind of influence will these works end up having?

Well, in the words of Niels Bohr: *"Prediction is very difficult, especially if it's about the future"*. Even so, there is no doubt in my mind that in general, micro- and nanostructured devices will play an increasing role in biomedical applications in the next years. Cell culture remains a fantastic research tool, simplifying and reducing costs of early stage biomedical research. Ever increasing demands of more precise and controlled cell studies require development and targeted application of micro- and nanotechnologies. In this regard, there are some interesting synergies between the different systems developed here. In particular, I believe that combination of both micro- and nanoscale engineering with controlled manipulation of surface chemistry and high resolution optical and electron imaging platforms is a promising direction for cell studies in general. Which technologies will actually reach widespread adoption will depend on the balance between fabrication complexity, usability and what problem is addressed. So far it is not clear if any of the systems presented here, or even described in the literature, will reach this stage. Hopefully, they at least contribute a small portion of useful technology and insight in our endeavour of understanding the natural world.

# Bibliography

[1] Zurlo J, et al. *Animals and alternatives in testing: History, science, and ethics.* Mary Ann Liebert, 2 edition. 1994.

[2] Stevens MM et al. *Exploring and engineering the cell surface interface.* Science, 310(5751):1135–8. 2005.

[3] Alberts AJB, et al. *Molecular Biology of the Cell.* Garland Science, Taylor and Francis Group. 2008.

[4] Singer SJ et al. *The fluid mosaic model of the structure of cell membranes.* Science, 175(23):720–731. 1972.

[5] Engelman DM. *Membranes are more mosaic than fluid.* Nature, 438(7068):578–80. 2005.

[6] Vereb G, et al. *Dynamic, yet structured: The cell membrane three decades after the Singer-Nicolson model.* Proceedings of the National Academy of Sciences of the United States of America, 100(14):8053–8. 2003.

[7] Sens P et al. *Membrane tension and cytoskeleton organization in cell motility.* Journal of Physics: Condensed Matter, 27(27):273103. 2015.

[8] Pontes B, et al. *Membrane elastic properties and cell function.* PloS one, 8(7):e67708. 2013.

[9] Diz-Muñoz A, et al. *Use the force: membrane tension as an organizer of cell shape and motility.* Trends in cell biology, 23(2):47–53. 2013.

[10] Figard L et al. *A membrane reservoir at the cell surface: unfolding the plasma membrane to fuel cell shape change.* Bioarchitecture, 4(2):39–46. 2014.

[11] Groulx N, et al. *Membrane reserves and hypotonic cell swelling.* The Journal of membrane biology, 214(1):43–56. 2006.

[12] Vlahakis NE et al. *Invited review: plasma membrane stress failure in alveolar epithelial cells.* Journal of applied physiology (Bethesda, Md. : 1985), 89(6):2490–2496. 2000.

[13] Pollard TD et al. *Actin, a central player in cell shape and movement.* Science, 326(5957):1208–1212. 2009.

[14] Rotsch C et al. *Drug-induced changes of cytoskeletal structure and mechanics in fibroblasts: an atomic force microscopy study.* Biophysical journal, 78(1):520–35. 2000.

[15] Yang S et al. *Force response and actin remodeling (agglomeration) in fibroblasts due to lateral indentation.* Acta biomaterialia, 3(1):77–87. 2007.

[16] Morone N, et al. *Three-dimensional reconstruction of the membrane skeleton at the plasma membrane interface by electron tomography.* Journal of Cell Biology, 174(6):851–862. 2006.

[17] Murase K, et al. *Ultrafine membrane compartments for molecular diffusion as revealed by single molecule techniques.* Biophysical journal, 86(6):4075–4093. 2004.

[18] Huang H, et al. *Cell mechanics and mechanotransduction: pathways, probes, and physiology.* American journal of physiology. Cell physiology, 287(1):C1–C11. 2004.

[19] Campbell ID et al. *Integrin structure, activation, and interactions.* Cold Spring Harbor perspectives in biology, 3(3):a004994–. 2011.

[20] Ruoslahti E. *RGD and other recognition sequences for integrins.* Annual review of cell and developmental biology, 12:697–715. 1996.

[21] Huttenlocher A et al. *Integrins in cell migration.* Cold Spring Harbor perspectives in biology, 3(9):a005074. 2011.

[22] Peskin CS, et al. *Cellular motions and thermal fluctuations: the Brownian ratchet.* Biophysical journal, 65(1):316–24. 1993.

[23] Ananthakrishnan R et al. *The forces behind cell movement.* International Journal of Biological Sciences, 3(5):303–317. 2007.

[24] Geiger B, et al. *Environmental sensing through focal adhesions.* Nature reviews. Molecular cell biology, 10(1):21–33. 2009.

[25] Digman MA, et al. *Stoichiometry of molecular complexes at adhesions in living cells.* Proceedings of the National Academy of Sciences of the United States of America, 106(7):2170–5. 2009.

[26] Ridley AJ, et al. *Cell migration: integrating signals from front to back.* Science, 302(5651):1704–9. 2003.

[27] Conner SD et al. *Regulated portals of entry into the cell.* Nature, 422(6927):37–44. 2003.

[28] Heitz F, et al. *Twenty years of cell-penetrating peptides: from molecular mechanisms to therapeutics.* Br. J. Pharmacol., 157(2):195–206. 2009.

[29] Doherty GJ et al. *Mechanisms of endocytosis.* Annual review of biochemistry, 78:857–902. 2009.

[30] Goldstein JL, et al. *Receptor-mediated endocytosis: concepts emerging from the LDL receptor system.* Annual review of cell biology, 1:1–39. 1985.

[31] Verma P, et al. *Continuum model of mechanical interactions between biological cells and artificial nanostructures.* Biointerphases, 5(2):37–44. 2010.

[32] Kaksonen M, et al. *Harnessing actin dynamics for clathrin-mediated endocytosis.* Nat. Rev. Mol. Cell Biol., 7(6):404–414. 2006.

[33] Schermelleh L, et al. *A guide to super-resolution fluorescence microscopy.* The Journal of cell biology, 190(2):165–75. 2010.

[34] ConsortiumInternational HGS. *Finishing the euchromatic sequence of the human genome.* Nature, 431(7011):931–45. 2004.

[35] Elbashir SM, et al. *Duplexes of 21-nucleotide RNAs mediate RNA interference in cultured mammalian cells.* Nature, 411(6836):494–8. 2001.

[36] Kim TK et al. *Mammalian cell transfection: the present and the future.* Analytical and bioanalytical chemistry, 397(8):3173–3178. 2010.

[37] Weaver JC et al. *Theory of electroporation: A review.* Bioelectrochemistry and Bioenergetics, 41(2):135–160. 1996.

[38] Fechheimer M, et al. *Transfection of mammalian cells with plasmid DNA by scrape loading and sonication loading.* Proceedings of the National Academy of Sciences of the United States of America, 84(23):8463–7. 1987.

[39] Sharei A, et al. *A vector-free microfluidic platform for intracellular delivery.* Proceedings of the National Academy of Sciences of the United States of America, 110(6):2082–7. 2013.

[40] Dowty ME, et al. *Plasmid DNA entry into postmitotic nuclei of primary rat myotubes.* Proceedings of the National Academy of Sciences, 92(10):4572–4576. 1995.

[41] Shimizu N, et al. *Tracking of microinjected DNA in live cells reveals the intracellular behavior and elimination of extrachromosomal genetic material.* Nucleic acids research, 33(19):6296–307. 2005.

[42] Vaughan EE et al. *Intracellular trafficking of plasmids during transfection is mediated by microtubules.* Molecular Therapy, 13(2):422–428. 2006.

[43] Luo D et al. *Enhancement of transfection by physical concentration of DNA at the cell surface.* Nature biotechnology, 18(8):893–5. 2000.

[44] Ziauddin J et al. *Microarrays of cells expressing defined cDNAs.* Nature, 411(6833):107–10. 2001.

[45] Erfle H, et al. *Reverse transfection on cell arrays for high content screening microscopy.* Nature protocols, 2(2):392–399. 2007.

[46] Norde W. *Driving forces for protein adsorption at solid surfaces.* Macromolecular Symposia, 103(1):5–18. 1996.

[47] Adkins JN. *Toward a Human Blood Serum Proteome: Analysis By Multidimensional Separation Coupled With Mass Spectrometry.* Molecular & Cellular Proteomics, 1(12):947–955. 2002.

[48] Vroman L, et al. *Interaction of high molecular weight kininogen, factor XII, and fibrinogen in plasma at interfaces.* Blood, 55(1):156–9. 1980.

[49] Walkey CD et al. *Understanding and controlling the interaction of nanomaterials with proteins in a physiological environment.* Chemical Society reviews, 41(7):2780–99. 2012.

[50] Chen S, et al. *Surface hydration: Principles and applications toward*

*low-fouling/nonfouling biomaterials.* Polymer, 51(23):5283–5293. 2010.

[51] Heuberger M, et al. *Interaction forces and morphology of a protein-resistant poly(ethylene glycol) layer.* Biophysical journal, 88(1):495–504. 2005.

[52] Lord MS, et al. *Influence of nanoscale surface topography on protein adsorption and cellular response.* Nano Today, 5(1):66–78. 2010.

[53] Hardt DE, et al. *Process Control in Micro-Embossing: A Review.* Innovation in Manufacturing Systems and Technology. 2004.

[54] Qin D, et al. *Soft lithography for micro- and nanoscale patterning.* Nature protocols, 5(3):491–502. 2010.

[55] Folch A, et al. *Microfabricated elastomeric stencils for micropatterning cell cultures.* J. Biomed. Mater. Res., 52(2):346–353. 2000.

[56] Wright D, et al. *Generation of static and dynamic patterned co-cultures using microfabricated parylene-C stencils.* Lab on a Chip, 7(10):1272–1279. 2007.

[57] Cho CH, et al. *Layered patterning of hepatocytes in co-culture systems using microfabricated stencils.* Biotechniques, 48(1):47–52. 2010.

[58] Roth EA, et al. *Inkjet printing for high-throughput cell patterning.* Biomaterials, 25(17):3707–3715. 2004.

[59] Fu Y, et al. *Synthesis of Fe2O3 nanowires by oxidation of iron.* Chem. Phys. Lett., 350(5-6):491–494. 2001.

[60] Yao BD, et al. *Formation of ZnO nanostructures by a simple way of thermal evaporation.* Applied Physics Letters, 81(4):757–759. 2002.

[61] Li JY, et al. *Synthesis of β-Ga2O3 nanorods.* Journal of Alloys and Compounds, 306(1-2):300–302. 2000.

[62] Iwanaga H, et al. *Morphology of SnO2 whiskers.* J. Cryst. Growth, 83(4):602–605. 1987.

[63] Jiang X, et al. *CuO nanowires can be synthesized by heating copper substrates in air.* Nano letters, 2(12):1333–1338. 2002.

[64] Hansen BJ, et al. *Short-circuit diffusion growth of long bi-crystal CuO nanowires.* Chemical Physics Letters, 504(1-3):41–45. 2011.

[65] Mumm F et al. *Oxidative fabrication of patterned, large, non-flaking CuO nanowire arrays.* Nanotechnology, 22(10):105605. 2011.

[66] Xie C, et al. *Noninvasive neuron pinning with nanopillar arrays.* Nano letters, 10(10):4020–4. 2010.

[67] Tan EPS, et al. *Crystallinity and surface effects on Young's modulus of CuO nanowires.* Applied Physics Letters, 90(16):163112. 2007.

[68] Stormonth-Darling JM, et al. *Injection moulding of ultra high aspect ratio nanostructures using coated polymer tooling.* Journal of Micromechanics and

Microengineering, 24(7):075019. 2014.

[69] Zhang Y, et al. *Replica molding of high-aspect-ratio polymeric nanopillar arrays with high fidelity.* Langmuir, 22(20):8595–8601. 2006.

[70] Hu W, et al. *Inhibited cell spreading on polystyrene nanopillars fabricated by nanoimprinting and in situ elongation.* Nanotechnology, 21(38):385301. 2010.

[71] Pepin A, et al. *Exploring the high sensitivity of SU-8 resist for high resolution electron beam patterning.* Microelectronic engineering, 73:233–237. 2004.

[72] Verma A et al. *Effect of surface properties on nanoparticle-cell interactions.* Small, 6(1):12–21. 2010.

[73] Siow KS, et al. *Plasma Methods for the Generation of Chemically Reactive Surfaces for Biomolecule Immobilization and Cell Colonization - A Review.* Plasma Processes and Polymers, 3(6-7):392–418. 2006.

[74] Whittle JD, et al. *A method for the deposition of controllable chemical gradients.* Chemical Communications, (14):1766. 2003.

[75] Klebe RJ, et al. *Adhesive substrates for fibronectin.* Journal of cellular physiology, 109(3):481–8. 1981.

[76] Lee H, et al. *Mussel-inspired surface chemistry for multifunctional coatings.* Science, 318(5849):426–430. 2007.

[77] Liebscher J, et al. *Structure of polydopamine: A never-ending story?* Langmuir, 29(33):10539–10548. 2013.

[78] Ulman A. *Formation and Structure of Self-Assembled Monolayers.* Chemical Reviews, 96(4):1533–1554. 1996.

[79] Wasserman SR, et al. *Structure and reactivity of alkylsiloxane monolayers formed by reaction of alkyltrichlorosilanes on silicon substrates.* Langmuir, 5(4):1074–1087. 1989.

[80] Wu CC, et al. *Effect of polydimethylsiloxane surfaces silanized with different nitrogen-containing groups on the adhesion progress of epithelial cells.* Surface and Coatings Technology, 205(10):3182–3189. 2011.

[81] Fissi LE, et al. *Amine functionalized SU-8 layer guiding Love mode surface acoustic wave.* Sensors and Actuators B: Chemical, 144(1):23–26. 2010.

[82] Krasnoslobodtsev AV et al. *Effect of water on silanization of silica by trimethoxysilanes.* Langmuir, 18(8):3181–3184. 2002.

[83] Smith EA et al. *How to prevent the loss of surface functionality derived from aminosilanes.* Langmuir, 24(21):12405–12409. 2008.

[84] Zhu M, et al. *How to prepare reproducible, homogeneous, and hydrolytically stable aminosilane-derived layers on silica.* Langmuir, 28(1):416–423. 2012.

[85] Love JC, et al. *Self-assembled monolayers of thiolates on metals as a form of nanotechnology.* Chem Rev, 105(4):1103–1169. 2005.

[86] Chen C, et al. *Micropatterned Surfaces for Control of Cell Shape, Position, and Function.* Biotechnology Progress, 14(3):356–363. 1998.

[87] Kane RS, et al. *Patterning proteins and cells using soft lithography.* Biomaterials, 20(23-24):2363–76. 1999.

[88] Fernandes TG, et al. *High-throughput cellular microarray platforms: applications in drug discovery, toxicology and stem cell research.* Trends in biotechnology, 27(6):342–9. 2009.

[89] Wang N, et al. *Micropatterning tractional forces in living cells.* Cell motility and the cytoskeleton, 52(2):97–106. 2002.

[90] Théry M, et al. *Anisotropy of cell adhesive microenvironment governs cell internal organization and orientation of polarity.* Proceedings of the National Academy of Sciences of the United States of America, 103(52):19771–6. 2006.

[91] McBeath R, et al. *Cell Shape, Cytoskeletal Tension, and RhoA Regulate Stem Cell Lineage Commitment.* Developmental Cell, 6(4):483–495. 2004.

[92] Tang J, et al. *The regulation of stem cell differentiation by cell-cell contact on micropatterned material surfaces.* Biomaterials, 31(9):2470–2476. 2010.

[93] Kumar G, et al. *Guiding cell migration using one-way micropattern arrays.* Advanced Materials, 19(8):1084–1090. 2007.

[94] Tchir J et al. *Mitochondria and membrane cryoinjury in micropatterned cells: effects of cell-cell interactions.* Cryobiology, 61(1):100–7. 2010.

[95] Fink J, et al. *Comparative study and improvement of current cell micro-patterning techniques.* Lab. Chip, 7(6):672–680. 2007.

[96] Yamato M, et al. *Thermally responsive polymer-grafted surfaces facilitate patterned cell seeding and co-culture.* Biomaterials, 23(2):561–567. 2002.

[97] Kaji H, et al. *Engineering systems for the generation of patterned co-cultures for controlling cell–cell interactions.* BBA: Gen. Subjects, 1810(3):239–250. 2011.

[98] Fukuda J, et al. *Micropatterned cell co-cultures using layer-by-layer deposition of extracellular matrix components.* Biomaterials, 27(8):1479–1486. 2006.

[99] Khademhosseini A, et al. *Layer-by-layer deposition of hyaluronic acid and poly-L-lysine for patterned cell co-cultures.* Biomaterials, 25(17):3583–3592. 2004.

[100] Khetani SR et al. *Microscale culture of human liver cells for drug development.* Nature biotechnology, 26(1):120–126. 2008.

[101] Heymann JAW, et al. *Site-specific 3D imaging of cells and*

*tissues with a dual beam microscope.* Journal of structural biology, 155(1):63–73. 2006.

[102] Denk W et al. *Serial block-face scanning electron microscopy to reconstruct three-dimensional tissue nanostructure.* PLoS biology, 2(11):e329. 2004.

[103] Agronskaia AV, et al. *Integrated fluorescence and transmission electron microscopy.* Journal of structural biology, 164(2):183–9. 2008.

[104] Cortese K, et al. *Advanced correlative light/electron microscopy: current methods and new developments using Tokuyasu cryosections.* Journal of histochemistry and cytochemistry, 57(12):1103–1112. 2009.

[105] Perrie WT et al. *The correlation of light and electron microscope observations.* Journal of Microscopy, 130(1):73–77. 1983.

[106] Hanson HH, et al. *Streamlined embedding of cell monolayers on gridded glass-bottom imaging dishes for correlative light and electron microscopy.* Microscopy and microanalysis, 16(6):747–754. 2010.

[107] Spiegelhalter C, et al. *From dynamic live cell imaging to 3D ultrastructure: novel integrated methods for high pressure freezing and correlative light-electron microscopy.* PloS one, 5(2):e9014. 2010.

[108] Jiménez N, et al. *Gridded Aclar: preparation methods and use for correlative light and electron microscopy of cell monolayers, by TEM and FIB-SEM.* Journal of microscopy, 237(2):208–20. 2010.

[109] Murphy GE, et al. *Correlative 3D imaging of whole mammalian cells with light and electron microscopy.* Journal of structural biology, 176(3):268–278. 2011.

[110] Bonde S, et al. *Exploring arrays of vertical one-dimensional nanostructures for cellular investigations.* Nanotechnology, 25(36):362001. 2014.

[111] Elnathan R, et al. *Engineering vertically aligned semiconductor nanowire arrays for applications in the life sciences.* Nano Today, 9(2):172–196. 2014.

[112] McKnight TE, et al. *Tracking Gene Expression after DNA Delivery Using Spatially Indexed Nanofiber Arrays.* Nano Letters, 4(7):1213–1219. 2004.

[113] Mann DGJ, et al. *Inducible RNA interference-mediated gene silencing using nanostructured gene delivery arrays.* ACS nano, 2(1):69–76. 2007.

[114] Shalek AK, et al. *Vertical silicon nanowires as a universal platform for delivering biomolecules into living cells.* Proceedings of the National Academy of Sciences of the United States of America, 107(5):1870–5. 2010.

[115] Vandersarl JJ, et al. *Nanostraws for direct fluidic intracellular access.* Nano Letters, 12(8):3881–3886. 2012.

[116] Aalipour A, et al. *Plasma Membrane and Actin Cytoskeleton as Synergistic Barriers to*

*Nanowire Cell Penetration.* Langmuir, 30(41):12362–12367. 2014.

[117] Kim W, et al. *Interfacing silicon nanowires with mammalian cells.* J. Am. Chem. Soc., 129(23):7228–7229. 2007.

[118] Hällström W, et al. *Gallium phosphide nanowires as a substrate for cultured neurons.* Nano letters, 7(10):2960–5. 2007.

[119] Mumm F, et al. *A transparent nanowire-based cell impalement device suitable for detailed cell-nanowire interaction studies.* Small, 9(2):263–272. 2013.

[120] Pan J, et al. *Stimulation of gene transfection by silicon nanowire arrays modified with polyethylenimine.* ACS applied materials & interfaces, 6(16):14391–8. 2014.

[121] Peng J, et al. *Molecular recognition enables nanosubstrate-mediated delivery of gene-encapsulated nanoparticles with high efficiency.* ACS nano, 8(5):4621–9. 2014.

[122] Wang Y, et al. *Poking cells for efficient vector-free intracellular delivery.* Nature communications, 5:4466. 2014.

[123] Chiappini C, et al. *Biodegradable Nanoneedles for Localized Delivery of Nanoparticles in Vivo: Exploring the Biointerface.* ACS nano. 2015.

[124] Shalek AK, et al. *Nanowire-mediated delivery enables functional interrogation of primary immune cells: application to the analysis of chronic lymphocytic leukemia.* Nano letters, 12(12):6498–504. 2012.

[125] Yosef N, et al. *Dynamic regulatory network controlling TH17 cell differentiation.* Nature, 496(7446):461–8. 2013.

[126] Chiappini C, et al. *Biodegradable silicon nanoneedles delivering nucleic acids intracellularly induce localized in vivo neovascularization.* Nature Materials, 14(5):532–539. 2015.

[127] Xu AM, et al. *Quantification of nanowire penetration into living cells.* Nature communications, 5:3613. 2014.

[128] Peer E, et al. *Hollow nanoneedle array and its utilization for repeated administration of biomolecules to the same cells.* ACS nano, 6(6):4940–6. 2012.

[129] Merchant RK, et al. *Silica directly increases permeability of alveolar epithelial cells.* J Appl Physiol, 68(4):1354–1359. 1990.

[130] Singh SV et al. *Interrelationship between hemolysis and lipid peroxidation of human erythrocytes induced by silicic acid and silicate dusts.* Journal of applied toxicology, 7(2):91–96. 1987.

[131] Reynwar BJ, et al. *Aggregation and vesiculation of membrane proteins by curvature-mediated interactions.* Nature, 447(7143):461–4. 2007.

[132] Angle MR, et al. *Nanotechnology and neurophysiology.* Current opinion in neurobiology, 32:132–140. 2015.

[133] Yu Z, et al. *Vertically aligned carbon nanofiber arrays record electrophysiological signals from hippocampal slices.* Nano letters, 7(8):2188–95. 2007.

[134] Robinson JT, et al. *Vertical nanowire electrode arrays as a scalable platform for intracellular interfacing to neuronal circuits.* Nature nanotechnology, 7(3):180–4. 2012.

[135] Xie C, et al. *Intracellular recording of action potentials by nanopillar electroporation.* Nature nanotechnology, 7(3):185–90. 2012.

[136] Xie C, et al. *Vertical nanopillars for highly localized fluorescence imaging.* Proceedings of the National Academy of Sciences of the United States of America, 108(10):3894–3899. 2011.

[137] Na YR, et al. *Probing enzymatic activity inside living cells using a nanowire-cell "sandwich" assay.* Nano letters, 13(1):153–8. 2013.

[138] Hanson L, et al. *Vertical nanopillars for in situ probing of nuclear mechanics in adherent cells.* Nature Nanotechnology, advance on. 2015.

[139] Li Z, et al. *Quantifying the traction force of a single cell by aligned silicon nanowire array.* Nano letters, 9(10):3575–80. 2009.

[140] Hällström W, et al. *Fifteen-piconewton force detection from neural growth cones using nanowire arrays.* Nano letters, 10(3):782–7. 2010.

[141] Persson H, et al. *Fibroblasts cultured on nanowires exhibit low motility, impaired cell division, and DNA damage.* Small, 9(23):4006–4016. 2013.

[142] Bucaro Ma, et al. *Fine-tuning the degree of stem cell polarization and alignment on ordered arrays of high-aspect-ratio nanopillars.* ACS nano, 6(7):6222–30. 2012.

[143] Qi S, et al. *Cell adhesion and spreading behavior on vertically aligned silicon nanowire arrays.* ACS applied materials & interfaces, 1(1):30–4. 2009.

[144] Kim DJ, et al. *Statistical analysis of immuno-functionalized tumor-cell behaviors on nanopatterned substrates.* Nanoscale research letters, 7(1):637. 2012.

[145] Yoon HJ, et al. *Emerging role of nanomaterials in circulating tumor cell isolation and analysis.* ACS nano, 8(3):1995–2017. 2014.

[146] Lee SK, et al. *Nanowire substrate-based laser scanning cytometry for quantitation of circulating tumor cells.* Nano letters, 12(6):2697–704. 2012.

[147] Wang S, et al. *Effects of nanopillar array diameter and spacing on cancer cell capture and cell behaviors.* Nanoscale, 6(21):12482–9. 2014.

[148] Obataya I, et al. *Mechanical sensing of the penetration of various nanoneedles into a living cell using atomic force microscopy.* In *Biosensors and Bioelectronics*,

volume 20, pages 1652–1655. Research Institute for Cell Engineering (RICE), National Institute of Advanced Industrial Science and Technology (AIST), 3-11-46 Nakoji, Amagasaki, Hyogo 661-0974, Japan.. 2005.

[149] Obataya I, et al. *Nanoscale operation of a living cell using an atomic force microscope with a nanoneedle.* Nano Letters, 5(1):27–30. 2005.

[150] Kagiwada H, et al. *The mechanical properties of a cell, as determined by its actin cytoskeleton, are important for nanoneedle insertion into a living cell.* Cytoskeleton, 67(8):496–503. 2010.

[151] Amemiya Y, et al. *Formation of nanofilms on cell surfaces to improve the insertion efficiency of a nanoneedle into cells.* Biochemical and biophysical research communications, 420(3):662–5. 2012.

[152] Xie X, et al. *Mechanical model of vertical nanowire cell penetration.* Nano Letters, 13(12):6002–6008. 2013.

[153] Buch-Må nson N, et al. *Towards a Better Prediction of Cell Settling on Nanostructure Arrays-Simple Means to Complicated Ends.* Advanced Functional Materials, advance on. 2015.

[154] Vakarelski IU, et al. *Penetration of living cell membranes with fortified carbon nanotube tips.* Langmuir, 23(22):10893–10896. 2007.

[155] Angle M, et al. *Penetration of Cell Membranes and Synthetic Lipid Bilayers by Nanoprobes.* Biophysical Journal, 107(9):2091–2100. 2014.

[156] Xie X, et al. *Nanostraw-electroporation system for highly efficient intracellular delivery and transfection.* ACS Nano, 7(5):4351–4358. 2013.

[157] Duan X, et al. *Intracellular recordings of action potentials by an extracellular nanoscale field-effect transistor.* Nature Nanotechnology, 7(3):174–179. 2011.

[158] Hanson L, et al. *Characterization of the cell-nanopillar interface by transmission electron microscopy.* Nano letters, 12(11):5815–20. 2012.

[159] Berthing T, et al. *Cell membrane conformation at vertical nanowire array interface revealed by fluorescence imaging.* Nanotechnology, 23(41):415102. 2012.

[160] Nogalski MT, et al. *A quantitative evaluation of cell migration by the phagokinetic track motility assay.* Journal of visualized experiments : JoVE, 121(70):4165. 2012.

[161] Bonde S, et al. *Tuning InAs nanowire density for HEK293 cell viability, adhesion, and morphology: perspectives for nanowire-based biosensors.* ACS applied materials & interfaces, 5(21):10510–9. 2013.

[162] Persson H, et al. *Vertical oxide nanotubes connected by subsurface microchannels.* Nano Research, 5(3):190–198. 2012.

[163] Kim SY et al. *Collective behaviors of mammalian cells on amine-coated silicon nanowires.* Nanotechnology, 24(45):455704. 2013.

[164] SanMartin A, et al. *Microarray Analysis Reveals Moderate Gene Expression Changes in Cortical Neural Stem Cells Cultured on Nanowire Arrays.* Journal of Nanoscience and Nanotechnology, 14(7):4880–4885. 2014.

[165] Bassett DC, et al. *Dissolution of copper mineral phases in biological fluids and the controlled release of copper ions from mineralized alginate hydrogels.* Biomedical Materials, 10(1):015006. 2014.

[166] Young EWK et al. *Fundamentals of microfluidic cell culture in controlled microenvironments.* Chemical Society reviews, 39(3):1036–48. 2010.

[167] Neuži P, et al. *Revisiting lab-on-a-chip technology for drug discovery.* Nature reviews. Drug discovery, 11(8):620–32. 2012.

[168] Huh D, et al. *Reconstituting organ-level lung functions on a chip.* Science (New York, N.Y.), 328(5986):1662–8. 2010.

[169] Falconnet D, et al. *Surface engineering approaches to micropattern surfaces for cell-based assays.* Biomaterials, 27(16):3044–3063. 2006.

# Paper I

IOP Publishing Biofabrication
Biofabrication **5** (2013) 045009 (13pp) doi:10.1088/1758-5082/5/4/045009

# Patterned cell arrays and patterned co-cultures on polydopamine-modified poly(vinyl alcohol) hydrogels

**Kai M Beckwith and Pawel Sikorski**

Department of Physics, Norwegian University of Science and Technology, N-7491 Trondheim, Norway

E-mail: kai.beckwith@ntnu.no

Received 10 July 2013
Accepted for publication 18 September 2013
Published 26 November 2013
Online at stacks.iop.org/BF/5/045009

**Abstract**
Live cell arrays are an emerging tool that expand traditional 2D *in vitro* cell culture, increasing experimental precision and throughput. A patterned cell system was developed by combining the cell-repellent properties of polyvinyl alcohol hydrogels with the cell adhesive properties of self-assembled films of dopamine (polydopamine). It was shown that polydopamine could be patterned onto spin-cast polyvinyl alcohol hydrogels by microcontact printing, which in turn effectively patterned the growth of several cell types (HeLa, human embryonic kidney, human umbilical vein endothelial cells (HUVEC) and prostate cancer). The cells could be patterned in geometries down to single-cell confinement, and it was demonstrated that cell patterns could be maintained for at least 3 weeks. Furthermore, polydopamine could be used to modify poly(vinyl alcohol) *in situ* using a cell-compatible deposition buffer (1 mg mL$^{-1}$ dopamine in 25 mM tris with a physiological salt balance). The treatment switched the PVA hydrogel from cell repellent to cell adhesive. Finally, by combining microcontact printing and *in situ* deposition of polydopamine, patterned co-cultures of the same cell type (HeLa/HeLa) and dissimilar cell types (HeLa/HUVEC) were realized through simple chemistry and could be studied over time. The combination of polyvinyl alcohol and polydopamine was shown to be an attractive route to versatile, patterned cell culture experiments with minimal infrastructure requirements and low complexity.

S Online supplementary data available from stacks.iop.org/BF/5/045009/mmedia

(Some figures may appear in colour only in the online journal)

## 1. Introduction

Patterning live cells in arrays is emerging as a powerful technique to enable the study of single cells or clusters of cells in a high-throughput manner, with increased control over cell–cell interactions and cell morphology [1–5]. Patterned cell arrays have been used to assess the relation between cell shape and function [6, 7] assay biological functions at a single cell level [8–10], induce stem cell differentiation and study stem cell biology and growth [11–15] and analyze cell migration [16, 17]. A range of materials and techniques has emerged to allow micropatterning of cells in a controlled manner, typically combining anti-fouling and cell-repellent materials such as poly(ethylene glycol) (PEG) [18] with chemistries to which cells can bind [19]. Micropatterning of cell-directing materials can be achieved in numerous ways [20], such as by photo lithography [21], stencil patterning [22] or soft lithography [23]. Micropatterned co-cultures, where the spatial positions of two or more different cell types are controlled through the patterning process, are a further extension of micropatterned cell cultures. Co-cultures can enable the design of more tissue-reminiscent *in vitro* cell culture systems [24], allowing the interactions between different cell types to be studied [25, 26].

Hydrogels are becoming widely used as cell culturing materials due to their large potential within tissue engineering [27] and the ability to tune properties, such as elasticity,

© 2013 IOP Publishing Ltd Printed in the UK & the USA

cell ligand density, porosity and other physical and chemical factors in a controlled manner [28, 29]. Poly(vinyl alcohol) (PVA) is a widely available synthetic biocompatible polymer with interesting applications within tissue engineering [30]. PVA can form stable hydrogels through chemical or radiation-induced cross-linking or freeze-thaw methods [31]. However, the simplest method to form PVA hydrogels is thermal treatment above the glass transition temperature of PVA (85 °C [32]), resulting in gels that are stable for long periods in solution [33]. PVA has good film-forming and surface adhesion properties, allowing it to form thin, surface-bound hydrogel films through, e.g., dip coating or spin coating on substrates [34, 35]. Pristine PVA has low protein adsorption [36] and inhibits cell attachment [37], and cell adhesive areas can be made by patterning PVA films. Micropatterning methods of PVA include micro photoablation [38], micromolding on surfaces [39] or in capillaries [40], UV light-enabled degradation [37], photo-cross-linking [41, 42] or inkjet printing of oxidizing solutions [37]. However, so far the available patterning methods are still somewhat limited in either resolution, chemical functionality or by the complex chemistry and instrumentation involved.

Recently, self-assembled films of catecholamines such as dopamine have emerged as versatile and multifunctional coatings for a variety of materials [43]. By exposing a surface to a mildly alkaline solution containing dopamine, the dopamine oxidizes and self-assembles into a thin surface layer of 'polydopamine' that is highly stable, but still reactive toward several nucleophiles [44]. Polydopamine has been shown to be cell compatible [45] and has been applied to surfaces by microcontact printing to generate cell patterns [46, 47] also on the typical non-fouling surface of PEG-containing monolayers [48, 49]. Furthermore, polydopamine has been blended with PVA to make a partially cell-repellent polymer [50] and has been used to make PVA hydrogels more cell adhesive [51].

In this paper, we present the development of a cell micropatterning system based on PVA and polydopamine. Through the use of polydopamine as an adhesive layer, stable, cell-repellent PVA hydrogel films were formed on multiple substrates such as glass, polystyrene (PS), poly(dimethyl siloxane) (PDMS) and Aclar. Microcontact-printed polydopamine on PVA is shown to pattern cells for up at least 3 weeks without pattern degradation. Polydopamine on PVA is demonstrated as a versatile patterning method through the patterning of several cell types, modification of polydopamine with poly(ethyleneimine) (PEI) for altered functionality and integration with microfluidic channels. Finally, we present a method to deposit polydopamine during cell culturing, allowing *in situ* switching of non-patterned PVA areas. By combining microcontact printing and *in situ* polydopamine deposition, both same cell (HeLa/HeLa) and dissimilar cell (HeLa/human umbilical vein endothelial cells (HUVEC)) co-cultures are demonstrated.

Thus, the current study demonstrates that through the use of off-the-shelf chemicals such as PVA and polydopamine and using only simple, mild chemistry and methods, several advanced cell culture applications are achievable. Thereby, this system can expand the possibilities available to many cell biology labs without the need for custom materials or extensive equipment.

## 2. Materials and methods

### *2.1. Production of PDMS stamps*

A PDMS stamp was made from an SU-8 master in a standard soft-lithography process [52]. Briefly, plastic foil masks were designed using Clewin 4 (Wieweb software) and printed by JD Photo-Tools (Lancaster, UK). SU-8 masters were made by performing photolithography with the foil masks on SU-8 5 (MicroChem corp.) on silicon wafers according to the manufacturer's instructions. An anti-adhesion coating was applied to the master by placing it in a vacuum desiccator with a drop of trichloro(1H,1H,2H,2H-perfluorooctyl)silane (Sigma) for 20 min. PDMS (Sylgard 184, Dow Corning), mixed at a 10:1 (base:cross-linker) ratio was cast over the master, and cured at 80 °C for 2 h, then carefully peeled off the master.

### *2.2. Substrate preparation and PVA coating*

Glass cover slips (VWR) were cleaned by immersion in 1M HCl (Sigma) at 60 °C for 2 h, then sonicated for 5 min in deionized water (DIW). They were stored in DIW until use. Polyethylene terephthalate (PET) (cut from culture medium bottle), PS (cut from a PS petri dish), PDMS (cast into a petri dish and peeled off) and Aclar film (Ted Pella) were cleaned by sonication for 5 min in ethanol and blown dry before use. An adhesion layer of polydopamine was applied by floating the substrate on a 1 mg mL$^{-1}$ solution of dopamine hydrochloride (Sigma) in 10 mM tris (Tris(hydroxymethyl)aminomethane, Sigma) buffer, pH = 8.5 for 30 min [43]. To avoid the surface debris caused by large polydopamine particles that appear in solution when samples are immersed, the substrates were instead floated upside down on a drop of the dopamine solution.

A 1% PVA solution was prepared by dissolving PVA (Mw = 22 000, degree of hydrolysis >98%, BDH, VWR) in DIW at 90 °C. After stirring for 15 min, all the PVA had dissolved and the solution was cooled to room temperature. To produce a thin PVA film, a small drop was placed onto the substrates and spin-cast for 30 s at 3000 rpm on a custom-built spin coater, giving a PVA film of about 15 nm in thickness. The PVA film was heat annealed for 30 min at 130 °C (90 °C on polymer supports), which was necessary to immobilize the film [37]. For live-cell imaging experiments, PVA was spin-coated in the bottom of a Willco confocal dish (Willco Wells, The Netherlands).

### *2.3. Microcontact printing*

To produce cell patterns, microcontact printing of polydopamine was performed [47]. The PDMS stamp was floated on a 1 mg mL$^{-1}$ solution of dopamine hydrochloride in 10 mM tris buffer, pH = 8.5 for 30 min, then blown dry with compressed air. To transfer the polydopamine, the stamp was placed face-down on the PVA-coated substrate under a 100 g weight for 2 min. For certain patterns, such as small features with large spacings, or if the substrates were slightly bent (as was the case with some of the polymeric substrates), it was more beneficial to use a compressed air gun instead of a weight, as the weight could cause uneven pattern replication or pattern collapse. When held at a height of 1–2 cm above the stamp, the flow of air from a compressed air gun was adjusted to give a total force equivalent to the weight of 10–20 g, as measured by performing the same operation on a scale. The air was blown until an even-colored interference reflection could be observed under the entire stamp. The stamp was then left on the substrate for 2 min. Before reusing the stamps, residual polydopamine was removed by sticky tape. The stamps could be reused multiple (at least 50) times without observable changes in the patterns.

In some cases, 0.1 mg $mL^{-1}$ poly(ethyleneimine) (PEI, 25kDa, branched, Sigma Aldrich) was added to the polydopamine deposition solution. To visualize if PEI had been incorporated into the patterns, PEI was labeled with FITC as described in [53] to produce FITC-PEI. FITC-PEI was purified by dialysis against DIW for 3 days (changed after 4 h, then every day) with a 10kDa MWCO dialysis membrane (VWR). To compare the stability of micropatterns of poly(L-lysine) (PLL) and PEI with polydopamine micropatterns, 1 mg $mL^{-1}$ of FITC-PLL (Sigma) or FITC-PEI was incubated with a PDMS stamp for 10 min, and stamped onto the substrate. Substrates were rinsed with DIW after stamping.

The geometry and stability of PVA films with microcontact-printed polydopamine was tested by immersing the samples in DIW or cell culture medium for up to 3 weeks, rinsing in DIW, blowing dry with compressed air and performing AFM measurements on the surface (see below).

### 2.4. Solution modification of PVA with polydopamine

Prior to co-culturing experiments, it was observed if polydopamine could modify initially cell-repellent films to allow cell adhesion. Immobilized PVA films were post-modified with polydopamine by first shortly equilibrating them in DIW for 30 min, then immersing or floating them in a 10 mM tris buffer, pH = 8.5 with 1 mg $mL^{-1}$ dopamine. Cells were then cultured as described below.

For *in situ* post-modification of PVA with polydopamine during cell culturing and for dopamine toxicity tests, the cells were washed in PBS, then incubated with 1 mg $mL^{-1}$ dopamine in a modified tris-buffered saline (modified TBS, consisting of 25 mM tris, 140 mM NaCl, 2.5 mM KCl, 1.8 mM $CaCl_2$ and 1 mM $MgCl_2$, pH = 8.5) to maximize cell health while still allowing polydopamine deposition. The deposition buffer pH was adjusted at 37 °C as the pH of tris buffers has a high temperature dependence [54]. The cells were then washed in PBS before changing back to growth medium for further culturing.

### 2.5. Cell culturing

All cell lines were purchased from ATCC. Human cervical cancer cells (HeLa), human embryonic kidney cells (HEK293) and human prostate cancer cells (PC3) were grown in DMEM (Gibco, Invitrogen) supplemented with 1 mM nonessential amino acids (Gibco, Invitrogen), 10% FBS (Gibco, Invitrogen), and 1 mM L-glutamine (Sigma Aldrich). HUVEC were cultured in EBM-2 medium (Lonza). The cells were cultivated at 37 °C in a humidified atmosphere with 5% $CO_2$ and passaged regularly. HUVEC cells were used in passages 4–6. For cell culture experiments, the samples were sterilized in 70% ethanol and rinsed in PBS before use. The samples were then placed in 24-well plates. Typically, 20 000–50 000 cells were seeded into each well in 0.5 mL of cell medium.

### 2.6. Cytotoxicity assay

For dopamine toxicity testing, an MTT assay (In Vitro Toxicology Assay Kit, MTT based, Sigma) was performed. 10 000 HeLa cells were cultured in each well in a 96-well plate for 24 h, then exposed to a dopamine deposition solution (1 mg $mL^{-1}$ in modified TBS) for 0–60 min or buffer controls. In some samples, the solution was refreshed, this was performed without a rinsing step in between. 24 h after dopamine exposure, 10 $\mu$L of 10 mg $mL^{-1}$ MTT was added to each well. The cells were incubated with MTT for 4 h, after which the medium was aspirated and the formazan crystals were dissolved in 50 $\mu$L DMSO. The absorbance was measured at 570 nm, subtracting a 690 nm background reference using a Tecan Infinite M200 Pro microplate reader. Each sample was done in four duplicates, and $p$-values were found using a two-tailed paired Student's $t$-distribution. To assess the effect of different radical oxygen scavengers on dopamine cytotoxicity, 1 mM of ascorbic acid (Sigma Aldrich) or 0.25 mg $mL^{-1}$ (500 U $mL^{-1}$) of catalase (Bovine Serum Catalase, Sigma Aldrich) was added to the dopamine deposition solution.

### 2.7. PDMS microfluidic device

PDMS microchannels 300 $\mu$m wide 100 $\mu$m high and were made in the same manner as the PDMS stamps above. To bond them to the samples, the PDMS microchannels were exposed to oxygen plasma at 0.5 millibar with a power of 50 W for 18 s in a Diener Femto Plasma System (Diener Electronics), then placed with the channel down on the pre-patterned samples and cured for 10 min at 130 °C.

For cell culturing in microfluidic channels, the cells were injected at a density of $10 \times 10^6$ cells $mL^{-1}$ using a micropipette into channels bonded to pre-patterned PVA/polydopamine surfaces. Once the channel was filled, cell medium was pipetted on top of the entire PDMS device (maintained there by surface tension) to equilibrate pressure between the entrances and maintain a suitable channel environment without the need to include a pumping and tubing system in the cell incubator.

### 2.8. Co-culturing

To assess the effect of various polydopamine deposition treatments on co-culture efficacy, 50 000 cells $cm^2$ (HeLa) were cultured overnight on microcontact-printed patterns. Then, 4 × 5, 4 × 10 or 4 × 15 min polydopamine depositions were performed in modified TBS, before 50 000 cells $cm^{-2}$ (HeLa) were seeded. Cell counts were performed at 16 and 40 h

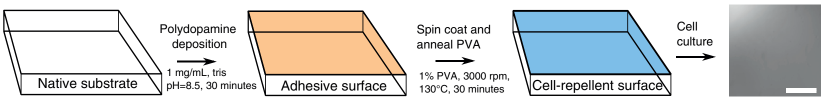

**Figure 1.** Production of the initial cell-repellent poly(vinyl alcohol) surface. Cell attachment is completely inhibited, as shown by the lack of cells in the right-most panel, here shown 3 days after 25 000 cells cm$^{-2}$ (HeLa) were seeded. Scale bar 500 $\mu$m.

using the CellCounter plugin for FIJI [55]. For each sample, three areas were imaged and counted, discriminating between cells on and off the microcontact-printed patterns. A total of 4868 cells were counted. *P*-values were calculated as above.

For patterned co-culturing experiments, HUVEC or HeLa cells were first grown in patterns as above (typically over night, but from 4 h to several days gave similar results). These cells were then labeled with 1 $\mu$M calcein-AM (Invitrogen) in cell growth medium for 1 h and rinsed several times in PBS. The surface was then modified *in situ* as described above. A second batch of HeLa or HUVEC cells was labeled with 5 $\mu$M CellTracker Red (Invitrogen) in DMEM or 1 $\mu$M calcein red-orange-AM (Invitrogen) for 1 h, rinsed several times in PBS, then removed by trypsin/EDTA treatment and seeded onto the activated surfaces with patterned calcein-labeled cells.

### *2.9. Optical and atomic force microscopy*

Cells were imaged live using a Leica SP5 confocal microscope, a Leica SP8 confocal microscope or a Nicon Diaphot widefield fluorescence microscope. For actin filament and nucleus imaging, the cells were fixed in 4% paraformaldehyde in PBS for 15 min at room temperature, permeabilized in 0.1% Triton X-100 and labeled with 165 nM Alexa488-phalloidin (Invitrogen) for actin filaments, while the nuclei were labeled with 1 $\mu$g mL$^{-1}$ PI (Sigma Aldrich) and 10 $\mu$g mL$^{-1}$ RNase A (Sigma) in PBS or Hoechst 33 248 in PBS. For live cell imaging, the medium was exchanged to HEPES-buffered live cell imaging medium (Invitrogen) for short-term (up to 1 h) imaging, while for long-term time lapse imaging, the medium was exchanged to Leibovitz L-15 (Invitrogen) for HeLa cells or 1:1 L-15 and EBM-2 for HUVEC or HUVEC/HeLa co-cultures. Willco 35 mm glass bottom confocal dishes were used for long-term time lapse imaging. 1.5 mL of medium was used, then covered with white mineral oil (VWR) and maintained on the microscope stage which was maintained at 37 °C with a closed box system.

For AFM microscopy, microcontact-printed polydopamine patterns, buffer-soaked patterns and post-modified samples were prepared as described above. The samples were then rinsed in DIW and blown dry using compressed air, before imaging in a Veeco Nanosight V AFM in ScanAsyst mode. The data were analyzed using Gwyddion [56]. The data were leveled by matching the height median and fitting to a plane, and the root mean square roughness was analyzed at four distinct positions on each sample. Sample *p*-values were compared using a paired Student's *t*-test.

## 3. Results

To produce patterned cell cultures, we present two alternate methods of modifying the cell-repellent hydrogel PVA using polydopamine: microcontact printing and solution deposition. We show that the first method can be used to pattern several cell types on the polyvinyl alcohol surface and explore further aspects of this system, such as patterning on alternate substrates and PDMS microchannel integration. We further show that PVA can also be made cell adhesive by solution deposition of polydopamine and find conditions that allow this to be done *in situ* during cell culturing. Finally, we show how the combination of cell patterning by microcontact printing of polydopamine with *in situ* polydopamine deposition can be used to make patterned cell co-cultures.

### *3.1. Cell-repellent PVA films*

Cell-repellent surfaces were made by spin-casting and heat annealing PVA thin films on glass (figure 1) [37]. To minimize potential swelling effects in the film during cell culturing, the thickness of PVA was adjusted to 15–20 nm by using a PVA concentration of 1% in the spin-casting solution. This still gave homogeneous, defect-free and cell-repellent coatings (figures 1 and 2). If no heat annealing step was performed, the surfaces were not cell repellent, presumably due to rapid film detachment and dissolution (figure S1, available from stacks.iop.org/BF/5/045009/mmedia). However, even with heat annealing, film detachment could occur if the experiments lasted longer than around 2–3 days or if fully hydrated samples were extensively handled. To increase the PVA adhesion, aldehyde-containing silanes or silane-linked glutaraldehyde have been used in the past to chemically immobilize PVA hydrogels [37, 38]. However, to avoid introducing chemicals which can potentially be cytotoxic if not completely removed prior to cell culture experiments, we instead used an adhesive film of polydopamine, applied to the substrate prior to PVA film spin casting under mild aqueous conditions [43]. By combining the polydopamine adhesive layer with heat annealing of PVA, no film detachment or PVA dissolution was observed, even after immersion in cell medium at 37 °C for extended periods (at least 3 weeks, see figure S2, available from stacks.iop.org/BF/5/045009/mmedia).

In addition, the pre-treatment of substrates with polydopamine renders materials hydrophilic [43], which allowed spin casting of PVA onto several alternative substrates, such as PET, PS, PDMS and poly(chlorotrifluoroethylene) (Aclar). Although all substrates supported cell adhesion to some extent before applying the PVA, cell attachment was not observed after applying the PVA film (figure S3, available from stacks.iop.org/BF/5/045009/mmedia).

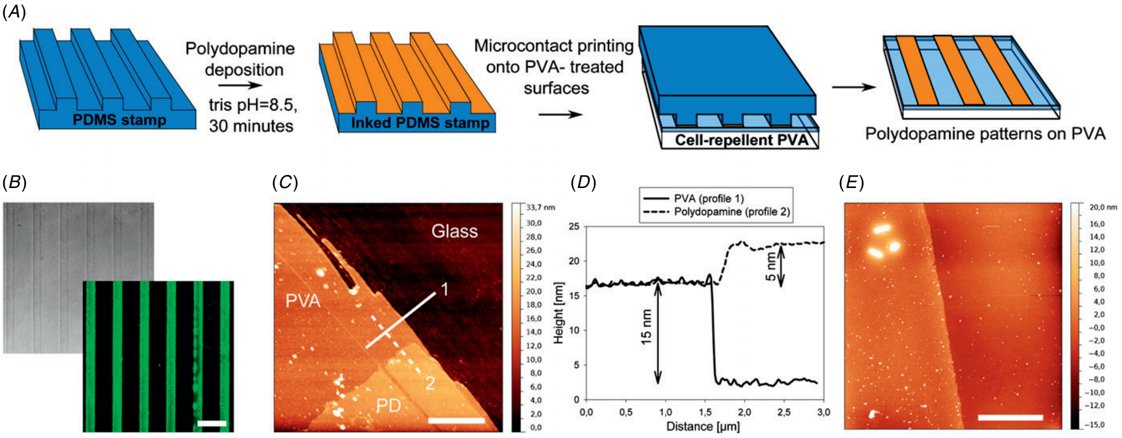

**Figure 2.** (*A*) Schematic of the production of polydopamine patterns on PVA surfaces. (*B*) Upper: phase contrast image of polydopamine micropattern on a PVA surface. Lower: polydopamine incorporating fluorescently labeled PEI. Scale bar 100 $\mu$m. (*C*) AFM micrograph of microcontact-printed polydopamine (PD) onto a PVA film. A large scratch was made into the PVA, exposing the glass underneath and allowing a thickness measurement of the PVA. Scale bar 2 $\mu$m. (*D*) Height profiles of the PVA (profile 1) and polydopamine on PVA (profile 2), respectively, along the lines marked by (1) and (2) in (*B*). (*E*) Large-scale AFM scan demonstrating the homogeneous surface coverage of the spin-cast PVA and the microcontact-printed polydopamine films. Scale bar 10 $\mu$m.

### *3.2. Microcontact printing of polydopamine on PVA*

Microcontact printing is a simple method to transfer patterns of an ‘ink’ (e.g. polymers, proteins or reactive chemicals) onto a substrate and can be used to generate patterns of cell-adhesive and cell-repelling areas for cell patterning [23]. However, when common cell-adhesive polymers, such as PLL or PEI, were microcontact printed onto PVA, they were quickly washed off due to the anti-fouling nature of PVA (figure S4, available from stacks.iop.org/BF/5/045009/mmedia). Thus, we investigated microcontact printing of polydopamine onto PVA due to its reported highly adhesive properties [43, 48]. Polydopamine was first deposited as a thin film on a PDMS stamp [47] and then transferred to the PVA-coated substrate by microcontact printing (figure 2(*A*)). The patterns could be visualized by phase contrast microscopy when dry (figure 2(*B*)) or in reflection microscopy when wet (figure S5, available from stacks.iop.org/BF/5/045009/mmedia) and showed a high degree of fidelity to the relief patterns of the stamp, indicating complete film transfer.

Due to the ability to covalently bind amino groups, polydopamine has been co-deposited with amine-containing polymers such as PEI [57]. We were able to produce polydopamine patterns that contained fluorescent PEI (PEI was added to the solution used to deposit the polydopamine film on the PDMS stamp, see section 2) that remained stable after rinsing when deposited onto PVA films (figures 2(*B*) and S4, available from stacks.iop.org/BF/5/045009/mmedia).

The height and microscale morphology of the PVA and polydopamine films were investigated by AFM. In the initial dry state, the PVA film was around 15 nm, while the polydopamine film was around 5 nm (figures 2(*C*) and (*D*)). The films appeared homogeneous with few defects, indicating complete coverage by both spin-casted PVA and microcontact-printed polydopamine (figure 2(*E*)). After 3 weeks immersed in DIW, no changes to the polydopamine patterns could be seen, while when immersed in cell culture medium, the thickness of the polydopamine increased, presumably due to adsorption of serum proteins (figure S2, available from stacks.iop.org/BF/5/045009/mmedia).

### *3.3. Cell micropatterning on polydopamine/PVA*

Polydopamine is reported to be bio-compatible and cell adhesive [45, 47], so microcontact-printed polydopamine on PVA hydrogel films should be a simple method to pattern cells in culture. Initial tests were done using HeLa cells, a common model cell line. HeLa cells were successfully cultured on the patterned substrates and adhered well and spread on the polydopamine areas (figure 3, see also figure S5 (available from stacks.iop.org/BF/5/045009/mmedia) showing how the cells fill out the patterns but not beyond). No migration onto pristine PVA areas was observed even after 3 weeks in culture (figure 3(*C*)). Initial experiments showed similar patterning ability with HEK293, PC3 and HUVEC cells after 3 days on the patterns (figures 3(*D*)–(*F*)). The attachment rate depended on the cell type, but typically, the cells were adhered to the patterns within a few hours, and un-attached cells could be rinsed away. A time lapse of the attachment of HUVEC cells to polydopamine patterns is shown in figure S6 (available from stacks.iop.org/BF/5/045009/mmedia). Other cell types, such as HEK293, had lower adhesion and often detached during routine handling (washing, media change, etc). To increase the adhesion, PEI (0.1 mg mL$^{-1}$) was co-deposited with polydopamine on the PDMS stamp. Patterns containing PEI increased the HEK293 cell adhesion sufficiently to avoid detachment during handling.

Microcontact-printed patterns could be used to control areas for cell growth in areas of multiple cells, but could also

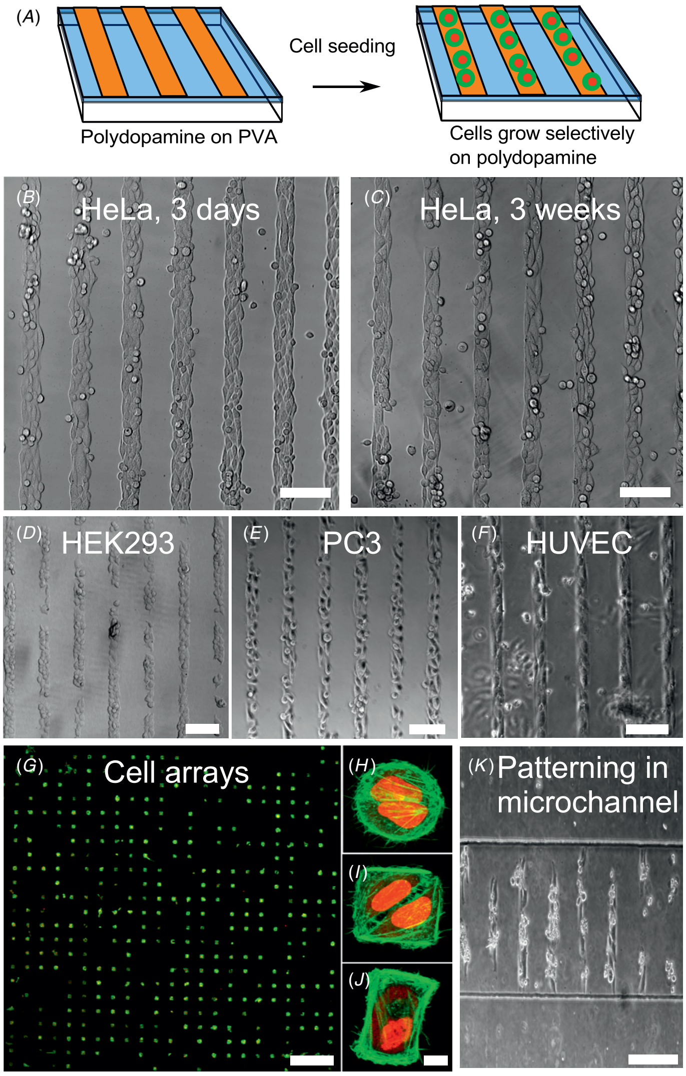

**Figure 3.** (*A*) Cells only adhere to the polydopamine areas and are unable to attach to the PVA background. (*B*) and (*C*) HeLa cells tightly followed the polydopamine patterns, both short term (*B*, 3 days) and long term (*C*, 3 weeks). The patterns are 40 $\mu$m lines with 80 $\mu$m gaps. (*D*)–(*E*) Other typical model adherent cell lines also can be patterned, as shown here for (*D*) HEK293, (*E*) PC3 and (*F*) HUVEC cells after 3 days on the patterns. (*G*) Actin filaments and nuclei of HeLa cells visualized on an array of 37 $\mu$m squares, demonstrating the possibility of patterned cell arrays over large areas. (*H*)–(*J*) Close-up of HeLa cells (actin and nucleus labeled green and red, respectively) on different pattern geometries, such as (*H*) circles, (*I*) squares and (*J*) H-shaped, demonstrating cell shape control with the patterns. (*K*) Microchannels could be bonded on top of the patterned surfaces, and HeLa cells were cultured inside the channels, growing only on vertical lines (channel is in the middle part of the figure). Scale bars (*A*)–(*F*), (*J*) 100 $\mu$m, (*G*) 200 $\mu$m and (*H*)–(*I*) 10 $\mu$m.

be used to control the geometry of single cells (figures 3(*G*)–(*J*)). Although true single-cell arrays with only one cell at each array site should be achievable with this method, the exact feature size and seeding procedures were not optimized for this purpose in this work. Additionally, the optimal pattern size varied by cell type. At a cell density of 50 000 cells cm$^{-2}$, typically 2–3 HeLa cells were attached at each array spot after 24 h when using 37 $\mu$m circular features, while PC3 cells typically were single cells on the same features (figure S7, available from stacks.iop.org/BF/5/045009/mmedia).

To investigate cell patterning on substrates other than PVA-coated glass, we performed identical experiments on PVA-coated PET, PS, PDMS and Aclar. Spin casting of PVA hydrogel films was possible on these substrates after a hydrophilic polydopamine adhesion layer was applied. The resulting substrates were cell repellent (figure S3, available

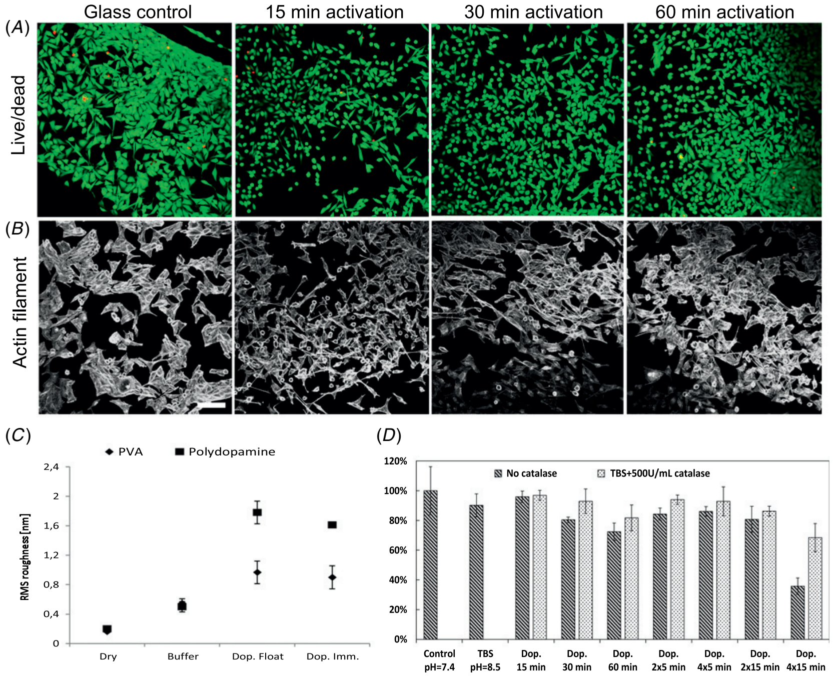

**Figure 4.** (*A*) HeLa cells grown for 1 day on PVA hydrogels modified with polydopamine before cell growth. Live/dead (calcein-AM, green/propidium iodide, red) staining indicates high cell viability, similar to glass control, on all modified samples. (*B*) To better visualize cell spreading, actin filaments were labeled. Increasing the dopamine deposition time appears to give a cell morphology more similar to glass. Scale bar 100 $\mu$m. (*C*) Root mean square roughness of microcontact printed polydopamine and PVA areas as measured by AFM on untreated samples (Dry), samples immersed for 60 min in 10 mM tris buffer at pH = 8.5 (Buffer) and floating (Dop. Float) or immersed (Dop. Imm.) in 1 mg mL$^{-1}$ dopamine in 10 mM tris buffer at pH = 8.5. Dopamine immersion significantly ($p < 0.05$) increased the roughness of both PVA and polydopamine compared to dry samples and buffer treatment alone. Error bars show ± SEM. (*D*) Cell viability measured by MTT assay, 24 h after the cells have been treated with cell medium (control, 60 min), modified TBS (TBS, 60 min) and 1 mg mL$^{-1}$ dopamine in modified TBS for 0–60 min (Dop.), in some cases refreshing the dopamine solution at given intervals. The data is normalized compared to the control. Error bars show ± SEM.

from stacks.iop.org/BF/5/045009/mmedia). Furthermore, by microcontact printing of polydopamine, cell patterning was achieved in the same way as on glass on these substrates (figure S3).

Increased environmental control of cultured cells through microfluidic systems is an important route to further extend the possibilities of *in vitro* experiments [58]. To this end, we investigated if the PVA-polydopamine cell patterning system could be integrated with microfluidic channels. We found that PDMS bonded irreversibly with the patterned PVA/polydopamine surfaces after only the surface of the PDMS microchannels device was activated with oxygen plasma, thereby preserving cell patterning ability. This allowed the placement of a PDMS microchannel onto a pre-patterned PVA/polydopamine surface. The bond was maintained with liquid in the microfluidic channel for more than 1 week (figure S8(*A*), available from stacks.iop.org/BF/5/045009/mmedia), although in this case, the PVA had to be limited to the channel area, as stress around the plugs for the associated tubing could rupture the PDMS-PVA bond (figure S8(*B*)). By bonding PDMS microchannels on top of pre-patterned polydopamine-PVA surfaces, cells could be grown on pre-defined patterns inside the microfluidic channel (figure 3(*K*)). Interestingly, if the entire device was immersed in an aqueous solution, the PVA film was slowly hydrated from the edges, reducing the PVA-PDMS bond strength. This allowed for simple release of the microchannel device if desired for, e.g., further microscopy or extraction of the cultured cells.

### *3.4. Solution polydopamine modification of hydrated PVA films*

Next, we explored the possibility of using the versatile surface deposition properties of polydopamine to modify PVA films by solution deposition (the same methods as used to produce polydopamine coating on PDMS stamps). This would enable switching of an initially cell-repellent hydrogel surface to cell adhesive using only mild aqueous chemistry. PVA films on glass were pre-hydrated in DIW to mimic the state during cell culturing and floated on the polydopamine deposition solution (1 mg mL$^{-1}$ in 10 mM tris, pH = 8.5) to avoid precipitation of large polydopamine particles. Surfaces modified for 15–60 min all supported cell adhesion and spreading with high cell viability (figure 4(*A*)), while unmodified surfaces did

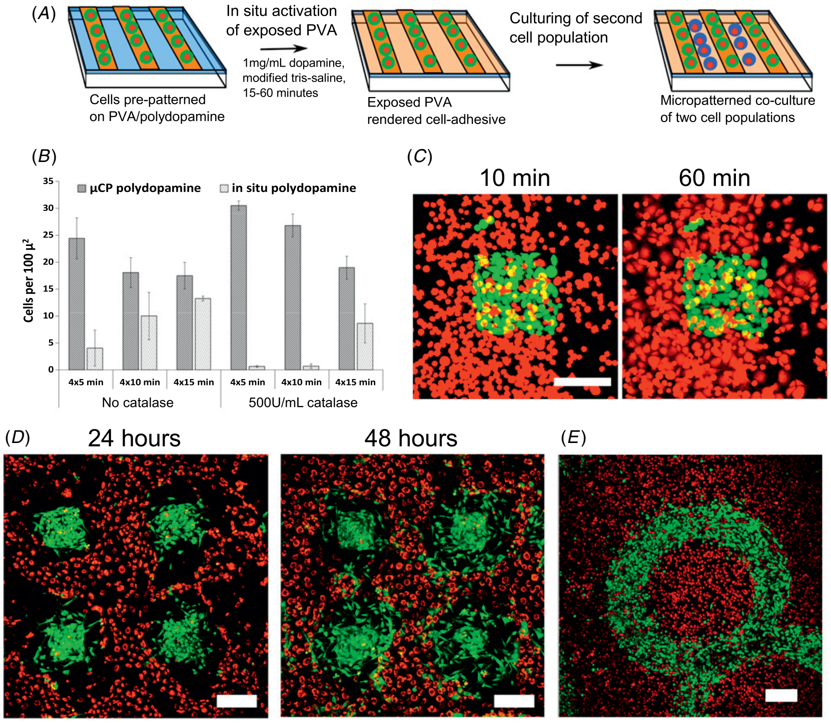

**Figure 5.** (*A*) The co-culture process starts with patterned cells, then polydopamine is deposited *in situ* on the cell-repellent PVA before adding the second cell population, which will attach onto the newly cell adhesive areas. (*B*) The surface modification strength of different dopamine deposition treatments as measured by the ratio between the number of cells per unit area on microcontact-printed polydopamine and *in situ* deposited polydopamine. Addition of 500 U mL$^{-1}$ catalase gave significantly ($p < 0.05$) lower activation for 4 × 5 and 4 × 10 min treatments. (*C*) After *in situ* activation samples pre-patterned with HeLa cells (green, calcein-AM labeled), HUVEC cells (red, calcein red-orange-AM labeled) quickly adhered and spread on the newly available areas outside the HeLa cell patterns. Scale bar 100 $\mu$m. (*D*) Longer term observation after 24 and 48 h of co-culturing of HeLa cells (green, calcein-AM labeled) and HUVEC cells (red, calcein red-orange-AM labeled) shows how the HeLa cells spread outward from their initial patterns, while the HUVEC cells simultaneously recede, although also forming a tight endothelial network surrounding the HeLa cells. Scale bar 200 $\mu$m. (*E*) Arbitrary patterns of co-cultures, even of the same cell type, can be made using this technique. Here shown by a 24 h co-culture of patterned HeLa cells (green cells, calcein-AM labeled) and HeLa cells seeded after *in situ* dopamine modification of the surrounding PVA (red cells, CellTracker red labeled). Scale bar 200 $\mu$m.

not support cell adhesion. The morphology of the cells on the polydopamine-activated PVA surfaces was visualized by actin filament staining (figure 4(*B*)). The HeLa cells showed a spindly morphology for shorter activation times, but resembled glass controls more with somewhat longer (30–60 min) surface activation times. This change in cell morphology is presumably a result of increasing number of cell attachment sites created by longer polydopamine treatment of the PVA surface.

To observe the changes that occurred on PVA films and microcontact-printed polydopamine patterns on PVA when subjected to the polydopamine deposition solution, samples were modified as above, rinsed, dried and then imaged by AFM, and the surface roughness was analyzed (figure 4(*C*), AFM images shown in figure S9, available from stacks.iop.org/BF/5/045009/mmedia). Buffer (10 mM tris, pH = 8.5) for 60 min slightly increased the roughness of both the polydopamine layer and the PVA layer, although the reason for this is not known. When subjected to a dopamine deposition solution for 60 min, there was a significant increase ($p < 0.05$ compared to buffer treatment) in surface roughness both on the polydopamine and PVA areas, likely indicating deposition of polydopamine on these samples. To investigate if gravity played a role in polydopamine deposition, e.g., through the precipitation of larger particles first formed in solution, samples were also floated on top of the deposition solution. The roughness was similar to the immersed sample in this case, indicating polydopamine film formation on typically non-fouling PVA hydrogels independent of orientation.

### 3.5. *Cytotoxicity of in situ dopamine deposition*

Switching of initially cell-repellent PVA to cell adhesive could allow us for co-culturing of two cell populations in a patterned geometry, as shown schematically in figure 5(*A*). A requirement is that the switching must occur after the first cell population is cultured on the microcontact-printed patterns, so the switching chemistry must be cell compatible. To comply with this, the polydopamine deposition solution was modified. The standard 10 mM tris buffer was substituted with a modified tris-buffered saline (TBS) to maintain a typical cell culture salt balance, although at an increased pH of 8.5, which is optimal for polydopamine deposition [59]. A typical deposition solution with 1 mg $mL^{-1}$ dopamine in the modified TBS changed color to brown, indicating that the altered buffer allowed dopamine oxidation and likely also polydopamine formation (figure S10, available fromstacks.iop.org/BF/5/045009/mmedia) [59].

As a measure of cytotoxicity, the metabolic activity of HeLa cells 24 h after exposure to different polydopamine deposition conditions was assessed using the MTT assay (figure 4(*C*)). The modified TBS buffer at pH = 8.5 was not significantly cytotoxic for up to 60 min. It was seen that shorter dopamine incubations were not appreciably cytotoxic either. However, longer deposition times did induce somewhat of a cytotoxic effect, especially if the deposition solution was replenished at regular intervals. Dopamine is reported to be toxic to cell culture due to the generation of reactive oxygen species (ROS) during dopamine oxidation [60, 61]. Thus, an ROS scavenger could reduce the cytotoxic effect of dopamine deposition. Ascorbic acid, a common antioxidant, was investigated first, but this inhibited any oxidation of dopamine, and thus prevented the formation of polydopamine (figure S10, available from stacks.iop.org/BF/5/045009/mmedia). Therefore, catalase, an enzyme that catalyzes the degradation of hydrogen peroxide, was introduced as a more specific ROS scavenger. Indeed, catalase did not inhibit dopamine oxidation, as indicated by color change in solution and the formation of precipitate particles if left for a long time, but it did significantly reduce dopamine cytotoxicity for longer incubation times ($p < 0.05$).

### *3.6. Patterned co-culture by in situ polydopamine modification of PVA*

To produce patterned co-cultures, the first cell population was seeded as before on microcontact-printed patterns (figure 5(*A*)). Then, the initially cell-repellent areas of the PVA were rendered cell adhesive by a cell-compatible polydopamine deposition in modified TBS before the second cell population was introduced. To maintain an effective surface activation while avoiding the formation of visible polydopamine particles in the deposition solution, the solutions were replenished at intervals of 5–15 min. (Typically, the particles became visible after 30 min without a solution change.) The number of cells per area was measured on the microcontact-printed ($\mu$CP) polydopamine and on the *in situ* deposited polydopamine (figure 5(*B*), both 16 h and 40 h time-points are included in figure S11, available from stacks.iop.org/BF/5/045009/mmedia). Increasing treatment length reduced the cell density difference between $\mu$CP and *in situ* deposited polydopamine. A larger cell density was observed on the $\mu$CP areas of the less activated samples, presumably due to cell crowding in these areas, since spreading into the *in situ* modified areas beyond was limited. Although catalase was shown by the MTT assay to reduce cytotoxicity of the *in situ* polydopamine treatment, it also reduced the strength of the *in situ* activation for shorter activation times ($p < 0.05$). For the 4 × 5 min and 4 × 10 min activations, the cell density on the $\mu$CP areas also increased in the presence of catalase, presumably due to a stronger cell crowding effect. With a 4 × 15 min activation time, the *in situ* polydopamine deposition was sufficient to generate cell densities on the previously cell-repellent PVA of up to about 75% of the cell density on microcontact-printed polydopamine on the same sample.

Model patterned co-cultures were produced using dissimilar cell types (HeLa and HUVEC, figures 5(*C*) and (*D*)) and the same cell types (differentially labeled HeLa cells, figure 5(*E*)). HUVEC cells seeded after *in situ* activation of samples with patterned HeLa cells rapidly adhered (within 60 min) to the areas rendered cell adhesive (figure 5(*C*)). A time lapse of the two first hours of co-culturing can be seen in Supplementary Movie S1 (available from stacks.iop.org/BF/5/045009/mmedia). In this example, a 4 × 15 min *in situ* activation was used, and although this was shown to give a certain cytotoxicity after 24 h, the observed HeLa cell patterns remained quite viable and dense, as indicated by the live cell staining with calcein-AM (green). HeLa-HUVEC co-cultures were also observed 24 and 48 h after the co-culturing was initiated by HUVEC seeding (figure 5(*D*)). After 24 h, a clear interaction between the cells could be observed, with the HUVEC cells somewhat receding from the areas with HeLa cells compared to the attachment after 2 h, and the HeLa cells expanding out from their initially defined patterns. At 48 h, the HeLa cells were spreading further, while the HUVEC cells formed a dense network surrounding the expanding HeLa cells, but with little overlap between the cell types. Note that even at 48 h, the patterned HeLa cells that were the initial cell population for the co-culture experiment remain viable, as indicated by the retainment of the calcein-AM (green fluorescence) loaded prior to co-culturing. This interaction between HeLa and HUVEC cells is consistent with other reports on HeLa/HUVEC co-cultures [62], although it has not been observed in a micropatterned arrangement before.

To further demonstrate that this method of co-culturing can produce arbitrary patterns of cells without any requirements for differential adhesive properties among cell types, two differentially labeled HeLa cell populations were co-cultured (figure 5(*D*)). The first population was cultured on microcontact-printed patterns as before, and after an *in situ* polydopamine deposition, the second population was introduced and grew overnight. Large-scale patterns could be maintained with high cell densities of each cell type, while successfully segregating the cell populations. Smaller scale patterns could also be used, although cell migration between the different areas caused mixing of the cell populations over time, a phenomenon more noticeable for smaller patterns (figure S12, available from stacks.iop.org/BF/5/045009/mmedia).

## 4. Discussion

In this paper, we show that by using off-the-shelf chemicals and simple fabrication strategies, it is possible to provide tools for advanced cell culture experiments, such as cell confinement, cell migration, cell–cell interactions and co-culture studies. Hydrogels formed from spin-cast PVA immersed in culture medium is an excellent and stable cell-repellent material, and when PVA is tightly attached to the underlying substrate, it was shown to be stable under culture conditions. Since the cell-repellent material is a hydrogel film and not a monolayer (such as PLL-*graft*-PEG) as typically used in other cell-patterning approaches [63], the surface behavior is less dependent on the chemistry of the underlying substrate. In comparison with similar systems, the use of a hydrogel film allows us longer anti-fouling stability and more versatility with regard to substrate type [49].

In our system, polydopamine has three functions. Firstly, it is deposited on the culture substrate to decrease the contact angle, facilitating spin coating, and to increase the adhesion of the PVA film. Secondly, thin polydopamine patches are microcontact printed onto PVA, providing stable cell adhesive areas. Finally, it can be deposited onto the PVA surface in cell-compatible conditions, allowing for activation of the cell-repellent surface.

Using polydopamine as an adhesion layer allows PVA immobilization on nearly any surface, as polydopamine deposits on most materials [43]. Additionally, the chemistry involved is mild and does not require the use of toxic compounds, such as glutaraldehyde [37]. Thus, we were able to generate cell-repellent films and cell patterns on PS, PDMS, PET, glass and Aclar. The last material is often used to grow cells prior to embedding for electron microscopy, which potentially could open up new possibilities for correlative imaging of patterned cells with optical and electron microscopy [64]. As PVA does not contain functional groups, such as amines or thiols, which are known to bind covalently with polydopamine [43], the bonding at the interface between PVA and polydopamine is not known. It is plausible that non-covalent interactions such as hydrogen bonding could play a role, as PVA is known to strongly interact through hydrogen bonds [65]. In a study on polydopamine/PVA mixed films, this was also indicated as a possible mechanism of interaction between polydopamine and PVA [50]. Further study is needed to determine the details of the PVA–polydopamine interaction both in the case of microcontact printing and deposition from solution.

Microcontact-printed polydopamine was shown as an attractive route to hydrogel functionalization without prior modification of PVA hydrogel chemistry [66, 67], additionally providing the option for micropatterned features. Polydopamine was further shown to support patterned cell adhesion, where the cells selectively adhered to unmodified (in the case of HeLa, HUVEC and PC3 cells) or PEI-modified (in the case of HEK293 cells) polydopamine. Thus, the same methods provide the ability to pattern several adherent cell lines. Other reports demonstrate cell adherence to both unmodified and modified polydopamine for yet other cell types [43, 46, 47, 49, 68, 69], indicating that microcontact printing of polydopamine can be a general platform to pattern a range of cell types on PVA hydrogel surfaces. Furthermore, as both cell geometry and substrate stiffness can have important effects on cell biology, including gene expression and stem cell differentiation [14, 70], polydopamine patterns on stiffness-tunable PVA hydrogels [30, 71] is an exciting prospect.

It is widely described that polydopamine can be modified further by binding to functional molecules [57, 72] and proteins [44, 73] through amine and thiol groups. As demonstrated with PEI in this work, such modifications can provide necessary modifications for certain cell types without the need to develop new printing processes for each molecules. Thus, polydopamine is not only a convenient platform for further modifications, but was in fact necessary to provide sufficient adhesion to, e.g., include PEI in patterns on the anti-fouling PVA hydrogel. Direct patterning of proteins and polyelectrolytes has been shown to be possible on anti-fouling PEG-silane monolayers or on anti-fouling PEG/methacrylate brush polymers [74, 75], but in our work, both PEI and PLL were quickly rinsed away from the PVA hydrogels. Thus, through microcontact printing of polydopamine, a range of biomolecules could potentially be presented in a micropatterned arrangement on the anti-fouling hydrogel surface, which can further extend the usefulness in cell biology research.

*In situ* deposition of polydopamine was demonstrated as a method to render PVA cell adhesive under cell-compatible conditions. Switching a surface from generally cell repellent (i.e., cell repellent to most cell types) to cell adhesive typically requires external triggers, such as temperature [76, 77] or electrical fields [78], mechanical handling [26, 79], extensive prior chemical alteration of the cell-patterning materials [80] or complex infrastructure such as printing robotics [81]. The presented method is therefore rather simple, in that only pipetting of solutions is involved and not depended on the type of co-cultured cells, as long as they are adherent. By tuning the deposition time, the cell adhesiveness of the polydopamine-modified PVA could be modified, providing further options for future studies. Polydopamine is adhesive for a range of cell types as shown in this and other work [46, 68, 69, 82].

Our approach has certain limitations that should be investigated further. It must be noted that during co-culturing, only the first cell population is precisely patterned, while the second cell population will fill in the entire surrounding area not occupied by the first cell population after *in situ* polydopamine deposition. Cell migration also degraded the spatial localization of the two cell populations as the experiment progressed. For certain applications, such as automated high-throughput single-cell screening where the interaction between two cell types at pre-defined locations is of interest, this presents a challenge, and a focus of future development should be the increased spatial control of both cell populations. However, since large-scale cell–cell interactions and cell migration are often phenomena one wishes to study in co-culture systems [24], this is not necessarily a limitation for all applications.

There is a certain cytotoxicity involved in *in situ* dopamine deposition, likely mediated by the formation of reactive oxygen species (ROS) during dopamine oxidation [61]. By reducing the incubation time and by introducing catalase as a reactive oxygen species scavenger, we have significantly reduced the cytotoxicity as measured by the MTT assay.

However, it is not entirely clear what the effect of catalase is on the *in situ* deposition of polydopamine. Polydopamine appears to form in solution, however, a significant reduction in cell adhesion was observed on *in situ* modified PVA in the presence of catalase. Further investigations into the deposition of polydopamine in the presence of catalase are underway in our lab.

A second factor to consider is that *in situ* deposited polydopamine likely not only adheres to the PVA, but also coats the initial cell population. Polydopamine has been used previously to encapsulate live yeast cells [83] by polydopamine deposition in solution, which somewhat reduced the yeast cell viability and growth rate, although higher dopamine concentrations (2 mg $\mathrm{mL}^{-1}$) and longer deposition times (3 h) were used. On the other hand, no cytotoxicity was observed when myoblasts ingested polydopamine-coated liposomes [84] or when MDCK cells were exposed to polydopamine-coated $Fe_2O_3$ nanoparticles [85]. Polydopamine also bears a structural resemblance to melanin [86], which can be phagocytosed and degraded through lysosomal degradation by macrophages in human retinas [87]. Although these examples are not necessarily directly comparable, it appears that it is the oxidative processes, and potentially reactive intermediates involved in the formation of polydopamine, rather than the polydopamine itself that induces cytotoxicity.

The level of cytotoxicity was low enough that it did not prevent the generation of well-defined co-cultures at shorter (a few hours) or longer (at least 48 h) times. It is likely that further optimizing of factors, such as dopamine concentration, deposition time, solution refreshing and medium composition will lead to further reduced cytotoxicity while still enabling functional and versatile co-cultures.

## 5. Conclusion

PVA and polydopamine each have unique advantages as cell-directing materials. PVA is a tunable, biocompatible hydrogel that, in the form of a thin film, can confer cell repellence to multiple substrates. Polydopamine has multiple roles as a nearly universal adhesive, facilitating both attachment of and onto PVA, patterned cell adhesion of multiple cell types, *in situ* surface modification as well as the possibility for a range of further modifications. Thus, patterned cell culture and patterned co-culture were realized through simple chemistry with low-cost commercially available materials and a minimum of infrastructure, while maintaining the versatility and customization options needed for advanced applications. These type of simple and readily available systems could allow non-specialized labs access to more advanced cell culturing methods without the need to invest in complex equipment or involved chemical procedures.

## Acknowledgments

For financial support, we thank NTNU and NTNU NanoLab. The Research Council of Norway is acknowledged for the support to the Norwegian Micro- and Nano-Fabrication Facility, NorFab (197411/V30). We would also like to thank K Sæterbø and Sjoerd Hak for assistance with cell culturing and Vegar Ottesen for testing of microcontact printing of PLL and PEI on PVA surfaces and Volker Wirth for helpful tips.

## References

[1] Walling M A and Shepard J R E 2011 Cellular heterogeneity and live cell arrays *Chem. Soc. Rev.* **40** 4049–76

[2] Yarmush M L and King K R 2009 Living-cell microarrays *Annu. Rev. Biomed. Eng.* **11** 235–57

[3] Papp K, Szittner Z and Prechl J 2012 Life on a microarray: assessing live cell functions in a microarray format *Cell. Mol. Life Sci.* **69** 2717–25

[4] Yun H, Kim K and Lee W G 2013 Cell manipulation in microfluidics *Biofabrication* **5** 022001

[5] Rodríguez-Dévora J I, Zhang B, Reyna D, Shi Z D and Xu T 2012 High throughput miniature drug-screening platform using bioprinting technology *Biofabrication* **4** 035001

[6] Singhvi R, Kumar A, Lopez G P, Stephanopoulos G N, Wang D I, Whitesides G M and Ingber D E 1994 Engineering cell shape and function *Science* **264** 696–8

[7] Huang S, Chen C S and Ingber D E 1998 Control of cyclin d1, p27(kip1), and cell cycle progression in human capillary endothelial cells by cell shape and cytoskeletal tension *Mol. Biol. Cell.* **9** 3179–93

[8] Yamamura S, Kishi H, Tokimitsu Y, Kondo S, Honda R, Rao S R, Omori M, Tamiya E and Muraguchi A 2005 Single-cell microarray for analyzing cellular response *Anal. Chem.* **77** 8050–6

[9] Roach K L, King K R, Uygun B E, Kohane I S, Yarmush M L and Toner M 2009 High throughput single cell bioinformatics *Biotechnol. Prog.* **25** 1772–9

[10] Jain N, Iyer K V, Kumar A and Shivashankar G 2013 Cell geometric constraints induce modular gene-expression patterns via redistribution of HDAC3 regulated by actomyosin contractility *Proc. Natl. Acad. Sci. USA* **110** 11349–54

[11] Tang J, Peng R and Ding J 2010 The regulation of stem cell differentiation by cell-cell contact on micropatterned material surfaces *Biomaterials* **31** 2470–6

[12] Yang M T, Fu J, Wang Y K, Desai R A and Chen C S 2011 Assaying stem cell mechanobiology on microfabricated elastomeric substrates with geometrically modulated rigidity *Nature Protocols* **6** 187–213

[13] Titmarsh D M, Chen H, Wolvetang E J and Cooper-White J J 2012 Arrayed cellular environments for stem cells and regenerative medicine *Biotechnol. J.* **8** 167–79

[14] Kilian K A, Bugarija B, Lahn B T and Mrksich M 2010 Geometric cues for directing the differentiation of mesenchymal stem cells *Proc. Natl. Acad. Sci. USA* **107** 4872–7

[15] Song W, Lu H, Kawazoe N and Chen G 2011 Adipogenic differentiation of individual mesenchymal stem cell on different geometric micropatterns *Langmuir* **27** 6155–62

[16] Jiang X, Bruzewicz D A, Wong A P, Piel M and Whitesides G M 2005 Directing cell migration with asymmetric micropatterns *Proc. Natl. Acad. Sci. USA* **102** 975–8

[17] Kumar G, Co C C and Ho C C 2011 Steering cell migration using microarray amplification of natural directional persistence *Langmuir* **27** 3803–7

[18] Kingshott P and Griesser H 1999 Surfaces that resist bioadhesion *Curr. Opin. Solid State Mater. Sci.* **4** 403–12

[19] Kane R S, Takayama S, Ostuni E, Ingber D E and Whitesides G M 1999 Patterning proteins and cells using soft lithography *Biomaterials* **20** 2363–76

[20] Park T H and Shuler M L 2003 Integration of cell culture and microfabrication technology *Biotechnol. Prog.* **19** 243–53

[21] Lom B, Healy K E and Hockberger P E 1993 A versatile technique for patterning biomolecules onto glass coverslips *J. Neurosci. Methods* **50** 385–97

[22] Folch A, Jo B H, Hurtado O, Beebe D J and Toner M 2000 Microfabricated elastomeric stencils for micropatterning cell cultures *J. Biomed. Mater. Res.* **52** 346–53

[23] Chen C S, Mrksich M, Huang S, Whitesides G M and Ingber D E 1997 Geometric control of cell life and death *Science* **276** 1425–8

[24] Kaji H, Camci-Unal G, Langer R and Khademhosseini A 2011 Engineering systems for the generation of patterned co-cultures for controlling cell–cell interactions *Biochim. Biophys. Acta* **1810** 239–50

[25] Bhatia S N, Yarmush M L and Toner M 1997 Controlling cell interactions by micropatterning in co-cultures: hepatocytes and 3T3 fibroblasts *J. Biomed. Mater. Res.* **34** 189–99

[26] Cho C H, Park J, Tilles A W, Berthiaume F, Toner M and Yarmush M L 2010 Layered patterning of hepatocytes in co-culture systems using microfabricated stencils *Biotechniques* **48** 47–52

[27] Lee K Y and Mooney D J 2001 Hydrogels for tissue engineering *Chem. Rev.* **101** 1869–79

[28] Drury J L and Mooney D J 2003 Hydrogels for tissue engineering: scaffold design variables and applications *Biomaterials* **24** 4337–51

[29] Brandl F, Sommer F and Goepferich A 2007 Rational design of hydrogels for tissue engineering: impact of physical factors on cell behavior *Biomaterials* **28** 134–46

[30] Hassan C M and Peppas N A 2000 *Structure and Applications of Poly(vinyl alcohol) Hydrogels Produced by Conventional Crosslinking or by Freezing/Thawing Methods* (Berlin: Springer) pp 37–65

[31] Peppas N A and Stauffer S R 1991 Reinforced uncrosslinked poly (vinyl alcohol) gels produced by cyclic freezing-thawing processes: a short review *J. Control. Release* **16** 305–10

[32] Huglin M R 1989 *Hydrogels in Medicine and Pharmacy* ed N A Peppas (Boca Raton, FL: CRC Press)

[33] Peppas N and Tennenhouse D 2004 Semicrystalline poly (vinyl alcohol) films and their blends with poly (acrylic acid) and poly (ethylene glycol) for drug delivery applications *J. Drug Deliv. Sci. Technol.* **14** 291–7

[34] Du J R, Peldszus S, Huck P M and Feng X 2009 Modification of poly(vinylidene fluoride) ultrafiltration membranes with poly(vinyl alcohol) for fouling control in drinking water treatment *Water Res.* **43** 4559–68

[35] Barrett D, Hartshorne M, Hussain M, Shaw P and Davies M 2001 Resistance to nonspecific protein adsorption by poly (vinyl alcohol) thin films adsorbed to a poly (styrene) support matrix studied using surface plasmon resonance *Anal. Chem.* **73** 5232–9

[36] Rabinow B E, Ding Y S, Qin C, McHalsky M L, Schneider J H, Ashline K A, Shelbourn T L and Albrecht R M 1994 Biomaterials with permanent hydrophilic surfaces and low protein adsorption properties *J. Biomater. Sci. Polym. Ed.* **6** 91–109

[37] Peterbauer T, Heitz J, Olbrich M and Hering S 2006 Simple and versatile methods for the fabrication of arrays of live mammalian cells *Lab Chip* **6** 857–63

[38] Doyle A D 2009 Generation of micropatterned substrates using micro photopatterning *Curr. Protocols Cell Biol.* **45** 1–35

[39] Cheng C M and LeDuc P R 2006 Micropatterning polyvinyl alcohol as a biomimetic material through soft lithography with cell culture *Mol. Biosyst.* **2** 299–303

[40] Jensen B, Alves M, Fejerskov B, Städler B and Zelikin A 2012 Surface adhered poly (vinyl alcohol) physical hydrogels as tools for rational design of intelligent biointerfaces *Soft Matter* **8** 4625–34

[41] Pourciel M, Launay J, Sant W, Conédéra V, Martinez A and Temple-Boyer P 2003 Development of photo-polymerisable polyvinyl alcohol for biotechnological applications *Sensors Actuators* B **94** 330–6

[42] Kawazoe N, Guo L, Wozniak M, Imaizumi Y, Tateishi T, Zhang X and Chen G 2009 Adipogenic differentiation of mesenchymal stem cells on micropatterned polyelectrolyte surfaces *J. Nanosci. Nanotechnol.* **9** 230–9

[43] Lee H, Dellatore S M, Miller W M and Messersmith P B 2007 Mussel-inspired surface chemistry for multifunctional coatings *Science* **318** 426–30

[44] Lee H, Rho J and Messersmith P 2008 Facile conjugation of biomolecules onto surfaces via mussel adhesive protein inspired coatings *Adv. Mater.* **21** 431–4

[45] Lynge M E, van der Westen R, Postma A and Städler B 2011 Polydopamine—a nature-inspired polymer coating for biomedical science *Nanoscale* **3** 4916–28

[46] Ku S, Lee J and Park C 2010 Spatial control of cell adhesion and patterning through mussel-inspired surface modification by polydopamine *Langmuir* **26** 15104–8

[47] Chien H W, Kuo W H, Wang M J, Tsai S W and Tsai W B 2012 Tunable micropatterned substrates based on poly(dopamine) deposition via microcontact printing *Langmuir* **28** 5775–82

[48] Sun K, Song L, Xie Y, Liu D, Wang D, Wang Z, Ma W, Zhu J and Jiang X 2011 Using self-polymerized dopamine to modify the antifouling property of oligo(ethylene glycol) self-assembled monolayers and its application in cell patterning *Langmuir* **27** 5709–12

[49] Sun K, Xie Y, Ye D, Zhao Y, Cui Y, Long F, Zhang W and Jiang X 2011 Mussel-inspired anchoring for patterning cells using polydopamine *Langmuir* **28** 2131–6

[50] Zhang Y, Thingholm B, Goldie K, Ogaki R and Städler B 2012 Assembly of poly (dopamine) films mixed with a non-ionic polymer *Langmuir* **28** 17585–92

[51] Hosta-Rigau L, Jensen B, Fjeldsø K, Postma A, Li G, Goldie K, Albericio F, Zelikin A and Städler B 2012 Surface-adhered composite poly (vinyl alcohol) physical hydrogels: polymersome-aided delivery of therapeutic small molecules *Adv. Healthc. Mater.* **1** 791–5

[52] Qin D, Xia Y and Whitesides G M 2010 Soft lithography for micro-and nanoscale patterning *Nature Protocols* **5** 491–502

[53] Yue Y, Jin F, Deng R, Cai J, Chen Y, Lin M, Kung H F and Wu C 2011 Revisit complexation between DNA and polyethylenimine—effect of uncomplexed chains free in the solution mixture on gene transfection *J. Control. Release* **155** 67–76

[54] Durst R A and Staples B R 1972 Tris/tris-HCl: a standard buffer for use in the physiologic pH range *Clin. Chem.* **18** 206–8

[55] Schindelin J *et al* 2012 Fiji: an open-source platform for biological-image analysis *Nature Methods* **9** 676–82

[56] Nečas D and Klapetek P 2012 Gwyddion: an open-source software for SPM data analysis *Cent. Eur. J. Phys.* **10** 181–8

[57] Chien H W and Tsai W B 2012 Fabrication of tunable micropatterned substrates for cell patterning via microcontact printing of polydopamine with poly(ethylene imine)-grafted copolymers *Acta Biomater.* **8** 3678–86

[58] El-Ali J, Sorger P K and Jensen K F 2006 Cells on chips *Nature* **442** 403–11

[59] Bernsmann F, Ball V, Addiego F, Ponche A, Michel M, Gracio J, Toniazzo V and Ruch D 2011 Dopamine- melanin film deposition depends on the used oxidant and buffer solution *Langmuir* **27** 2819–25

[60] Herlinger E, Jameson R and Linert W 1995 Spontaneous autoxidation of dopamine *J. Chem. Soc., Perkin Trans. 2* 259–63

[61] Clement M, Long L, Ramalingam J and Halliwell B 2002 The cytotoxicity of dopamine may be an artefact of cell culture *J. Neurochem.* **81** 414–21

[62] Kaji H, Yokoi T, Kawashima T and Nishizawa M 2009 Controlled cocultures of hela cells and human umbilical vein endothelial cells on detachable substrates *Lab Chip* **9** 427–32

[63] Csucs G, Michel R, Lussi J W, Textor M and Danuser G 2003 Microcontact printing of novel co-polymers in combination with proteins for cell-biological applications *Biomaterials* **24** 1713–20

[64] Murphy G E, Narayan K, Lowekamp B C, Hartnell L M, Heymann J A, Fu J and Subramaniam S 2011 Correlative 3D imaging of whole mammalian cells with light and electron microscopy *J. Struct. Biol.* **176** 268–78

[65] Li H, Zhang W, Xu W and Zhang X 2000 Hydrogen bonding governs the elastic properties of poly (vinyl alcohol) in water: single-molecule force spectroscopic studies of PVA by AFM *Macromolecules* **33** 465–9

[66] Nuttelman C R, Mortisen D J, Henry S M and Anseth K S 2001 Attachment of fibronectin to poly (vinyl alcohol) hydrogels promotes NIH3T3 cell adhesion, proliferation, and migration *J. Biomed. Mater. Res.* **57** 217–23

[67] Schmedlen R H, Masters K S and West J L 2002 Photocrosslinkable polyvinyl alcohol hydrogels that can be modified with cell adhesion peptides for use in tissue engineering *Biomaterials* **23** 4325–32

[68] Ku S H and Park C B 2010 Human endothelial cell growth on mussel-inspired nanofiber scaffold for vascular tissue engineering *Biomaterials* **31** 9431–7

[69] Ku S H, Ryu J, Hong S K, Lee H and Park C B 2010 General functionalization route for cell adhesion on non-wetting surfaces *Biomaterials* **31** 2535–41

[70] Yeung T, Georges P C, Flanagan L A, Marg B, Ortiz M, Funaki M, Zahir N, Ming W, Weaver V and Janmey P A 2005 Effects of substrate stiffness on cell morphology, cytoskeletal structure, and adhesion *Cytoskeleton* **60** 24–34

[71] Gupta S *et al* 2013 Stiffness-and wettability-dependent myoblast cell compatibility of transparent poly (vinyl alcohol) hydrogels *J. Biomed. Mater. Res.* B **101** 346–54

[72] Kang K, Choi I S and Nam Y 2011 A biofunctionalization scheme for neural interfaces using polydopamine polymer *Biomaterials* **32** 6374–80

[73] Ogaki R, Bennetsen D T, Bald I and Foss M 2012 Dopamine-assisted rapid fabrication of nanoscale protein arrays by colloidal lithography *Langmuir* **28** 8594–9

[74] Wang Z, Zhang P, Kirkland B, Liu Y and Guan J 2012 Microcontact printing of polyelectrolytes on PEG using an unmodified PDMS stamp for micropatterning nanoparticles, DNA, proteins and cells *Soft Matter* **8** 7630–7

[75] Ma H, Hyun J, Zhang Z, Beebe T P and Chilkoti A 2005 Fabrication of biofunctionalized quasi-three-dimensional microstructures of a nonfouling comb polymer using soft lithography *Adv. Funct. Mater.* **15** 529–40

[76] Hirose M, Yamato M, Kwon O H, Harimoto M, Kushida A, Shimizu T, Kikuchi A and Okano T 2000 Temperature-responsive surface for novel co-culture systems of hepatocytes with endothelial cells: 2-D patterned and double layered co-cultures *Yonsei Med. J.* **41** 803–13

[77] Yamato M, Kwon O H, Hirose M, Kikuchi A and Okano T 2001 Novel patterned cell coculture utilizing thermally responsive grafted polymer surfaces *J. Biomed. Mater. Res.* **55** 137–40

[78] Yousaf M N, Houseman B T and Mrksich M 2001 Using electroactive substrates to pattern the attachment of two different cell populations *Proc. Natl. Acad. Sci. USA* **98** 5992–6

[79] Wright D, Rajalingam B, Selvarasah S, Dokmeci M R and Khademhosseini A 2007 Generation of static and dynamic patterned co-cultures using microfabricated parylene-c stencils *Lab Chip* **7** 1272–9

[80] Mendes P M 2008 Stimuli-responsive surfaces for bio-applications *Chem. Soc. Rev.* **37** 2512–29

[81] Xu F, Celli J, Rizvi I, Moon S, Hasan T and Demirci U 2011 A three-dimensional *in vitro* ovarian cancer coculture model using a high-throughput cell patterning platform *Biotechnol. J.* **6** 204–12

[82] Hong S, Kim K Y, Wook H J, Park S Y, Lee K D, Lee D Y and Lee H 2011 Attenuation of the *in vivo* toxicity of biomaterials by polydopamine surface modification *Nanomedicine* **6** 793–801

[83] Yang S H, Kang S M, Lee K B, Chung T D, Lee H and Choi I S 2011 Mussel-inspired encapsulation and functionalization of individual yeast cells *J. Am. Chem. Soc.* **133** 2795–7

[84] van der Westen R, Hosta-Rigau L, Sutherland D S, Goldie K N, Albericio F, Postma A and Städler B 2012 Myoblast cell interaction with polydopamine coated liposomes *Biointerphases* **7** 1–9

[85] Si J and Yang H 2011 Preparation and characterization of bio-compatible $Fe_3O_4$@polydopamine spheres with core/shell nanostructure *Mater. Chem. Phys.* **128** 519–24

[86] Liebscher J, Mrówczyński R, Scheidt H A, Filip C, Hădade N D, Turcu R, Bende A and Beck S 2013 The structure of polydopamine—a never ending story? *Langmuir* **29** 10539–48

[87] Gouras P, Brown K, Ivert L and Neuringer M 2011 A novel melano-lysosome in the retinal epithelium of rhesus monkeys *Exp. Eye Res.* **93** 937–46

## Supplementary Information

# Patterned cell arrays and co-cultures on polydopamine-modified poly(vinyl alcohol) hydrogels.

**Kai M. Beckwith, Pawel Sikorski**

Department of Physics, Norwegian University of Science and Technology, N-7491 Trondheim, Norway

E-mail: `kai.beckwith@ntnu.no`

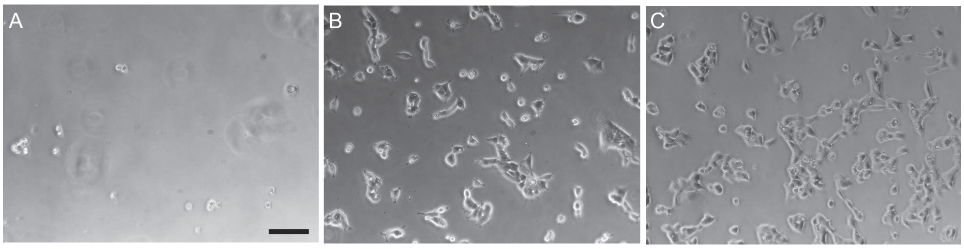

**Figure S1:** Unless heat-treated, PVA does not function as a cell repellent layer, presumably due to rapid dissolution. Here demonstrated with HEK293 cells after 1 day in culture on (A) PVA heat-treated at 90 °C for 30 minutes (b) non heat-treated PVA, and (C) glass control sample. Scale bar 100 µm.

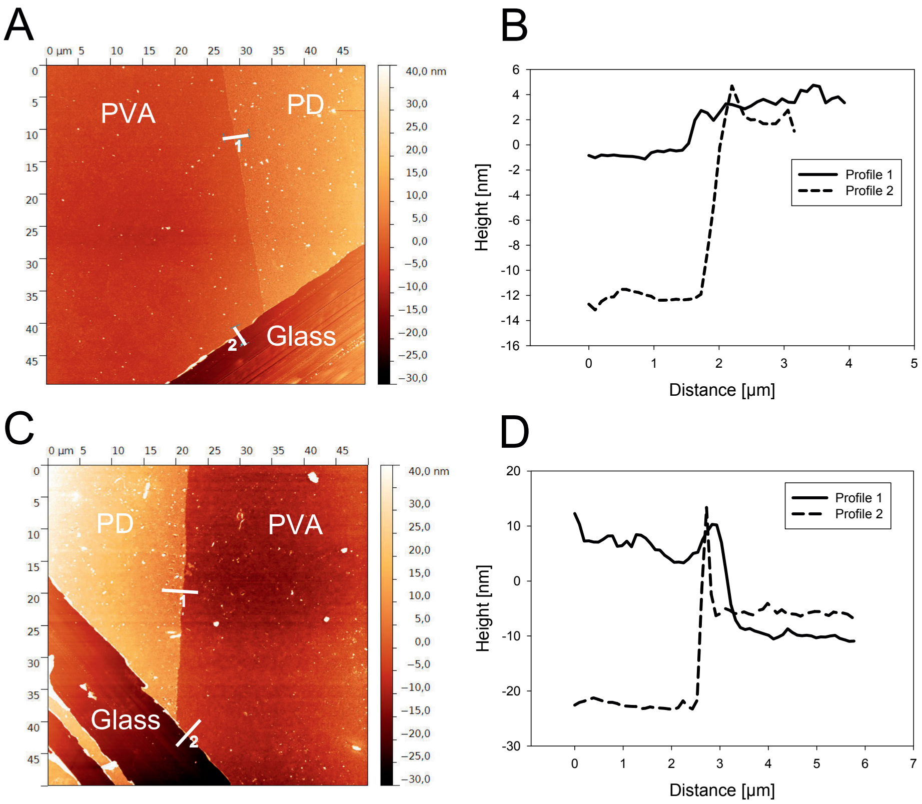

**Figure S2:** AFM height micrograph of PVA films and polydopamine microcontact printed on PVA. The films remained stable, even after long-term (3 weeks) immersion into de-ionized water (A) or full cell medium (C). The PVA film was scratched with a scalpel to aid in thickness measurement. The height curves (B, D) show that the PVA film thickness remains constant at about 15 nm regardless of treatment, which is the same thickness as pristine samples (see main text). Thus little or no PVA dissolution occurs in this period. The same holds true for the polydopamine patterns, with the exception of immersion in cell culture medium (C), where the microcontact printed polydopamine appears to increase to about 15 nm in height. This is presumably due to adsorption of serum components from the serum-containing medium onto the polydopamine.

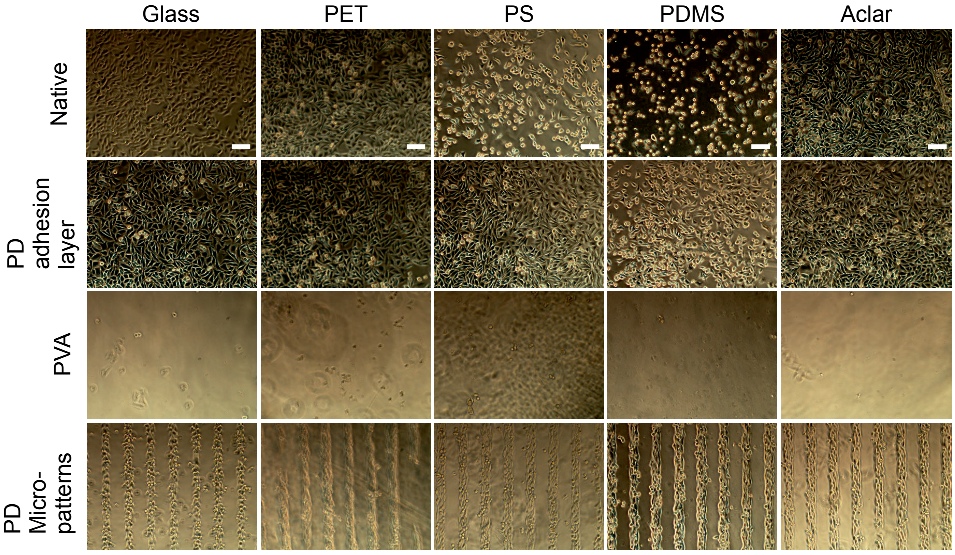

**Figure S3:** Many materials natively support cell adhesion to some extent, including glass, polyethylene terephtalate (PET), polystyrene (PS), poly(chlorotrifluoroethylene) (Aclar) and poly(dimethyl siloxane) (PDMS). A polydopamine (PD) layer deposited by substrate immersion in $1\,\mathrm{mg\,mL^{-1}}$ dopamine in $10\,\mathrm{mM}$ tris at pH=8.5 increases cell adhesion for certain substrates, such as PS and PDMS. A heat-treated PVA hydrogel film formed on polydopamine-treated substrates by spin-casting a 1% PVA solution completely inhibits cell attachment. Finally, microcontact printed polydopamine patterns on the PVA enabled micropatterned cell cultures on all substrates. All images are acquired after 3 days of HeLa cell culture and rinsing, with an initial seeding density of $25\,000\,\mathrm{cell/cm^2}$. Scale bars are $100\,\mu\mathrm{m}$.

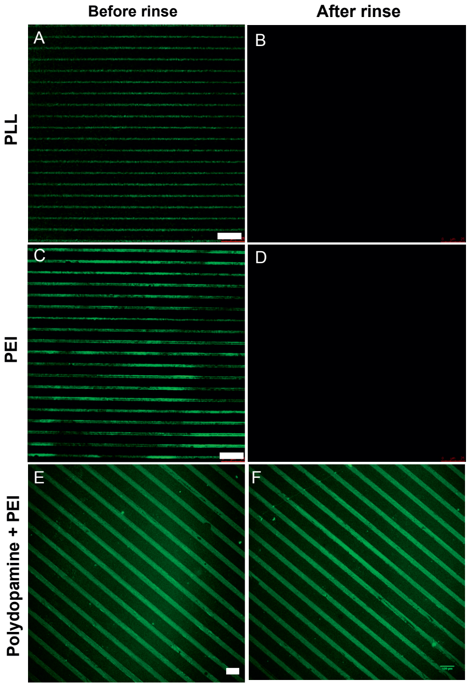

**Figure S4:** Rinsing removes patterns of (A,B) poly(L-lysine) and (C,D) poly(ethyleneimine) when they are printed onto heat-treated PVA films, while (E,F) polydopamine-PEI patterns on PVA remain unaltered by rinsing. FITC-PLL and FITC-PEI were printed a PDMS stamp after immersion in $1\,\mathrm{mg\,mL^{-1}}$ solutions for 10 minutes, while polydopamine with FITC-PEI was printed after immersing a PDMS stamp in a $1\,\mathrm{mg\,mL^{-1}}$ dopamine deposition solution with $0.1\,\mathrm{mg\,mL^{-1}}$ FITC-PEI. Scale bar (A-D) 25 µm, (E,F) 100 µm.

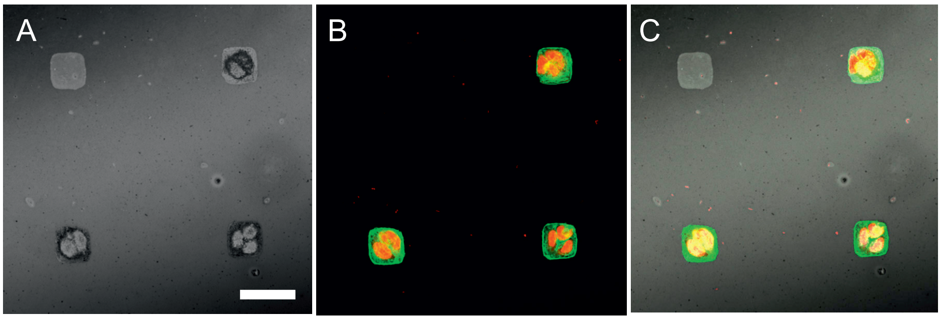

**Figure S5:** (A) Microcontact printed polydopamine patches can be visualized in reflection mode in confocal microscopes, allowing simple pattern visualization without fluorescent labeling. Here the upper-left patch is uninhabited by cells, while the rest are inhabited, altering the reflection signal slightly. (B) Fluorescently labeled HeLa cells grown on the patches. Actin filaments (green) and nuclei (red) are labeled with Alexa488-phalloiding and propidium iodide. (C) Overlay of fluorescent cells and reflection mode, showing how the cells tightly follow the polydopamine areas, filling them but not spreading onto the PVA areas. Scale bar 50 µm.

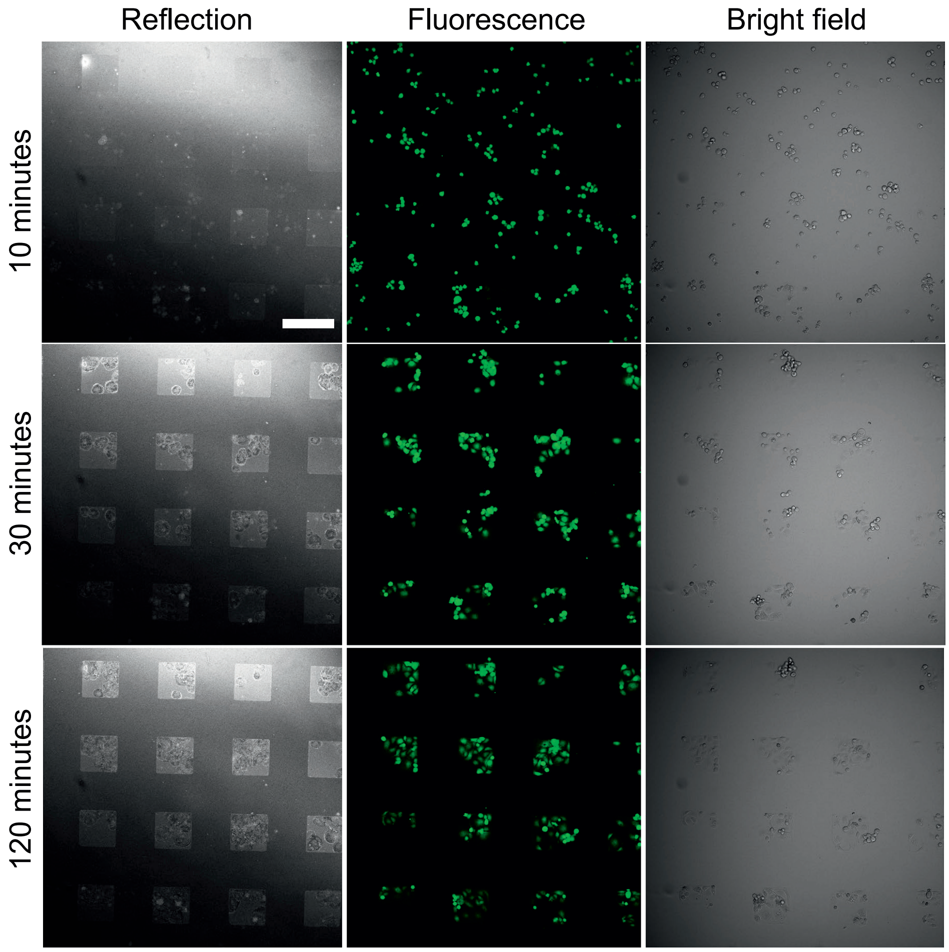
Reflection
Fluorescence
Bright field
10 minutes
30 minutes
120 minutes

**Figure S6:** Time lapse of human vein endothelial (HUVEC) cells after seeding on the patterns. Initially, they are randomly distributed, but quite quickly they start adhering to the patterns, and within 120 minutes they are quite well spread in the patterns. The patterns can be visualized in reflection mode in a confocal microscope. The cells were pre-stained with calcein-AM (live cell indicator and tracker). Scale bar 200 µm.

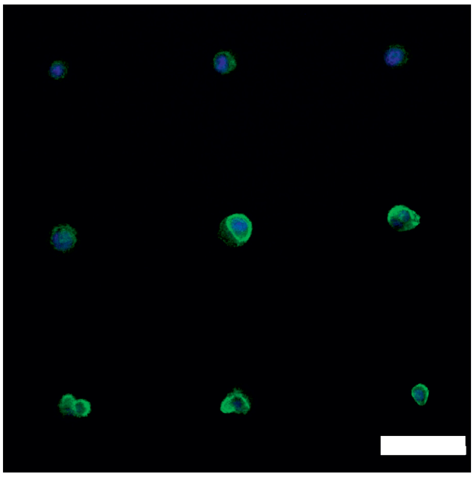

**Figure S7:** (A) PC3 cells on 37 µm circular patterns, mostly as single cells. Scale bar 50 µm.

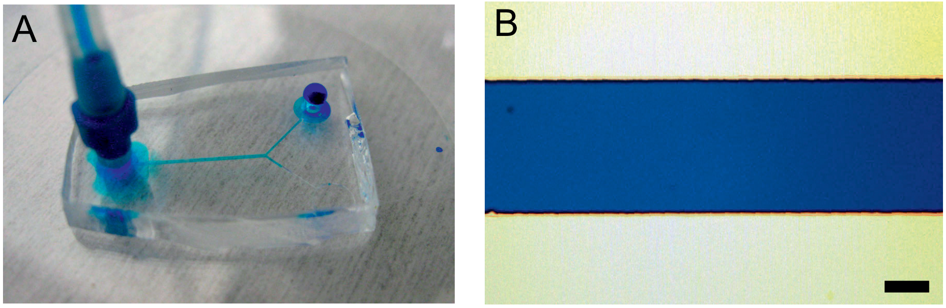

**Figure S8:** (A) Photograph of PDMS microchannel bonded onto PVA-coated glass. There is some leakage around the tubing connector due to the applied strain, but no leakage is observed in the channel area. (B) Micrograph of dyed water in the PDMS microchannel, no leakage outside the channel is evident. Scale bar 100 µm.

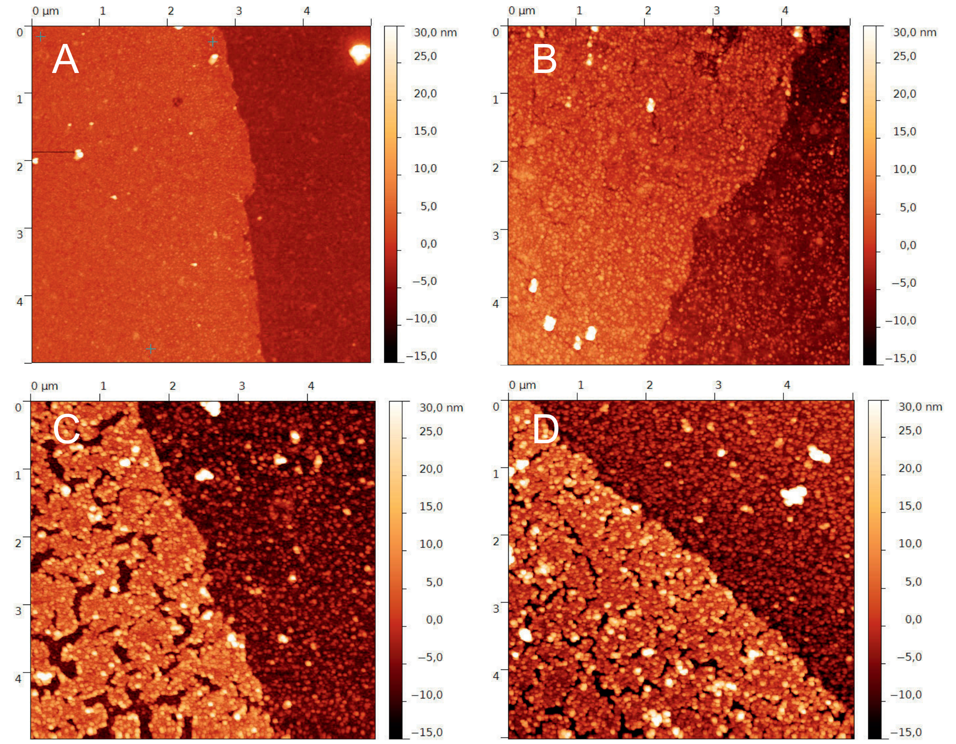
A
B
C
D
0 µm
1
2
3
4
30,0 nm
25,0
20,0
15,0
10,0
5,0
0,0
−5,0
−10,0
−15,0

**Figure S9:** AFM height images of PVA/polydopamine surfaces (A) as made, (B) immersed in buffer for 1 hour, (C) floating on a drop of polydopamine deposition buffer and (D) immersed in polydopamine deposition buffer. All scans are 3 µm × 3 µm with a 45 nm height scale.

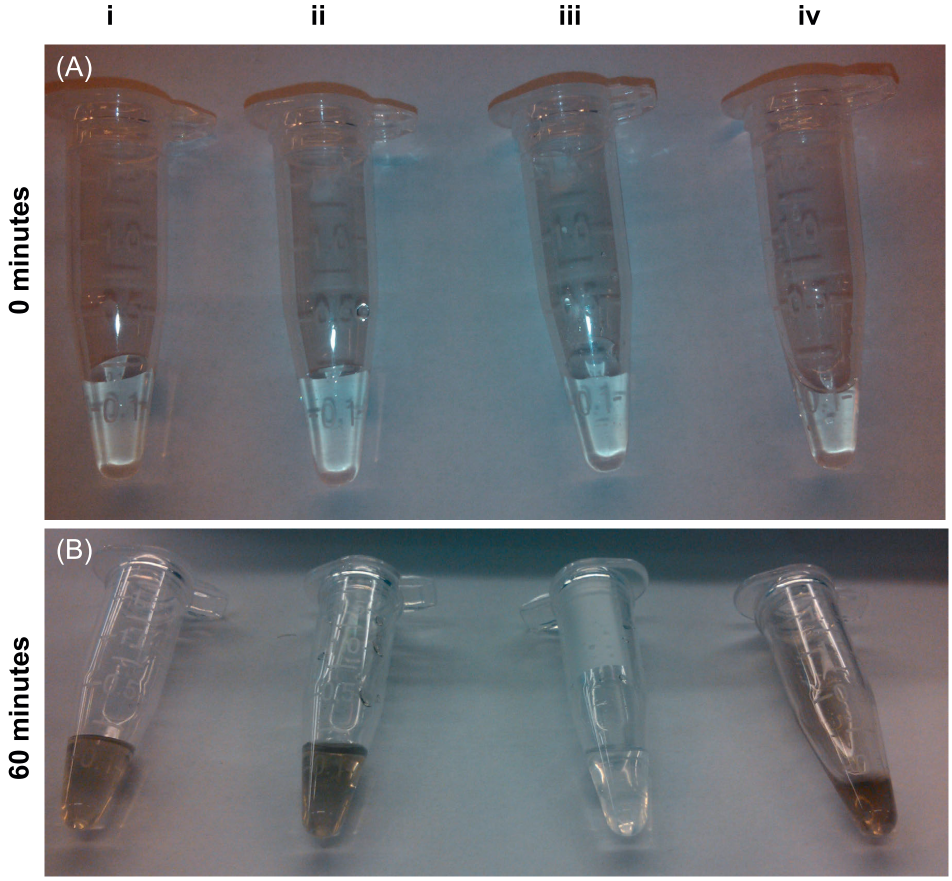

**Figure S10:** Comparison of different buffer conditions for dopamine oxidation: (i) 10 mM tris, pH=8.5 (standard deposition solution), (ii) modified tris-buffered saline (see main text for recipe) with 20 mM tris, pH=8.5, (iii) same as (ii), but containing 1 mM ascorbic acid, and (iv), same as (ii), but containing 0.25 mg mL$^{-1}$ catalase. 1 mg mL$^{-1}$ dopamine was mixed with each solution at the start of the experiment. (A) At 0 minutes, all the solutions are clear. (B) After 60 minutes, solution (i), (ii) and (iv) changed color, indicating oxidition of dopamine, while (iii) remained clear, indicating an anti-oxidant effect of ascorbic acid that inhibits dopamine oxidation.

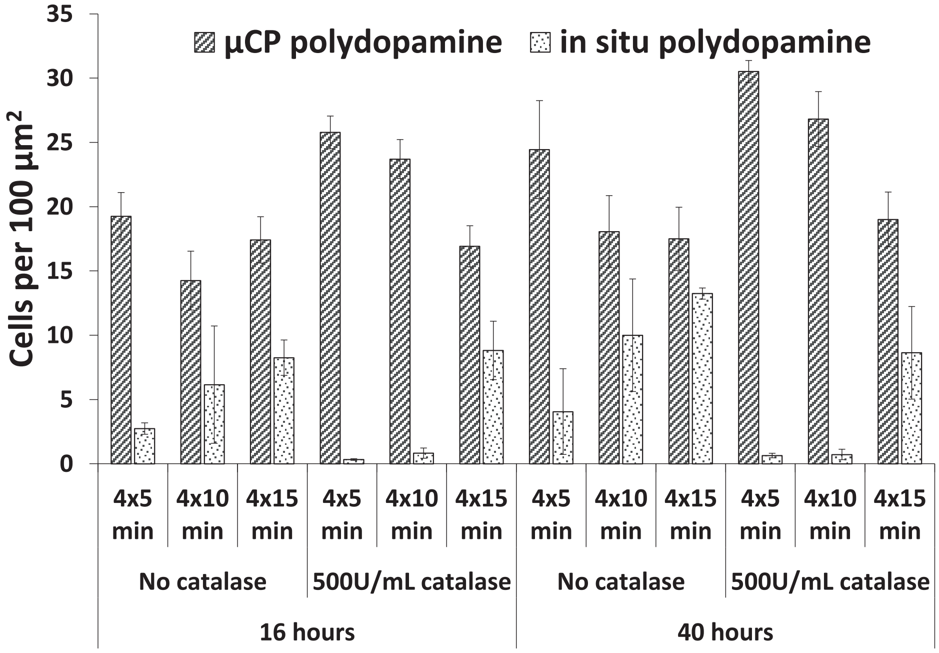

**Figure S11:** 16 hour and 40 hour timepoints measuring the cell density of microcontact printed ($\mu$CP) polydopamine areas and PVA areas activated by polydopamine *in situ*. See main text for discussion. Error bars show ±SEM.

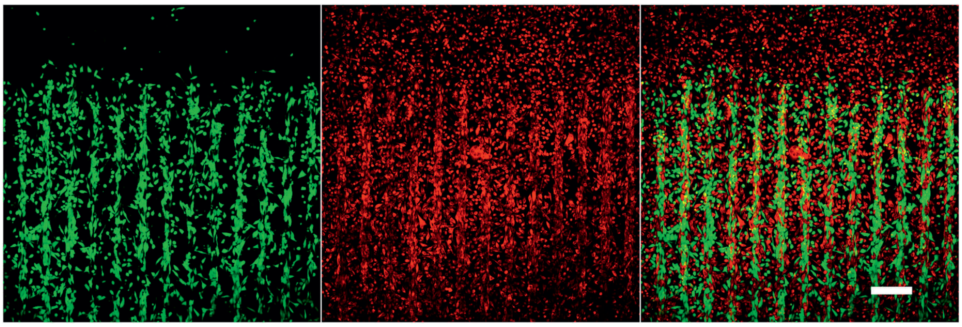

**Figure S12:** HeLa/HeLa co-culture, initial cell population labeled green with calcein-AM, second cell population labeled red with CellTracker Red. Smaller co-culture patterns, shown here with 40 µm lines with 80 µm spacings, are somewhat spread out over time due to cell migration. Here it is 24 hours since the co-culture was initiated. However, in the areas where there is a larger distance to the first cell population (top area), very few of the initial cells are spread. Scale bar 100 µm.

# Paper II

PLOS | ONE

# Seeing a Mycobacterium-Infected Cell in Nanoscale 3D: Correlative Imaging by Light Microscopy and FIB/SEM Tomography

Marianne Sandvold Beckwith[1,2]*, Kai Sandvold Beckwith[3], Pawel Sikorski[3], Nan Tostrup Skogaker[4], Trude Helen Flo[1,2¶] and Øyvind Halaas[2¶]

[1]Centre of Molecular Inflammation Research, Norwegian University of Science and Technology (NTNU), Trondheim, Norway

[2]Department of Cancer Research and Molecular Medicine, NTNU, Trondheim, Norway

[3]Department of Physics, NTNU, Trondheim, Norway

[4]Department of Laboratory Medicine, Children's and Women's Health, NTNU, Trondheim, Norway

**Short title:**

**3D Correlative Imaging of Mycobacterium-Infected Cell**

* Corresponding author
E-mail: marianne.beckwith@ntnu.no (MSB)

¶ These authors contributed equally to this work.

## Abstract

Mycobacteria pose a threat to the world health today, with pathogenic and opportunistic bacteria causing tuberculosis and non-tuberculous disease in large parts of the population. Much is still unknown about the interplay between bacteria and host during infection and disease, and more research is needed to meet the challenge of drug resistance and inefficient vaccines. This work establishes a reliable and reproducible method for performing correlative imaging of human macrophages infected with mycobacteria at an ultra-high resolution and in 3D. Focused Ion Beam/Scanning Electron Microscopy (FIB/SEM) tomography is applied, together with confocal fluorescence microscopy for localization of appropriately infected cells. The method is based on an Aclar poly(chloro-tri-fluoro)ethylene substrate, micropatterned into an advantageous geometry by a simple thermomoulding process. The platform increases the throughput and quality of FIB/SEM tomography analyses, and was successfully applied to detail the intracellular environment of a whole mycobacterium-infected macrophage in 3D.

## Introduction

*Mycobacterium tuberculosis* is the causative agent of tuberculosis, which is the second most deadly infectious disease in the world today [1]. Nontuberculous mycobacteria such as *M. avium* cause serious infections in immunocompromised, and sometimes healthy, individuals [2, 3]. Inefficient vaccines and long treatment together with emerging drug resistance demand new strategies to fight mycobacterial diseases [4, 5].

Upon host entry, mycobacteria are phagocytosed by macrophages and dendritic cells. Within macrophages, pathogenic mycobacteria are able to avoid being killed by blocking phagosomal maturation and fusion with the lysosomes [6, 7], yet still retaining the ability for nutritional acquisition [8, 9]. Some mycobacteria are in contact with or even enter the cytosol, becoming targets for autophagy [10-16]. The details and significance of these and similar events are still unknown, and we believe that direct observations of mycobacterium localization and trafficking relative to the host cell compartments could improve the understanding of mycobacterial virulence, survival and killing, and thus contribute in the search towards novel treatment strategies.

High-resolution 3D imaging is required to fully detail the intracellular habitat of the mycobacteria, but many cellular structures of interest are beyond the resolution of light microscopes. Focused Ion Beam/Scanning Electron Microscopy (FIB/SEM) tomography is a valuable and little explored alternative, with significantly reduced manual labor compared to non-automated 3D electron microscopy (EM) techniques. During FIB/SEM tomography, a dualbeam instrument comprising a FIB and SEM is used to successively mill away thin slices of material (typically 10-100nm thick) from a sample block, and image the appearing sample surface with the scanning electron beam. This results in an ultra-high resolution image stack representing the cell or region of interest in three dimensions.

To increase the specificity of FIB/SEM studies, initial selection of a region of interest and imaging of labeled structures can be performed in an optical fluorescent microscope. If the very same region can be relocated and imaged at the EM level, this is called correlative imaging. Correlative imaging studies with light microscopy (LM) and FIB/SEM have been performed [17-20], but most systems for correlative light and electron microscopy (CLEM) have been optimized for imaging on ultrathin sections with TEM [21-25]. In contrast to TEM, FIB/SEM tomography is an *en bloc* technique, and thus requires a different approach, especially when it comes to LM and EM imaging and correlation between the two. Due to the geometry of the FIB/SEM instrument, the throughput of FIB/SEM tomography experiments can be increased if regions of interest are located close to a sample edge rather than on a flat surface, avoiding the need for trench milling around the region of interest [26]. This would also reduce sample damage from ion beam exposure, and increase the volume readily accessible during FIB/SEM tomography experiments by reducing shadow and charge effects.

To meet the need for a 3D CLEM platform optimized for LM and FIB/SEM tomography, we developed a reproducible system allowing targeted high throughput and high quality FIB/SEM tomography studies of adherent cells such as macrophages. The presented system is based on a micropatterned Aclar substrate, on which adherent cells are cultured within microwells of a predefined size. The cells can be studied with light microscopy within the wells, and an integrated reference system ensures proper cell localization. After contrasting for EM and plastic embedding, the aclar substrate is removed, leaving cells embedded in small protruding epoxy blocks. We show the successful use of this system for investigation of mycobacterium-infected primary human macrophages. Cells imaged using confocal microscopy were easily relocated for 3D imaging with FIB/SEM, allowing identification of the labeled structures with significantly enhanced resolution. The sample geometry allowed for straightforward overlay between data sets from confocal and FIB/SEM, with minimum manual adjustments. Important cellular structures such as mycobacterium-containing phagosomes were accurately resolved during FIB/SEM imaging. The presented system is simple to produce and use, and increases the quality, specificity and throughput of correlative 3D confocal fluorescence microscopy and FIB/SEM tomography studies.

## Results

Biological samples are fixed, dehydrated, stained and embedded in a plastic block (e.g. epoxy) before imaging is performed in a FIB/SEM instrument. A system for correlative imaging of adherent cells must therefore consist of a platform where light microscopy imaging and localization of cells can be performed, and where both imaged cells and the reference system used for localization can be transferred to an epoxy block. The following sections describe the production and performance of such a substrate for 3D CLEM, where the optimal geometry for FIB/SEM tomography has been taken into account (S1 Fig.). The substrate is based on thermomoulded Aclar, a transparent poly(chloro-tri-fluoro)ethylene film often used for CLEM studies of cellular monolayers due to its compatibility with cell growth, light and fluorescence microscopy and EM sample preparation methods for biological samples [18, 27, 28].

### Production of aclar microwell substrates for cell growth and imaging

To create a substrate suitable for cell growth, precise localization of cells and correlative light and FIB/SEM imaging, an array of microwells arranged in a reference system was imprinted into aclar by thermomoulding (Fig. 1). A silicon master of regularly spaced 100 µm × 100 µm × 20 µm microblocks superimposed on a 3µm high reference grid was produced by a combination of UV- and electron-beam lithography and two-step etching (see Materials and Methods). The pattern from the silicon master was transferred into aclar by a simple thermomoulding process, where the polymer film was pressed against the heated silicon mould (see Materials and Methods) (Fig. 1b). The process allowed patterning of areas suitable for cell experiments (typically ~1 $\text{cm}^2$ was used in this work). The pattern was transferred with high fidelity, preserving features down to sub micrometer scale (S2 Fig.). The transfer process was equally reliable at the step from aclar to epoxy, allowing the initial design of the master to be replicated at this final step.

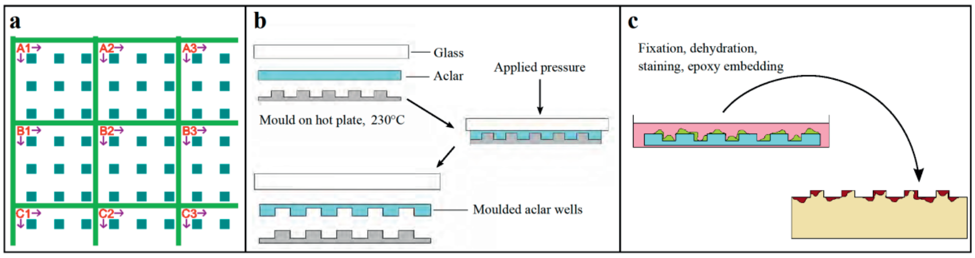

*Fig. 1: **Master design and aclar substrate production.** A silicon master was designed and produced in order to pattern aclar films by thermomoulding. a) The master design, including an array of 100 µm sized squares and a reference system for simple localization of cells with various imaging techniques. b) Micropatterned aclar substrates were produced from the master by thermomoulding. The master was heated to 230°C, before a piece of aclar and a glass microscopy slide was placed on top. An even pressure was applied to the assembly, before subsequently cooling down and separating the individual components. After thermomoulding, the microblocks from the master became wells in the aclar substrate. c) Illustration of how primary human macrophages could be cultured in the wells. After M. avium infection and confocal imaging, cells were fixed, stained, dehydrated and embedded in epoxy for FIB/SEM tomography. The aclar substrate was removed after resin polymerization, creating an array of protruding microblocks containing immobilized cells.*

### Light microscopy and FIB/SEM tomography of mycobacterium infected macrophages

Monocytes isolated from healthy human blood donors could be reproducibly grown and differentiated into macrophages by adherence to the micropatterned aclar substrates (Fig. 2). The aclar well size of 100 µm × 100 µm was suitable to accommodate macrophages, which routinely stretched out more than 50 µm. The repeating pattern of closely spaced microwells assured that a large number of cells grew close to or attached to one of the well edges. This resulted in a large number of cells located on straight sample edges after epoxy embedding, all of which are particularly well suited for FIB/SEM tomography analysis (Fig. 3). The number of cells per well was typically between five and ten.

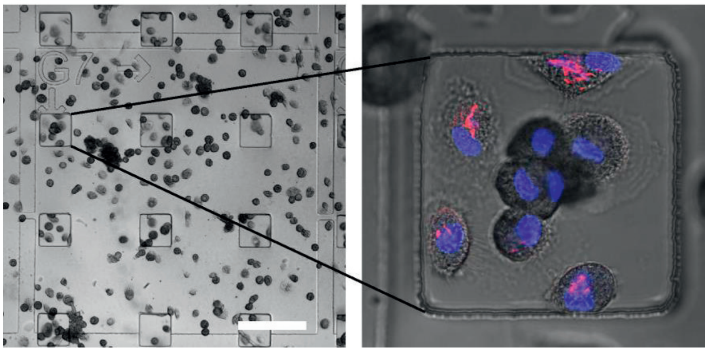

*Fig. 2:* ***Light microscopy.*** *Primary human macrophages were grown and infected with CFP-expressing M. avium on aclar microwell substrates. The cells were then aldehyde fixed and fluorescence stained for nucleus, before light microscopy imaging was performed. a) DIC image illustrating the excellent visibility of both microwells and reference system that were imprinted in aclar by thermomoulding. b) Confocal fluorescence microscopy image with DIC overlay, displaying nuclei in blue and bacteria in red. About 70% of infected macrophages contained at least one bacterium (n=100). Scale bar 200µm.*

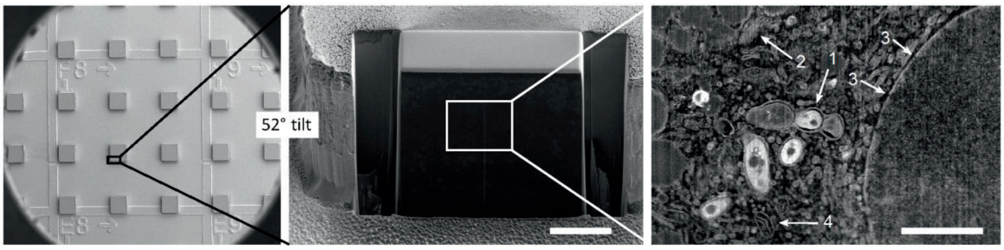

*Fig. 3:* ***FIB/SEM imaging.*** *After confocal imaging, M. avium-infected primary human macrophages were dehydrated, stained and embedded in epoxy. a) SEM micrograph of the final epoxy sample surface after removal of the aclar substrate. The topography of the reference system is sufficient to remain visible at this level. All cells located at an edge of a small protruding block are immediately accessible for FIB/SEM tomography analyses. b) After localization of a region of interest (indicated by the black rectangle in a), the sample was tilted to 52° and the cell of interest was exposed by ion-beam milling. c). SEM micrograph collected during a FIB/SEM tomography experiment, from the surface area indicated by a white rectangle in b). White arrows indicate the following observable details: 1: mycobacteria surrounded by phagosomal membranes, 2: Golgi, 3: nuclear pores recognized by discontinuities in the double nuclear membrane, 4: mitochondrion. Scale bars: 10 µm in b, 2µm in c. The blocks in a) are about 100µm wide.*

Macrophages were examined minimum two days post infection with *M. avium* expressing cyan fluorescent protein (CFP), to address viable mycobacteria having escaped the initial destructive phase. Infected cells could be fixed and stained for cellular components, without detachment from the aclar substrate. For confocal imaging, aclar substrates were placed upside down in a glass-bottomed dish suitable for confocal imaging. Light microscopy was performed on fixed cells in buffer, and was usually best with a water objective due to a thin liquid layer present between the cells and the glass bottom. Both microwells and the reference grid were clearly visible with wide field light microscopy, and z-stacks of stained cells and CFP-expressing bacteria could be gathered by confocal fluorescence imaging (Fig. 2). After confocal imaging, the cells were dehydrated, contrasted for FIB/SEM and infiltrated with epoxy resin (see Materials and Methods). After epoxy polymerization, the aclar substrate was peeled off, and immobilized cells remained in small epoxy blocks protruding upwards from a flat surface (Fig. 3a). The separation process of aclar from cured epoxy was reliable, with no cells remaining attached to the aclar after separation. Cells of interest in microwells identified by confocal microscopy before embedding could easily be localized in corresponding protruding epoxy blocks in the FIB/SEM instrument by using the reference grid that remained visible after transfer to epoxy (Fig. 3a). Regions of interest within single wells were further located by measuring the distance from the well/block edge both on confocal images and on secondary electron images. During SEM imaging, a high acceleration voltage of the electron beam (15kV - 25kV) allowed observation of the shape of the underlying cells due to increasing electron penetration depth with acceleration voltage (S3 Fig.). This further facilitated a correct placement of the region to be investigated in correlation with the confocal images gathered earlier.

After localization of the exact region of interest, the region was prepared for FIB/SEM tomography (Fig. 3b), and slice and view data was collected (see Materials and Methods). In the collection of 3D FIB/SEM data, the slice thickness was chosen at 35nm. Each electron microscopy image covered an area of about 20 µm x 20 µm, resulting in a pixel size of about 10nm. Despite the relatively large pixel size resulting from the large field of view, SEM images were of a quality comparable with TEM images, with sufficient contrast and resolution to discern features such as mycobacterium-containing phagosomes, mitochondrial and Golgi cisternae, the double nuclear membrane and nuclear pore complexes (Fig. 3c, see S4 Fig. for a more detailed comparison). Similar features were poorly resolved in cells prepared as a pellet, due to insufficient penetration of the contrast agent into the block (data not shown). The increase in contrast for cells prepared as monolayers compared to cells prepared as pellets is likely due to a drastic decrease in sample thickness for cellular monolayers, resulting in improved contrast agent penetration.

## Volume correlation and 3D reconstruction

As illustrated in Fig. 4a, the imaging planes from confocal and FIB/SEM imaging are perpendicular to each other. A unified coordinate system for both light and electron images was defined by designating the confocal imaging plane as the x-y plane, and the FIB/SEM tomography imaging plane as the x-z plane. To overlay the 3D datasets of the cells obtained by confocal microscopy and FIB/SEM tomography, an alignment procedure based on distinct geometrical features of the sample (such as well edges) was implemented using Avizo. Briefly, the confocal dataset was first aligned in the x-y plane to ion beam images acquired simultaneously with the tomography data during the FIB/SEM tomography experiment (Fig. 4b). Further, the relative z-positions were aligned by identifying the confocal slice at the base of the well from differential interference contrast (DIC) image sections of the confocal stack. The first and last images of the SEM image stack resulting from the FIB/SEM tomography experiment were then aligned to the edges of the tomography volume swept by the ion images (Fig. 4b). Finally, an overview image from the block face prepared for FIB/SEM tomography was used to overlay the SEM image stack to the ion images in the x-z plane. In this way, correlation between the SEM stack and confocal microscopy stack was performed purely on the basis of sample geometry, allowing accurate 2D and 3D correlation and overlays between light and electron microscopy data (Fig. 4c).

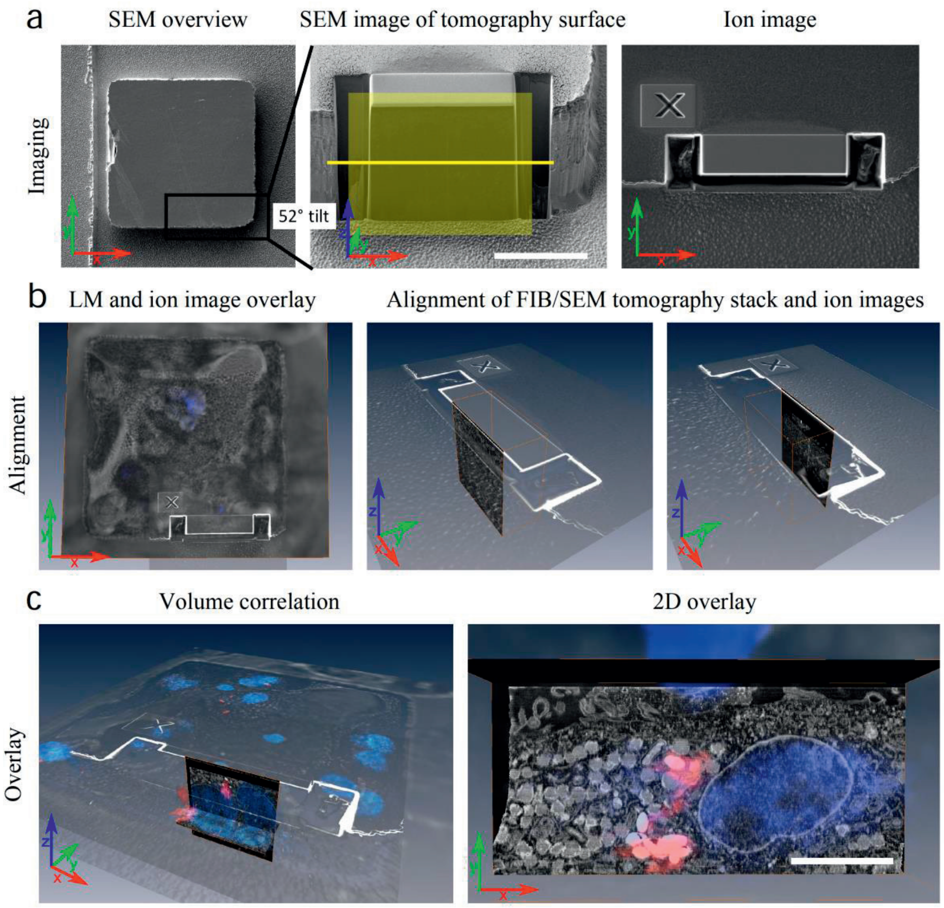

*Fig. 4: **Volume correlation procedure**. One entire microwell was imaged by light microscopy (DIC and confocal fluorescence microscopy), while one cell at an edge of the same well was imaged by FIB/SEM tomography. a) Overview SEM image of the well of interest after epoxy embedding, and SEM image of the region of interest at the corner of the well after preparing the region for FIB/SEM tomography. The images collected during the tomography experiment are in the x-z plane (yellow square), while the images collected during LM imaging are in the x-y plane, parallel to the well surface (yellow line). Ion images are collected in the x-y plane before each milling step, where the cross serves as a reference marker enabling each slice to be milled with nanometer precision. b) Illustration of how the shape of the microwells can be used to place the volume imaged during FIB/SEM tomography correctly within the larger volume imaged during LM imaging. The ion images are first aligned with the edges of the well as imaged by LM. The perpendicular FIB/SEM tomography images can then be aligned with the ion images, with the first and the last image overlapping with the edge observed in the first and last ion image. c) After alignment the two volumes are correlated, and an overlay between fluorescence and EM images can be done in any plane or volume. In the 2D overlay, an xy projection from the FIB/SEM stack is overlaid on the corresponding fluorescence image, with nuclei displayed in blue and bacteria in red. Scale bars: a: 20µm, c: 5µm.*

3D models of an *M. avium* infected macrophage were created from the image stacks collected with both confocal and FIB/SEM techniques, using Avizo. To create 3D models from the FIB/SEM tomography image stack, contours with increased contrast (typically lipid membranes) of structures of interest were manually traced on each image of the stack. A surface was generated from the traced contours by interpolating over the known distance between each image (i.e. 35 nm in this case) throughout the whole stack (Figs. 5a and 6). Clearly resolved membranes were used to determine boundaries and internal structures of organelles, bacteria and phagosomes. The process of generating surfaces from the FIB/SEM stack is also illustrated in S1 Video. 3D surfaces were rendered from the confocal image stack was surface rendered by a threshold algorithm.

Figs. 5a and b demonstrate corresponding confocal and FIB/SEM 3D volume reconstruction results of the nucleus and bacteria in an *M. avium* infected macrophage. The models derived from confocal and SEM imaging data correspond well in terms of the shape of the nucleus and the localization of the bacteria, confirming that the system is well suited for performing targeted FIB/SEM studies after selecting cells of interest by confocal imaging. In the 2D overlay displayed in Fig. 4c, not all fluorescent areas from the confocal image correspond precisely to features in the SEM image. However, all features correspond if the datasets are visualized in 3D as illustrated by the models in Figs. 5a and b. This highlights the difference in resolution of the two methods, where the fluorescent signal of one image in the confocal stack is collected from a much larger volume (optical slice thickness of several hundred nm) than the signal of one SEM image from the FIB/SEM stack (a few nm).

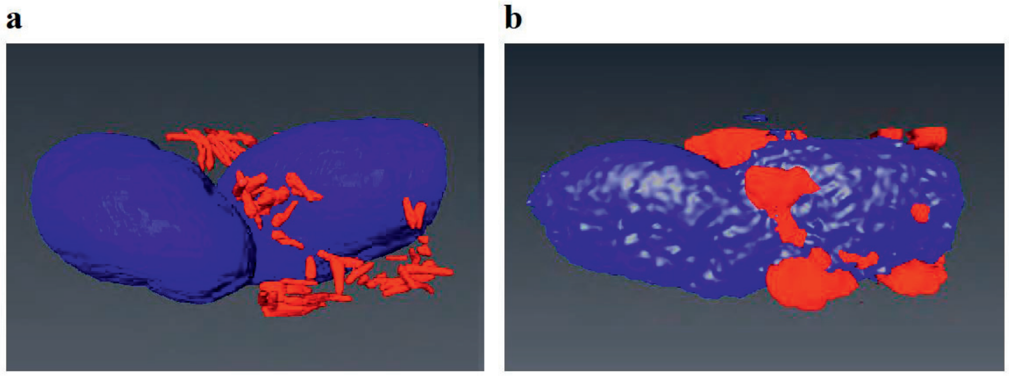

*Fig. 5: **3D reconstruction after correlative imaging**. a) and b) 3D models of the same cell, reconstructed from a FIB/SEM tomography stack and a confocal z stack respectively. The nuclei are displayed in blue and mycobacteria in red. The correspondence between the two models is good.*

## 3D rendered model portray intracellular environment of *M. avium*-infected macrophage at high resolution

The electron image data obtained by FIB/SEM tomography together with corresponding 3D rendered models allowed further elaboration of the intracellular environment of mycobacteria in macrophages during an established infection (Fig. 6). Reconstruction of the nucleus revealed that the cell of interest contained two separate nuclei, both pierced by several bifurcated tunnels (Fig. 6a). The trans-nuclear tunnels contained cytoplasmic components such as mitochondria, strongly suggesting that these structures were not artifacts from sample preparation. The trans-nuclear tunnels are consistent with earlier descriptions of nucleoplasmic reticula [29, 30]. Nucleoli could be identified as bright regions within both nuclei, and nuclear pores and the double nuclear membrane could be discerned. Mitochondria showed a large variability in size and shape, as illustrated by 3D models of selected entities (Fig. 6a).

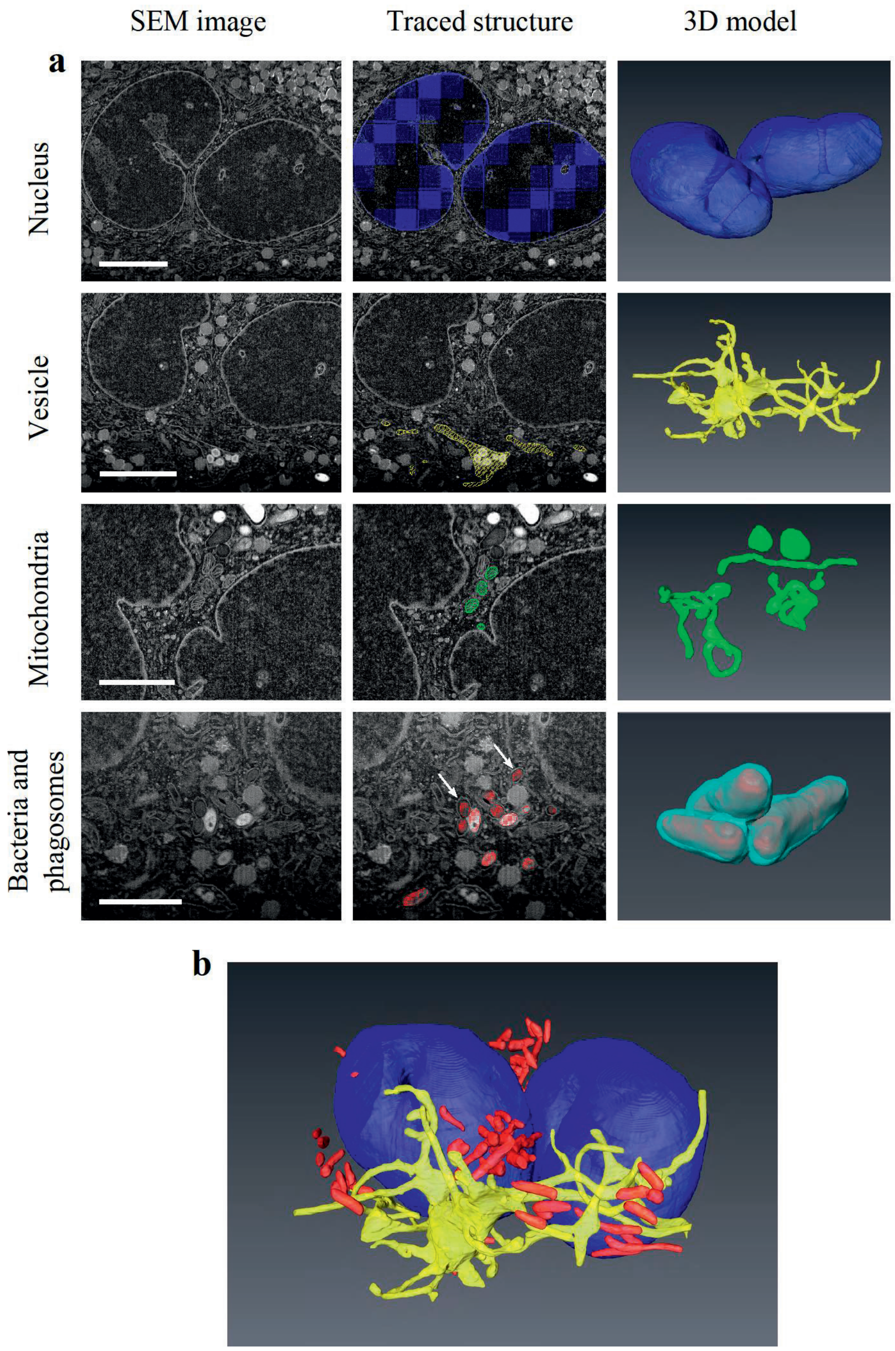
SEM image
Traced structure
3D model
a
Nucleus
Vesicle
Mitochondria
Bacteria and phagosomes
b

*Fig. 6:* ***3D models.*** *Selected structures were reconstructed in 3D from the image stack obtained during a FIB/SEM tomography experiment. a) Column 1 shows a representative SEM image from the original stack while column two outlines how the segmentation was performed on these images to create the 3D models shown in column 3. Nuclei are colored in blue, mitochondria in green, a continuous vesicular structure in yellow, bacteria in red and a selected phagosome in cyan. In row 4, white arrows point to two phagosomal membranes surrounding. Similar membranes were traced to reconstruct the phagosome enveloping 3 bacteria in the lower right Fig. b) 3D model including nuclei, vesicle and bacteria. Scale bars: Nucleus and vesicle: 5µm, Mitochondria and bacteria/phagosomes: 3µm.*

Importantly, mycobacteria were easily identifiable by their strong contrast and distinct slightly ellipsoid cross-sections, aided by the confocal overlays of the fluorescent bacteria. The bacteria were often observed in clusters surrounded by phagosomal membranes which were traced and reconstructed in 3D, discerning neighboring mycobacteria in separate compartments as well as multiple mycobacteria within the same phagosome (Fig. 6a). The interconnection of the phagosomes was only visible after reconstruction in 3D of the SEM images, and would thus be difficult to confirm in standard TEM experiments on selected thin sections. This highlights the importance of high-resolution 3D imaging of large volumes for proper characterization of an intracellular environment. Similarly, single images displayed a number of seemingly separate vesicles, but these were revealed as a single large tubulovesicular structure after 3D reconstruction through the complete image stack (Fig. 6a). This structure further contained internal vesicles and structures, reminiscent of a multivesicular body or a tubular lysosomal compartment. The relation between reconstructed structures could be observed when 3D models of various components were combined, giving a greater understanding of spatial relations between intracellular compartments (Fig. 6b and S1 Video).

## Discussion

We report the use of FIB/SEM tomography correlated with confocal fluorescence microscopy to image primary human macrophages infected with mycobacteria. FIB/SEM tomography enables imaging of whole cells at an ultra-high resolution and in 3D, while light microscopy can identify specific fluorescently labelled structures. Correlation of the two techniques allows to map labelled structures in the broader structural and cellular context offered by FIB/SEM tomography. Also, since primary human macrophages differ in morphology and the infection efficiency with mycobacteria varies greatly, the success rate of FIB/SEM tomography in these experiments could be increased if initial selection of cells of interest is performed at the LM level. A challenge is that current CLEM systems have been optimized for the use of TEM and not FIB/SEM applications. FIB/SEM samples need to be contrasted *en bloc* and embedded in plastic before imaging, and volumes of interest should be located on a sample edge rather than on a flat surface. One group has reported on correlative imaging of adherent cells using FIB/SEM tomography, but the sample geometry was then not taken into account [18].

In order to create a system of optimal geometry for FIB/SEM tomography experiments, while retaining compatibility with both light and electron microscopy preparation procedures and imaging, we chose to base our platform on the polymer film aclar. Aclar allows growth and preparation of adherent cells (such as macrophages) for EM, compatibility with EM-chemicals, and convenient separation of the substrate from the epoxy-embedded cells after resin curing. To create a substrate of the desired geometry, we exploited a well-known but little used characteristic of aclar, namely its thermoformability. Bunge et al. used this method to create custom shaped cell culture dishes already in 1973 [31]. Here, we extended thermoforming into the micron scale. To create well-defined and durable silicon masters, standard micro fabrication processes were applied. Once the master was created, a large number of substrates could be thermomoulded using standard lab equipment. The straight-edged well/block geometry presented here assures that a large number of cells were located on sample edges, thus drastically increasing the number of cells readily accessible for FIB/SEM tomography. As the lithographic patterning of the master is highly versatile, different well/block geometries or reference patterns are easily within reach. For instance, microblocks with a suitable size and shape for TEM sectioning could be produced.

The aclar substrates supported differentiation and growth of primary human macrophages, and long-term infection with *M. avium*. Here the infected cells were imaged with a confocal microscope after chemical fixation, but as other groups have shown, aclar is also compatible with live cell imaging and subsequent high-pressure freezing and freeze substitution [28, 32], with the possibility of preservation of fast temporal events. This would also reduce autofluorescence from glutaraldehyde that decreased the quality of confocal images in our experiments [33]. It should be noted however, that in this work confocal imaging was performed on a large area (125 µm × 125 µm) to scan a large number of cells for the presence of bacteria. Although not the focus of this work, fixation and imaging procedures could be optimized for higher resolution fluorescence imaging of single cells if desired, which would presumably enhance the detail of the resulting overlay data.

In particular, modern developments in superresolution fluorescence imaging has pushed the resolution of light microscopy towards the realm of electron microscopy. Single molecule localization techniques such as PALM and STORM have demonstrated 10-20 nm lateral and axial resolution of labelled proteins [34]. Localization microscopy benefit strongly from correlative imaging approaches, and indeed, several variations of correlative superresolution microscopy and electron microscopy have been reported [35, 36]. Superresolution optical microscopy would contribute to the investigations of the intracellular life of *M. avium* bacteria in macrophages by providing further details of protein localization and potential interactions. However, it remains to be investigated if the aclar substrates developed here are suitable for superresolution imaging.

After EM sample preparation and embedding in epoxy, the convenient reference grid allowed localization of cells imaged by confocal microscopy in the FIB/SEM instrument. This allowed both initial screening of interesting cells and later correlation of specific confocal data with ultrastructural FIB/SEM data. Volume correlation between the datasets collected by confocal fluorescence microscopy and FIB/SEM tomography was performed based only on the geometrical features present in the moulded aclar substrate. In contrast to methods involving correlation based on biological features or added reference particles [19] the method presented here allows greater flexibility in terms of sample preparation and labeling. Further, possible biases introduced by using sample data for both alignment and analysis are avoided.

In our system, the accuracy of the correlation procedure was limited by the accuracy of the overlay between ion images of the well replica acquired during the tomography experiment, and DIC images of the edges and base of the aclar well collected in parallel with the confocal data set. The overlay accuracy could thus be further improved by using smaller, easily identified patterns at the bottom of the wells or the rest of the substrate, that could be included in the initial silicon stamp. Optimally, the accuracy of the volume correlation is in the order of the voxel size of the DIC/confocal data set.

There are also certain inherent limits to the overlay accuracy, imposed by possible changes to the sample after LM imaging, the limited resolution obtainable by LM and the subjective interpretation of the limits of a fluorescent signal (e.g. the threshold chosen for 3D reconstruction). Dehydration has been reported in the literature to cause tissue shrinkage of various degree [37-39]. Here, a strong fixation protocol was used, which has been shown to result in minimal shrinkage after dehydration [38]. The percentage of shrinkage of our samples was too small to assess by measurements on the respective LM and FIB/SEM data. 2D representations of data overlays from volume techniques will differ from correlative imaging based on thin slices due to the large difference in signal volume and axial resolution between 3D light and electron microscopy, reducing the apparent 2D overlay precision. However, full 3D imaging of comparatively large volumes and overlay of resulting 3D data offer great advantages that in many cases outweigh the reduced overlay precision of single 2D images from the datasets.

FIB/SEM tomography has been demonstrated on several biological systems [17, 40-46], but the technique is still new and under development. TEM techniques have had a more widespread use, including important contributions revealing the phagosomal escape of strains of pathogenic mycobacteria like *M. tuberculosis* into the cytosol [11, 15]. TEM is indeed a powerful technique, but the third dimension added by FIB/SEM tomography is central for certain studies. Autophagy is a cellular process of great interest in the context of infection, and intracellular structures such as mitochondria and ER have been confused with autophagosomes on thin sections for TEM [47]. Correlation with LM can further improve studies of autophagy and similar processes where known proteins are involved. Subramaniam and his team used FIB/SEM tomography to reveal new aspects of the immunological synapse between T-cells and dendritic cells during HIV infection, and to reveal conduits in HIV-infected macrophages [40, 41]. Similar ultrastructural 3D investigations would be of interest for mycobacterium infections. FIB/SEM tomography also enables complete identification of the intracellular habitat for all bacterial colonies, as it is unlikely that all bacteria inside an infected cell are equal [48].

In our investigations, FIB/SEM tomography allowed identification of *M. avium* bacteria localized by fluorescence microscopy, as well as characterization of their intracellular surroundings within host macrophages with nanometer resolution. *En bloc* staining of macrophage monolayers on aclar gave sufficient contrast to observe the detailed cellular ultrastructure during FIB/SEM tomography experiments, at a resolution comparable to TEM. In one representative cell, no bacteria were observed without a surrounding phagosomal membrane, and single phagosomes often contained several bacteria. Phagosomal membranes were closely spaced around bacteria, corresponding well to descriptions of *M. avium*-containing phagosomes observed with TEM [49], and different from the phagosomal escape that has been demonstrated for *M. tuberculosis* and *M. marinum* [14, 15]. In addition to bacteria and phagosomes, structures such as mitochondria, nuclei and vesicles could be characterized from the same FIB/SEM image stack. Mitochondria of various shapes could be observed after 3D reconstruction, and one large tubulovesicular body that was continuous throughout a significant volume of the cell was identified. The vesicle, which contained additional cellular components, could be the endocytic recycling compartment or a tubular lysosomal compartment [50], however this remains to be verified by CLEM using specific labels for this and other compartments. Interestingly, a clear manifestation of the nucleoplasmic reticulum was apparent after 3D reconstruction. The nucleoplasmic reticulum has only recently been described, but has never been observed in primary human macrophages and has not been imaged in 3D at a comparable resolution [29, 30]. The high resolution and large diversity of observed structures highlights the power of FIB/SEM tomography when compared to confocal fluorescence microscopy, where only specifically labeled molecules or organelles are imaged at a more limited resolution. However, the combination of confocal microscopy and FIB/SEM tomography is even more beneficial than either of the two alone, as intracellular structures can be identified using specific labels and stains visible by confocal imaging and thereafter resolved in high-resolution 3D images along with their surroundings.

In summary, the system developed in the present study constitutes an accessible and easy to use-platform, suitable for streamlined high resolution FIB/SEM investigation of adherent cells. The platform also enables reproducible correlative imaging by high resolution, high numerical aperture confocal fluorescence microscopy and FIB/SEM tomography. Throughout the process, cells are maintained in their adherent state, without resorting to potentially destructive techniques such as scraping or pelleting. Cell growth is performed according to standard protocols, and confocal imaging can be carried out without any modifications to the light microscope. The use of aclar as a growth substrate allows for simple EM sample preparation, including reliable and quick separation of the substrate from cured epoxy. Not only do the wells largely simplify the localization of the exact same cell with several microscopy techniques, but they also constitute a platform that is very advantageous to work with in a FIB/SEM. Straight edges assure good accessibility to many cells for FIB/SEM tomography, and decrease the time required for milling before starting the automatic image acquisition. The correlative imaging platform allowed volume correlation based only on features of the substrate, without bias from cellular components. It was shown to be very useful for inspection of primary human macrophages infected with *M. avium*, and the method could be similarly applied to detail the intracellular milieu of any adherent cell in high-resolution 3D.

# Materials and Methods

## Stamp production

The master for molding Aclar poly(chloro-tri-fluoro)ethylene microwells was made using silicon microfabrication processes. The hard mask for etching the wells was patterned using photolithography, while the reference grid was patterned with electron beam lithography, before a two-step cryoetching process was performed to transfer the patterns into the silicon wafer.

A p-type [110] silicon wafer was cleaved into 2x2 cm square pieces. SPR700.1 photoresist (Microchem) was patterned using photolithography with an inversed 100/200 µm well-pattern in a Carl Suss MA6 mask aligner. A hard mask for etching the wells was deposited by first DC-sputtering 15 nm aluminum, and then allowing 10% $O_2$ into the chamber for reactive DC-sputtering of 15 nm of $Al_2O_3$. The sputtering was performed in an AJA Custom ATC-2200V sputter-coater at 300W and 3 mtorr. Lift-off was performed by sonicating for 5 minutes in Remover PG (Microchem).

For producing the reference grid, a double-layer of Omnicoat (Microchem) was applied prior to the SU-8 for simple removal of SU-8 later. A 1 µm SU-8 2 film was patterned by electron beam lithography using a Hitachi S-4300 FEG-SEM modified with a Raith Quantum patterning system, with a voltage of 30 kV, a beam current of 500 pA and a dose of 1 µC $cm^{-2}$, leading to a total patterning time of only 20 minutes despite the large area. After development, the exposed areas of Omnicoat were removed by exposure to a 50 W 0.6 mbar oxygen plasma for 1 minute in a plasma cleaner (Diener Femto).

The reference grid was transferred into the silicon substrate by a highly selective and anisotropic $SF_6/O_2$ cryogenic etch in an Oxford PlasmaLab 180 ICP-RIE. The etch was performed at $-120^{\circ}C$, with 90 sccm $SF_6$, 11.5 sccm $O_2$, an RF platen power of 4W, an ICP power of 750 W and a process pressure of 7.5 mtorr, which gave an etch rate of about 1.45 µm $min^{-1}$. After 2 minutes of etching, the sample was removed and the remaining SU-8 resist was removed by sonication for 2 minutes in Remover PG at 80 °C. The sample was then etched for a further 13 minutes with only the alumina hard mask, defining the wells. The deep silicon etching process ensured straight vertical well edges, which is optimal for FIB/SEM milling and imaging

Finally, the aluminum/alumina mask was removed by soaking in MF-26A developer (Microchem) for 2 minutes. The surface was cleaned with a 50 W oxygen plasma for 18s at 0.6 mbar, before the surface was treated with an anti-stick layer of 1H,1H,2H,2H-Perfluorooctyltriethoxysilane (Sigma Aldrich) by vapor silanization for 15 minutes.

## Thermomoulding of aclar

Aclar poly(chloro-tri-fluoro)ethylene films (7.8 mil, Ted Pella) were cleaned by rinsing in ethanol. The silicon master was heated to 230 °C on a hot plate, and the aclar film was carefully placed on top and allowed to conform to the surface. A 2x2 cm piece of a glass microscopy slide was briefly heated on the hot-plate, and then placed on top. Force was applied on top of the glass with the blunt end of a pair of tweezers until no air bubbles in the aclar could be observed. The master, film and glass stack was removed from the hot-plate and allowed to cool down for 5 minutes, before carefully separating the pieces using a scalpel at the edge. The maximum durability of the master was not tested, but it still performed consistently after patterning at least 50 aclar substrates.

## Cell culture and bacterial infection

Moulded aclar films of size 1x1 cm were sterilized in ethanol, air dried in a sterile bench and placed in 24 well plate flat bottomed culture dishes (Corning Costar) for cell culture.

Human peripheral blood mononuclear cells (PBMCs) were isolated from buffy coats obtained from the Blood Bank, St Olavs Hospital, Trondheim by density gradient centrifugation (Lymphoprep; Axis-Shield). The Regional Committees for Medical and Health Research Ethics at NTNU approved use of PBMCs from healthy adult blood donors after written informed consent (identification number 2009/2245-2). 2.5 million PBMCs were seeded per well in a 24-well plate, about 10% of which are monocytes. Monocyte-derived macrophages were generated from those by plastic adherence to the aclar substrates and maintenance in RPMI1640 (GIBCO) supplemented with 30% for 6 days (before infection) or 5% (after infection) of pooled human serum (The Blood Bank).

Transformants of the virulent *M. avium* clone 104 expressing CFP were used for all infection experiments, see [8] for details. Single colonies of were picked from Middlebrook 7H10 agar plates (Difco/Becton Dickinson) and grown to exponential phase (5 days) in Middlebrook 7H9 medium (Difco/Becton Dickinson) supplemented with glycerol, Tween 80, and albumin dextrose catalase. Bacteria were washed and sonicated in PBS to ensure single-cell suspensions before macrophages growing on aclar substrates were infected at a multiplicity of infection of 10. Excess bacteria were removed 4 hours post infection by washing with Hanks Balanced Salt Solution (Sigma Aldrich) and infected macrophages were left in RPMI/5% pooled human serum for two more days before examination. On average about 70% of the macrophages in microwells were infected (n=100).

## Light microscopy

Two days post infection, macrophages were fixed using glutaraldehyde (GA, 50% EM grade, Chemi-teknik AS) in 0.15M HEPES (Sigma-Aldrich) at pH 7,2. Fixation was performed in two steps. First double strength fixative (4% GA) preheated to 37 °C was added 1:1 directly to the growth medium of the macrophages. After 20 minutes, the solution was exchanged with normal strength fixative (2% GA) and fixation continued for 2 hours. After fixation the cells were washed in 0.3M HEPES. Subsequently fluorescence staining of DNA for nuclear visualization was performed by adding 2.5 µM Draq5 (AH diagnostics) for 10 minutes at room temperature. Confocal imaging of fixed cells was performed with a Zeiss LSM 510 Meta, by putting the film upside down in a glass bottomed dish of thickness 170µm. Cells of interest were protected from being crushed towards the confocal dish because they grew in wells and were hence lifted up 20 µm from the bottom glass. Using a 63x water objective with numerical aperture 1.2, all cells were within the accepted working distance of the objective.

## FIB/SEM sample preparation

After confocal imaging, samples were postfixed and stained for 4 hours in 1,5% potassiumferrocyanide and 2% osmium tetroxide in 0,1M cacodylate buffer. The samples were then washed 3 times in Milli-Q (MQ) water and left in MQ-water at 4°C over night. The subsequent day, samples were dehydrated in a graded series of 50%, 70% and 90% ethanol (15min per step on shaker), before they were *en bloc* stained in 2% uranyl acetate (UA) in 75% ethanol for 1 hour and 20 minutes. After staining, the samples were washed three times in 90% ethanol and further dehydrated 10 min in 90%, 4x15min in 100% ethanol and 2x15min in acetone. The epoxy resin used for infiltration was a mixture of 51% LX-112 epoxy resin, 27% DDSA (Dodecenyl succinic anhydride) and 22% NMA (Nadic methyl anydride), all from LADD Research Industries. 0.15ml DMP-30 (2,4,6-tris (dimethylaminomethyl) phenol, Chemi-Teknik AS) was added to 10ml of mixed epoxy resin just before use. Resin infiltration was performed in three steps of 45min, 1:2, 1:1 and 2:1 resin:acetone respectively. The samples were then left in fresh epoxy on a rotator over night. The following day, monolayer embedding was carried out using epoxy newly mixed with DMP-30 and TEM embedding moulds. The moulds were filled with resin, and the aclar substrates were placed wells-down on top, resting on the edges of the embedding moulds. The resin was polymerized at 60 °C for 2 days, before the aclar was peeled off using tweezers. Empty epoxy extending outside the monolayer was cut off using a razor blade. The epoxy blocks were mounted on aluminum sample stubs using a drop of epoxy that was cured over night at 60 °C. Total curing time thus became 3 days for FIB/SEM samples. Before imaging, samples were sputter coated twice at different angles with a Cressington sputter coater model 208 HR, each time with a 20 nm thick layer of platinum/palladium.

## FIB/SEM imaging

All FIB/SEM experiments were performed with a Helios NanoLab DualBeam FIB/SEM instrument from FEI Company. Cells of interest were localized using the gridded reference system on the epoxy block, and a protective platinum (Pt) layer of thickness 1 µm was deposited on the top face of the volume of interest using the gas injection system (GIS) in the FIB/SEM instrument. The ion beam was used to induce Pt deposition, at 30kV acceleration voltage and a current corresponding to a current density of 2.55 pA $\mu m^{-2}$. The front face of the relevant well was then milled with the ion beam at 2.7 nA beam current. To avoid shadow effects and redeposition of material during imaging, trenches of about 8 µm width were milled on each side of the cell of interest with an ion beam current of 2.7 nA. The desired position of the trenches could be accurately localized by measuring distances on the corresponding confocal image of the well of interest. Finally the front face of the volume of interest was polished with an ion beam current of 0.9 nA.

FIB/SEM tomography was carried out using the Slice and View G2 software from FEI. The electron beam acceleration voltage was set to 3kV, the beam current to 0.69 nA, the resolution to 2048 × 1768 pixels and the dwell time to 10 µs. Images were collected in immersion mode, using the in-lens detector set to secondary electron detection. A magnification of x6500 was used for electron imaging. The number of slices was set so that the slice thickness became 35 nm, and the ion beam current was set to 0.9 nA for milling during the experiment. The milling depth was set to 3.5 µm and the milling material to Si. A protective pad of Pt with a thickness of 0.6 µm was deposited, before a fiduciary marker was etched with the ion beam. Ion beam drift correction images were collected with a resolution of 1024 × 884 and a dwell time of 3µs, using the Everhart-Thornley detector in secondary electron mode.

## TEM

One sample that was prepared for FIB/SEM as described above, was further processed for TEM imaging after epoxy embedding. Thin sections of 60 nm were cut using a Leica UC6 Microtome with a Diatome diamond knife. Sections were picked up on formvar coated Gilder copper slot grids. Some sections were stained in 4% UA in 50% ethanol for 12 minutes, rinsed in distilled water then counterstained in 4% lead citrate for 4 minutes, while some were imaged without further processing. TEM imaging was performed using a Philips Tecnai 12 Microscope.

## Data processing

The images collected during the FIB/SEM tomography experiment were first aligned in Fiji using StackReg or linear stack alignment with SIFT, with the transformation set to translation [51-53]. Then all images were scaled with a factor of 1.27 in y-direction using a bicubic interpolation. This scaling is necessary to obtain a realistic volume rendering, due to the geometry of the beams in the FIB/SEM instrument. Image background was subtracted with a rolling ball radius of 100 pixels, and the brightness and contrast was adjusted. After this initial processing in Fiji, the image stack was imported into Avizo (Avizo fire v 8.0, FEI Visualization Sciences Group), with a scale factor of 3.63 in z direction. The z scaling comes from the fact that the stack was collected with a slice thickness of 35nm, while the width of a pixel in x-y was 9.63nm. In Avizo, surfaces were rendered by creating labelfields and using the segmentation module. Structures of interest were traced mostly manually, because no automatic segmentation performed satisfactorily on the large and detailed dataset. Interpolation between slices was applied when appropriate. After surface generation, the number of surface triangles was reduced, and surface smoothing was performed with 10 iterations and lambda 0.6.

The z stack images collected with confocal fluorescence microscopy (with DIC overlay) were adjusted for brightness and contrast in all channels, and a Gaussian blur filter of radius 1 was applied in Fiji to reduce noise. Following this the stack was imported into Avizo, with a scale factor of 7.25 in z direction (pixel size in x-y was 120nm, while images from the z stack were collected with a distance of 870nm). Bacteria and nucleus were then surface rendered using Isosurface Rendering in Avizo, with a threshold of 43.2 and 60.7 respectively.

Images from FIB/SEM tomography and confocal fluorescence microscopy of the same cell were correlated in Avizo, based on features of the aclar substrate. All relevant images and stacks (ion image stack taken for drift correction purposes during the slice and view experiment, confocal z-stack, FIB/SEM tomography stack and overview image from the tomography surface) were first imported into Avizo with the correct nm/pixel values. The ion images were aligned using the linear stack alignment with SIFT in Fiji [51, 52] before import, and the z voxel size was set to 0.00001 upon import to Avizo since these images all originate from the same plane. The image corresponding to the bottom of the well in the confocal z stack was identified, and this image was placed at z=0 in the coordinate system of Avizo. In the 0 plane, the drift correction images were then aligned with this confocal image. As a result, a connection between electron images and light microscopy images was established, with the depth of the well correctly placed. The FIB/SEM tomography stack was then placed with the first image in the plane of the first drift correction image, and the last image in the plane of the last. The overview image of the tomography surface taken just before the experiment started was aligned with the first drift correction image, at the correct z and xy position. The correct xy position of the FIB/SEM tomography stack was then found by overlay of the first image with the latter. After this procedure, the volume from the FIB/SEM tomography experiment was correctly placed within the confocal z stack volume, and corresponding images in all planes could be identified.

## Acknowledgements

Experiments were performed at NTNU NanoLab and at the Cellular and Molecular Imaging Core Facility (CMIC), NTNU. We thank Richard Horton from The Lancet for reading through and commenting on an early version of the manuscript.

## References

1. World Health O. Global tuberculosis report 2013. 2013 978 92 4 156465 6.

2. Griffith DE. Nontuberculous mycobacterial lung disease. Current opinion in infectious diseases. 2010;23:185-90. doi: 10.1097/QCO.0b013e328336ead6.

3. Wagner D, Young LS. Nontuberculous mycobacterial infections: a clinical review. Infection. 2004;32:257-70. doi: 10.1007/s15010-004-4001-4.

4. Andersen P, Doherty TM. The success and failure of BCG - implications for a novel tuberculosis vaccine. Nature reviews Microbiology. 2005;3:656-62. doi: 10.1038/nrmicro1211.

5. van Ingen J, Egelund EF, Levin A, Totten SE, Boeree MJ, Mouton JW, et al. The pharmacokinetics and pharmacodynamics of pulmonary Mycobacterium avium complex disease treatment. American journal of respiratory and critical care medicine. 2012;186:559-65. doi: 10.1164/rccm.201204-0682OC.

6. Russell DG, Mwandumba HC, Rhoades EE. Mycobacterium and the coat of many lipids. The Journal of cell biology. 2002;158(3):421-6.

7. Via LE, Deretic D, Ulmer RJ, Hibler NS, Huber LA, Deretic V. Arrest of mycobacterial phagosome maturation is caused by a block in vesicle fusion between stages controlled by rab5 and rab7. Journal of Biological Chemistry. 1997;272(20):13326-31.

8. Halaas Ø, Steigedal M, Haug M, Awuh JA, Ryan L, Brech A, et al. Intracellular Mycobacterium avium intersect transferrin in the Rab11+ recycling endocytic pathway and avoid lipocalin 2 trafficking to the lysosomal pathway. Journal of Infectious Diseases. 2010;201(5):783-92.

9. Kelley VA, Schorey JS. Mycobacterium's arrest of phagosome maturation in macrophages requires Rab5 activity and accessibility to iron. Molecular biology of the cell. 2003;14:3366-77. doi: 10.1091/mbc.E02-12-0780.

10. Gutierrez MG, Master SS, Singh SB, Taylor GA, Colombo MI, Deretic V. Autophagy Is a Defense Mechanism Inhibiting BCG and< i> Mycobacterium tuberculosis</i> Survival in Infected Macrophages. Cell. 2004;119(6):753-66.

11. Houben D, Demangel C, van Ingen J, Perez J, Baldeón L, Abdallah AM, et al. ESX-1-mediated translocation to the cytosol controls virulence of mycobacteria. Cellular microbiology. 2012;14(8):1287-98.

12. Jo E-K, Yuk J-M, Shin D-M, Sasakawa C. Roles of autophagy in elimination of intracellular bacterial pathogens. Frontiers in immunology. 2013;4:97-. doi: 10.3389/fimmu.2013.00097.

13. Smith J, Manoranjan J, Pan M, Bohsali A, Xu J, Liu J, et al. Evidence for pore formation in host cell membranes by ESX-1-secreted ESAT-6 and its role in Mycobacterium marinum escape from the vacuole. Infection and immunity. 2008;76(12):5478-87.

14. Stamm LM, Morisaki JH, Gao LY, Jeng RL, McDonald KL, Roth R, et al. Mycobacterium marinum escapes from phagosomes and is propelled by actin-based motility. J Exp Med. 2003;198(9):1361-8. doi: 10.1084/jem.20031072. PubMed PMID: 14597736; PubMed Central PMCID: PMC2194249.

15. van der Wel N, Hava D, Houben D, Fluitsma D, van Zon M, Pierson J, et al. M. tuberculosis and M. leprae Translocate from the Phagolysosome to the Cytosol in Myeloid Cells. Cell. 2007;129(7):1287-98.

16. Watson RO, Manzanillo PS, Cox JS. Extracellular< i> M. tuberculosis</i> DNA Targets Bacteria for Autophagy by Activating the Host DNA-Sensing Pathway. Cell. 2012;150(4):803-15.

17. Armer HEJ, Mariggi G, Png KMY, Genoud C, Monteith AG, Bushby AJ, et al. Imaging transient blood vessel fusion events in zebrafish by correlative volume electron microscopy. PLoS One. 2009;4(11):e7716-e. doi: 10.1371/journal.pone.0007716.

18. Jiménez N, Van Donselaar EG, De Winter DAM, Vocking K, Verkleij AJ, Post JA. Gridded Aclar: preparation methods and use for correlative light and electron microscopy of cell monolayers, by TEM and FIB--SEM. Journal of Microscopy. 2010;237(2):208-20.

19. Murphy GE, Narayan K, Lowekamp BC, Hartnell LM, Heymann JAW, Fu J, et al. Correlative 3D imaging of whole mammalian cells with light and electron microscopy. Journal of Structural Biology. 2011;176:268-78. doi: 10.1016/j.jsb.2011.08.013.

20. Narayan K, Danielson CM, Lagarec K, Lowekamp BC, Coffman P, Laquerre A, et al. Multi-resolution correlative focused ion beam scanning electron microscopy: applications to cell biology. J Struct Biol. 2014;185(3):278-84. doi: 10.1016/j.jsb.2013.11.008. PubMed PMID: 24300554; PubMed Central PMCID: PMC3943650.

21. Agronskaia AV, Valentijn JA, van Driel LF, Schneijdenberg CTWM, Humbel BM, van Bergen en Henegouwen PMP, et al. Integrated fluorescence and transmission electron microscopy. Journal of Structural Biology. 2008;164:183-9. doi: 10.1016/j.jsb.2008.07.003.

22. Kukulski W, Schorb M, Welsch S, Picco A, Kaksonen M, Briggs JAG. Correlated fluorescence and 3D electron microscopy with high sensitivity and spatial precision. The Journal of cell biology. 2011;192:111-9. doi: 10.1083/jcb.201009037.

23. Sartori A, Gatz R, Beck F, Rigort A, Baumeister W, Plitzko JM. Correlative microscopy: bridging the gap between fluorescence light microscopy and cryo-electron tomography. J Struct Biol. 2007;160(2):135-45. doi: 10.1016/j.jsb.2007.07.011. PubMed PMID: 17884579.

24. Schwarz H, Humbel BM. Correlative light and electron microscopy using immunolabeled resin sections. Methods in molecular biology. 2007;369:229-56. doi: 10.1007/978-1-59745-294-6_12. PubMed PMID: 17656754.

25. van Rijnsoever C, Oorschot V, Klumperman J. Correlative light-electron microscopy (CLEM) combining live-cell imaging and immunolabeling of ultrathin cryosections. Nat Methods. 2008;5(11):973-80. doi: 10.1038/nmeth.1263. PubMed PMID: 18974735.

26. Bushby AJ, P'ng KMY, Young RD, Pinali C, Knupp C, Quantock AJ. Imaging three-dimensional tissue architectures by focused ion beam scanning electron microscopy. Nat Protoc. 2011;6(6):845-58. doi: DOI 10.1038/nprot.2011.332. PubMed PMID: WOS:000291218300011.

27. Kingsley RE, Cole NL. Preparation of cultured mammalian cells for transmission and scanning electron microscopy using Aclar film. Journal of electron microscopy technique. 1988;10:77-85. doi: 10.1002/jemt.1060100110.

28. Spiegelhalter C, Tosch V, Hentsch D, Koch M, Kessler P, Schwab Y, et al. From dynamic live cell imaging to 3D ultrastructure: novel integrated methods for high pressure freezing and correlative light-electron microscopy. PloS one. 2010;5:e9014-e. doi: 10.1371/journal.pone.0009014.

29. Fricker M, Hollinshead M, White N, Vaux D. Interphase nuclei of many mammalian cell types contain deep, dynamic, tubular membrane-bound invaginations of the nuclear envelope. The Journal of cell biology. 1997;136:531-44. doi: 10.1083/jcb.136.3.531.

30. Malhas A, Goulbourne C, Vaux DJ. The nucleoplasmic reticulum: form and function. Trends in cell biology. 2011;21(6):362-73. doi: 10.1016/j.tcb.2011.03.008. PubMed PMID: 21514163.

31. Bunge RP, Wood P. Studies on the transplantation of spinal cord tissue in the rat. I. The development of a culture system for hemisections of embryonic spinal cord. Brain Research. 1973;57(2):261-76. doi: 10.1016/0006-8993(73)90135-2.

32. Jiménez N, Humbel BM, van Donselaar E, Verkleij AJ, Burger KNJ. Aclar discs: a versatile substrate for routine high-pressure freezing of mammalian cell monolayers. Journal of microscopy. 2006;221:216-23. doi: 10.1111/j.1365-2818.2006.01558.x.

33. Collins JS, Goldsmith TH. Spectral properties of fluorescence induced by glutaraldehyde fixation. The journal of histochemistry and cytochemistry : official journal of the Histochemistry Society. 1981;29(3):411-4. PubMed PMID: 6787116.

34. Hell SW. Far-field optical nanoscopy. Science. 2007;316(5828):1153-8. doi: 10.1126/science.1137395. PubMed PMID: 17525330.

35. Kopek BG, Shtengel G, Xu CS, Clayton DA, Hess HF. Correlative 3D superresolution fluorescence and electron microscopy reveal the relationship of mitochondrial nucleoids to membranes. 2012. p. 6136-41.

36. Watanabe S, Punge A, Hollopeter G, Willig KI, Hobson RJ, Davis MW, et al. Protein localization in electron micrographs using fluorescence nanoscopy. Nature methods. 2011;8:80-4. doi: 10.1038/nmeth.1537.

37. Glauert AM, Lewis PR. Biological specimen preparation for transmission electron microscopy. Princeton, N.J.: Princeton University Press; 1998. xxi, 326 p. p.

38. Gusnard D, Kirschner RH. Cell and organelle shrinkage during preparation for scanning electron microscopy: effects of fixation, dehydration and critical point drying. J Microsc. 1977;110(1):51-7. PubMed PMID: 409847.

39. Mollenhauer HH. Artifacts caused by dehydration and epoxy embedding in transmission electron microscopy. Microsc Res Tech. 1993;26(6):496-512. doi: 10.1002/jemt.1070260604. PubMed PMID: 8305727.

40. Bennett AE, Narayan K, Shi D, Hartnell LM, Gousset K, He H, et al. Ion-abrasion scanning electron microscopy reveals surface-connected tubular conduits in HIV-infected macrophages. PLoS Pathog. 2009;5(9):e1000591-e. doi: 10.1371/journal.ppat.1000591.

41. Felts RL, Narayan K, Estes JD, Shi D, Trubey CM, Fu J, et al. 3D visualization of HIV transfer at the virological synapse between dendritic cells and T cells. Proceedings of the National Academy of Sciences. 2010;107(30):13336-41.

42. Heymann JAW, Hayles M, Gestmann I, Giannuzzi LA, Lich B, Subramaniam S. Site-specific 3D imaging of cells and tissues with a dual beam microscope. J Struct Biol. 2006;155(1):63-73. doi: 10.1016/j.jsb.2006.03.006.

43. Knott G, Marchman H, Wall D, Lich B. Serial section scanning electron microscopy of adult brain tissue using focused ion beam milling. J Neurosci. 2008;28(12):2959-64. doi: 10.1523/JNEUROSCI.3189-07.2008.

44. Merchán-Pérez A, Rodriguez JR, Alonso-Nanclares L, Schertel A, DeFelipe J. Counting synapses using FIB/SEM microscopy: a true revolution for ultrastructural volume reconstruction. Frontiers in neuroanatomy. 2009;3.

45. Wei D, Jacobs S, Modla S, Zhang S, Young CL, Cirino R, et al. High-resolution three-dimensional reconstruction of a whole yeast cell using focused-ion beam scanning electron microscopy. BioTechniques. 2012;53:41-8. doi: 10.2144/000113850.

46. Winter DA, De M, Schneijdenberg C, Lebbink MN, Lich B, Verkleij AJ, et al. Tomography of insulating biological and geological materials using focused ion beam (FIB) sectioning and low-kV BSE imaging. Journal of microscopy. 2009;233(3):372-83.

47. Klionsky DJ, Abdalla FC, Abeliovich H, Abraham RT, Acevedo-Arozena A, Adeli K, et al. Guidelines for the use and interpretation of assays for monitoring autophagy. Autophagy. 2012;8(4):445-544. PubMed PMID: 22966490; PubMed Central PMCID: PMC3404883.

48. Hosseini R, Lamers GE, Hodzic Z, Meijer AH, Schaaf MJ, Spaink HP. Correlative light and electron microscopy imaging of autophagy in a zebrafish infection model. Autophagy. 2014;10(10):1844-57. doi: 10.4161/auto.29992. PubMed PMID: 25126731; PubMed Central PMCID: PMC4198367.

49. de Chastellier C, Thilo L. Cholesterol depletion in Mycobacterium avium-infected macrophages overcomes the block in phagosome maturation and leads to the reversible sequestration of viable mycobacteria in phagolysosome-derived autophagic vacuoles. Cellular Microbiology. 2006;8:242-56. doi: 10.1111/j.1462-5822.2005.00617.x.

50. Gruenberg J, Stenmark H. The biogenesis of multivesicular endosomes. Nat Rev Mol Cell Biol. 2004;5(4):317-23. doi: 10.1038/nrm1360. PubMed PMID: 15071556.

51. Lowe DG. Distinctive image features from scale-invariant keypoints. Int J Comput Vision. 2004;60(2):91-110. doi: Doi 10.1023/B:Visi.0000029664.99615.94. PubMed PMID: WOS:000222967700001.

52. Schindelin J, Arganda-Carreras I, Frise E, Kaynig V, Longair M, Pietzsch T, et al. Fiji: an open-source platform for biological-image analysis. Nat Methods. 2012;9(7):676-82. doi: 10.1038/nmeth.2019. PubMed PMID: 22743772; PubMed Central PMCID: PMC3855844.

53. Thevenaz P, Ruttimann UE, Unser M. A pyramid approach to subpixel registration based on intensity. IEEE transactions on image processing : a publication of the IEEE Signal Processing Society. 1998;7(1):27-41. doi: 10.1109/83.650848. PubMed PMID: 18267377.

# Supporting information

## Seeing a Mycobacterium-Infected Cell in Nanoscale 3D: Correlative Imaging by Light Microscopy and FIB/SEM Tomography

Marianne Sandvold Beckwith1,2*, Kai Sandvold Beckwith3, Pawel Sikorski3, Nan Tostrup Skogaker4, Trude Helen Flo1,2¶ and Øyvind Halaas2¶

[1]Centre of Molecular Inflammation Research, Norwegian University of Science and Technology (NTNU), Trondheim, Norway

[2]Department of Cancer Research and Molecular Medicine, NTNU, Trondheim, Norway

[3]Department of Physics, NTNU, Trondheim, Norway

[4]Department of Laboratory Medicine, Children's and Women's Health, NTNU, Trondheim, Norway

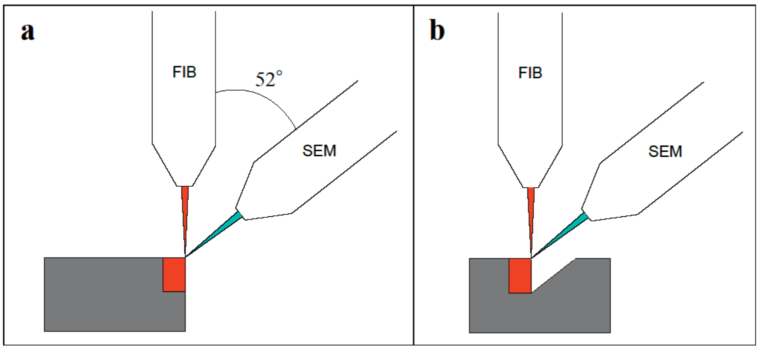

*Fig. S 1:* ***Geometry of the FIB/SEM instrument, and imaging at a flat surface or at a sample edge.*** *In the Dualbeam instrument from FEI used in this study, the electron beam and the ion beam are positioned at 52° tilt compared to each other. During FIB/SEM tomography experiments, the ion beam mills off successive slices at a gracing incidence, while the electron beam images each appearing surface of interest at an angle of 52° compared to the image plane. a) Situation where the region of interest (red) is at a sample edge, and milling and imaging can be started immediately. b) The region of interest is in the middle of a flat surface, and a lot of material needs to be removed before the electron beam can access the whole surface to be imaged. Even more material needs to be removed to avoid shadow effects, because secondary electrons emitted close to a trench wall can be absorbed and will never reach the detector. Trench milling is often done with high ion beam currents to reduce milling time, but this is potentially harmful for the sample.*

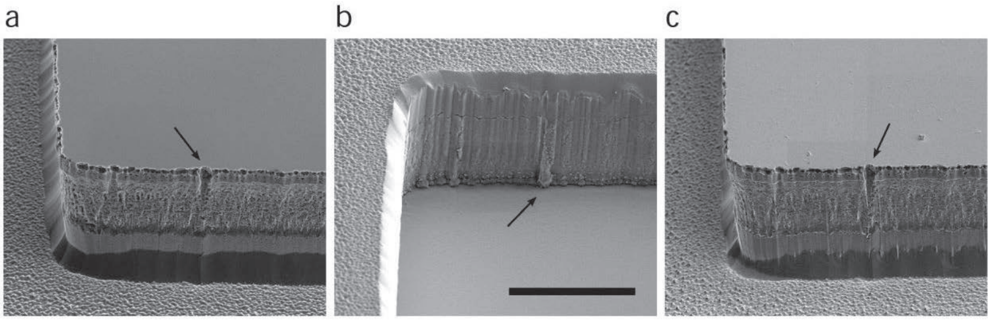

*Fig. S 2:* ***Quality of the master and the moulding process.*** *The master, aclar and final epoxy block were characterized by SEM imaging. SEM imaging was performed at a 52◦ tilt angle in order to better observe edge profiles. a) SEM micrograph of a corner of a protruding square on the silicon master. b) The corresponding well on a patterned aclar substrate. c) SEM micrograph displaying the final small epoxy block after embedding. All features are conserved throughout the moulding process, exemplified by the small notch indicated by the arrow on all images. After epoxy embedding, the microwell geometry enabled access to a large number of cells at these straight, vertical sample edges, which greatly facilitated FIB/SEM tomography when compared to flat monolayers. Scale bar 20 µm.*

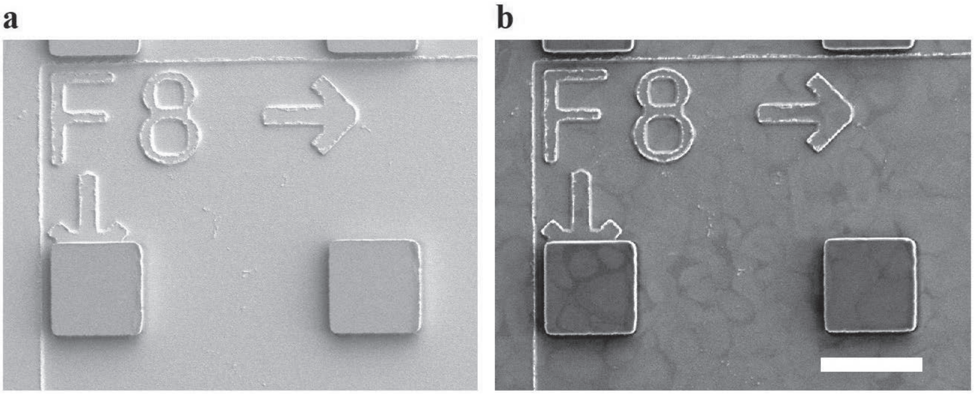

*Fig. S 3:* ***SEM imaging at low and high kV.*** *a) and b) are SEM micrographs collected from the surface of the same epoxy block containing embedded macrophages. a) SEM micrograph collected with an acceleration voltage of 3kV. b) SEM micrograph collected with an acceleration voltage of 15kV. The high acceleration voltage used in in b) allows observing the shape of cells just below the surface, while 3kV imaging (a) only shows the surface topography of the block. Scale bar 100µm.*

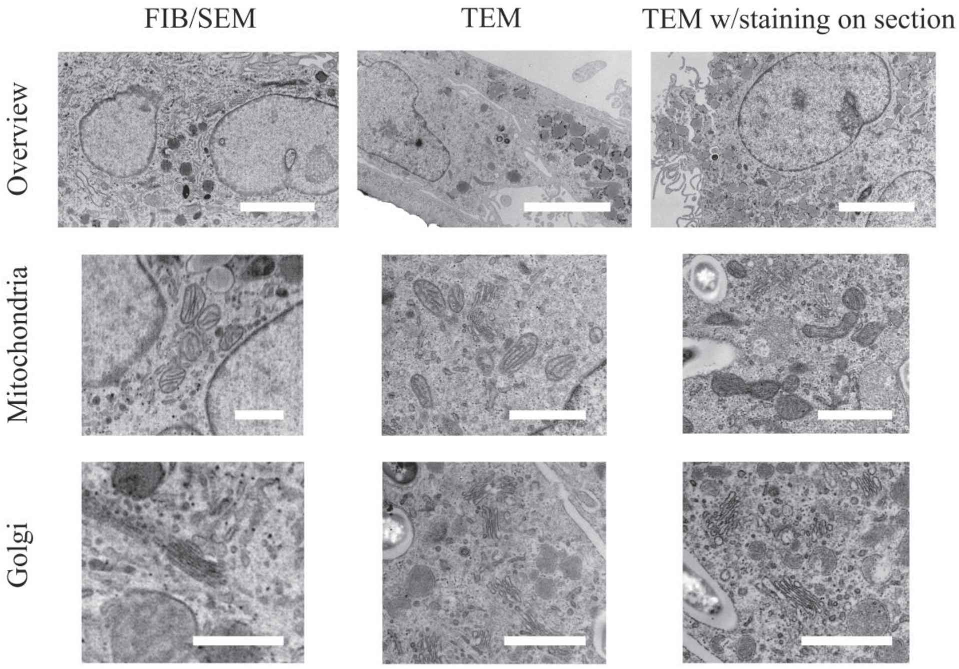

*Fig. S 4:* ***SEM vs TEM Comparison.*** *Two samples with primary human macrophages grown on aclar substrates were prepared in parallel, i.e. with identical conditions for cell growth and sample preparation. One was imaged with SEM during a FIB/SEM tomography experiment (column 1), while the other was sectioned and imaged with TEM, both without (column 2) and with additional staining on the thin sections (column 3). Mitochondria and Golgi are shown as a comparison of the level of detail caught by the two imaging techniques. SEM images all originate from the same tomography data, meaning detail images are cropped out from a larger image of 20 µm x 20 µm. The magnification for the TEM images varies. Scale bars row 1: 5µm, row 2-3: 1µm*

**S1 Video 1.** Video going through all images from the FIB/SEM tomography image stack (in the x-z and y-z planes), before the generation of surfaces from the stack is illustrated. Clearly resolved membranes were used to determine boundaries of the nucleus (blue), a vesicle (yellow) and bacteria (red).

# Paper III

# A Transparent Nanowire-Based Cell Impalement Device Suitable for Detailed Cell–Nanowire Interaction Studies

*Florian Mumm, Kai M. Beckwith, Sara Bonde, Karen L. Martinez, and Pawel Sikorski**

We would like to dedicate this paper to Florian Mumm, who unfortunately passed away just before the paper was submitted for publication. Florian played an essantial role in the research described here and he is greatly missed.

*A method to fabricate inexpensive and transparent nanowire impalement devices is invented based on CuO nanowire arrays grown by thermal oxidation. By employing a novel process the nanowires are transferred to a transparent, cell-compatible epoxy membrane. Cargo delivery and detailed cell-nanowire interaction studies are performed, revealing that the cell plasma membrane tightly wraps the nanowires, while cell membrane penetration is not observed. The presented device offers an efficient investigation platform for further optimization, leading towards a simple and versatile impalement delivery system.*

## 1. Introduction

Cells are the basic functional units of life, and form the components of everything from single- celled bacteria to advanced multi-cellular organisms such as humans. The cell itself is an incredibly complicated system which is able to read, copy and process genetic information, convert chemical energy, perform complex chemical synthesis and communicate with the surrounding environment and neighboring cells. The study of cells to further the biomedical sciences relies on using advanced tools to investigate and perturb single cells and cell colonies. The use of nanomaterials has shown a large promise towards the development of the necessary tools.

Nanomaterials with a high aspect ratio, such as nanowires, nanotubes or nanofibers are regarded as one area of increasing interest.[1] High aspect ratio nanomaterials often show novel properties due to their geometric anisotropy, and can be readily used as probes, needles or sensors by protruding into cells.[2–4] An especially interesting system is that of arrays of vertically aligned nanowires protruding from a flat, cell compatible substrate.[5–7] This geometry allows the combination of detailed high throughput measurements and precise perturbations of cells cultured on such devices. Arrays of high aspect ratio nanomaterials have been used to guide neurons,[8,9] for intracellular electrical access,[10,11] to measure cellular forces,[12,13] localized imaging[14] and to deliver molecules across the cell membrane.[2,3,5,6,15] The latter process is commonly referred to as “impalefection”. The advantages of the impalefection technique include high throughput combined with spatially defined delivery in microarray format, as well as the possibility to transfect typically hard-to-transfect cells such as primary cells.[2]

The efficiency of current impalefection systems varies. Cytoplasmic delivery of many biomolecules has been reported to be highly efficient on arrays of silicon nanowires,[2] while

F. Mumm, K. M. Beckwith, P. Sikorski
Department of Physics
Norwegian University of Science and Technology
Høgskoleringen 5, Trondheim, N-7491, Norway
E-mail: pawel.sikorski@ntnu.no
S. Bonde, K. L. Martinez
Bio-Nanotechnology Laboratory
Department of Chemistry
University of Copenhagen
Universitetsparken 5, Copenhagen, DK-2100, Denmark

DOI: 10.1002/smll.201201314

© 2012 Wiley-VCH Verlag GmbH & Co. KGaA, Weinheim

nuclear delivery and subsequent expression of plasmid DNA has met more limited success. McKnight et al. reported an efficiency below 5% for Chinese hamster ovary cells expressing yellow fluorescent protein after impalement by vertically aligned carbon nanofiber arrays,[15] but improved this to about 50% in later work.[16] Using silicon nanowires, Kim et al. successfully transfected human embryonic kidney cells, although with an efficiency below 1%.[6]

Critical for the successful use of nanofiber or nanowire arrays for biomedical purposes is understanding their interaction with cells. This has been studied in some detail for nanomaterials dispersed in cell medium.[17] Endocytosis appears to be the dominant mechanism of nanomaterial uptake, although endosomal escape of nanowires has been proposed.[18,19] In contrast, approaches using nanowires attached to AFM tips clearly show membrane penetration and quite efficient gene delivery, probably due to the fact that cell penetration speed and applied force can be controlled in these experiments.[20] Han et al., for example, reported success rates of green fluorescent protein expression in adherent human mesenchymal stem cells above 70% using silicon nanoneedles at the tip of atomic force microscope (AFM) cantilevers.[21]

When cells settle on arrays of nanofibers or nanowires the resulting interaction is likely some intermediate between the above extremes. Especially nanowires are often assumed to penetrate through the cell membrane,[2,6] however this currently has not been studied in much detail. Recent experiments show that most nanowires are excluded by the cell plasma membrane when cells settle on nanowire arrays.[22] To improve the usability of impalefection systems, understanding which factors that could allow for successful impalefection is of great importance.

A second issue of the nanowire array systems described above is that they rely largely on the use of microfabrication methods adopted from the electronics industry, used primarily in the production of optical or electronic devices. To produce arrays of vertically aligned nanowires, vapor-liquid-solid-type growth from catalyst seed particles or anisotropic etching is usually preferred.[23] The substrates involved are typically semi-conductors, which are often expensive, non-transparent, hard and brittle. Cell culture substrates are commonly made from plastics or glass and are, thus, often analyzed optically through the bottom. Additionally, due to the strict needs for cleanliness and sterility, cell biology relies almost exclusively on disposable, single use materials. This indicates the advantages of inexpensive and transparent devices for aims in cell biology outside of proof of concept experiments.

Here, we present a low-cost, disposable and cell-culture compatible impalefection device with nanowires extending from a transparent epoxy membrane. We demonstrate that the device is suitable for both upright light microscopy and inverted light microscopy through the transparent substrate. As the nanowire device consists mainly of polymers, microtomy slices for transmission electron microscopy (TEM) could be made of the entire device with cells. Taking advantage of this versatility, we combine high-magnification TEM investigation with light microscopy to investigate the detailed interface between the nanowires and the cells on the device.

## 2. Results and Discussion

### 2.1. Device Fabrication

We propose a novel fabrication approach, in which nanowires grown on a flat surface are incorporated in a polymer membrane in a relatively easy and highly reproducible process. Since this fabrication approach likely can be applied to other nanowire systems, it is important to explain the main steps of the process, in addition to the technical details given in the Experimental Section. **Figure 1** illustrates the main steps of the device fabrication process, together with scanning electron microscopy (SEM) micrographs and photographs of the device at different stages.

The basis for the impalement device is a dense array of copper oxide nanowires, which can be produced in a catalyst-free thermal oxidation reaction when heating copper substrates in air.[24] After the oxidation, the CuO nanowires form the top part of a Cu/$Cu_2O$/CuO layer system. We have recently developed a simple method to produce homogeneous $cm^2$ sized arrays of such CuO nanowires.[25] The nanowires were up to 10 µm long with a diameter varying broadly around 100 nm.

As CuO is dissolvable in cell culture medium such as DMEM and as the resulting free copper ions are toxic to cells,[26] the nanowires were passivated with an about 10 nm thick layer of silicon oxide deposited by DC sputtering (see Supporting Information (SI), S1 and S2).[27] In order to control the nanowire density and to introduce a suitable surface for the later separation of the nanowires from their substrate, a layer of poly(methyl methacrylate) (PMMA) was then spin coated on the nanowire array. As shown in the second row of Figure 1, this bent many nanowires towards the substrate and incorporated them into the PMMA. Next, a thin PDMS layer was deposited on the sample by spin coating it with a solution of 10% PDMS in tert-butanol.[28] In general, the adhesion between PMMA and PDMS is poor and the layers easily separate upon heating and cooling.[29] In our fabrication process, we did not observe any detachment of the layers at this point in the fabrication process, probably because they are stapled together by the nanowires. The spinning of PDMS also introduced a thin PDMS layer around the nanowires (SI, Figure S1.2b). This layer was subsequently transformed to a silica-like material by exposing the PDMS to oxygen plasma.[30] The higher surface energy introduced by the oxygen plasma made it possible to spin an SU-8 layer onto the device, providing a rigid substrate for cultured cells (third row of Figure 1). Finally, a longer oxygen plasma treatment was employed to remove any residual SU-8 sticking to the wires and to render the SU-8 hydrophilic. Plasma treated SU-8 has been shown to remain both hydrophilic and cell compatible for extended periods of time.[31,32]

In order to transfer the nanowire arrays from the non-transparent copper-based substrate to glass, the water-soluble mounting adhesive Crystalbond 555 was cast on top of the SU-8 layer as illustrated in the fourth row of Figure 1. With the adhesive on, a weak mechanical force applied to the Crystalbond by e.g. cutting it with a scalpel split the samples at

© 2012 Wiley-VCH Verlag GmbH & Co. KGaA, Weinheim

DOI: 10.1002/smll.201201314

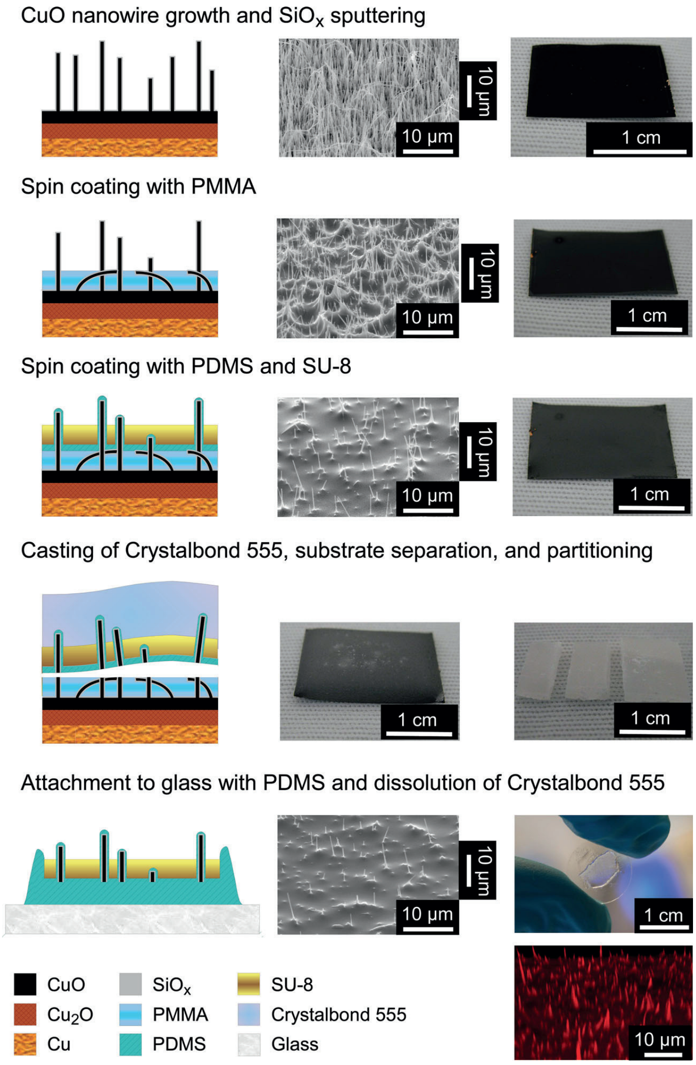
CuO nanowire growth and $SiO_x$ sputtering
10 µm
10 µm
1 cm
Spin coating with PMMA
10 µm
10 µm
1 cm
Spin coating with PDMS and SU-8
10 µm
10 µm
1 cm
Casting of Crystalbond 555, substrate separation, and partitioning
1 cm
1 cm
Attachment to glass with PDMS and dissolution of Crystalbond 555
10 µm
10 µm
1 cm
10 µm
CuO
$SiO_x$
SU-8
$Cu_2O$
PMMA
Crystalbond 555
Cu
PDMS
Glass

**Figure 1.** Illustration of the most important fabrication steps of the device. Left: scheme, centre: SEM image, right: photograph (except for the gluing and separation step, where photographs before and after separation and partitioning are shown). The vertical scale bar has been adjusted for sample tilt during imaging. Bottom right: 3D reconstruction of a confocal stack of Alexa 633-labeled nanowires.

the PMMA/PDMS interface (see also SI). The top part of the sample containing the nanowire-penetrated PDMS and SU-8 as well as Crystalbond adhesive was then attached to a glass substrate using PDMS, and the Crystalbond 555 was dissolved in hot water (Figure 1, fifth row). Samples prepared for transmission electron microscopy (TEM) were instead placed on a drop of epoxy which subsequently cured before removing the wax. This ensured that the entire structure was made out of polymer, facilitating sample preparation for TEM.

Finally, an amino-silane layer was assembled on the nanowires (and the substrate, as both the silica-covered nanowires and the SU-8 substrate itself were silanized). This activates the surface for electrostatic adsorption of negatively charged biomolecules such as plasmid DNA. Directly visualizing the nanowires was possible by covalently coupling a fluorescent dye such as Alexa633 to the aminosilanes on the surface (Figure 1 bottom right). On the final device protruding nanowire lengths are on the order of 0.5 µm to 5 µm and diameters are about 100 nm to 150 nm.

### 2.2. Cell Viability and Morphology on Nanowire Devices

For experiments with cells, human cervical cancer cells (HeLa cells) or human embryonic kidney cells (HEK293) were cultured on nanowire devices attached to glass. The devices showed good transparencies and could be used in inverted optical microscopes to image live cultured cells through the device (**Figure 2**). The polymer layers of the samples were not totally flat due to the roughness induced by the nanowires, so confocal microscopy was beneficial for high resolution imaging.

To assess the cell compatibility of the device HeLa cells were imaged 1 and 4 days after seeding (**Figure 3**a–d). The cells were labeled with calcein-AM, which is rendered fluorescent by enzymatic cleavage in live cells. Non-viable cells with a compromised plasma membrane were detected using propidium iodide. It is apparent that the cells have comparable survival rates as control cells cultured on glass (Figure 3e). The difference in cell coverage of the surface between 1 and 4 days arises from an extended period of cell division. A quantitative cell viability assay was not performed, as cells growing outside the nanowire array could influence these results. Cell spreading on the nanowire surfaces is similar to cells cultured on flat SU-8 (Figure 3b, d, f), indicating that the cells are not excessively perturbed by the presence of the nanowires. Cells were seen to interact with nanowires in their periphery as the spread out (SI, Section S3). Additionaly, HeLa and HEK293 cells were cultured on the device and transiently transfected with a plasmid coding for a membrane protein by calcium phosphate precipitation (SI, Figure S3). The membrane protein was labeled through its extracellular SNAP-tag and a clear signal was observed from the cell plasma membrane, demonstrating functional gene expression and membrane protein localization in the cultured HeLa and HEK293 cells.

DOI: 10.1002/smll.201201314
© 2012 Wiley-VCH Verlag GmbH & Co. KGaA, Weinheim

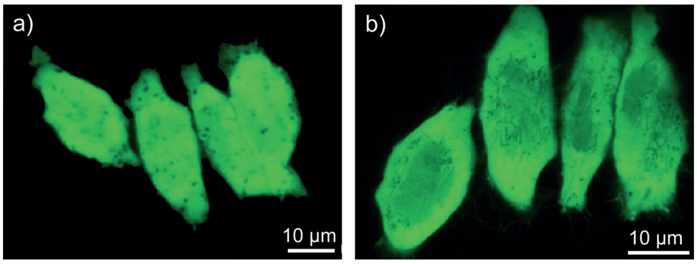

Figure 2. (a,b) Images of the same GFP expressing cells on nanowire surface. a): imaged from the bottom through the device, and b): imaged from the top. Nanowires are visible as black dots in the green cell cytosol.

### 2.3. Nanowire-Mediated Delivery

To investigate possible uptake of cargo, cells were seeded on nanowire devices on which plasmid DNA (pDNA) had been deposited. In a first experiment, the plasmids were fluorescently labeled with YOYO-1. After one day, the cells were detached from the nanowire surface by trypsin-EDTA treatment and reseeded on glass for one more day. This procedure is necessary to avoid the high fluorescent background of the original sample due to the deposited fluorescent material. **Figure 4**a shows how the fluorescent DNA has been internalized by the reseeded cells. This is in agreement with observations with previously published nanowire arrays.[2] However, when the same surface functionalizations, cargo concentrations, and cell seeding procedures were employed to cells on glass slides, similar delivery results could be obtained (Figure 4b). In both cases the number of cells with internalized fluorescent material was 80–90%, however the amount or pathway of internalized material might be different, this is under investigation in our lab. This control experiment has not been done in previous attempts of nanowire array mediated transfection, where delivery in solution was used as control instead.[2,33] The real delivery percentage might be higher, as it is challenging to distinguish between cells that came from the nanowire surface with deposited material and cells from outside this area (flat surface with no plasmid) prior to reseeding.

From microinjection experiments it has been observed that only a very small fraction of plasmid DNA introduced to the cytoplasm actually reaches the nucleus and becomes transcribed.[34–36] This low efficiency is attributed to the

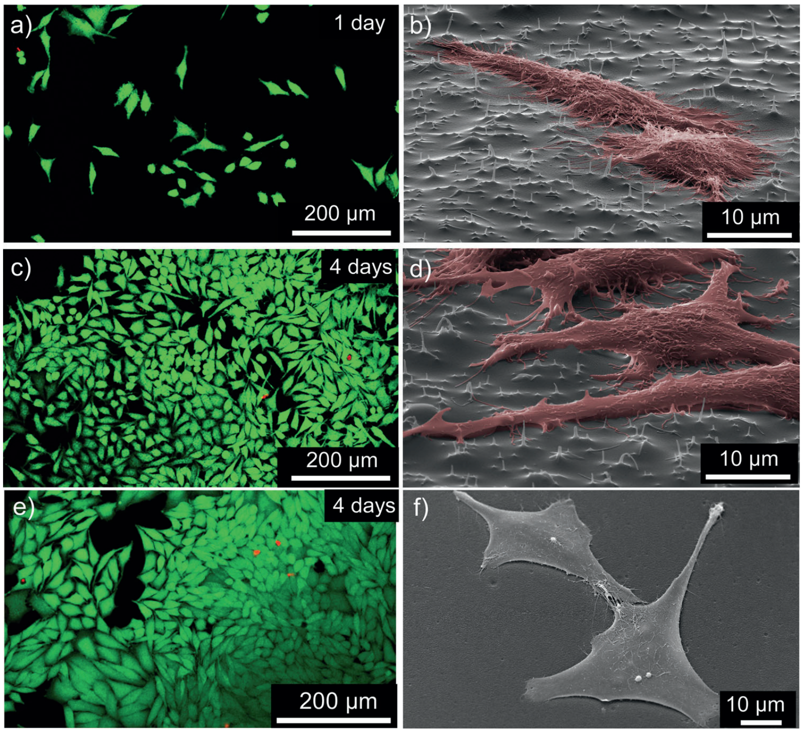

Figure 3. HeLa cells cultured on a–d): the nanowire impalement device, e): glass cover slips, and f): flat SU-8. a,b,f): for 1 day, c–e): for 4 days. The confocal micrographs (left) are of live cells stained with calcein-AM and propidium iodide, while the SEM micrographs (right) are of fixed, dehydrated cells.

© 2012 Wiley-VCH Verlag GmbH & Co. KGaA, Weinheim

DOI: 10.1002/smll.201201314

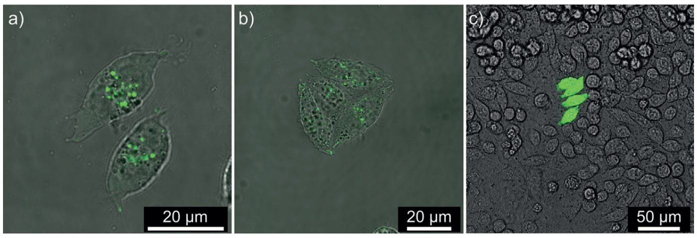

**Figure 4.** (a,b,c) Cargo delivered into HeLa cells, brightfield micrographs with green fluorescence overlay. a): Uptake of labeled plasmid DNA in cells grown on nanowires, then trypsinated and reseeded on glass, b): Uptake of labeled plasmid DNA from a flat glass surface functionalized in the same way as the nanowires after trypsination and reseeding of the cells, c): Expression of GFP in transfected cells imaged directly on the nanowires.

dependency of the pDNA to be actively transported to the nucleus,[37] to then actively cross the nuclear envelope,[38] and to avoid degradation by cytosolic nucleases in the meantime.[39] In order to find out to which extent the delivered plasmids actually are able to reach the nucleus and get transcribed, cells were seeded on nanowires with deposited unlabeled EGFP plasmids and grown on these arrays for two days. As illustrated in Figure 4c, expression of EGFP could only be observed in isolated small spots, probably originating from single EGFP-expressing cells that then underwent cell division. The global efficiency was below 1%, similar to previous results on Si nanowires,[6] although this is still higher than on glass, where no EGFP expression was observed on delivery attempts.

### 2.4. Cell-Nanowire Interactions

To better understand the interaction between the cells and the nanowires, SEM, confocal fluorescence microscopy and TEM was performed on the device with cultured HeLa and HEK293 cells.

SEM could be used to observe cells cultured on the nanowire surfaces as shown in Figure 3b,d. Closer investigations showed that the protruding nanowires regularly seemed to be covered by a membrane (SI, Figure S3.1), although the limited penetration depth of the SEM did not allow further investigations into the detailed interaction.

Confocal microscopy of live HeLa cells reveal the nanowires as dark shadows against the homogeneous intracellular fluorescence from calcein-AM (**Figure 5**a). Cross-sections of confocal stacks show how the nanowires penetrate out from the substrate and are in close contact with the cells (Figure 5b). Similar results were observed for cells cultured on Alexa633-labeled nanowires (Figure 5c). In this case, the nanowires are directly visible also outside of the cells. In both cases no propidium iodide signal is visible in these cells despite the apparent nanowire penetration, indicating an intact cell membrane. These results are in agreement with previously published results for alternative impalement systems,[6,7,15] which also observe the nanowires as dark shadows against similarly labeled cells without impacts on cell viability or membrane integrity.

To further elucidate the mode of interaction between the cells and nanowires a recently developed method[22] was used to reliably and clearly label the plasma membrane of HEK293 and HeLa cells cultured on the nanowire device (**Figure 6**a and SI, Figure S3.4). After plating on the nanowire device, the cells were transiently transfected with a plasmid coding for a membrane protein fused to an extra-cellular SNAP-tag. The SNAP-tag was covalently labeled with cell-impermeable substrate BG547, allowing specific visualization of the plasma membrane of live cells (Figure 6ai and SI, Figure S4a). As before, labeled nanowires were observed to penetrate into the cell interior (Figure 6a-ii and a-iii). However, in all cases there was a clear signal from the plasma membrane observed together with the nanowires (Figure 6a-ii and a-iv). This demonstrates that the nanowires in fact do not penetrate the plasma membrane, but rather that the cell tightly conforms around the protruding nanowires. These results are in good agreement with recent results obtained on InAs nanowires of various lengths and densities interfaced with HEK293 cells.[22] Further support for this was observed by visualizing the actin filament of fixed HeLa cells (Figure 6b and SI, Figure S4b). In most cases there was an increased actin signal at the location of the nanowires. Actin is known

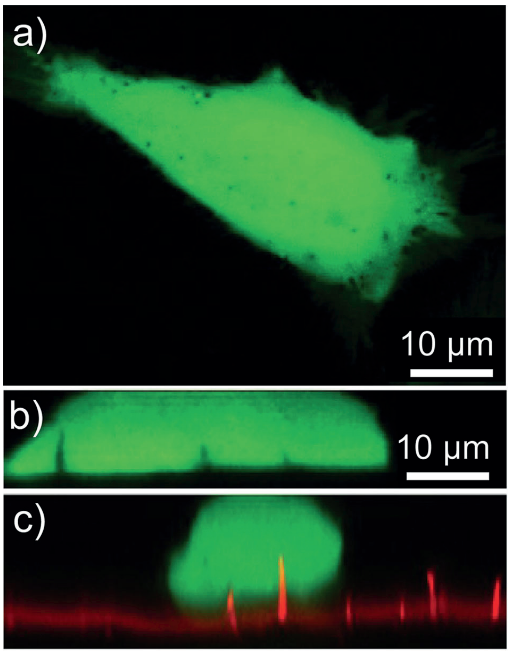

**Figure 5.** a): confocal micrograph of a cell with nanowires visible as black shadows; b,c): cross sections through a cell with (b) unlabeled and (c) Alexa633-labeled nanowires.

© 2012 Wiley-VCH Verlag GmbH & Co. KGaA, Weinheim

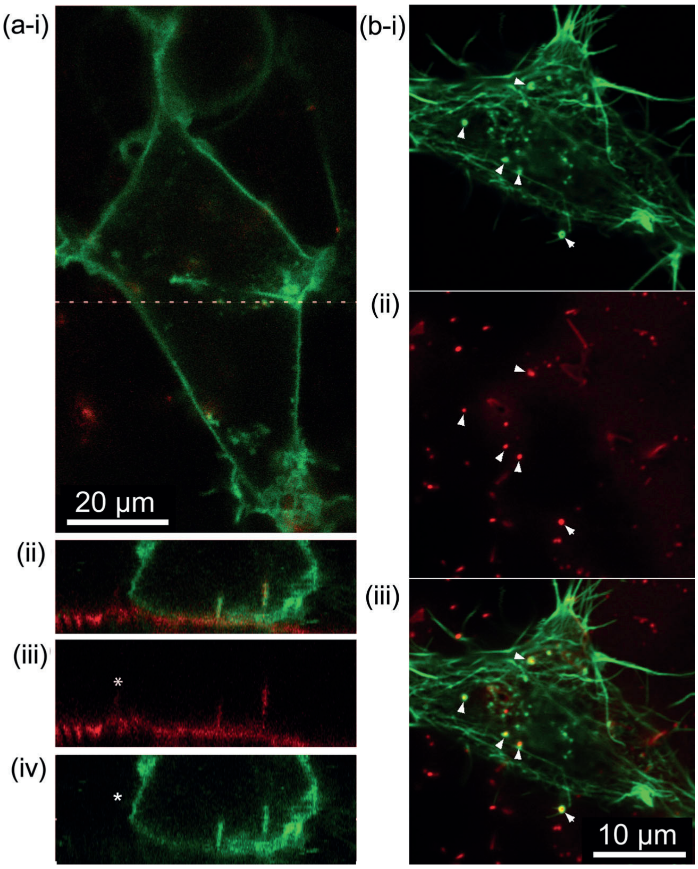

Figure 6. (a,b): Interactions between labeled nanowires and cell plasma membrane (a) and actin filaments (b). (a): HEK293 cells successfully express a SNAP-tagged membrane protein that is covalently labeled (i, green) on Alexa633-labeled nanowires (i, red). (ii–iv): Cross section through the cell (white dashed line in (i)) shows the presence of NWs (iii) within the cell. However, the nanowires co-localize with the membrane (iv). The membrane label shows no non-specific binding to NWs outside cells (iv, asterisk). (b): Confocal micrograph showing co-localization between phalloidin-labeled actin filaments (i, green), Alexa633-labeled nanowires (ii) and overlay (iii, green and red) in fixed HeLa cells. Positions of several intracellular nanowires which show co-localization with actin are indicated with white triangles.

to be involved in processes associated with restructuring of the plasma membrane, including many forms of endocytotic uptake.[40] Similar colocalization has been observed by, e.g., Persson et al., for cells cultured on silica nanotubes.[41]

To further characterize the effects of the nanowires within the cells with the necessary resolution to determine the detailed intracellular organization, nanowire devices with cultured HeLa cells were prepared for and investigated by TEM. The TEM samples were prepared as thin cross-sections perpendicular to the device surface, with the nanowires protruding upwards into the cultured cells. In contrast to other nanowire impalement systems, this can be performed directly after cell embedding with our device since it is made up of soft, polymeric materials. The outer cell membrane, the nucleus as well as different compartments in the cell could be clearly visualized using this technique due to selective membrane staining using standard TEM sample preparation protocols (see **Figure 7** and Experimental Section). Investigations of the cell-nanowire boundary typically showed that the wires were surrounded by the cell plasma membrane, in agreement with the results from the fluorescent plasma membrane label above. Whereas such a membrane may be expected for nanowires at the periphery of the cell (Figure 7b), i.e., nanowires like those in SI, Figure S3.1a or which the cell encountered while spreading out horizontally on the surface, it was also observed for nanowires located centrally, e.g., directly below the nucleus as shown in Figure 7d. Indeed, the nucleus can often be seen to bulge around the nanowires, indicating that the nanowires are also excluded from the cell nucleus.

In Figure 7c possible formation of vesicles at the location of the nanowire in the cell is also observed. For endocytosis, it has been suggested that both the substrate topography[42] and the local membrane curvature[43] play key roles in its regulation. For the nanowire decorated surfaces this might result in upregulated endocytotic uptake due to the constantly high membrane curvature around the wires exactly at the location of maximum cargo concentration. This is a mechanism that could account for increased nanowire-mediated delivery efficiency observed by other groups,[2] and also the small increase in plasmid expression efficiency observed on nanowire surfaces in this work.

Of course, it remains to be seen to which extent the observed interactions are a special case for the device or the nanowire density presented here. Compared to previously described devices, our nanowires are for instance not always perpendicular to the underlying substrate and have a different tip geometry, which both might influence their interactions with cells. The nanowire density is rather at the lower end compared to previous systems, although such densities have been used before e.g. with rat hippocampal neurons, human fibroblasts[2] and dendritic cells.[33] However, indirect evidence for close cell interactions without direct membrane penetration as we observe has been reported by the group of H. Park in a follow-up study to their 2010 article,[2] where Si nanowires were used as electrical interfaces to HEK293 cells and neurons.[11] The nanowires were used in arrays of nine wires per electrical contact. Even though the electrical response from the group of wires indicated a direct electrical contact between the electrode and the interior of the cell in

© 2012 Wiley-VCH Verlag GmbH & Co. KGaA, Weinheim

DOI: 10.1002/smll.201201314

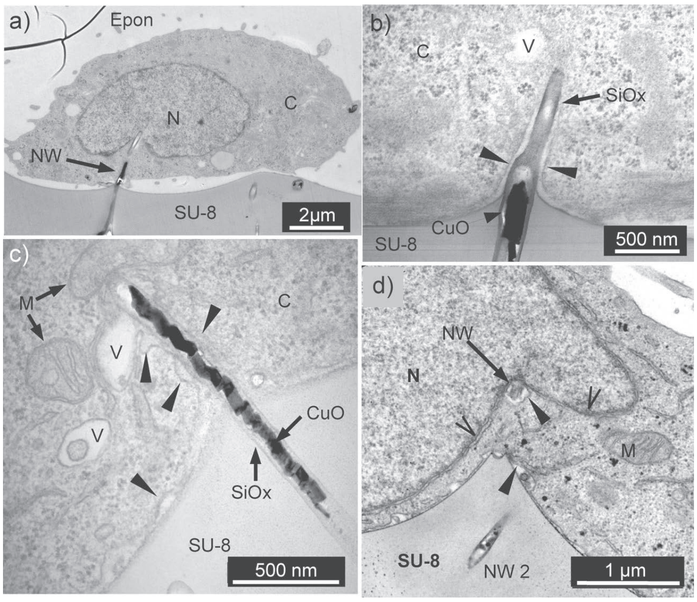

**Figure 7.** TEM micrographs of 70 nm microtomy sections HeLa cells on the nanowire devices a): Overview of a cell with the device surface (SU-8), a nanowire (NW), the cell's cytoplasm (C) and nucleus (N) clearly visible, embedded in Epon epoxy. b): Membrane-covered nanowire at the cell's periphery, membrane is indicated by closed triangles. Also visible is a vesicle (V) and the core (CuO) and shell (SiOx) of a section of the nanowire. Note that due to a slight tilt of the nanowire compared to the microtomed slice, only part of the dark CuO of the wire is visible. c): Nanowire in center of cell showing possible induction of a endocytotic vesicle (V). Cell organelles such as mitochondria (M) are also visible, d): Slanted section of a nanowire directly below the nucleus (N), showing clear bulging of the nuclear membrane (open triangles) and signs of the outer cell membrane (closed triangles) around the nanowire (NW).

more than half of the cases, the electrical signal decreased over the course of a few minutes in experiments without constant current flow at the nanowire tips. This was attributed to the partial recovery of the permeabilized membrane and required a re-permeabilization by a short voltage pulse. For the case of direct penetration a recent article by Van Der Sarl et al.[3] investigating delivery through 100 nm nanostraws estimate a membrane penetration chance of roughly 1–10% per nanostraw. Although our investigations have not revealed evidence of spontaneous membrane penetration, more extensive observations must be made before the different observations can be explained.

## 3. Conclusion

In this article a fabrication scheme was presented, which allows the production of transparent and inexpensive cell impalement devices suitable for investigations both in standard upright and inverted optical microscopy set-ups as well as by SEM and TEM. In contrast to similar systems fabricated with traditional microfabrication techniques and materials, only comparatively cheap copper foils and polymeric materials are used. The only instruments needed are a bench top oven, sputter coater, a spinner, a hot plate, a plasma cleaner, and a source of UV light. Providing cheap and simple methods to make novel functional devices is important for their wider utilizations in cell biology, as cell culture substrates are commonly disposed after use. Additionally, as the devices are easily producible in large quantities, they are suitable for the development of improved designs or more efficient cell impalement procedures by using "trial and error" problem solving strategies. Cells were observed to have similar growth characteristics on the devices as on glass and SU-8 control surfaces, and inducing gene expression using typical transfection was possible. Nanowire mediated delivery of material and expression of nanowire-delivered plasmids was observed, although the latter was at low efficiencies. Detailed investigations were performed into the interactions between the cultured cells and the nanowire surfaces, and notably it was possible to produce samples suitable for detailed investigation by TEM. Confocal microscopy and preliminary TEM data obtained for HEK293 and HeLa cells cultured on the devices show that both the outer cell membrane and nuclear membrane typically excluded the nanowires from the cell interior. To produce an efficient delivery device, breaching these barriers in a non-invasive way is a major goal and attempts are underway in our laboratory. The presented system serves as a valuable tool as it combines a high availability of impalement devices with the possibility to observe the cell-nanowire interactions in great detail.

## 4. Experimental Section

*$SiO_x$/CuO Nanowire Array Synthesis:* Copper foils (25 µm, 99.98% pure, Sigma Aldrich) were used as base materials for the nanowires. The foils were cleaned and oxidized using a previously described procedure.[24] Briefly, they were cleaned in subsequently 2 M HCl, water, acetone, and ethanol in an ultrasonic bath and dried with a wipe. They were then folded around glass slides and oxidized in a preheated Carbolite CWF 1200 laboratory oven at 500 °C for 2 h. Aluminum foil could be used as intermediate layer between the foils and the glass slide in order to prevent the foils sticking to the glass after oxidation. After oxidation, the foils could be handled with tweezers and were wetted with ethanol and cut to suitable sizes for the production of devices, commonly a few centimetres in length and width. The ethanol was used to reduce detachment of the oxide layers from the foils at the cutting lines (as detachments can occur, this should be done in a fume hood). The wire density of the oxidized samples can be estimated from their color with very black samples having a high density of nanowires. As the nanowires diffract light differently than the substrate, they

DOI: 10.1002/smll.201201314
© 2012 Wiley-VCH Verlag GmbH & Co. KGaA, Weinheim

can be seen in an optical microscope as shown in SI, Figure S1.1 in the Supplementary material. This makes it easy to control and observe their density during the different process steps. Adopting a previously published procedure,[25] the foils were then sputter coated using a custom made p-Si target in a Cressington 308R DC magnetron sputter with a 100 W plasma source at 0.01 mbar argon and 80 mA for about 4 min. This introduced an about 10 nm thick $SiO_x$ layer around the wires (see SI Section S1).

*Device Fabrication:* Next, 950 PMMA A9 (MicroChem) was spun at 3000 rpm for 90 s followed by a baking step on a hotplate at 180 °C for 5 min. The PDMS layer was made by spinning PDMS (Dow Corning Sylgard 184, mixed in a 10:1 ratio, diluted to 10% in tert-butanol)[26] at 6000 rpm for 90 s. It was not yet cured, but instead plasma cleaned in a Diener Electronics Femto plasma cleaner at 50 W and 0.6 mbar $O_2$ pressure for 12 seconds. Then SU-8 2 (MicroChem) was spin coated at 5000 rpm for 90 s and soft baked according to the manufacturer's instructions (on a hotplate at 65 °C and 95 °C for 1 and 3 min, respectively). It was then flood exposed with about 300 mJ $cm^{-2}$ in a Karl Suss MJB3 mask aligner (intensity measured at 365 nm [i-line]). The SU-8 was post-exposure baked at 65 °C and 95 °C for 1 min each and plasma cleaned at 100 W and 0.8 mbar $O_2$ pressure for 5 min.

To separate the nanowires, SU-8 and PDMS from the substrate, the samples and Crystalbond 555 (SPI Supplies) were warmed to 95 °C. The Crystalbond was then cast onto the samples. When carefully applied, it did not spill from the sample due to its surface tension. The samples with the adhesive were then allowed to cool for 10 min during which the Crystalbond hardens. Finally, separation was achieved by cutting along the edges of the sample and by sectioning it in the desired device sizes for cell culture. The actual separation is probably introduced by sheer forces applied to the adhesive. If the layer did not separate by cutting alone, they were separated with tweezers or by using sticky tape to peel off the backside. Separation at the correct interface is visible in the optical microscope as a flat layer instead of the more fractal pattern of the wax (SI, Figure S1.3).

The samples were then pressed with the Crystalbond facing up and the PDMS facing down in a small drop of uncured PDMS sitting on a glass cover slip. The PDMS was allowed to cure at 45 °C overnight after which the wax was dissolved in 75 °C warm MQ-water. For TEM experiments a small drop of epoxy on a cured sheet of PDMS was used as a carrier for the device instead of glass. After curing the epoxy, the device could be removed from the PDMS and processed further as usual.

*Surface Functionalization and Labeling:* The surfaces of the nanowires (and the substrate) were functionalized by incubating them in a solution of (3-trimethoxysilylpropyl) diethylenetriamine (1% v/v) in MQ-water for 10 min followed by washing in water and ethanol. To fluorescently label the nanowires fresh solutions of N-(3-dimethylaminopropyl)-N-ethylcarbodiimide hydrochloride (EDC, 0.4M, Sigma-Aldrich) and N-hydroxysuccinimide (NHS, 0.1M, Sigma-Aldrich) were made in MQ-water and mixed with each other and an equal volume of 10 µg $mL^{-1}$ Alexa633 (Invitrogen) in MQ-water. The sample was incubated in this solution for 30 minutes before being rinsed thoroughly in MQ-water and blown dry with compressed air.

*Cell Culturing:* Human cervical cancer cells (HeLa) and HEK293 cells were grown in DMEM (Gibco, Invitrogen) supplemented with 1 mM nonessential amino acids (Gibco, Invitrogen), 10% FBS (Gibco, Invitrogen), and 1 mM L-glutamine (Sigma Aldrich). The cells were cultivated at 37 °C in a humidified atmosphere with 5% $CO_2$, and passaged regularly. For cell culture experiments, the samples were sterilized in 70% ethanol on a sterile bench and allowed to dry. The samples were then placed in 24-well plates. For experiments with HeLa cells, 20 000 cells were seeded into each well in 0.5 mL of cell medium. For transfection and delivery experiments, pmaxGFP plasmid (Lonza) or YOYO-1 iodide (Invitrogen) labeled pWIZ-luciferase plasmids were diluted to 100 µg $mL^{-1}$ in PBS. 10 µL of this solution was placed on each sample and allowed to dry. Then 20 000 HeLa cells in 20 µL of cell medium were seeded onto the samples and allowed to adhere for 30 min, before 0.5 mL of cell medium was added. This was done to increase the number of cells exposed to the nanowire-covered surface (which only fills a part of the well), while keeping the overall cell density the same as control wells. Identical procedures were used for delivery from glass control surfaces. For replating experiments the cells were cultured for 24 h, and then rinsed before 0.5 mL of trypsin/EDTA (0.25%/0.2 mM) solution was added to the well with the sample and incubated for 10 min at 37 °C. The cells were then transferred, pelleted and suspended in cell medium and reseeded on a glass cover slip. For SNAP-KOR transfected HEK293 and HeLa cells, 120 000 cells were seeded in each well in cell medium containing 10% fetal bovine serum. The transfection of the cells with DNA for a membrane protein with an extracellular SNAP-tag has been described elsewhere.[7]

*Live Cell Imaging:* For live/dead observations 1–4 days after seeding, the cells were rinsed in warm PBS, and incubated in a 1 µM solution of Calcein-AM (Sigma Aldrich) in DMEM for 45 min at 37 °C. The last 10 min 25 mg $mL^{-1}$ propidium iodide in PBS was added. The slides were transferred into a thin-bottom dish containing warm PBS. Delivery to cultured cells was monitored after 2 days (for pmaxGFP expression), or 24 hours after replating (YOYO-labeled plasmid delivery). Imaging was done with a Leica TCS SP5 confocal microscope at room temperature using 488 nm excitation and emission collected at 500–550 nm (calcein/pmaxGFP/YOYO-1) or 600-650 nm (propidium iodide). A total of 31 cells from glass surfaces and nanowire surfaces were analyzed for uptake of YOYO-1 labeled plasmid. All images were analysed and prepared using NIH ImageJ (http://rsbweb.nih.gov/ij/).

*Imaging of Transfected HEK293 and HeLa Cells:* At 24 h after transfection, the membrane and cytosol of the cells were labeled and imaged by confocal microscopy as described elsewhere.[22] The Alexa633 fluorophore on the nanowires was excited at 633 nm, and emission collected at 653–800 nm. A total of 37 nanowires in 19 HEK293 cells on 2 samples and 68 nanowires in 24 HeLa cells on 2 samples were analyzed for colocalization with the cell membrane label.

*Actin Staining and Imaging:* 1 day after cell seeding on the Alexa633-labeled nanowire surfaces the samples were rinsed in PBS, then incubated in paraformaldehyde (4%) in PBS at room temperature for 15 min and rinsed. The cells were then permeabilized for 3 min in Triton X-100 (0,1%, Sigma Aldrich) and rinsed before 165 nM Alexa488-phalloidin (Invitrogen) in PBS was applied to the device. After 30 min the samples were rinsed in PBS and transferred to fresh PBS for imaging as above. A total of 143 nanowires inside 13 cells were analyzed for colocalization between nanowires and actin filaments.

© 2012 Wiley-VCH Verlag GmbH & Co. KGaA, Weinheim

DOI: 10.1002/smll.201201314

*SEM Imaging:* For observations using SEM, the samples were rinsed in PBS and fixed in 2.5% glutaraldehyde in Sørensen's phosphate buffer for a minimum of 2 h at room temperature or overnight or longer at 4 °C. They were then dehydrated by incubating for 3 min in PBS, water, solutions of increasing ethanol concentration in water, 2 times absolute ethanol and finally 2 times in hexamethyldisilazane (HMDS, Sigma Aldrich) from which the samples were dried in a fume hood.[44] 8 nm gold or platinum/palladium was sputtered on the samples to render them conductive. Imaging was done with a Zeiss Ultra, Zeiss Supra, or Hitachi S-5500 S(T)EM.

*TEM Imaging:* For observations using TEM, the samples were fixed as above, rinsed thoroughly in 100 mM HEPES buffer, then postfixed and stained for 2 h in 2% osmium tetraoxide and 1.5% hexacyanoferrate in HEPES. They were then rinsed thoroughly in HEPES buffer and dehydrated in a series of 50%, 70%, 90%, 2 times 100% ethanol and 2 times 100% propylene oxide for 5 minutes each, then infiltrated with epoxy by incubating in 30% Epon epoxy resin in propyleneoxide, 70% Epon epoxy resin, and 100% Epon epoxy resin for 30 min each, before changing to fresh 100% Epon epoxy resin and leaving the samples on a rotator overnight. The samples and resin were finally cast into a silicone mold and cured for 3 days at 60 °C. TEM sections of the block were made with a microtome, transferred to a formvar-coated nickel TEM grid, and contrasted further in 2% uranyl acetate and Reynold's lead citrate. 70 nm microtomed slices of the samples were imaged with a FEI Tecnai 12 TEM at 80 kV. The $SiO_x$ coated nanowire in SI, Figure S1.2a was imaged with a Philips CM30 at 150kV.

## Supporting Information

*Supporting Information is available from the Wiley Online Library or from the author.*

## Acknowledgements

*F. M. and K. M. B. contributed equally to this work. For financial support, we thank NTNU, NTNU NanoLab, NorFab, the Danish Agency for Science, Technology and Innovation (The Danish Council for Strategic Research and The Danish Natural Science Research Council), and UNIK Synthetic Biology. We would also like to thank E. Rogstad for fabricating a p-Si target, K. Sæterbø for assistance with cell culturing and N. Skogaker for assistance with TEM sample preparation and imaging. Various researchers are thanked for their part in the scientific discussions in this article including from NTNU S. Lelu, S. Strand, A. Lægreid and C. Fjeldbo and from Harvard University A. Shalek.*

---

[1] P. Yang, R. Yan, M. Fardy, *Nano Lett.* **2010**, *10*, 1529–1536.
[2] A. K. Shalek, J. T. Robinson, E. S. Karp, J. S. Lee, D. R. Ahn, M. H. Yoon, A. Sutton, M. Jorgolli, R. S. Gertner, T. S. Gujral, G. MacBeath, E. G. Yang, H. Park, *Proc. Natl. Acad. Sci. USA* **2010**, *107*, 1870.
[3] J. J. Vandersarl, A. M. Xu, N. A. Melosh, *Nano Lett.* **2012**, *12*, 3881–3886.
[4] R. Gao, S. Strehle, B. Tian, T. Cohen-Karni, P. Xie, X. Duan, Q. Qing, C. M. Lieber, *Nano Lett.* **2012**.
[5] T. E. McKnight, A. V. Melechko, G. D. Griffin, M. A. Guillorn, V. I. Merkulov, F. Serna, D. K. Hensley, M. J. Doktycz, D. H. Lowndes, M. L. Simpson, *Nanotechnology* **2003**, *14*, 551.
[6] W. Kim, J. K. Ng, M. E. Kunitake, B. R. Conklin, P. Yang, *J. Am. Chem. Soc* **2007**, *129*, 7228–7229.
[7] T. Berthing, S. Bonde, C. B. Sørensen, P. Utko, J. Nygård, K. L. Martinez, *Small* **2011**, *7*, 640–647.
[8] W. Hällström, C. N. Prinz, D. Suyatin, L. Samuelson, L. Montelius, M. Kanje, *Langmuir* **2009**, *25*, 4343–4346.
[9] C. Xie, L. Hanson, W. Xie, Z. Lin, B. Cui, Y. Cui, *Nano Lett.* **2010**, *10*, 4020–4024.
[10] C. Xie, Z. Lin, L. Hanson, Y. Cui, B. Cui, *Nat. Nanotechnol.* **2012**, *7*, 185–190.
[11] J. T. Robinson, M. Jorgolli, A. K. Shalek, M. H. Yoon, R. S. Gertner, H. Park, *Nat. Nanotechnol.* **2012**, *7*, 180–184.
[12] Z. Li, J. Song, G. Mantini, M. Y. Lu, H. Fang, C. Falconi, L. J. Chen, Z. L. Wang, *Nano Lett.* **2009**, *9*, 3575–3580.
[13] W. Hällström, M. Lexholm, D. B. Suyatin, G. Hammarin, D. Hessman, L. Samuelson, L. Montelius, M. Kanje, C. N. Prinz, *Nano Lett.* **2010**, *10*, 782–787.
[14] C. Xie, L. Hanson, Y. Cui, B. Cui, *Proc. Natl. Acad. Sci. USA* **2011**, *108*, 3894–3899.
[15] T. E. McKnight, A. V. Melechko, D. K. Hensley, D. G. J. Mann, G. D. Griffin, M. L. Simpson, *Nano Lett.* **2004**, *4*, 1213–1219.
[16] D. G. J. Mann, T. E. McKnight, J. T. McPherson, P. R. Hoyt, A. V. Melechko, M. L. Simpson, G. S. Sayler, *ACS Nano* **2007**, *2*, 69–76.
[17] F. Zhao, Y. Zhao, Y. Liu, X. Chang, C. Chen, Y. Zhao, *Small* **2011**, *7*, 1322–1337.
[18] M. M. Song, W. J. Song, H. Bi, J. Wang, W. L. Wu, J. Sun, M. Yu, *Biomaterials* **2010**, *31*, 1509–1517.
[19] M. Safi, M. Yan, M.-A. Guedeau-Boudeville, H. Conjeaud, V. Garnier-Thibaud, N. Boggetto, A. Baeza-Squiban, F. Niedergang, D. Averbeck, J.-F. Berret, *ACS Nano* **2011**, *5*, 5354–5364.
[20] I. Obataya, C. Nakamura, S. Han, N. Nakamura, J. Miyake, *Nano Lett.* **2005**, *5*, 27–30.
[21] S. W. Han, C. Nakamura, N. Kotobuki, I. Obataya, H. Ohgushi, T. Nagamune, J. Miyake, *Nanomedicine* **2008**, *4*, 215–225.
[22] T. Berthing, S. Bonde, K. R. Rostgaard, M. H. Madsen, C. B. Sørensen, J. Nygård, K. L. Martinez, *Nanotechnology*, **2012**, *23*, 415102.
[23] Y. Xia, P. Yang, Y. Sun, Y. Wu, B. Mayers, B. Gates, Y. Yin, F. Kim, H. Yan, *Adv. Mater.* **2003**, *15*, 353–389.
[24] X. Jiang, T. Herricks, Y. Xia, *Nano Lett.* **2002**, *2*, 1333–1338.
[25] F. Mumm, P. Sikorski, *Nanotechnology* **2011**, *22*, 105605.
[26] K. Midander, P. Cronholm, H. L. Karlsson, K. Elihn, L. Mller, C. Leygraf, I. O. Wallinder, *Small* **2009**, *5*, 389–399.
[27] C. Jin, H. Kim, C. Hong, H. W. Kim, C. Lee, *Appl. Phys. A* **2010**, *100*, 151–157.
[28] J. H. Koschwanez, R. H. Carlson, D. R. Meldrum, *PLoS One* **2009**, *4*, 4572.
[29] C. Liu, D. Cui, H. Li, *Biosens. Bioelectron.* **2010**, *26*, 255–261.
[30] S. Beéfahy, P. Lipnik, T. Pardoen, C. Nascimento, B. Patris, P. Bertrand, S. Yunus, *Langmuir* **2009**, *26*, 3372–3375.
[31] F. Walther, P. Davydovskaya, S. Zurcher, M. Kaiser, H. Herberg, A. M. Gigler, R. W. Stark, *J. Micromech. Microeng.* **2007**, *17*, 524.
[32] M. Hennemeyer, F. Walther, S. Kerstan, K. Schurzinger, A. Gigler, R. Stark, *Microelectron. Eng.* **2008**, *85*, 1298–1301.

© 2012 Wiley-VCH Verlag GmbH & Co. KGaA, Weinheim

[33] N. Chevrier, P. Mertins, M. N. Artyomov, A. K. Shalek, M. Iannacone, M. F. Ciaccio, I. Gat-Viks, E. Tonti, M. M. DeGrace, K. R. Clauser, M. Garber, T. M. Eisenhaure, N. Yosef, J. Robinson, A. Sutton, M. S. Andersen, D. E. Root, U. von Andrian, R. B. Jones, H. Park, S. A. Carr, A. Regev, I. Amit, N. Hacohen, *Cell* **2011**, *147*, 853–867.
[34] M. R. Capecchi, *Cell* **1980**, *22*, 479–488.
[35] R. Mirzayans, R. A. Aubin, M. C. Paterson, *Mutat. Res.* **1992**, *281*, 115–122.
[36] H. Pollard, J. S. Remy, G. Loussouarn, S. Demolombe, J. Behr, D. Escande, *J. Biol. Chem.* **1998**, *273*, 7507–7511.
[37] E. E. Vaughan, D. A. Dean, *Mol. Ther.* **2006**, *13*, 422–428.
[38] M. A. E. M. van der Aa, E. Mastrobattista, R. Oosting, W. Hennink, G. Koning, D. Crommelin, *Pharm. Res.* **2006**, *23*, 447–459.
[39] D. Lechardeur, K. J. Sohn, M. Haardt, P. B. Joshi, M. Monck, R. W. Graham, B. Beatty, J. Squire, H. O'Brodovich, G. L. Lukacs, *Gene Ther.* **1999**, *6*, 482–497.
[40] M. Kaksonen, C. P. Toret, D. G. Drubin, *Nat. Rev. Mol. Cell Biol.* **2006**, *7*, 404–414.
[41] H. Persson, J. P. Beech, L. Samuelson, S. Oredsson, C. N. Prinz, J. O. Tegenfeldt, *Nano Res.* **2012**, *5*, 190–198.
[42] A. F. Adler, K. W. Leong, *Nano Today* **2010**, *5*, 553–569.
[43] J. Liu, Y. Sun, G. F. Oster, D. G. Drubin, *Curr. Opin. Cell Biol.* **2010**, *22*, 36–43.
[44] F. Braet, R. De Zanger, E. Wisse, *J. Microsc.* **1997**, *186*, 84–87.

Received: June 13, 2012
Revised: August 28, 2012
Published online:

© 2012 Wiley-VCH Verlag GmbH & Co. KGaA, Weinheim

DOI: 10.1002/smll.201201314

Copyright WILEY-VCH Verlag GmbH & Co. KGaA,69469 Weinheim,Germany,2012.

NANO MICRO
small

# Supporting Information

for *Small*,DOI: 10.1002/smll.201201314

# A Transparent Nanowire-Based Cell Impalement Device Suitable for Detailed Cell–Nanowire Interaction Studies

*Florian Mumm, Kai M. Beckwith, Sara Bonde, Karen L. Martinez, and Pawel Sikorski**

# Supplementary Material to:

# A transparent nanowire-based cell impalement device suitable for detailed cell-nanowire interaction studies

Florian Mumm,[†,¶] Kai Müller Beckwith,[†,¶] Sara Bonde,[‡] Karen L. Martinez,[‡] and Pawel Sikorski[*,†]

*Department of Physics, Norwegian University of Science and Technology, Høgskoleringen 5, N-7491 Trondheim, Norway, and Bio-Nanotechnology Laboratory, Department of Chemistry, University of Copenhagen, Universitetsparken 5 DK-2100 Copenhagen*

E-mail: pawel.sikorski@phys.ntnu.no

NANO MICRO small

## S1 Supplements to the Fabrication Section

### Nanowire Monitoring with Optical Microscopy

The nanowires could usually be seen as dark spots using a yellow light reflective optical microscope with a 50x magnification objective. This probably results from the fact that the depth of field of

---

[*] To whom correspondence should be addressed

[†] Norwegian University of Science and Technology

[‡] University of Copenhagen

[¶] Contributed equally to this work

high magnification objectives is quite small, which makes it possible to focus slightly above the substrate so that the nanowires reach into the focal plane and are visible as black spots. This is illustrated in Figure S1.1 for slightly tilted samples after the different polymer processing steps. The observation of the nanowires is easer in reality compared to the images, as one can see them moving in and out of focus when carefully focusing up and down.

As optical microscopy is fast and non-destructive, it was frequently employed to check the surface topology during the different process steps.

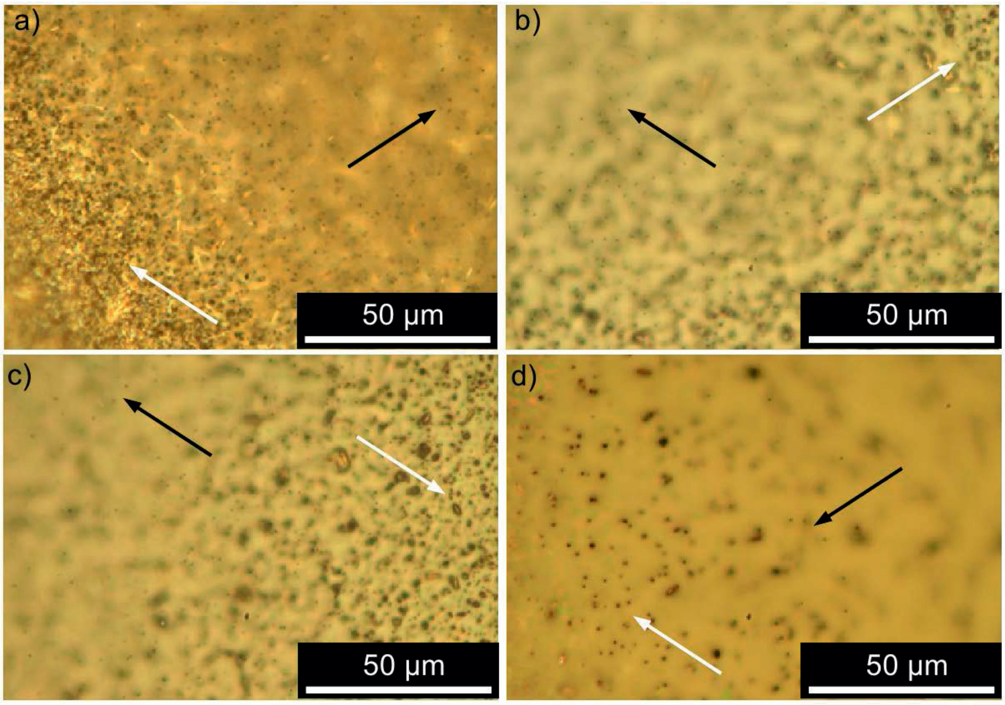

Figure S1.1: Yellow light reflective micrographs of the sample with different polymer layers a): CuO nanowires with $SiO_x$ coating, b): with PMMA, c): with PDMS, d): with SU-8. White arrows indicate areas with the substrate in focus, black arrows indicate an out of focus substrate with nanowires reaching in the focal plane visible as black dots.

## Layers Around the Nanowires

In the fabrication, two silica based layers are fabricated around the nanowires. In the beginning, about 10 nm $SiO_x$ are deposited by DC magnetron sputtering using a p-doped Si wafer as target[1]. As we did not have a wafer with the correct size to fit the sputterer at hand, a slightly larger wafer was selectively etched along its rim by reactive ion etching. Before being used as a target, the wafer was glued to an aluminium disk with conductive silver epoxy to minimize thermal damage. A transmission electron micrograph of the $SiO_x$ layer around the nanowires is shown in Figure

S1.2a.

The second layer around the wires formed during the addition of PDMS. As shown in Figure S1.2b, this layer extends from the PDMS at the substrate and forms the outer surface of the nanowires. As it is plasma cleaned several times, it probably transformed into a silica-like layer[2] that is the later anchoring point for the nanowires functionalization by silanization.

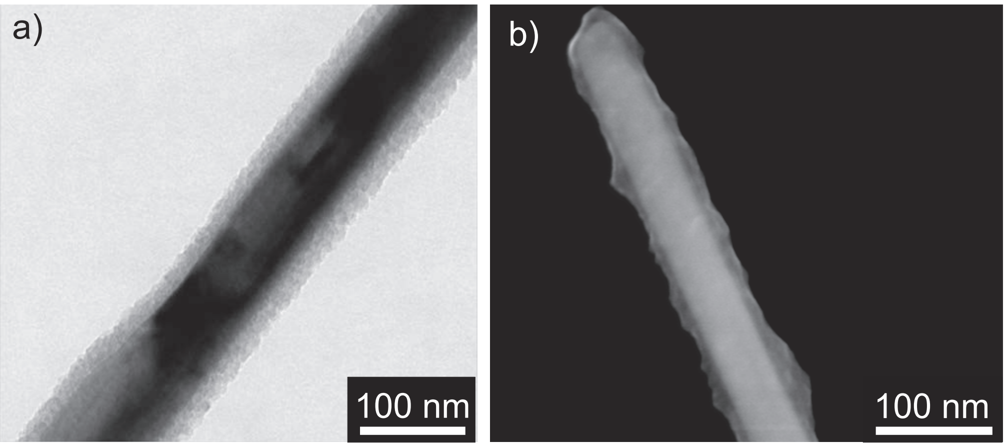

Figure S1.2: a): TEM image of the $SiO_x$ layer around a CuO nanowire after sputter coating, b): silica-like layer around nanowires after PDMS spinning and plasma treatment.

## Separation at the PMMA/PDMS Interface

The key feature of the device fabrication process is the ability to separate the nanowires with the SU-8 and PDMS from the underlying PMMA and copper based layers. Figure S1.3a shows a side view of the device immediately prior to separation. The PDMS layer forming the new underside of the nanowire sample (colorized turquois), as well as the remaining PMMA (blue), CuO (gray), and $Cu_2O$ (orange) can be seen. A yellow light microscope could be used to confirm that the separation worked successfully. Figure S1.3b shows a micrograph of the underside of the PDMS layer, obtained after a correct separation. Figure S1.3c, on the other hand, shows the most common incorrect separation (*e.g.* when the wire density was too high), where the Crystalbond ruptured internally. The relatively flat, somewhat dented surface of the bottom of the PDMS layer can be clearly differentiated from the more crystalline appearance of the Crystalbond.

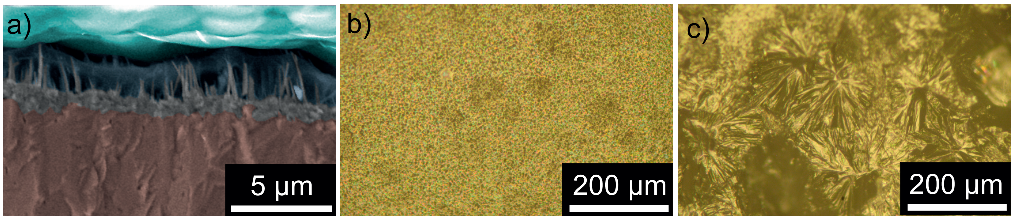

Figure S1.3: a): colorized SEM image of the device before separation, b): micrograph showing correct separation, c): micrograph showing internal rupturing of the Crystalbond.

## S2 CuO Cytotoxicity

CuO is toxic to cells, as it gets dissolved in culture medium releasing Cu ions.[4] For the device presented in this article, this is problematic on two levels: On the one hand, dissolving the CuO means dissolving the nanowires and, thus, loosing the functional surface structure of the system. On the other hand, the free copper ions could be a problem for the cells. However, due to the small volume of the wires, cytotoxicity is probably less problematic than losing them.

Assuming a nanowire density of 10 wires per $100\,\mu m^2$ with a length of $5\,\mu m$ and a diameter of $100\,nm$ each, results in about $2\,\mu g/cm^2$ CuO (with a density of $4.9\,g/cm^3$) in the solution if all nanowires are completely dissolved. Whereas a device with totally dissolved wires would clearly be without use for impalement studies, this value is *e.g.* only half as big as the lowest one to which human laryngeal epithelial cells were exposed in order to determine the toxicity of CuO nanoparticles[3] (extrapolating the reported dose dependency to $2\,\mu g/cm^2$ results in about 100% cell viability) and a factor of 20 smaller than that used in toxicity and dissolution tests done with CuO nanoparticles and cultivated human lung cells[4] (here it was actually observed that the particles themself were considerably more toxic than the Cu ions released from them). In reality, as seen in Figure 2 in the article, the nanowires are not significantly dissolved and the cells show survival rates comparable to glass at least for 4 days (some dissolution of nanowires could indeed be observed). As only a small fraction of the nanowires (possibly those with a defective $SiO_x$ coating or those, which break during the seperation step) are dissolved in the cell medium, the effects of the potentially released Cu are probably negligible .

If cytotoxicity turns out to be a problem in specific experiments, *e.g.* if long culture times or sensitive cells are used, one could also increase the thickness of the $SiO_x$ layer or include an incubation step in cell medium without cells to pre-dissolve the broken wires.

## S3 Nanowire-cell interactions

SEM images of the cells on the nanowires taken after one day in culture commonly show nanowires tightly covered by a membrane. Figure S6.1a shows this for a shorter wire at the outside of a cell.

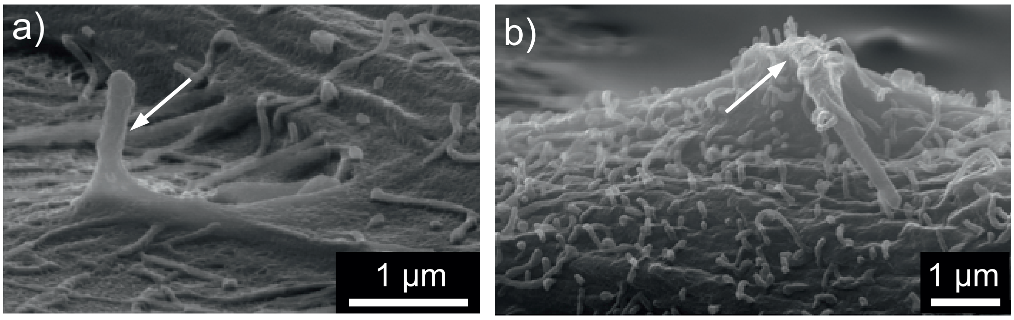

Figure S3.1: a): SEM micrograph of an engulfed nanowire, b): SEM micrograph of a bent nanowire apparently lifting the cell's top. The nanowires are indicated by arrows.

Larger, more central wires often seemed to reach through cells and to actually lift the cell membrane (see Figure S6.1b). However, discriminating between actual results and artefacts induced by cell shrinkage during dehydration remains a challenge. Especially such wires reaching through the cells are often tilted, which together with the absence of such features on confocal micrographs indicates the strong influence of the SEM sample preparation procedure.

After 4 days in culture, HeLa cells were found to spread out to and engulf the nanowires also at their wider periphery. This is in agreement with previously made observations on InAs nanowires[5]. Figure S6.2 shows a representative confocal image and SEM micrograph.

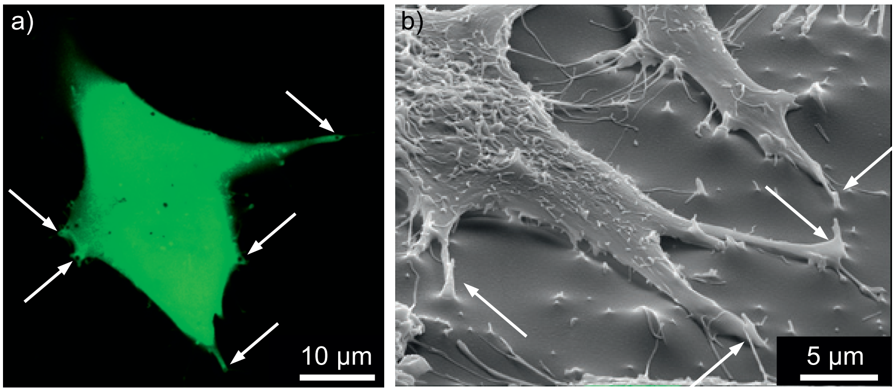

Figure S3.2: HeLa cells interacting with nanowires after 4 days in culture. a: confocal micrograph, b: SEM image. Engulfed nanowires are labelled with arrows.

The SNAP-$\kappa$-opiod receptor system successfully allows the selective and homogeneous labeling of the plasma membrane in live HEK293 cells (Figure S3.3a). Actin clearly co-localized with the nanowires also when observed in a cross-section (Figure S3.3b), although typically it shows higher localization and specific points along the nanowire than then membrane label does (see main text). This could be due to how the actin interacts at the site of the nanowire, but detailed analysis in challenging due to limited z-resolution in the confocal microscope. Similar to the HEK293 cells in the main text, HeLa cells also were able to express the SNAP-$\kappa$-opioid receptor. The HeLa cells showed similar nanowire-membrane interactions as reported for the HEK293 cells (Figure S3.4 and Figure 6 in the main text).

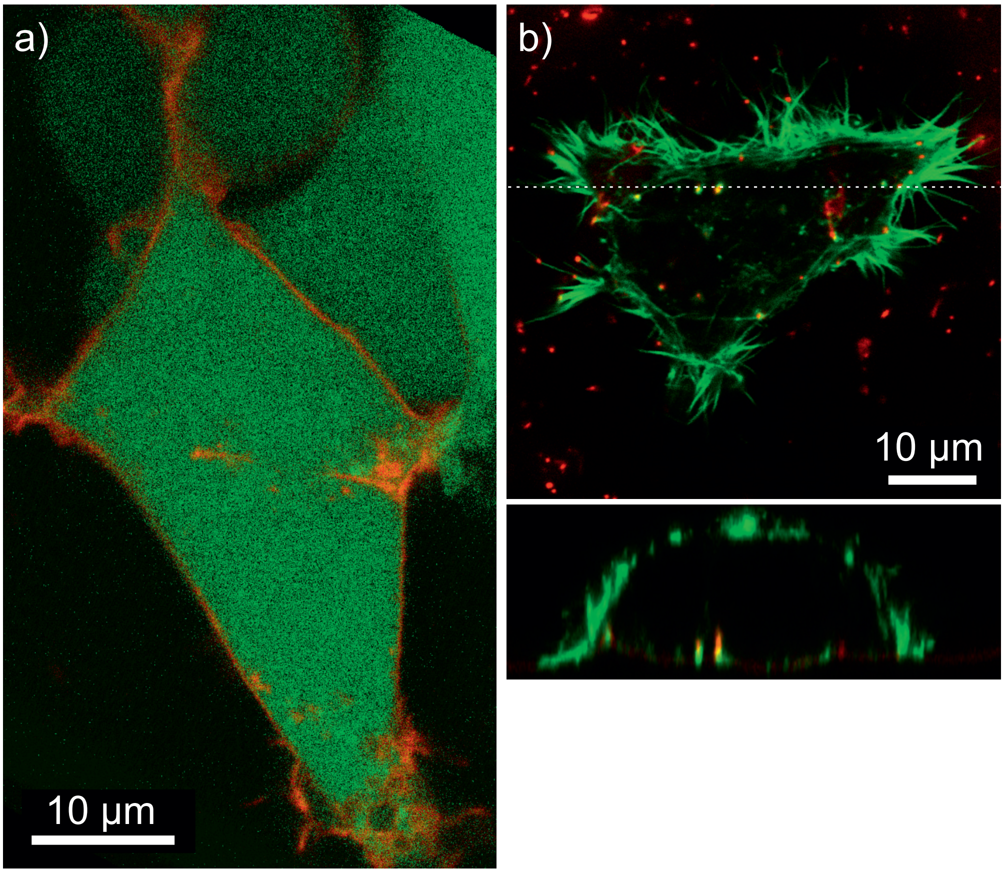

Figure S3.3, a): Successful expression and labeling of SNAP-$\kappa$-opioid receptor (red) in live HEK293 cells indicated by calcein-AM (green). b): Top view and cross-section of a HeLa cell labeled with Alexa488-phalloidin (actin filmanent, green) on Alexa633-labeled nanowires (red). Actin co-localizes with the nanowires also in the cross-section. The location of the cross-section is marked by the white dashed line.

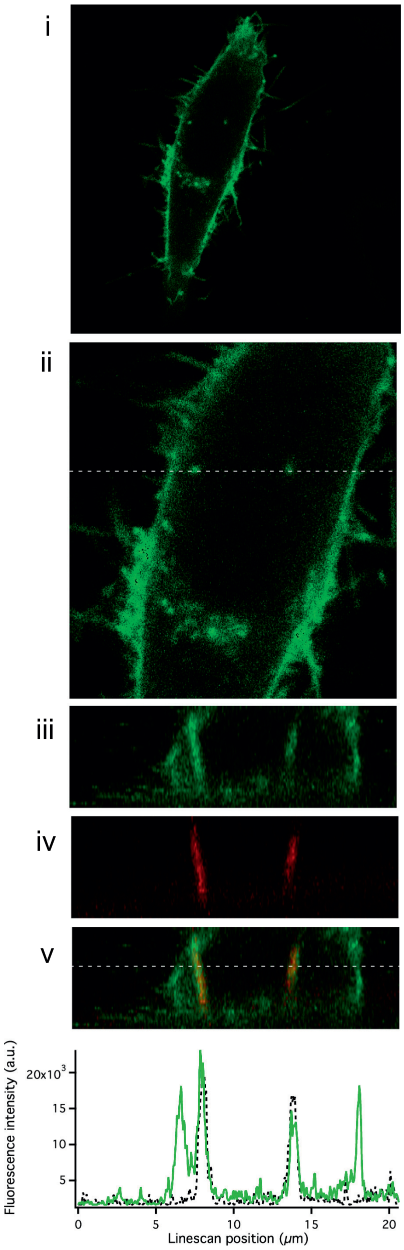
i
ii
iii
iv
v
Fluorescence intensity (a.u.)
20x10$^3$
15
10
5
0
5
10
15
20
Linescan position ($\mu$m)

Figure S3.4: HeLa cell transiently transfected with SNAP-$\kappa$-opioid receptor (i-iii, green) grown on nanowires (iv, red), showing clear colocalization of the membrane signal and the nanowires (v). A linescan through the line indicated in (v) highlights the colocalization between the cell membrane (green line) and nanowires (black dashed line).

## References

1. Jin, C.; Kim, H.; Hong, C.; Kim, H.; Lee, C. Preparation and Photoluminescence Properties of Silica-Coated CuO Nanowires. *Appl. Phys. A-Mater.* **2010**, *100*, 151–157

2. Béfahy, S.; Lipnik, P.; Pardoen, T.; Nascimento, C.; Patris, B.; Bertrand, P.; Yunus, S. Thickness and Elastic Modulus of Plasma Treated PDMS Silica-Like Surface Layer. *Langmuir* **2009**, *26*, 3372–3375

3. Fahmy, B.; Cormier, S. Copper Oxide Nanoparticles Induce Oxidative Stress and Cytotoxicity in Airway Epithelial Cells. *Toxicol. in Vitro* **2009**, *23*, 1365–1371

4. Midander, K.; Cronholm, P.; Karlsson, H.; Elihn, K.; Möller, L.; Leygraf, C.; Wallinder, I. Surface Characteristics, Copper Release, and Toxicity of Nano-and Micrometer-Sized Copper and Copper (II) Oxide Particles: A Cross-Disciplinary Study. *Small* **2009**, *5*, 389–399

5. Berthing, T.; Bonde, S.; Sørensen, C.; Utko, P.; Nygård, J.; Martinez, K. Intact Mammalian Cell Function on Semiconductor Nanowire Arrays: New Perspectives for Cell-Based Biosensing. *Small* **2010**

# Paper IV

Published on 03 April 2015. Downloaded by Norwegian University of Science and Technology on 23/04/2015 13:33:11.

Nanoscale

PAPER

View Article Online
View Journal

Cite this: DOI: 10.1039/c5nr00674k

# Tunable high aspect ratio polymer nanostructures for cell interfaces†

Kai Sandvold Beckwith,* Simon P. Cooil, Justin W. Wells and Pawel Sikorski

Received 29th January 2015,
Accepted 1st April 2015

DOI: 10.1039/c5nr00674k

www.rsc.org/nanoscale

Nanoscale topographies and chemical patterns can be used as synthetic cell interfaces with a range of applications including the study and control of cellular processes. Herein, we describe the fabrication of high aspect ratio nanostructures using electron beam lithography in the epoxy-based polymer SU-8. We show how nanostructure geometry, position and fluorescence properties can be tuned, allowing flexible device design. Further, thiol–epoxide reactions were developed to give effective and specific modification of SU-8 surface chemistry. SU-8 nanostructures were made directly on glass cover slips, enabling the use of high resolution optical techniques such as live-cell confocal, total internal reflection and 3D structured illumination microscopy to investigate cell interactions with the nanostructures. Details of cell adherence and spreading, plasma membrane conformation and actin organization in response to high aspect ratio nanopillars and nanolines were investigated. The versatile structural and chemical properties combined with the high resolution cell imaging capabilities of this system are an important step towards the better understanding and control of cell interactions with nanomaterials.

## Introduction

The analysis, perturbation and manipulation of cells *in vitro* are of fundamental importance in unravelling the molecular mechanisms of life. In turn these insights can lead to better understanding and treatment of pathologies, as well as driving developments within fields such as tissue engineering and neuroscience. Adherent cells interact strongly with their surroundings and this interactivity can be exploited to study and modify cell behaviour by introducing topographical or chemical micro- and nanoscale features.[1–5]

Recently, there have been significant developments in the biological applications of nanostructured surfaces, in particular high aspect ratio nanowires, nanopillars and nanotubes.[6,7] ‡ In these systems, regular or randomly arranged nanostructures protrude vertically from a flat substrate. The geometry of the nanostructures allows them to form a cellular interface with a nanoscale cross-section (typically around 100 nm), while simultaneously protruding into the cell body, although the details of this interface still constitute an area of active research.[8–10] The biological use of high aspect ratio nanostructures has led to several novel applications, including electrical interrogation of neurons,[11–13] single-cell force measurements,[14] cell motility control,[15–17] induction of stem cell differentiation,[18] assessing differential cell response,[19] cell capture[20,21] and nanostructure-aided delivery of various functional molecules.[8,22–25]

So far, inorganic materials such as semiconductors with high stiffness (which translates into high potential aspect ratios) have been used in the design of high aspect ratio nanostructures for biological applications. However, there are several advantages in using polymer materials as nanostructured cell culture substrates.[4,26,27] These include low materials cost, rapid and mild processing, optical transparency for better readout and characterization possibilities, increased design flexibility, and biocompatibility. In this regard, SU-8 is a promising candidate material for realising high-aspect ratio nanostructures in polymer materials. SU-8 is a photosensitive epoxy-based resin that is widely used in MEMS technologies for creating patterned microscale features of high aspect ratios due to its relatively high stiffness, chemical resistance, optical transparency and ease of processing.[28] To achieve nanoscale features, SU-8 has also been explored as an electron-beam resist, demonstrating very high electron sensitivity and sub-100 nm resolution for thin films.[29] Although the focus of most studies has been on low aspect ratio features, one group has demonstrated the use of 500 nm high SU-8 nanopillars for bio-sensing purposes,[30,31]

---

Department of Physics, Norwegian University of Science and Technology, Trondheim, Norway. E-mail: kai.beckwith@ntnu.no

† Electronic supplementary information (ESI) available. See DOI: 10.1039/c5nr00674k

‡ Although there is no general consensus as to which dimensions constitute a high aspect ratio nanostructure, in a recent review on the field by Bonde *et al.*,[6] only nanostructures with a height above 500 nm and diameter below 500 nm were considered.

This journal is © The Royal Society of Chemistry 2015

Published on 03 April 2015. Downloaded by Norwegian University of Science and Technology on 23/04/2015 13:33:11.

and nanoimprinted SU-8 nanopillars have also been used for cell traction force measurements.[32]

In addition to the possibility of nanoscale patterning, SU-8 is chemically tunable and biocompatible.[33,34] SU-8 has been functionalized *via* several different routes, including unreacted surface epoxide groups,[35] epoxide ring-opening modification *via* treatment with strong oxidizing acids,[34,36] photografting[37] or by exposure to oxygen plasma[38] in many cases followed by *e.g.* silane treatment.[39] For surface chemistry specific to SU-8, and therefore potentially orthogonal to other materials in the device, the unreacted epoxide groups offer the most attractive route for conjugation. Multifunctional amines are standard curatives for epoxy resins, and thus amine–epoxide reactions are well characterized.[40] However, for surface chemistry modification of SU-8, amine-based procedures have not been highly successful, with the few reported successes being time-consuming and harsh, increasing the likelihood of damaging fragile structures.[35] Thus novel approaches to specifically modify SU-8 surface chemistry are needed. Thiol-based chemistry offers an attractive alternative, as thiol–epoxide "click" reactions are gaining popularity as a simple and efficient conjugation method.[41,42] Indeed, thiol-modified oligonucleotides have been conjugated to SU-8 in a rapid UV-mediated "click" reaction,[43] but this reactivity has not been explored in a more general sense.

In this work, we develop a flexible SU-8 based platform for biological applications, with emphasis on high aspect ratio nanostructures. We optimize the fabrication of up to 1 μm high SU-8 nanostructures by electron beam lithography directly on glass cover slips for facile integration with typical cell biology procedures and microscopy methods. Thiol–epoxide "click" reactions are implemented to selectively alter SU-8 surface chemistry. Further, cell responses to different high aspect ratio SU-8 nanostructures are investigated. In particular, we use methods such as high resolution live cell imaging and super-resolution microscopy for detailed characterization of the interface between cultured cells and SU-8 nanostructures. We show that the SU-8 nanostructures are highly cell compatible, but can influence cell shape, adhesion, membrane morphology and actin structure. The presented system offers promise for cell biological applications of high aspect ratio polymer nanostructures, while simultaneously allowing the investigation of the interface between the cells and nanostructures and subsequent cell responses to be studied in unprecedented detail.

## Results and discussion

### SU-8 nanostructure fabrication

High aspect ratio nanoscale features were defined in spin-coated SU-8 films on glass cover slips by electron beam lithography (Fig. 1). Uniform arrays of nanopillars (Fig. 1A and B) or nanolines (Fig. 1C) could be made over mm$^2$-sized areas in under 5 minutes of exposure time. The fabrication was initially optimized by tuning electron exposure doses and process parameters including post-exposure baking and development to give nanostructures that withstood capillary collapse upon drying after development, while retaining as high aspect ratio as possible (details given in Materials and methods). Using single pixel dots or lines as the exposure design, aspect ratios (height divided by feature width at half height) of about 7 could be obtained for the resulting nanoscale pillars and lines when 1 μm high, a doubling compared to previously reported results.[30] Tip diameters in this case were about 100–120 nm (see ESI Fig. S1†).

Nanostructure height could be altered by spinning the initial SU-8 film to different thicknesses (Fig. 1D). If thicker (*i.e.* ≥1 μm) SU-8 films were used, nanopillars and nanolines tapered outward toward their base due to electron scattering in the resist, limiting the height of well-defined nanoscale features to about 1 μm with our 30 kV electron beam lithography system (see ESI Fig. S2†). Nanostructures could be arbitrarily patterned, the only limitation being that the spacing (array pitch) could not be less than approximately half the height of the SU-8 (*i.e.* 500 nm spacing for 1 μm high nanopillars), otherwise a rough, semi-continuous SU-8 layer was formed between features due to the proximity effect. Nanostructure diameter could be both reduced and increased from the diameter obtained by single-pixel exposure (Fig. 1E). Increased feature diameters were obtained by exposing small areas rather than single pixels, to give arbitrary diameters above the initial 120 nm. To reduce nanostructure diameters, oxygen plasma etching was performed. A low power (50 W) oxygen plasma controllably reduced both the height and diameter of the nanostructures. For 1 μm high nanopillars, the tip diameter could be reduced to about 50 nm with 2 minutes of oxygen plasma treatment, giving tip : height aspect ratios of over 16 after taking the reduced height into account (see ESI Fig. S1†). The average aspect ratio remained similar to untreated nanopillars at about 7. 40–50 nm was a lower limit to the tip diameter using this method, as tips broke off and fragmented upon further etching.

Finally, the nanostructures could be made fluorescent by doping the SU-8 with a fluorescent dye (Fig. 1E). Here, Rhodamine 6G (excitation at 561 nm) and Oxazine 170 (excitation at 633 nm) were used successfully, but any fluorescent dye could in principle be used as long as it is sufficiently hydrophobic to dissolve in the SU-8 solvent while retaining its fluorescence properties.

Direct writing using electron beam lithography is inherently a serial, and thus a "low" throughput technique. The advantages include high flexibility and the possibility to quickly alter designs, as well as having a simple process consisting of only very few processing steps. Further, positional accuracy, geometric control and optional intrinsic fluorescence give reliable and consistent results across experiments, and allow transfer of results to other systems. Even with a basic EBL system such as the one used in this work, sufficient writing speed for laboratory-scale experiments (typically 1–2 minutes per mm$^2$) could be achieved due to the extreme sensitivity of the SU-8 resist.[29] Even this number would be greatly improved with modern, higher throughput EBL systems. One current limit-

This journal is © The Royal Society of Chemistry 2015

Published on 03 April 2015. Downloaded by Norwegian University of Science and Technology on 23/04/2015 13:33:11.

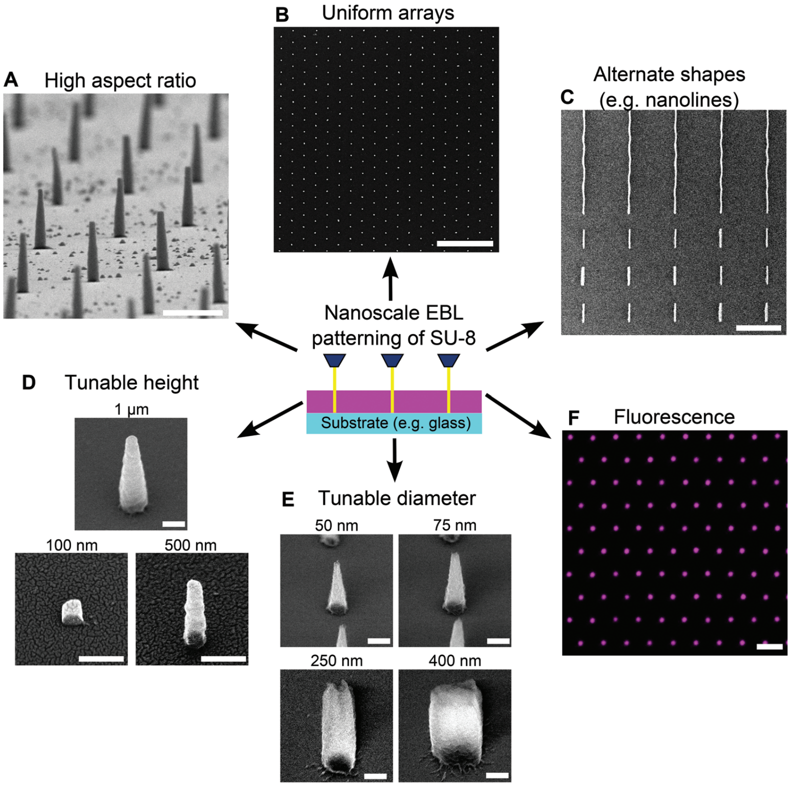

**Fig. 1** Properties of high aspect ratio SU-8 nanostructures produced on glass cover slips by electron beam lithography. (A) Tilted SEM image of a regular hexagonal array of 1 µm high nanopillars with 5 µm spacing. Tip diameters are about 100–120 nm, and aspect ratio (height divided by average diameter) are about 7. Scale bar 1 µm. (B) Top view of hexagonal nanopillar array with 2 µm spacing. Scale bar 10 µm. (C) Top view of nanolines of different lengths (2 and 200 µm), with corresponding aspect ratios as the nanopillars. Scale bar 5 µm. (D) Nanostructure height was varied by using different SU-8 resist thicknesses, in the range of 100 nm to 1 µm. Scale bars 200 nm. (E) The diameter of nanostructures was altered compared to the initial single-pixel defined features, upwards by exposing larger areas and downwards by oxygen plasma etching for 60 s (75 nm tips) or 120 s (50 nm tips). Scale bar 200 nm. (F) Oxazine 170 or Rhodamine 6G-doped SU-8 was used to make fluorescent nanostructures, such as the hexagonal array (similar to (A) and (B)) shown in the confocal micrograph. Scale bar 2 µm. The SEM images in (D) and (E) are collected at 40° tilt from a top view, while (A) is collected at 85°.

ation is the maximum feature height of about 1 µm, which is at the shorter end of the spectrum of high aspect ratio nanostructures reported in the literature.[6] However, EBL systems with higher acceleration voltages are available (typically 100–125 kV compared to 30 kV in our system), which would further increase the potential aspect ratio and height of the features,[44] due to significantly lower electron scattering in the resist (see ESI Fig. S3†). Other direct-writing techniques such as direct laser writing (DLW) or two-photon polymerization could potentially increase device production throughput, but suffer from lower feature resolution.[45,46] Higher throughput, high resolution methods to structure SU-8 such as nanoimprint lithography[47] are attractive for further development, while electron beam lithography offers simpler and faster prototyping for initial investigations.

### SU-8 surface chemistry modifications

Simultaneous control over surface chemistry and surface topography is of great interest in biological applications. In particular, if the nanostructures are made of a different material from the substrate, such as is the case of our SU-8 nanostructures on glass, new possibilities emerge for specifically tuning surface chemistry and cell response. To this end, we investigated the reactivity of unreacted epoxy-groups on SU-8 with candidate amino and thiol functional molecules under mild, aqueous conditions.

In particular, β-mercaptoethanol ($OH(CH_2)_2SH$, ME), 10 kDa PEG-thiol ($(CH_2CH_2O)_n$–SH, PEG-SH) and cysteamine ($NH_2(CH_2)_2SH$) were investigated as bi-functional thiols with different secondary groups. Ethanolamine ($OH(CH_2)_2NH_2$, EA)

Published on 03 April 2015. Downloaded by Norwegian University of Science and Technology on 23/04/2015 13:33:11.

was used for comparison as it is commonly used to quench epoxide groups.[48] Solutions were made at 1 M (except for PEG-SH which was made at 1 mM), and the pH was adjusted to the p$K_a$ of the reactive group (typically between pH = 8 and pH = 10) to ensure an equal concentration of the nucleophilic (deprotonated) species of each molecule. The surface modification potential of each molecule was initially assessed by measuring the static, advancing and receding water contact angles on uniform (unpatterned) SU-8 films after immersion in the modifying solution for up to 60 minutes at room temperature (Fig. 2A).

The increased reactivity of the thiol species compared to similar amine species was demonstrated by the stronger reduction of contact angle observed for β-mercaptoethanol compared to ethanolamine. Another thiol, cysteamine, was investigated for introducing amine groups to the SU-8 surface, a key functionality for further biofunctionalization. Unexpectedly, cysteamine showed an extremely strong reduction of the water contact angle. Already after 15 minutes of incubation a strong contact angle reduction was observed, and after 60 minutes the SU-8 surface was nearly completely wetted by the test droplet (Fig. 2B). This indicates a significant conversion of the epoxide groups to thioether-bound cysteamine. The reason for the increased efficacy of cysteamine compared to other thiol-species is unknown, but we speculate that it might be related to either an intra-molecular or inter-molecular catalytic effect of the amine group. For all surfaces a significant contact angle hysteresis (difference between advancing and receding contact angles) was observed, presumably reflecting the mixed surface chemistry present.[49]

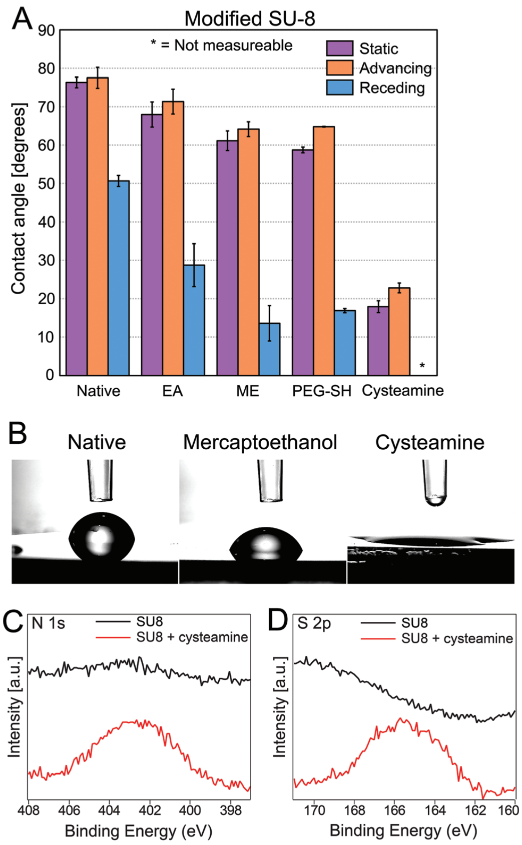

**Fig. 2** (A) Static, advancing and receding contact angle of SU-8 after reacting surface-epoxide groups with ethanolamine (EA), β-mercapto ethanol (ME), PEG-thiol and cysteamine. All treatments were performed for 1 hour at room temperature, except cysteamine which was 15 minutes, as 60 minutes of cysteamine gave non-measureable (<10°) contact angles. Error bars indicate ±S.D. (B) Examples of images acquired during contact angle measurements, illustrating the changes in contact angles that occurred. High resolution XPS spectra of nitrogen 1s (C) and sulphur 2p (D) peaks of native and cysteamine-modified SU-8.

To verify that the negatively charged thiolate ions were indeed responsible for the modification of the SU-8 surface, additional experiments were performed with thiol-containing and control solutions at various pH and concentrations (see ESI Fig. S4†). These indicate that 1 M cysteamine at alkaline pH was the most potent surface modification species, but also β-mercaptoethanol showed an increased effect at p$K_a$ compared to lower pH. Control solutions at high or low pH without amines or thiols only slightly altered the contact angle. As a positive control, freshly plasma cleaned SU-8 was observed to be completely wetting as previously described.[38]

Further details of the wet chemical modification of SU-8 with cysteamine were investigated by X-ray photoelectron spectroscopy (XPS), a surface sensitive method. XPS analysis was performed of native SU-8 and cysteamine-modified SU-8 (1 hour incubation). Selective nitrogen 1s (Fig. 2C) and sulphur 2p (Fig. 2D) scans demonstrate increased nitrogen and sulphur content on the surface of the modified SU-8 films compared to native SU-8, indicating binding of cysteamine to SU-8. The increase in signal around 170 eV in the native SU-8 sulphur 2p spectra was attributed to a silicon 2p plasmon loss peak from the underlying substrate through defects or scratches in the SU-8 film (see also ESI Fig. S5†). Peak area quantification of the cysteamine-modified SU-8 spectrum yielded normalized atomic percentages for carbon 1s (60%), oxygen 1s (37%), nitrogen 1s (2%) and sulphur 2p (1%), a nitrogen/carbon ratio of 0.03 and a sulphur/carbon ratio of 0.013. As each cysteamine molecule contains one nitrogen and one sulphur, the increased signal of nitrogen compared to sulphur indicates that it is the thiol group of cysteamine that binds to SU-8, as indicated in the contact angle studies. Although the atomic percentages apparently indicate a quite low coverage of cysteamine on SU-8, cysteamine monolayers on gold are known to absorb significant amounts of oxygen- and carbon-containing contaminating molecules. In one study, even at full monolayer coverage of cysteamine, the nitrogen/carbon ratio was only 0.1 compared to the theoretical value of about 0.5.[50] In our case the underlying surface (SU-8) also consists of carbon and oxygen, and it was not possible to distinguish the carbon and oxygen contribution from surface

Published on 03 April 2015. Downloaded by Norwegian University of Science and Technology on 23/04/2015 13:33:11.

contamination and the SU-8. Quantification of the cysteamine surface coverage was therefore not possible, but the surface coverage is likely significantly higher than indicated by the atomic percentages.

To demonstrate the chemical functionality of modified SU-8 surfaces, fluorescent NHS-rhodamine was used as a probe (Fig. 3A). NHS-rhodamine binds covalently to amine groups, such as those introduced by the cysteamine reaction with unreacted SU-8 epoxide groups. Conversely, due to its inherent hydrophobicity, native SU-8 is known to have high non-specific adsorption,[46] so other treatments were assessed to reduce non-specific adsorption of NHS-rhodamine to SU-8. Under the measurement conditions, some SU-8 autofluorescence was observed, constituting the signal in the unlabelled control. As expected, native SU-8 showed an increased fluorescence signal after treatment with NHS-rhodamine due to non-specific adsorption. Treatment of SU-8 with oxygen plasma, β-mercaptoethanol or PEG-SH reduced NHS-rhodamine binding to SU-8 to levels close to the unlabelled control. In comparison, cysteamine-treated SU-8 showed a substantial increase in fluorescence signal, indicating conjugation of NHS-rhodamine to the amine groups presented by the cysteamine-modified SU-8. It should be noted that during initial experiments it was observed that the chemistry of the glass substrate was altered after the SU-8 fabrication process, leading to an observable fluorescent background on the glass after NHS-rhodamine treatment. To regenerate the expected surface chemistry of glass, a NaOH-based wet chemical cleaning step was implemented for all experiments, as this cleaning method did not appear to alter SU-8 chemistry (see details in ESI†).

"Orthogonal" chemistry, *i.e.* introduction of independent functionality on SU-8 and glass, was demonstrated by specifically labelling the glass substrate after treatment of patterned SU-8 features with cysteamine and NHS-rhodamine (Fig. 3B). The glass was labelled with FITC-labelled poly(ethyleneimine) (PEI), which is a highly cationic polymer that binds strongly to the negatively charged glass. Conversely, PEI would not bind to the rhodamine-modified SU-8. Using this method, both larger SU-8 features and SU-8 nanopillars were selectively labelled with NHS-rhodamine, while the glass was selectively labelled with FITC-PEI.

Orthogonal modification could be used to tune cell adhesion properties to glass or SU-8. As PEG monolayers are well known for preventing cell adhesion, SU-8 was modified by PEG-SH to see if a reduction in cell adhesion was obtained. Although the standard modification procedure used above reduced the contact angle and NHS-rhodamine binding on SU-8, the PEG-layer formed was presumably not dense enough to significantly reduce cell adhesion, as little difference was observed compared to control samples. To increase the PEG-SH-epoxide reaction efficiency, UV-light was used to catalyse the reaction, as recently described for immobilizing thiolated DNA oligomers.[43,51] The UV-immobilized PEG-SH monolayer on SU-8 substantially reduced cell adhesion to SU-8 features, while cell adhesion was still supported on the surrounding glass areas (Fig. 3C).

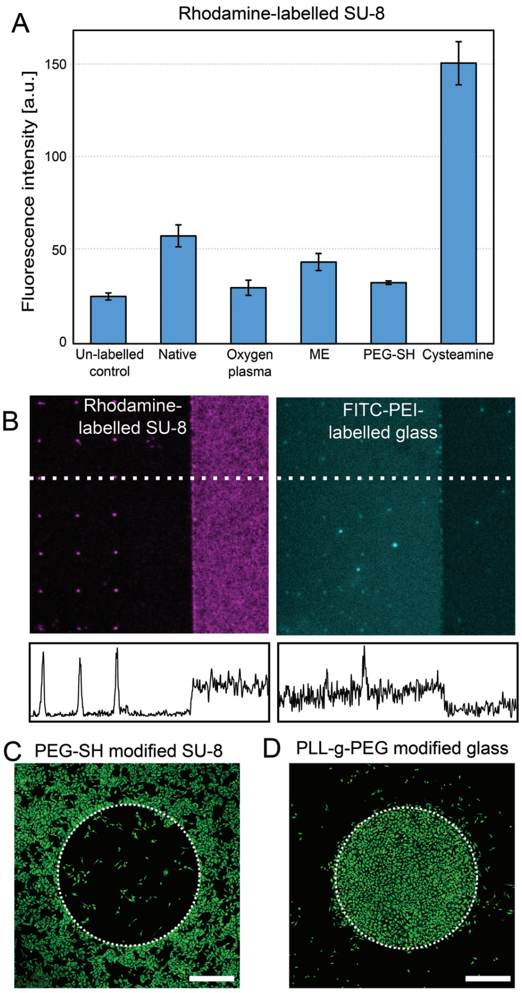

**Fig. 3** (A) Fluorescence intensity of flat SU-8 surfaces labelled by NHS-rhodamine after various surface treatments. The signal in the negative control is SU-8 autofluorescence. Error bars indicate ±S.D. (B) Orthogonal labelling of SU-8 and glass. SU-8 was functionalized with cysteamine and conjugated to NHS-rhodamine, while the negatively charged glass was subsequently labelled by FITC-PEI. Below each figure are intensity linescans from the indicated dashed lines. (C, D) Calcein-AM-labelled HeLa cells grown on large-scale SU-8 features on glass. When modified with PEG-SH (C), the cell adhesion was reduced on SU-8 features. When the glass was modified by PLL-*g*-PEG (D), cell adhesion was instead reduced on glass, while the unmodified SU-8 was able to support cell adhesion. The SU-8 area is delineated by the stippled circle, the scale bar is 500 μm.

Conversely, to avoid cell adhesion on glass, while allowing cells to attach to SU-8 features, the samples were cleaned as above and incubated in PLL-*g*-PEG, which creates a cell-repellent self-assembled monolayer on negatively charged

Published on 03 April 2015. Downloaded by Norwegian University of Science and Technology on 23/04/2015 13:33:11.

surfaces.[52] After cell culturing, almost no cells adhered on the glass, while adhering well to the unmodified SU-8 (Fig. 3D).

It is possible that other solution conditions such as increased pH or temperature or the inclusions of catalysts could increase the efficiency of the thiol-based SU-8 modification reactions. However, we have shown that even under mildly alkaline aqueous conditions the thiol-based solutions are potent in modifying SU-8 micro- and nanostructures, especially in the case of cysteamine forming an amine-rich surface on the SU-8. UV-enhanced grafting offers an alternative route that increases grafting efficiency, such as in the case of directly rendering SU-8 cell repellent by PEG-SH treatment. Such simple and robust surface modifications can have great impact on the use of SU-8 in *e.g.* DNA microarrays,[34] microfluidics[35] or for cell device applications[39] as also presented here.

### General influences of SU-8 nanostructures on cells

Cell compatibility, ease of use and high quality imaging are advantageous features of nanostructured devices when used for cell biological applications. Standard glass cover slips patterned with SU-8 nanostructures were mounted under 3.5 mm holes drilled in the base of 35 mm petri dishes, in a configuration similar to standard glass-bottom dishes used for microscopy (see schematic in ESI Fig. S6†). To reduce the number of variables investigated, only oxygen plasma treated nanostructures were used for cell investigations, ensuring a highly cell-compatible surface chemistry.[53] Unless otherwise specified, 1 μm high nanostructures in hexagonal arrays were used for all experiments.

To assess cell-nanostructure compatibility, HeLa cells were grown on nanopillars and nanolines 1 μm high and 120 nm in diameter with different spacings for 24 hours, stained with live/dead staining (calcein-AM and propidium iodide) and imaged live using confocal microscopy. Images were automatically analysed using CellProfiler. For all nanopillar spacings, the cell viability was about 98%, similar to glass controls (Fig. 4A), and cell density was also unchanged at about 400 cells per mm$^2$ for the chosen seeding density (20 000 cells per cm$^2$). A reduction in projected spreading area of the cells was observed for nanopillars spaced by 0.75 μm to 2 μm, while on nanopillars spaced by 5 μm the spreading area was not significantly different from glass controls. At the measured cell areas, 1 μm and 5 μm spacing correspond to about 500 and 30 nanopillars per cell, respectively. High viability but somewhat reduced spreading area is consistent with earlier reports of cells on *e.g.* polystyrene nanopillars of similar dimensions as ours (although more densely spaced),[54] and also general trends in studies of cells on other types of high aspect ratio nanostructures.[6]

In addition, it was investigated whether nanolines could induce directional effects in the cells (*i.e.* elongation and orientation alignment), as it is well known that cells tend to align along elongated topography in the substrate.[55] Indeed, on nanolines 1 μm high, with a top diameter of about 120 nm, spacings of 1–10 μm and lengths from 2 μm to 500 μm, both elongation and alignment of cell orientation with the nanolines was observed (Fig. 4C and D). Elongation was measured by the ratio of the major axis to minor axis of the best-fit ellipse for each cell, while alignment was measured by the standard deviation in the orientation of the major axis of the ellipse. In particular, nanolines substantially longer than the cells (*i.e.* 500 μm) gave the strongest elongation and alignment, although 5 and 10 μm lines also gave a stronger alignment

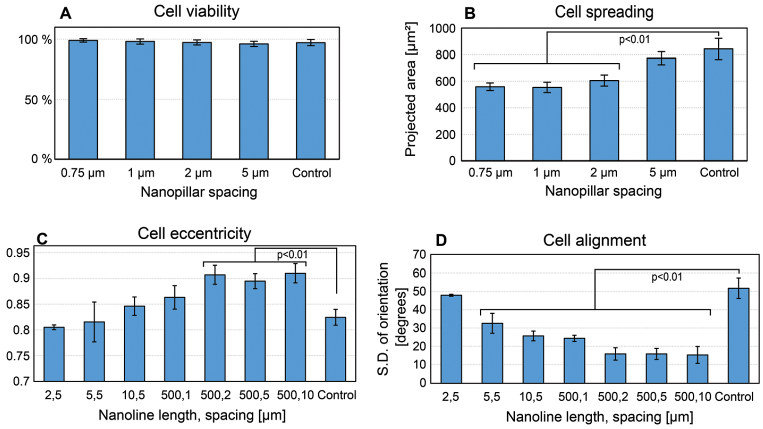

**Fig. 4** HeLa cells were cultured for 24 hours on substrates with 1 μm high, 120 nm diameter oxygen plasma treated hexagonal SU-8 nanopillar arrays with nanopillar spacings of 0.75–5 μm, or square nanoline arrays with 1 μm high, 120 nm diameter nanolines with lengths of 2–500 μm and spacings of 1–10 μm and compared to glass controls. The cells were labelled with calcein-AM (live cells) and propidium iodide (dead cells) and imaged live using a 10× objective and analysed for viability and cell shape using CellProfiler. (A) Cell viability was unchanged from glass controls for the different nanopillar spacings. (B) Projected cell area was significantly reduced on nanopillar array spacings of 0.75–2 μm, while the area was similar to flat glass for 5 μm spaced nanopillar arrays. (C) Cells became more elongated and (D) better aligned compared to glass controls on nanolines, especially longer nanolines. Error bars indicate ±S.D., significance assessed by Student's $t$-test, 2-tailed assuming unequal variance.

Published on 03 April 2015. Downloaded by Norwegian University of Science and Technology on 23/04/2015 13:33:11.

than 2 μm lines or glass control. On the other hand, for 500 μm long lines the spacing was less important in the investigated range, except in the case of 1 μm, where both elongation and alignment were reduced. The high degree of tunability and control over elongated high aspect ratio features can have important applications within neural studies and *in vitro* neural network construction.[45]

### Cell interactions with SU-8 nanostructures

To gain a better understanding of how single cells respond to the SU-8 nanostructures, in particular 1 μm high nanopillars and nanolines, high resolution optical microscopy was used to image HeLa cell cytoplasm, plasma membrane and actin filaments while growing on nanostructures. The cells were studied 24 hours after seeding, to ensure that all initial cell adherence processes had finished. For initial investigations, the cell cytoplasm was labelled with calcein-AM, and the cells were imaged live using a 63× 1.4NA oil immersion objective. As has been reported before for nanowires,[8,22] the nanostructures were visible as black features (dots or lines) against the fluorescent cell cytoplasm due to the cytoplasmic volume excluded by the nanopillars (Fig. 5). One noticeable feature was that cells on nanopillars spaced by ≤1 μm in many cases had a reduced cytoplasmic signal in significant portions of the cell body (Fig. 5A). This can be explained by a "bed of nails" effect, where areas of the cell body were suspended above the cover slip (and thus above the focal volume of the microscope), appearing darker. This situation was dynamic, as the area of the cell body in contact with the cover slip changed over time, as shown in excerpts from a one hour time-lapse in Fig. 5A. The full time-lapse is available in ESI Movie S1.† The opposite case, where initially adhered areas of a cell became suspended, was also observed (ESI Movie S1†). The occurrence of a number of mobile filopodial extensions was observed under the suspended areas of the cell.

Such a "bed-of-nails" effect on cells suspended by dense arrays of high aspect ratio nanostructures has been reported before,[9,56] but in these cases the nanowires were longer than our nanopillars (typically 5–10 μm compared to 1 μm), leading in most cases to suspension of the entire cell body (occasionally excluding longer protrusions such as axons). In contrast, we observed that in all cases at least a portion of the cell body remained in contact with the cover slip. Even in "fully adhered" cells, typically observed on nanopillars spaced by ≥2 μm, the height of the cytoplasm (and thus the contact with the cover slip) could also fluctuate in an area around the position of single nanopillars, as indicated by a temporary reduction in the cytoplasmic signal (Fig. 5B). This can be envisioned as the cell cytoplasm adopting a tent-shaped surface with the nanopillar as the tent-pole. This form of local cell cytoplasm deformation has been described theoretically,[57] and these results demonstrate these states as part of a dynamic interaction between the cells and nanopillars.

Shorter nanolines (2 μm long and spaced by 2 μm) caused a cytoplasm exclusion effect similar to that of nanopillars at all line positions (Fig. 5C), while longer lines (*e.g.* 500 μm spaced by 2 μm) additionally suspended larger areas of the cells, as indicated by darker areas in the cell cytoplasm (Fig. 5D).

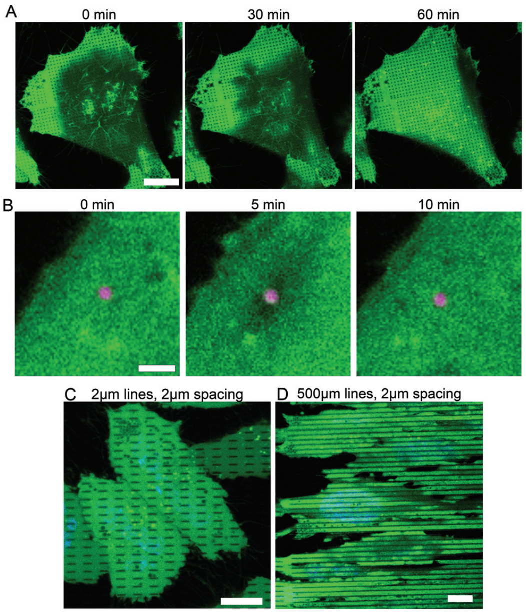

**Fig. 5** Confocal micrographs of live calcein-AM labelled (green) HeLa cells showing dynamics of cell adhesion on nanopillar substrates. The focal plane was fixed just above the substrate, brighter areas indicate cell cytoplasm close to the coverslip, darker areas indicate cell cytoplasm raised from the coverslip. (A) Single HeLa cell transitioning from a mostly suspended to nearly fully adhered state on 1 μm spaced nanopillars. Nanopillars are seen as black dots against the green cytoplasmic background. Scale bar 10 μm. (B) Cells were generally adhered on 5 μm spaced nanopillars, but the cell cytoplasm distance to the cover slip could still fluctuate locally around single nanopillars as observed by a temporary decrease of the intensity. An image of the nanopillar (magenta dot) is overlayed. Scale bar 2 μm. The full time-lapse sequences are available in the ESI as Movie S1 and S2.† (C) On shorter lines, such as 2 μm lines spaced by 2 μm, the cells remained fully adhered, only showing a cytoplasmic exclusion effect at the nanolines, while on longer lines of 500 μm spaced by 2 μm (D), larger areas of the cells could be suspended between the lines, as seen by the darker cytoplasmic signal in portions of the cells. Scale bars (C) and (D) are 10 μm, Hoechst-labelled nucleus shown in cyan.

Together, these results indicate that there is a constant and shifting balance of forces between adhesion energy to the cover slip (and possibly the nanostructures) on the one hand, and the energy required to engulf the nanostructures on the other hand, as also indicated by theoretical models.[57] These changes in modes of cell adhesions could have implications for applications within cell migration,[15] cell force studies,[14] as well as cell capture[58] and stem cell guidance.[27]

Although the cytoplasmic exclusion effect is occasionally indicated as proof of cell plasma membrane penetration, we and others have shown that the cell plasma membrane can wrap tightly around high aspect ratio nanostructures, leading

Published on 03 April 2015. Downloaded by Norwegian University of Science and Technology on 23/04/2015 13:33:11.

to similar cytoplasmic images without membrane penetration.[8,10,59] To gain increased insight into the cell membrane conformation around our SU-8 nanopillars, in particular to investigate whether nanopillars could be observed to penetrate the cell plasma membrane, we used combined widefield and TIRF fluorescence imaging of CellMask Orange-labelled HeLa cells (Fig. 6).

On 1 μm high square arrays, 120 nm tip diameter nanopillar arrays spaced by 1 μm, an increased membrane signal was observed at each nanopillar site, although the signal varied within each cell (Fig. 6A, left panel). This effect can be explained by considering that if the cell membrane wraps around the nanopillar, the number of fluorophores in the fluorescence excitation volume (which typically extends at least 500 nm in *z*-direction) increases as the membrane rises along the nanopillars in parallel with the optical axis.[60] The signal intensity variation can be explained by different degrees of cell membrane wrapping around the nanopillars, as the cell is suspended to various heights. Correspondingly, as TIRF microscopy is only sensitive to fluorescent structures within close proximity (50–100 nm) of the cover slip, adherent areas of the cell membrane gave a strong signal, while in areas where the cell membrane was suspended by the nanopillars the TIRF signal disappeared (Fig. 6A, center panel). This occurred both locally at each nanopillar, and over larger areas towards the cell centers, confirming the results from the cell cytoplasm imaging above. The cell body suspension effect disappeared as soon as the spacing between the nanopillars increased, even locally, as could be observed at the gap in the nanopillar pattern indicated in Fig. 6A. On 2 μm spaced pillars, the cells remained fully adhered as indicated by the corresponding TIRF and widefield signals (ESI Fig. S7†).

By comparing the relative intensities of the widefield and TIRF signals, three observed membrane states are proposed (Fig. 6B). State (1), with a strong TIRF signal adjacent to the nanopillars and the widefield membrane signal enhanced at the nanopillar site, indicates a tight wrapping of the nanopillar by the cell membrane. In state (2), the absence of a TIRF signal indicates that the membrane is suspended, and the reduced widefield signal indicates a low degree of nanopillar wrapping. In state (3), the presence of an increased widefield signal combined with the absence of a TIRF signal indicates partial membrane wrapping of the nanopillars, and thus is an intermediate state between fully wrapping (1) and suspended (2) states.

A fourth state is also possible, in which the nanopillars would directly penetrate the cell membrane and no wrapping would occur. This state would be characterized by a low widefield signal together with a high TIRF signal, but this was not observed in our experiments. Transmission electron microscopy (TEM) investigations of neurons on quartz nano-

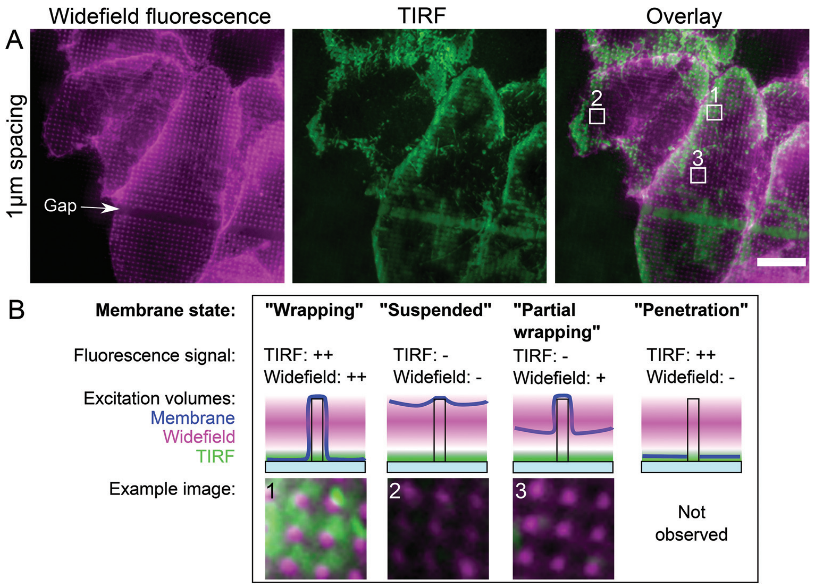

**Fig. 6** Widefield and TIRF micrographs of the plasma membrane of CellMask orange-labelled HeLa cells on 1 μm high square nanopillar arrays with 1 μm spacing. (A) An increase of widefield signal could be observed at nanopillar locations (left panel), although in general the membrane signal was stronger towards the periphery of the cells. Corresponding TIRF images (center panel) highlights areas of the cell membrane in contact with the cover slip, demonstrating that the cell membrane is in fact suspended towards the center of the cells on this nanopillar spacing. Gaps in the nanopillar array such as indicated in the left panel led to membrane contact with the cover slip. (B) By inspection of the intensity relations between widefield and TIRF signals of the same areas, several alternate membrane states are proposed. (1) Fully "wrapping", (2) fully "suspended" or (3) "partial wrapping", taken from the areas marked in (A). The fourth alternative state of "penetration" was not observed. Scale bars 5 μm.

Published on 03 April 2015. Downloaded by Norwegian University of Science and Technology on 23/04/2015 13:33:11.

pillar arrays have revealed similar results, indicating both wrapping and suspended states, depending on nanopillar diameter and spacing.[10] However, the interim states of partial wrapping of nanopillars, or that of different areas of the cell being suspended or adhering to the cover slip was not reported, and would be beneficial to investigate further using TEM. Note that a local membrane penetration only at the top of the nanopillar or at isolated places along the nanopillar could still occur as suggested in theoretical models,[57] as this state would not be distinguishable from state (1) or (3).

Actin filaments and cell membrane dynamics are highly interrelated.[61] Previous observations indicate that actin filaments might be influenced by the presence of high aspect ratio nanostructures.[8] This was observed to be the case for our SU-8 nanopillars and nanolines as well. Initial confocal microscopy showed colocalization between phalloidin-labelled actin in HeLa cells and nanopillars, but the resolution was insufficient to gain further insight into the actin structure (see ESI Fig. S8†). Due to the nature of our device (the 0.17 mm glass cover slip substrate in particular) super-resolution optical microscopy methods such as 3D-SIM and STED could be used to image actin filaments at higher resolution. Actin was observed to bundle around the nanopillars, although the amount of actin varied from pillar to pillar (Fig. 7A). Thus, it is unlikely that this effect arises only due to signal enhancement as described for the membrane signal above, rather a more specific interaction is likely in this case. Additionally, in certain cells (about 10%) on 1 μm spaced nanopillars, alignment of actin filaments was observed along specific directions in the nanopillar array (a hexagonal array in this case), as

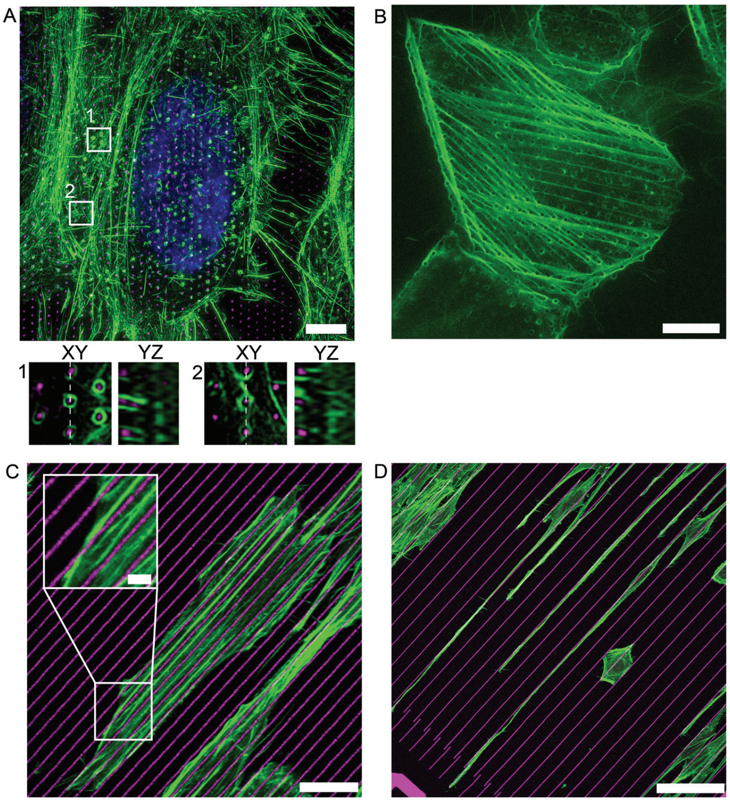

**Fig. 7** 3D-SIM, STED and confocal microscopy of HeLa cell actin in response to arrays of 1 μm high, 120 nm diameter nanopillars and nanolines. Maximum intensity projection of a 3D-SIM stack showing phalloidin-Alexa488-labelled actin (green), Hoechst 34580 labelled nucleus (blue) and 1 μm spaced nanopillars (magenta) in a hexagonal array. The actin filaments associated with the nanopillars at multiple locations both in the cell center and periphery. The cut-outs are single planes and cross-sections from the stack at the indicated positions. Scale bar 5 μm. (B) STED image of actin filaments forming aligned bundles that appear to be directed by the hexagonal array of nanopillars in the majority of the cell. (C) Confocal micrograph of cells on 1 μm high, 500 μm long nanolines spaced by 2 μm, showing that actin filaments orient along the direction of the nanolines, but do not appear to bind significantly to the nanolines. However, actin filaments could cross the nanolines, as shown in the inset. Scale bar 10 μm, inset 2 μm. (D) 500 μm long nanolines spaced by 10 μm could guide actin-containing cellular protrusions along the side of the lines, leading to highly elongated cells spanning up to 400 μm. Scale bar 50 μm.

Published on 03 April 2015. Downloaded by Norwegian University of Science and Technology on 23/04/2015 13:33:11.

shown in Fig. 7B. On 500 μm nanolines, which were shown to induce the strongest alignment and elongation previously, regular confocal microscopy showed alignment of the actin filaments along the direction of the nanolines (Fig. 7C). The actin filaments did not appear to bind to the nanolines, but rather formed between them, although actin filaments were observed to cross lines occasionally (Fig. 7C, inset). Finally, 500 μm nanolines could be seen to induce the formation of highly elongated, actin-containing cell protrusions (up to 200 μm in length), which were guided along the sides of single nanolines (Fig. 7D).

Although filopodia are known to react and bind to nanoscale topographies,[62] such local and specific actin structures have not been reported before on high aspect ratio nanostructures, and could contribute in the understanding cell interactions with nanostructured surfaces.

## Conclusion

Enhanced surface-based delivery of functional biomolecules,[23,24,63] neural guidance,[15,56] cell differentiation and response[18,19] and circulating tumour cell capture[21] are some examples of interesting applications of high aspect ratio nanostructures, and further developments rely on a better understanding of the fundamental interactions between cells and nanostructures. In this work we have developed a flexible nanostructured polymer-based system optimized for cell biology applications and investigations. Our results demonstrate strong interactions between cells and high aspect ratio polymer nanostructures, influencing several aspects of cell response. Due to the design of our system, where the nanostructures were produced directly on standard glass coverslips, super-resolution microscopy methods such as TIRF, STED and 3D-SIM together with live-cell imaging revealed details about how the actin cytoskeleton and cell membrane conform and bind to the nanostructures, giving important indications of the underlying mechanisms of cell responses. In particular, detailed views of actin associating with nanopillars, actin fiber guidance by nanolines, cell membrane wrapping of nanopillars and the dynamics of cell adherence on the nanopillars demonstrate the range of little characterized biological responses to high aspect ratio nanostructures that were investigated in the presented system. In addition, due to the flexibility of the single-step patterning and fabrication approach together with high control over nanostructure surface chemistry, the range of tunable parameters greatly increases, allowing us to, *e.g.*, explore the effects of nanolines compared to nanopillars. However, here we only investigated a small subset of the available parameter space offered by the presented fabrication and chemical modification processes. Although we focus on high aspect ratio nanostructures, the introduced platform can be extended to other types of nanoscale patterns. A range of further parameters, especially independent tuning of nanostructure geometry and surface chemistry, should be further investigated for their influence on the structure and functionality of different cell types. Through the use of systems that are controllable yet flexible, one can start to unravel the causal relationships between membrane dynamics, cytoskeletal arrangements, and functional cell responses that lead to novel biotechnological applications.

## Materials and methods

### SU-8 nanostructure fabrication

All chemicals and reagents were purchased for Sigma-Aldrich (Oslo, Norway) unless otherwise specified.

0.17 mm (#1.5) glass cover slips (Menzel-Glaser borosilicate glass) were cleaned in acetone, isopropanol and DIW, then subjected to oxygen plasma of 0.8 mbar at 100 W for 2 minutes in a Diener Femto plasma cleaner. The glass was then rinsed again in acetone, isopropanol and DIW, dehydrated for 2 minutes on a 95 °C hot plate, before spin coating SU-8.

To produce SU-8 solutions of different viscosities (and therefore final film thickness), SU-8 2100 (Microchem) was diluted in SU-8 2000 thinner (cyclopentanone, Microchem). Fluorescent SU-8 was made by mixing the SU-8 with the hydrophobic laser dyes Rhodamine 6G or Oxazine 170. The dyes were dissolved directly in the SU-8 resist to a final concentration of 100 μg mL$^{-1}$. SU-8 was spin coated at 6000 rpm for 36 s to produce SU-8 layers of the desired thickness (from 100–2000 nm). The samples were then soft-baked for 1 minute at 95 °C.

Electron beam exposure of the SU-8 was performed in a Hitachi S-4300 SEM modified with a Raith Quantum stage and pattern generator. The exposures were performed at 30 kV with a 100 pA beam current. The exposure dose was varied to find the optimal exposures as described in the main text. Nanopillars and nanolines were typically exposed as single-pixel dots or lines, but larger areas could be written to achieve larger features. Optimized exposure doses for different feature types are detailed in the ESI.† The samples were then post-exposure baked at 95 °C for 1 minute, developed with mild agitation for 20 s in SU-8 developer (mr-dev 600, Microchem), then 20 s in a fresh developer, and finally rinsed in isopropanol and dried with $N_2$. Longer post-exposure bakes (2–5 minutes) were possible, and led to nanostructures with increased diameter but also increased stability during handling. Oxygen plasma thinning of the nanopillars was performed for 30–210 s in a 0.4 mbar oxygen plasma at 50 W.

Finished devices were scribed using a Dynatex DX-III scriber into small samples (typically 6 × 6 mm). The samples were imaged using a Hitachi S-4300 or Hitachi S-5500 SEM after sputter coating a 5 nm Au layer for observation, and a Leica SP5 confocal microscope with the appropriate laser lines (561 nm for Rhodamine 6G, 633 nm for Oxazine 170). During SEM imaging the samples were tilted to 40° or 85° for observation of standing nanopillars. Electron trajectory simulations were performed using Casino v. 2.48.[64]

Published on 03 April 2015. Downloaded by Norwegian University of Science and Technology on 23/04/2015 13:33:11.

Unless specifically modified as described below, samples for cell culturing were typically treated with oxygen plasma at 0.4 mbar at 50 W for 30 s.

### SU-8 surface modification and surface characterization

Wet chemical surface modification of SU-8 was performed by incubating test surfaces in aqueous solutions containing molecules with thiol or amine groups. The SU-8 test surfaces were made as above, but instead of electron-beam lithography exposure, the SU-8 was flood-exposed or exposed through a quartz-chrome mask with 365 nm UV light (500 mJ cm$^{-2}$) in a Karl Suss MA6 mask aligner. Surfaces patterned by electron beam lithography were tested in the last step of the method development process. During initial experiments, a contaminating layer was observed on the glass surface after SU-8 processing (unless oxygen plasma treatment was used). Thus a cleaning step was implemented prior to surface modification: the sample was immersed for 1 minute in 1 M NaOH in MilliQ water at 50 °C.

The pH of each modification solution was set to the p$K_a$ of the active thiolate or amine species. Solutions of 1 M of ethanolamine (pH = 9.50), cysteamine (pH = 8.2), β-mercaptoethanol (pH = 9.64), and a 1 mM solution of *O*-(2-mercaptoethyl)-*O*-methylpolyethylene glycol (PEG-SH, molecular weight 10 kDa, p$K_a$ not available but assumed to be similar to 3-methyl mercaptopropionate at pH = 9.33) were made in MilliQ water and the pH was set by addition of 1 M HCl or 1 M NaOH, or 10 mM bicarbonate in the case of PEG-SH. Working solutions were freshly made to avoid auto-oxidation of the thiol species.[65] To increase the shelf life of stock thiol-containing solutions, 1 mM of EDTA was added, and the pH was left at the native pH of the solutions before adding NaOH, reducing the number of active thiolate species to a minimum. Just before use, the appropriate amount of 1 M NaOH was added to increase the pH to the value given above. After incubating the samples for a certain reaction time (typically 60 minutes) at room temperature, the surfaces were rinsed thoroughly in MilliQ water and dried using compressed air.

To assess the efficacy of the various modification solutions, water contact angles were measured on the modified SU-8 surfaces. 2 μL droplets were dispensed and static, advancing and receding contact angles were measured using an in-house made contact angle measuring apparatus. The contact angle images were analysed using the LB-ADSA part of the Droplet Analysis plugin[66] for FIJI.[67] At least three samples per condition were measured.

X-ray photoelectron spectroscopy (XPS) measurements were performed using a Specs PHOIBOS-150 hemispherical electron analyser and MgK$_\alpha$ X-ray lamp ($h_\nu$ = 1253.6 eV) connected to a custom UHV system with a base pressure of $1 \times 10^{-10}$ mbar. Survey scans were collected at $E_{\text{pass}}$ = 150 eV and $E_{\text{step}}$ = 1 eV, and selected regions (N 1s and S 2p) were captured for the same pass energy and $E_{\text{step}}$ = 0.1 eV. Silicon wafers with 500 nm SU-8 films, native or modified for 1 hour with cysteamine as described above, were washed in ethanol in an ultrasonic bath and then blown dry with $N_2$ gas before being introduced into the vacuum system.

To verify the functionality of the surfaces, SU-8 features prepared by UV-lithography or electron beam lithography and modified according to the procedures above were labelled using amine-reactive NHS-rhodamine. 1 μM NHS-rhodamine in 10 mM HEPES, pH = 8.0 was incubated for 1 hour on each sample, and the samples were rinsed thoroughly in ethanol and MilliQ water before imaging. The fluorescence intensity was measured using 561 nm excitation and 580–650 nm emission on a Leica SP5 confocal microscope, at least three samples per condition were measured.

Finally, SU-8 and glass were independently modified and labelled. For fluorescence visualization experiments, the SU-8 was first modified by cysteamine and labelled with NHS-rhodamine and cleaned as described above, then the glass was labelled with 1 mg ml$^{-1}$ FITC-labelled poly(ethylene imine) in MilliQ water for 1 hour, prepared as described previously.[68]

For differential cell adhesion experiments two modification schemes were employed. To repel cell attachment from glass while allowing cell attachment to SU-8 features, the samples were incubated in 0.1 mg ml$^{-1}$ PLL(20 kDa)-*g*-PEG (5 kDa) (Susos AG, Dübendorf, Switzerland) in 10 mM HEPES, pH = 7.4 at room temperature for 1 hour.[69] To repel cell attachment from the SU-8 features while allowing cell attachment on glass, the samples were incubated in 1 mM SH-PEG in 10 mM bicarbonate, pH = 9.33. The last incubation was performed under UV illumination from a Dymax Bluewave 50 UV lamp for 15 minutes (approximate illumination intensity of 30 mW cm$^{-2}$).[43]

### Cell experiments

For cell experiments, a simple procedure was used to integrate the nanostructured samples into suitable cell culturing dishes: 3.5 mm holes were drilled into the base of 35 mm polystyrene petri dishes (Nucleon, tissue culture treated). Subsequently, the sample was made to adhere underneath the petri dish with a thin layer of liquid paraffin. As the paraffin solidified, a robust, water-tight seal was formed, with the SU-8 features on glass in small, shallow wells in the base of the petri dish. See ESI Fig. S6† for a detailed schematic.

HeLa cells were grown in DMEM (Gibco, Invitrogen, Oslo, Norway) supplanted with 10% FBS (Invitrogen) and 1% pen/strep and passaged regularly. Cells were seeded in the modified 35 mm dishes at a typical density of 20 000 cells per cm$^2$, *i.e.* 200 000 cells per dish. For live cell imaging cells were labelled with 1 μM calcein-AM (Invitrogen) and Hoechst 34580 in complete DMEM for 30 minutes. The media was then changed to Leibovitz L-15, a $CO_2$ independent medium, and cells were imaged at 37 °C.

For fixed cell experiments, cells were fixed in 4% paraformaldehyde in PBS. Cells were then labelled with CellMask Orange (Invitrogen) or Hoechst 34580, or permeabilized for 3 minutes in 0.1% Triton X-100 and labelled with phalloidin-Alexa 488 (Invitrogen). For 3D-SIM experiments, cells were mounted in Vectashield, while for confocal and STED experiments cells were mounted in Mowiol with 0.05% PPD.

Published on 03 April 2015. Downloaded by Norwegian University of Science and Technology on 23/04/2015 13:33:11.

As CellMask Orange does not survive cell permeabilization, in experiments where both the membrane and actin were visualized the cells were fixed, labelled with CellMask and imaged, before permeabilizing and labelling actin. The same cells were re-located on the sample and the images were automatically overlayed using the StackReg plugin[70] for FIJI.

### Cell imaging

Live and fixed HeLa cells were imaged using a Leica SP8 or SP5 confocal microscope either with a 10× 0.4NA air objective or a 63× 1.4NA oil objective, a Zeiss Axio Observer Z1 TIRF with a 100× 1.4NA oil objective and a Andor iXon DU 897-BV EMCCD camera, a OMX V4 Blaze 3D-SIM microscope with a 100× 1.45NA oil objective and a Leica SP8 confocal microscope with a 592 nm STED depletion laser and a 100× 1.4NA oil objective. High resolution confocal images or stacks were acquired with a 70 nm pixel size and 200 nm slice spacing, TIRF images were acquired at 100 nm pixel size, 3D-SIM images were acquired at 80 nm pixel size with 120 nm slice spacing. STED images were acquired at system optimized pixel size, typically 20–30 nm in XY and 80–100 nm i Z. 3D-SIM images were deconvoluted using software supplied with the microscope, and STED images were deconvoluted using Huygens Professional.

Cell images were prepared using FIJI. Automated analysis of cell viability and cell shape was performed using CellProfiler.[71] For cells on nanopillars, 6 parallel samples were analysed, for a total of over 3600 cells (at least 600 cells for each condition, 4 different nanopillar spacings and 2 control areas). For cells on nanolines, 3 parallel samples were analysed, for a total of over 1800 cells. TIRF and widefield images were inspected manually, at least 25 cells per nanopillar spacing (spacings of 1 µm, 2 µm, 5 µm and 10 µm) were investigated, for a total of 120 analysed cells.

## Acknowledgements

For access to the TIRF instrument we would like to thank Prof. B. T. Stokke and the Research council of Norway (183338/S10). For assistance with 3D-SIM imaging, we thank V. Sørensen at the Core facility for Advanced Light Microscopy at the Oslo University Hospital. STED imaging was performed at the Cellular and Molecular Imaging Core Facility, Norwegian University of Science and Technology (NTNU), with the aid of B. Sporsheim. The Research Council of Norway is acknowledged for the support to the Norwegian Micro- and Nano-Fabrication Facility, NorFab (197411/V30). K.S.B. is additionally supported by grants from NTNU and the Norwegian PhD-school in Medical Imaging.

## References

1 M. M. Stevens and J. H. George, *Science*, 2005, **310**, 1135–1138.

2 N. D. Gallant, J. L. Charest, W. P. King and A. J. García, *J. Nanosci. Nanotechnol.*, 2007, **7**, 803–807.

3 C. J. Bettinger, R. Langer and J. T. Borenstein, *Angew. Chem., Int. Ed.*, 2009, **48**, 5406–5415.

4 H. V. Unadkat, M. Hulsman, K. Cornelissen, B. J. Papenburg, R. K. Truckenmüller, A. E. Carpenter, M. Wessling, G. F. Post, M. Uetz, M. J. T. Reinders, D. Stamatialis, C. A. van Blitterswijk and J. de Boer, *Proc. Natl. Acad. Sci. U. S. A.*, 2011, **108**, 16565–16570.

5 J. Y. Lim and H. J. Donahue, *Tissue Eng.*, 2007, **13**, 1879–1891.

6 S. Bonde, N. Buch-Månson, K. R. Rostgaard, T. K. Andersen, T. Berthing and K. L. Martinez, *Nanotechnology*, 2014, **25**, 362001.

7 R. Elnathan, M. Kwiat, F. Patolsky and N. H. Voelcker, *Nano Today*, 2014, **9**, 172–196.

8 F. Mumm, K. M. Beckwith, S. Bonde, K. L. Martinez and P. Sikorski, *Small*, 2013, **9**, 263–272.

9 S. Bonde, T. Berthing, M. H. Madsen, T. K. Andersen, N. Buch-Månson, L. Guo, X. Li, F. Badique, K. Anselme, J. Nygård and K. L. Martinez, *ACS Appl. Mater. Interfaces*, 2013, **5**, 10510–10519.

10 L. Hanson, Z. C. Lin, C. Xie, Y. Cui and B. Cui, *Nano Lett.*, 2012, **12**, 5815–5820.

11 Z. Yu, T. E. McKnight, M. N. Ericson, A. V. Melechko, M. L. Simpson and B. Morrison, *Nano Lett.*, 2007, **7**, 2188–2195.

12 C. Xie, Z. Lin, L. Hanson, Y. Cui and B. Cui, *Nat. Nanotechnol.*, 2012, **7**, 185–190.

13 J. T. Robinson, M. Jorgolli, A. K. Shalek, M.-H. Yoon, R. S. Gertner and H. Park, *Nat. Nanotechnol.*, 2012, **7**, 180–184.

14 W. Hällström, M. Lexholm, D. B. Suyatin, G. Hammarin, D. Hessman, L. Samuelson, L. Montelius, M. Kanje and C. N. Prinz, *Nano Lett.*, 2010, **10**, 782–787.

15 C. Xie, L. Hanson, W. Xie, Z. Lin, B. Cui and Y. Cui, *Nano Lett.*, 2010, **10**, 4020–4024.

16 S. Y. Kim and E. G. Yang, *Nanotechnology*, 2013, **24**, 455704.

17 H. Persson, C. Købler, K. Mølhave, L. Samuelson, J. O. Tegenfeldt, S. Oredsson and C. N. Prinz, *Small*, 2013, **9**, 4006–4016.

18 M. a. Bucaro, Y. Vasquez, B. D. Hatton and J. Aizenberg, *ACS Nano*, 2012, **6**, 6222–6230.

19 J. Padmanabhan, E. R. Kinser, M. A. Stalter, C. Duncan-Lewis, J. L. Balestrini, A. J. Sawyer, J. Schroers and T. R. Kyriakides, *ACS Nano*, 2014, **8**, 4366–4375.

20 S. T. Kim, D.-J. Kim, T.-J. Kim, D.-W. Seo, T.-H. Kim, S.-Y. Lee, K. Kim, K.-M. Lee and S.-K. Lee, *Nano Lett.*, 2010, **10**, 2877–2883.

21 S.-K. Lee, G.-S. Kim, Y. Wu, D.-J. Kim, Y. Lu, M. Kwak, L. Han, J.-H. Hyung, J.-K. Seol, C. Sander, A. Gonzalez, J. Li and R. Fan, *Nano Lett.*, 2012, **12**, 2697–2704.

22 W. Kim, J. K. Ng, M. E. Kunitake, B. R. Conklin and P. Yang, *J. Am. Chem. Soc.*, 2007, **129**, 7228–7229.

23 T. E. McKnight, A. V. Melechko, D. K. Hensley, D. G. J. Mann, G. D. Griffin and M. L. Simpson, *Nano Lett.*, 2004, **4**, 1213–1219.

24 A. K. Shalek, J. T. Robinson, E. S. Karp, J. S. Lee, D.-R. Ahn, M.-H. Yoon, A. Sutton, M. Jorgolli, R. S. Gertner,

This journal is © The Royal Society of Chemistry 2015

Published on 03 April 2015. Downloaded by Norwegian University of Science and Technology on 23/04/2015 13:33:11.

T. S. Gujral, G. MacBeath, E. G. Yang and H. Park, *Proc. Natl. Acad. Sci. U. S. A.*, 2010, **107**, 1870–1875.

25 L. Lampert, B. Timonen, S. Smith, B. Davidge, H. Li, J. F. Conley, J. D. Singer and J. Jiao, *Chem. Commun.*, 2014, **50**, 1234–1237.

26 J. Yang, F. R. J. Rose, N. Gadegaard and M. R. Alexander, *Adv. Mater.*, 2009, **21**, 300–304.

27 E. H. Ahn, Y. Kim, Kshitiz, S. S. An, J. Afzal, S. Lee, M. Kwak, K.-Y. Suh, D.-H. Kim and A. Levchenko, *Biomaterials*, 2014, **35**, 2401–2410.

28 H. Lorenz, M. Despont, N. Fahrni, N. LaBianca, P. Renaud and P. Vettiger, *J. Micromech. Microeng.*, 1997, **7**, 121–124.

29 A. Pepin, V. Studer, D. Decanini and Y. Chen, *Microelectron. Eng.*, 2004, **73**, 233–237.

30 D. López-Romero, C. Barrios, M. Holgado, M. Laguna and R. Casquel, *Microelectron. Eng.*, 2010, **87**, 663–667.

31 F. J. Ortega, M.-J. Bañuls, F. J. Sanza, R. Casquel, M. F. Laguna, M. Holgado, D. López-Romero, C. A. Barrios, A. Maquieira and R. Puchades, *Biosensors*, 2012, **2**, 291–304.

32 C.-W. Kuo, J.-Y. Shiu, F.-C. Chien, S.-M. Tsai, D.-Y. Chueh and P. Chen, *Electrophoresis*, 2010, **31**, 3152–3158.

33 V. N. Vernekar, D. K. Cullen, N. Fogleman, Y. Choi, A. J. García, M. G. Allen, G. J. Brewer and M. C. LaPlaca, *J. Biomed. Mater. Res., Part A*, 2009, **89**, 138–151.

34 M. Stangegaard, Z. Wang, J. P. Kutter, M. Dufva and A. Wolff, *Mol. BioSyst.*, 2006, **2**, 421.

35 P. Y. Yeh, Z. Zhang, M. Lin and X. Cao, *Langmuir*, 2012, **28**, 16227–16236.

36 S. L. Tao, K. Popat and T. a. Desai, *Nat. Protoc.*, 2006, **1**, 3153–3158.

37 Y. Wang, M. Bachman, C. E. Sims, G. P. Li and N. L. Allbritton, *Langmuir*, 2006, **22**, 2719–2725.

38 F. Walther, P. Davydovskaya, S. Zürcher, M. Kaiser, H. Herberg, A. M. Gigler and R. W. Stark, *J. Micromech. Microeng.*, 2007, **17**, 524–531.

39 P. Xue, J. Bao, Y. J. Chuah, N. V. Menon, Y. Zhang and Y. Kang, *Langmuir*, 2014, **30**, 3110–3117.

40 L. Shechter, J. Wynstra and R. P. Kurkjy, *Ind. Eng. Chem.*, 1956, **48**, 94–97.

41 S. De and A. Khan, *Chem. Commun.*, 2012, **48**, 3130–3132.

42 C. E. Hoyle, A. B. Lowe and C. N. Bowman, *Chem. Soc. Rev.*, 2010, **39**, 1355–1387.

43 E. Peris, M.-J. Bañuls, R. Puchades and A. Maquieira, *J. Mater. Chem. B*, 2013, **1**, 6245.

44 L. De Sio, J. G. Cuennet, A. E. Vasdekis and D. Psaltis, *Appl. Phys. Lett.*, 2010, **96**, 131112.

45 A. Marino, G. Ciofani, C. Filippeschi, M. Pellegrino, M. Pellegrini, P. Orsini, M. Pasqualetti, V. Mattoli and B. Mazzolai, *ACS Appl. Mater. Interfaces*, 2013, **5**, 13012–13021.

46 B. L. Aekbote, J. Jacak, G. J. Schütz, E. Csányi, Z. Szegletes, P. Ormos and L. Kelemen, *Eur. Polym. J.*, 2012, **48**, 1745–1754.

47 R. Liu, B. Lu, S. Xie, J. Wan, Z. Shu, X. Qu and Y. Chen, *J. Korean Phys. Soc.*, 2009, **55**, 1290–1294.

48 B. Thierry, M. Jasieniak, L. C. P. M. de Smet, K. Vasilev and H. J. Griesser, *Langmuir*, 2008, **24**, 10187–10195.

49 J. F. Joanny and P. G. de Gennes, *J. Chem. Phys.*, 1984, **81**, 552.

50 M. Wirde, U. Gelius and L. Nyholm, *Langmuir*, 1999, **15**, 6370–6378.

51 J. Escorihuela, M.-J. Bañuls, R. Puchades and A. Maquieira, *Bioconjugate Chem.*, 2012, **23**, 2121–2128.

52 G. Csucs, R. Michel, J. W. Lussi, M. Textor and G. Danuser, *Biomaterials*, 2003, **24**, 1713–1720.

53 M. Hennemeyer, F. Walther, S. Kerstan, K. Schürzinger, A. M. Gigler and R. W. Stark, *Microelectron. Eng.*, 2008, **85**, 1298–1301.

54 W. Hu, A. S. Crouch, D. Miller, M. Aryal and K. J. Luebke, *Nanotechnology*, 2010, **21**, 385301.

55 C. Oakley and D. Brunette, *J. Cell Sci.*, 1993, **106**, 343–354.

56 W. Hällström, T. Mårtensson, C. Prinz, P. Gustavsson, L. Montelius, L. Samuelson and M. Kanje, *Nano Lett.*, 2007, **7**, 2960–2965.

57 X. Xie, A. M. Xu, M. R. Angle, N. Tayebi, P. Verma and N. A. Melosh, *Nano Lett.*, 2013, **13**, 6002–6008.

58 S. Wang, Y. Wan and Y. Liu, *Nanoscale*, 2014, **6**, 12482–12489.

59 T. Berthing, S. Bonde, K. R. Rostgaard, M. H. Madsen, C. B. Sørensen, J. Nygård and K. L. Martinez, *Nanotechnology*, 2012, **23**, 415102.

60 K. R. Rostgaard, R. S. Frederiksen, Y.-C. C. Liu, T. Berthing, M. H. Madsen, J. Holm, J. Nygård and K. L. Martinez, *Nanoscale*, 2013, **5**, 10226–10235.

61 H. T. McMahon and J. L. Gallop, *Nature*, 2005, **438**, 590–596.

62 J. Albuschies and V. Vogel, *Sci. Rep.*, 2013, **3**, 1658.

63 J. Peng, M. A. Garcia, J.-S. Choi, L. Zhao, K.-J. Chen, J. R. Bernstein, P. Peyda, Y.-S. Hsiao, K. W. Liu, W.-Y. Lin, A. D. Pyle, H. Wang, S. Hou and H.-R. Tseng, *ACS Nano*, 2014, **8**, 4621–4629.

64 D. Drouin, A. R. Couture, D. Joly, X. Tastet, V. Aimez and R. Gauvin, *Scanning*, 2007, **29**, 92–101.

65 R. Stevens, L. Stevens and N. Price, *Biochem. Educ.*, 1983, **11**, 70.

66 A. F. Stalder, T. Melchior, M. Müller, D. Sage, T. Blu and M. Unser, *Colloids Surf., A*, 2010, **364**, 72–81.

67 J. Schindelin, I. Arganda-Carreras, E. Frise, V. Kaynig, M. Longair, T. Pietzsch, S. Preibisch, C. Rueden, S. Saalfeld, B. Schmid, J.-Y. Tinevez, D. J. White, V. Hartenstein, K. Eliceiri, P. Tomancak and A. Cardona, *Nat. Methods*, 2012, **9**, 676–682.

68 K. M. Beckwith and P. Sikorski, *Biofabrication*, 2013, **5**, 045009.

69 A. Azioune, M. Storch, M. Bornens, M. Théry and M. Piel, *Lab Chip*, 2009, **9**, 1640–1642.

70 P. Thévenaz, U. E. Ruttimann and M. Unser, *IEEE Trans. Image Process.*, 1998, **7**, 27–41.

71 L. Kamentsky, T. R. Jones, A. Fraser, M.-A. Bray, D. J. Logan, K. L. Madden, V. Ljosa, C. Rueden, K. W. Eliceiri and A. E. Carpenter, *Bioinformatics*, 2011, **27**, 1179–1180.

# Supplementary Information to Tunable High Aspect Ratio Polymer Nanostructures for Cell Interfaces

Kai Sandvold Beckwith,[*] Simon P. Cooil, Justin W. Wells, and Pawel Sikorski

*Department of Physics, Norwegian University of Science and Technology, Trondheim, Norway*

E-mail: kai.beckwith@ntnu.no

Table 1: Optimal electron beam exposure doses ensuring high aspect ratio nanostructures using single-pixel dot or single-pixel line exposures in 1 µm SU-8 resist on glass. These doses are above the absolute minimum for standing features, to ensure 100% yield. For thinner SU-8 films (possible down to 100 nm) the same doses can be used successfully to achieve ∼ 100 nm features, although lower doses should be used to reach the smallest feature size possible.

| Spacing | Pillar dose [aC] | Line dose [pC cm$^{-1}$] |
|---|---|---|
| 0.75 µm | 2250 | N/A |
| 1 µm | 2400 | 50 |
| 2 µm | 2600 | 60 |
| 5 µm | 2750 | 70 |
| 10 µm | 2750 | 70 |

---

[*] To whom correspondence should be addressed

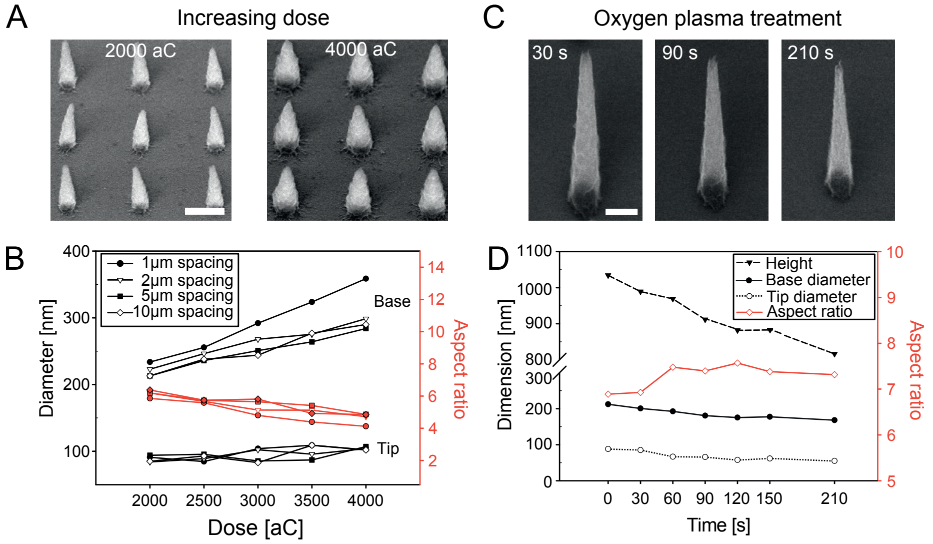

Figure S 1: (A) Tilted SEM images of 1 µm high nanopillars with a 1 µm spacing, with exposure doses of 2000 aC and 4000 aC, showing feature broadening with increasing dose. Scale bar 500 nm. (B) Base and tip diameters (defined as the cross-section 100 nm from the respective apexes) of 1 µm SU-8 nanopillars at various inter-pillar spacings and exposure doses were measured. The associated aspect ratios, defined as the height of the nanopillars divided by the average of the base and tip diameters was also calculated. In particular, nanopillars with 1 µm spacing show increased base broadening at higher doses compared to e.g. nanopillars with $\geq 2$ µm spacing, while the tip diameter does not increase as much. (C) Nanopillars were etched by increasing exposure times to oxygen plasma, which reduced both diameter and height of the nanopillars. Scale bar 200 nm. (D) Measured base diameter, tip diameter and height of nanopillars exposed to oxygen plasma for 0-120 s.

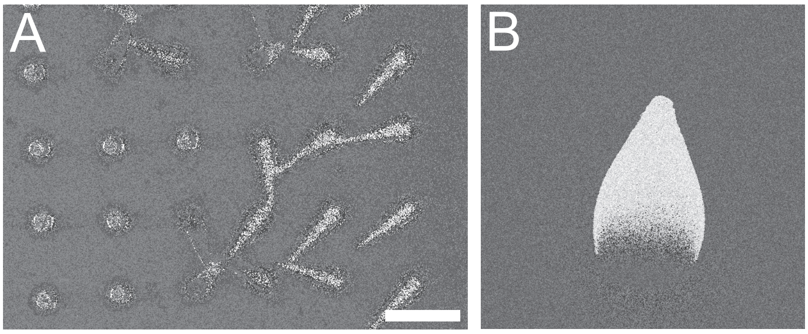

Figure S 2: Possibly encountered issues during processing. (A) Due to under-exposure, some pillars have collapsed during development due to capillary forces. To avoid this, increase dose or increase PEB time. (B) If thick resist films are used (2 µm is shown here), electron scattering through the resist causes features to become increasingly drop-shaped and broad towards the base. The maximum SU-8 thickness that gives relatively straight side-walls on the nanostructures depends on the acceleration voltage of the EBL system, but was around 1 µm for our 30 kV system.

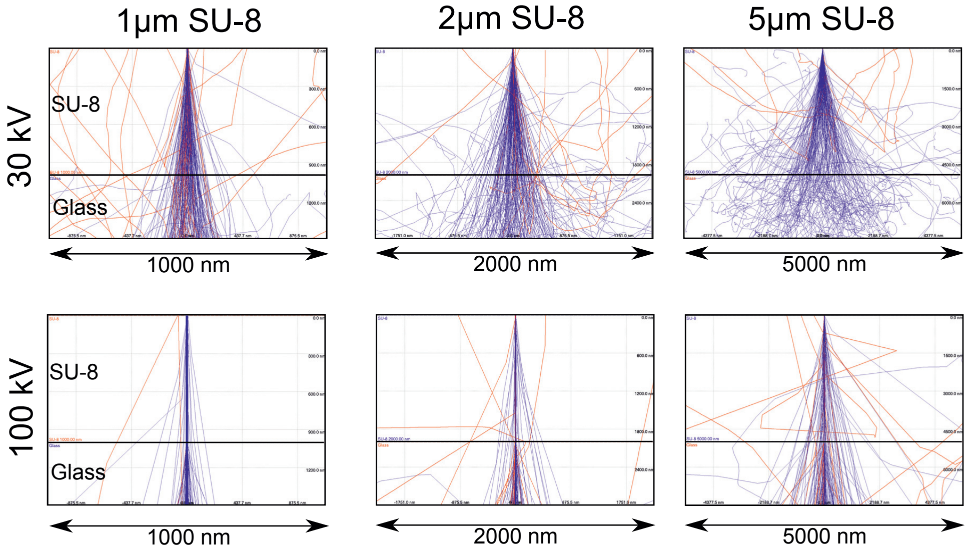

Figure S 3: Simulations of electron trajectories through SU-8 films of 1, 2 and 5 µm thickness on glass substrates with acceleration voltages of 30 and 100 kV. Blue trajectories are forward scattered electrons, while red trajectories are backscattered electrons, secondary electrons are not shown. Thicker resist films give more electron scattering, broadening features and reducing the minimal feature spacing possible. However, these effects are greatly diminished at 100 kV compared to 30 kV, indicating possibilities to make higher aspect ration nanostructures with 100 kV electron beam lithography systems. Simulations performed in Wincasino v. 2.48.

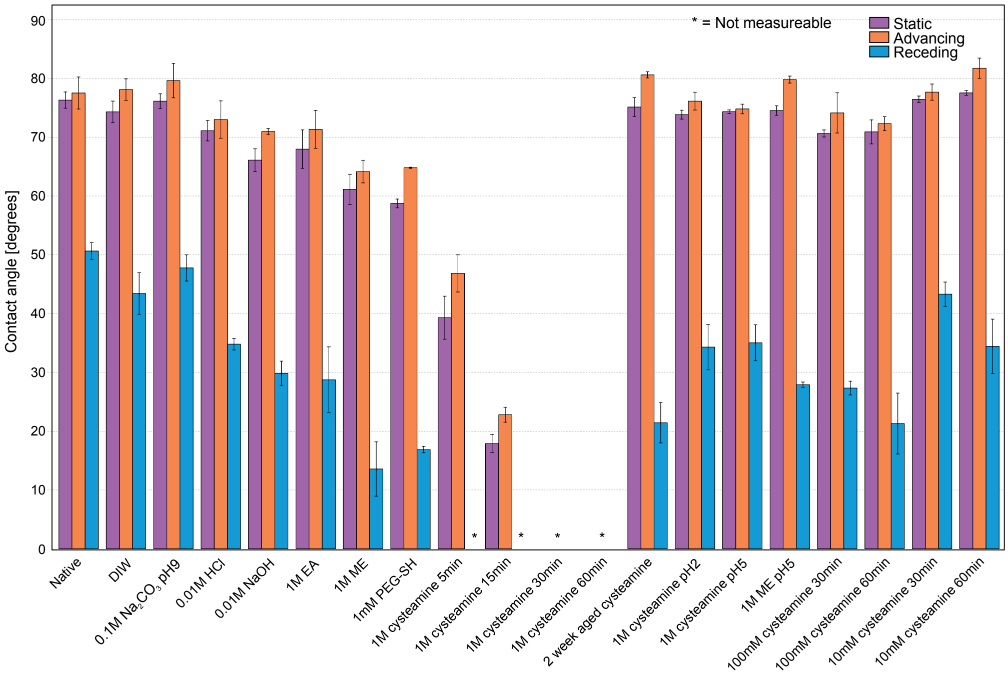

Figure S 4: Static, advancing and receding contact angles after SU-8 surface modifications. Treatment time was 60 minutes unless otherwise indicated, and performed at room temperature. EA = ethanolamine, ME=$\beta$-mercaptoethanol. If the contact angle was below approximately 10° it was deemed too low to measure and denoted by *. Most treatments except those with thiolates at pH 8-9 made only small changes in the contact angles. Thiolates at lower pH, aged working solutions (due to autooxidation) as well as lower concentrations showed reduced or absent alteration of contact angles, indicating a low reactivity.

### Notes on surface contamination of glass after SU-8 processing

During initial experiments on fluorescent labelling of modified SU-8 with NHS-rhodamine, a significant background signal was observed on the glass surrounding the measured SU-8 features, especially on cysteamine-modified samples. This undesired background signal was not present on control glass surfaces, and must thus be attributed to a surface alteration occurring during the SU-8 processing. Indeed, if an SU-8 film was simply spin-coated then removed again by immersion in the SU-8 developer, a marked increase in contact angle on the glass support was observed, indicating the formation of some form of contaminating residual layer. The contaminating layer could not be removed by thorough washing in fresh developer or other solvents. Although is was removed by oxygen plasma treatment, oxygen plasma also quickly breaks down the surface epoxide groups on SU-8, prohibiting any specific thiol-epoxide chemistry, so this was not a viable alternative. Finally, wet cleaning with NaOH at 50 °C for 1-5 minutes was able to thoroughly clean the glass, presumably due to slight etching of the glass by NaOH. The cleaning procedure usually did not harm microscale or nanoscale SU-8 features, although detachment was occasionally observed, especially at longer incubation times. The signal from the glass surrounding the SU-8 features after cleaning was indistinguishable from clean glass. All fluorescent measurements were performed after implementing the cleaning procedure, indicating that the specific thiol-based chemistry on SU-8 was not substantially influenced.

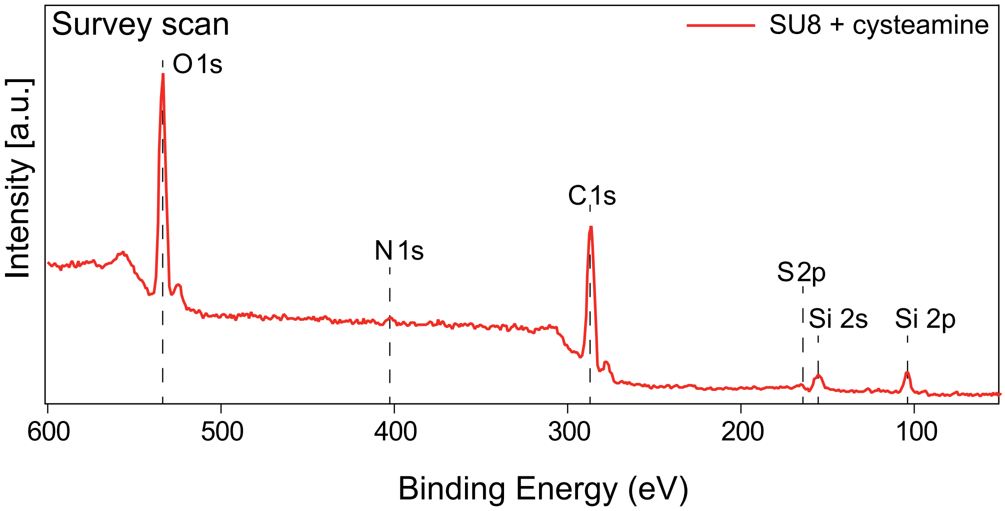

Figure S 5: XPS survey spectra of cysteamine-modified SU-8 film on a silicon wafer (1 hour incubation). The silicon peaks are most likely caused by a signal from the wafer substrate via defects or scratches in the film. Carbon and oxygen peaks originate from both the SU-8 film as well as surface contamination, while the nitrogen and sulphur peaks originate from cysteamine molecules binding to the SU-8.

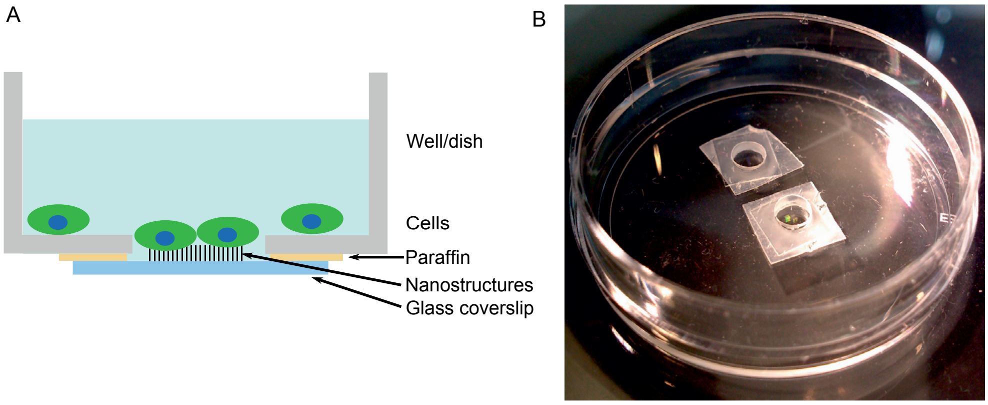

Figure S 6: (A) Schematic view of the mounting of glass coverslips with SU-8 nanostructures into dishes suitable for cell culturing and high resolution live and fixed cell microscopy. Typically, one or more holes of 3.5 mm were drilled into the base of a 35 mm petri dish. A matching hole was punctured in a piece of parafilm. The glass cover slip was then adhered by careful heating on a hot-plate or with a wide-tipped soldering iron until the parafilm melted, creating a water-tight seal. (B) Example of dish used, containing two samples mounted as described in (A).

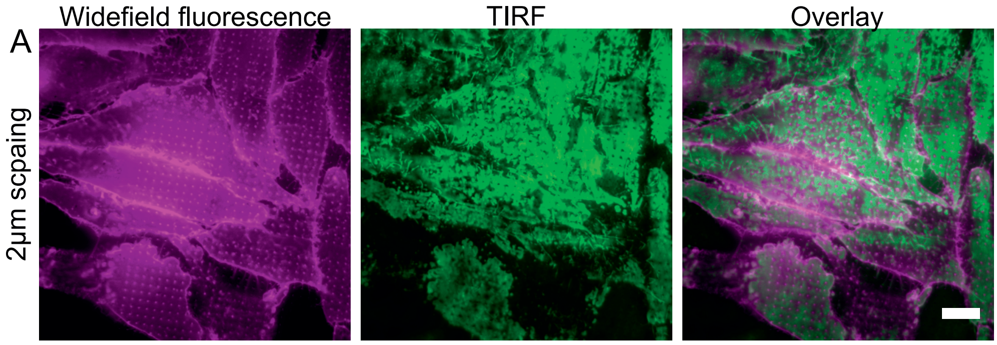

Figure S 7: Widefield and TIRF micrographs of the plasma membrane of CellMask orange-labelled HeLa cells on 1 µm high square nanopillar arrays with 2 µm spacing. An increase of widefield signal could be observed at nanopillar locations (left panel), compared to the membrane on glass (between the nanopillars, and left part of figure with no nanopillars). Corresponding TIRF images (center panel) highlights areas of the cell membrane in contact with the cover slip, demonstrating that the cell membrane is nearly fully in contact with the cover slip at this nanopillar spacing, as opposed to the 1 µm spaced nanopillars described in the main text.

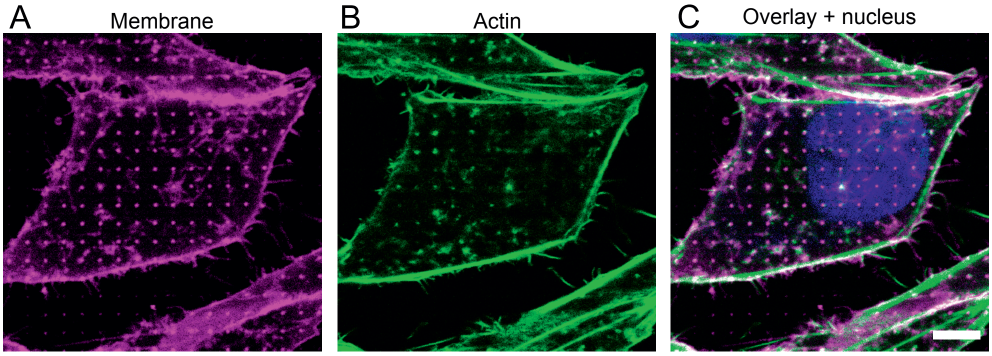

Figure S 8: Scanning confocal micrograph of HeLa cells growing on 2 µm spaced nanopillar array. The cells were labelled with (A) CellMask orange for the plasma membrane (magenta), (B) phalloidin-Alexa488 for actin filaments (green) and (C) overlay image with Hoechst 34580 for the nucleus (nucleus). The cell membrane shows an increased signal at each nanopillar site due to wrapping of the cell membrane around the nanopillars, while the actin shows a certain degree of colocalization at some nanopillar sites. Although the colocalization can be observed, further details are obscured by the resolution limits of the confocal microscope, even if these results were acquired at best possible resolution with a 63X 1.4 oil immersion objective. In the main text results on cell membrane and actin conformation are therefore presented and elaborated using superresolution methods such as TIRF, 3D-SIM and STED. Scale bar 5 µm.

# Paper V

Is not included due to copyright